

University of Strathclyde

Department of Electronic and Electrical Engineering

Advanced control of switched reluctance machines and electrical machine emulation

by

Euan Macrae

B.Sc.

A thesis presented in fulfilment of the requirements for the degree of
Doctor of Philosophy

2024

This thesis is the result of the author's original research. It has been composed by the author and has not been previously submitted for examination which has led to the award of any degree.

The copyright of this thesis belongs to the author under the terms of the United Kingdom Copyright Acts as qualified by University of Strathclyde Regulation 3.50. Due acknowledgement must always be made of the use of any material contained in, or derived from, this thesis.

Signed: Euan Macrae

Date: 04/11/2024

Acknowledgement

I would like to express my deep appreciation of my supervisors Prof. Khaled Ahmed and Prof. Barry Williams for their support during my research, offering their expertise, encouragement, ideas, advice, and their overall supervision which has been crucial for my progress throughout the doctorate.

I would like to thank my industrial sponsors Technelec, which includes Richard Pollock, Charles Pollock and Helen Pollock. Without their material support and vast knowledge, I would not have been able to make the developments I have.

I would also like to thank my colleagues and staff in PEDEC for their support, useful critique, and offering a positive atmosphere to work in, which has allowed me to progress in my research. Specifically, I would like to express my gratefulness to Dr. Ali Abdel Aziz, who has been there to support me throughout the whole process and has provided invaluable advice and knowledge. I would also like to thank Sophie Coffey, Victor Forbes, Sam Harrison, Luke Benedetti and Prof. Augusti Egea Alvarez.

Finally, I would like to thank my family, including my partner Zoe, my parents and my siblings for their support of me throughout the last three years.

Contents:

| | | |
|-----------|---|----|
| Chapter 1 | Introduction..... | 16 |
| 1.1 | Background and motivation..... | 16 |
| 1.2 | Objectives of the thesis..... | 20 |
| 1.3 | Outline of the thesis..... | 21 |
| | References..... | 22 |
| Chapter 2 | Fundamentals of SRM Operation..... | 24 |
| 2.1 | Introduction..... | 24 |
| 2.2 | SRM Torque Production..... | 26 |
| 2.3 | SRM Modelling..... | 31 |
| 2.4 | SRM Control..... | 33 |
| 2.5 | SRM Drive Converters..... | 40 |
| 2.6 | Summary..... | 46 |
| | References..... | 47 |
| Chapter 3 | Experimental Efficiency Comparison of a Superjunction MOSFET, IGBT and SiC MOSFET for SRM Drives..... | 49 |
| 3.1 | Background..... | 49 |
| 3.2 | SRM Power devices and converter topologies..... | 50 |
| 3.3 | Output capacitances of the superjunction MOSFET and the SiC MOSFET..... | 52 |
| 3.4 | Loss Estimation..... | 54 |
| 3.5 | Experimental Setup..... | 57 |
| 3.6 | Experimental Results..... | 59 |
| 3.6 | Discussion..... | 61 |
| 3.7 | Summary..... | 62 |
| | References..... | 63 |

| | |
|--|-----|
| Chapter 4 Novel Genetic Algorithm Based Approach of Torque Control and Increased Efficiency Across an Optimised Speed Range in SRM Drives..... | 66 |
| 4.1 Introduction | 66 |
| 4.2 Theoretically minimum rms current with ZTR operation..... | 68 |
| 4.3 Application of minimal rms current torque control across an SRMs speed range..... | 79 |
| 4.3.1 Current profiling envelopes | 79 |
| 4.3.2 Exhaustive ‘branching’ method for current profiling | 85 |
| 4.4 Optimisation techniques..... | 90 |
| 4.4.1 Optimisation techniques in SRM control..... | 90 |
| 4.4.2 Genetic Algorithms..... | 92 |
| 4.4.3 Crossover Stage | 93 |
| 4.4.4 Mutation Stage | 93 |
| 4.4.5 Fitness and objective function | 94 |
| 4.4.6 Selection Stage..... | 94 |
| 4.5 Genetic algorithm approach to current profiling for torque control and minimal rms current across TR free speed range | 95 |
| 4.5.1 Population Generation | 97 |
| 4.5.2 Population Crossover..... | 99 |
| 4.5.3 Population Mutation..... | 100 |
| 4.5.4 Population Evaluation..... | 103 |
| 4.5.5 Population Selection | 104 |
| 4.5.6 Simulation Results | 105 |
| 4.6 Torque ripple free speed range extension using greater than two-phase conduction... | 111 |
| 4.7 Genetic algorithm approach to current profiling for torque control and minimal rms current across an optimised speed range..... | 114 |
| 4.7.1 Augmented Population Generation..... | 116 |

| | | |
|-------|---|-----|
| 4.7.2 | Augmented Population Crossover | 117 |
| 4.7.3 | Augmented Population Mutation..... | 118 |
| 4.7.4 | Simulation Results | 119 |
| 4.8 | Application of GA optimal profiles in an SRM control scheme..... | 121 |
| 4.9 | Summary | 131 |
| | References..... | 132 |
| | Chapter 5 Electronic Machine Emulation for Inverters with Sensorless Position Control..... | 135 |
| 5.1 | Introduction..... | 135 |
| 5.2 | Drive inverter verification methods | 136 |
| 5.2.1 | Model based methods | 136 |
| 5.2.2 | Processor-n-the-loop and Hardware-in-the-loop | 137 |
| 5.2.3 | Power-hardware-in-the-loop..... | 138 |
| 5.3 | Power electronics based emulator testbenches..... | 139 |
| 5.3.1 | Inverter coupling..... | 139 |
| 5.3.2 | Power supply..... | 140 |
| 5.3.3 | Machine modelling | 142 |
| 5.3.4 | Emulator control | 143 |
| 5.4 | PEBE testbench for the verificaiton of position sensor and sensorless control based commerical drives..... | 145 |
| 5.4.1 | Testbench Hardware Design..... | 146 |
| 5.4.2 | Emulator Control Unit | 147 |
| 5.4.3 | Emulator Software Design..... | 149 |
| 5.5 | Inverter sensorless control..... | 151 |
| 5.6 | Simulation results..... | 155 |
| 5.7 | Experimental setup and results..... | 158 |

| | | |
|-----|--|-----|
| 5.8 | Discussion | 164 |
| | Summary | 167 |
| | References..... | 168 |
| | Chapter 6 Conclusions and Future Work..... | 173 |
| 6.1 | General conclusions | 173 |
| 6.2 | Author’s Contribution..... | 175 |
| 6.3 | Future Work..... | 176 |
| | Appendix A | 178 |
| | Appendix B | 179 |
| | Appendix C | 180 |
| | Appendix E | 184 |
| | Appendix F..... | 189 |
| | Appendix G..... | 190 |

Abstract

As society electrifies, there is a growing demand for electrical drive systems in the deployment of renewables and electric vehicles (EVs), along with the replacement of other traditional engine and hydraulic systems in order to reduce global emissions. For any drive system, there is a desire that the ideal candidate would have high efficiency, high power and torque density, low cost, fault tolerance and be relatively environmentally friendly.

There are multiple electrical machine topologies in common use for these applications, such as the permanent magnet synchronous machine (PMSM), induction machine, synchronous reluctance machine and the switched reluctance machine (SRM). The SRM has received interest in recent times, especially in the electrification of passenger vehicles. It is an attractive machine topology, given it is low cost, simple design, fault tolerance, high torque density and no use of permanent magnet materials. Despite this, the SRM suffers from a lower efficiency compared to other candidate topologies and has an inherently high torque ripple (hence noise and vibration), which limits its use across a wider range of applications.

In an SRM drive system, the drive converter can be a source of efficiency improvements. Dependent upon the device type used, the cost of the converter in terms of components price and volume can vary while also affecting the overall efficiency. An investigation is carried out into the power semiconductor devices used in SRM drives, where commonly used switching device types with near identical ratings are compared from a theoretical perspective, and then experimentally compared to gauge device losses. From this it is found that for the three variants (and models) of switching device, the Superjunction MOSFET outperforms both the Silicon Carbide MOSFET and Silicon IGBT in terms of losses in a limited use case scenario.

Another source for efficiency improvements and the main source of the elimination of torque ripple is the control of SRMs. Using the torque ripple minimisation strategy of current profiling as a starting point, the theoretically optimal rms current for an SRM phase is established for a given load torque. A genetic algorithm is designed which uses this rms current as a target for optimisation, which produces optimally low rms current profiles which across the full rated speed range of a four phase SRM, an increase in rms current only 4.3% above the theoretically optimal rms current is exhibited. Along with this, the algorithm design eliminates commutation torque

ripple (<1%) across the full rated speed range of an SRM by utilising intentional three-phase or more overlap. This results in a current profiling control scheme which can apply this efficiency improvement and commutation torque ripple elimination to any SRM with overlapping phase torque capability.

Along with improvements to drive systems, the design processes which create them can also be improved in terms of their testing. Typically, the verification of control software can be done using hardware-in-the-loop or dynamometers, while full power verification is only carried out using a dynamometer. Dynamometers have many known drawbacks such as being complex mechanical and electrical systems which are difficult to use and expensive. A potential alternative to dynamometers, known as power electronics based machine emulation, can be used to provide similar levels of verification using a fully electrical setup. A power electronics based emulator is proposed which aims to be an attractive testbench for full power verification in a commercial drive system design environment. The testbench maximises efficiency in terms of power supply usage being 2.7-3.5 times more efficient than an equivalent dynamometer, it is also modular and easily fabricated and uses a microcontroller architecture. This provides a significant cost saving compared to other power electronic emulators which typically use real time simulator (RTS) units which cost greater than £20000 at a minimum compared to Microcontrollers which can cost as little as £5 in this case. Along with this, ease of construction and use with no modification of commercial inverter circuitry required. The testbench is simulated using MATLAB/Simulink and is then verified experimentally by comparison against a dynamometer testbench, where the drive control inverters in each testbench are programmed with commercial sensorless position control, and tested with power levels up to 3.2kW in the three phase loop.

Acronyms

| | |
|------|--------------------------------------|
| AAC | Advanced Angle Control |
| ASHB | Asymmetric Half Bridge |
| BEMF | Back-Electromotive Force |
| CCC | Current Chopping Control |
| CPU | Central Processing Unit |
| DITC | Direct Instantaneous Torque Control |
| DPC | Deadbeat Predictive Control |
| DTC | Direct Torque Control |
| EMF | Electromotive Force |
| EMU | Emulating Inverter |
| EV | Electric Vehicle |
| FEA | Finite Element Analysis |
| FLT | Full Load Torque |
| GA | Genetic Algorithm |
| HBCC | Hysteresis Band Current Controller |
| HBTC | Hysteresis Band Torque Controller |
| HiL | Hardware-in-the-Loop |
| ICE | Internal Combustion Engine |
| IM | Induction Machine |
| LUT | Lookup Table |
| MPC | Model Predictive Control |
| MPTC | Model Predictive Torque Control |
| NIPC | Novel Integrated Power Converter |
| PEBE | Power Electronics Based Emulation |
| PHiL | Power Hardware-in-the-loop |
| PMSM | Permanent Magnet Synchronous Machine |
| PWM | Pulse Width Modulation |
| SJ | Super-Junction |
| SRM | Switched Reluctance Machine |

| | |
|-------|--------------------------------|
| SynRM | Synchronous Reluctance Machine |
| TR | Torque Ripple |
| TSF | Torque Sharing Function |
| VSC | Voltage Source Converter |
| ZTR | Zero Torque Ripple |

List of symbols

| | | |
|----------------------|---------|---|
| B_{fric} | | Frictional Constant |
| C_{oss} | F | Output Capacitance |
| dE_e | J | Incremental Increase in Input Electrical Energy |
| dE_f | J | Change in Stored Field Energy |
| dE_m | J | Energy Converted into Mechanical Energy |
| E | J | Energy |
| E_f | J | Field Energy |
| f_{rise}, f_{fall} | | TSF Rise And Fall Functions |
| I | A | Current |
| I_N | A | Discrete Current With Respect To Rotor Angle |
| I_d, I_q | A | DQ Axis Currents |
| I_{ph} | A | Phase Current |
| I_{rated} | A | Rated Current |
| I_{ref} | A | Reference Current |
| I_{rms} | A | RMS Current |
| $I_{rmsOptimal}$ | A | Theoretically Optimal RMS Current |
| J | kgm^2 | Inertia Constant |
| K_{Cu} | A^2 | Copper Losses Weighting |
| L | H | Inductance |
| L_d, L_q | H | DQ Axis Machine Inductances |
| L_{link} | H | Link Inductance |
| L_u | H | Unaligned Inductance |
| m | | Number Of Phases |
| N | | Number of Coil Turns |
| N_r | | Number of SRM Rotor Poles |

| | | |
|-------------------|---------------|---|
| N_s | | Number of SRM Stator Poles |
| p | | Electrical Machine Pole Pairs |
| P | W | Power |
| P_{Cu} | W | Copper Losses |
| P_e | W | Electrical Power |
| P_f | W | Field Power |
| P_m | W | Mechanical Power |
| Q | C | Charge |
| R_{Cu} | Ω | SRM Phase Resistance |
| $R_{DS(on)}$ | Ω | On-state Resistance |
| R_{G1}, R_{G2} | Ω | Gate Driver Circuit Resistance |
| R_{link} | Ω | Resistance Of Link Inductance |
| R_s | Ω | Stator Resistance |
| $R_{\theta hsa}$ | $^{\circ}C/W$ | Heatsink to Ambient Thermal Resistance |
| T_{aa} | $^{\circ}C$ | Steady State Temperature Rise Above Ambient |
| T_d | Nm | Torque Demand |
| T_e | Nm | Electrical Torque |
| T_{load} | Nm | Load Torque |
| T_{phase} | Nm | Phase Torque |
| T_{rated} | Nm | Rated Torque |
| T_{ref} | Nm | Reference Torque |
| $T_{ripple(max)}$ | Nm | Torque Ripple Above Load Torque |
| $T_{ripple(min)}$ | Nm | Torque Ripple Below Load Torque |
| u_d, u_q | V | Emulator DQ Voltage References |
| V | V | Voltage |
| V_{CE} | V | Collector-Emitter Voltage Drop |
| V_{CES} | V | Collector-Emitter Saturation Voltage |
| V_{DC} | V | DC Supply Voltage |
| V_{DSS} | V | Drain-Source Saturation Voltage |

| | | |
|---|----------|--|
| V_d, V_q | V | DQ Axis Voltages |
| X_s | Ω | Stator Reactance |
| \bar{E}_s | V | Stator BEMF Vector |
| \bar{I}_s | A | Stator Current Vector |
| \bar{V}_s | V | Stator Voltage Vector |
| θ_a | $^\circ$ | Aligned Angle |
| θ_{cond} | $^\circ$ | SRM Phase Conduction Period |
| θ_{diff} | $^\circ$ | Angular Difference Between Stator Voltage And Current Vectors With Reference To Rotating Reference Frame |
| θ_{err} | $^\circ$ | Angular Error |
| θ_{E_s} | $^\circ$ | Angle Between Rotating Reference Frame and \bar{E}_s |
| θ_{I_s} | $^\circ$ | Angle Between Rotating Reference Frame and \bar{I}_s |
| θ_{Mu} | $^\circ$ | Mutation Angle |
| $\theta_{on}, \theta_{off}$ | $^\circ$ | Turn On/Off Angles |
| $\theta_{on_{ref}}, \theta_{off_{ref}}$ | $^\circ$ | Reference Turn-On/Off Angles |
| $\theta_{on(3\phi)}, \theta_{off(3\phi)}$ | $^\circ$ | Three-phase Turn On/Off Angles |
| $\theta_{ov}, \theta_{ov(2\phi)}, \theta_{ov(3\phi)}$ | $^\circ$ | Overlap Angle, Two-Phase Overlap, Three-Phase Overlap |
| θ_r | $^\circ$ | Rotor Pole-Pitch |
| θ_{ref} | $^\circ$ | Reference Rotor Angle |
| θ_{step} | $^\circ$ | Current Profile Angular Resolution |
| θ_u | $^\circ$ | Unaligned Angle |
| λ | WbT | Magnetic Flux Linkage |
| λ_d, λ_q | WbT | DQ Axis Machine Flux Linkages |
| λ_f | Wb | Machine Flux Constant |
| $\lambda_{max}, \lambda_{min}$ | WbT | Maximum/Minimum Flux Linkage Step |
| ε | $^\circ$ | Stroke Angle |

| | | |
|--------------------|-------------|------------------|
| φ | Wb | Magnetic Flux |
| ϕ | | Machine Phase |
| ω, ω_m | $rads^{-1}$ | Mechanical Speed |
| ω_e | $rads^{-1}$ | Electrical Speed |
| ω_{err} | $rads^{-1}$ | Speed Error |
| ω_{rated} | $rads^{-1}$ | Rated Speed |
| ω_{ref} | $rads^{-1}$ | Reference Speed |

Chapter 1

Introduction

This chapter presents a brief overview of the thesis, highlighting the motivation behind the presented research. An introduction is given on electrical machine topologies and the testing methodologies for the machines drive converters, highlighting the desired characteristics for both in modern machine applications. From this, the switched reluctance machine is chosen as a candidate to be optimised. Power electronics-based emulation as a drive testing methodology is then presented, where a permanent magnet synchronous machine is used to extol the features of a general purpose emulator. The last section summaries the structure of the thesis.

1.1 Background and motivation

Recently, there has been a gradual push for the electrification of all possible areas of society. As it relates to electrical machines and drive converters, areas such as renewable energies [1-1], transportation electrification [1-2], and generally the replacement of internal combustion engine (ICE) and hydraulic systems [1-3] have taken the forefront in galvanising technological development as the climate crisis deepens.

For use in any of these fields, there is a prevailing desire for the drive system to have high efficiency, high power and torque density, low cost, fault tolerant and minimal environmental impact. Fig 1.1 shows a generalised layout of an electrical drive system which consists of three main components:

- Power Converter - can consist of multiple power semiconductor modules and receives control signals from the control unit, modulating input power to be fed to the electrical machine.
- Electrical Machine – converts input electrical energy to rotating mechanical energy (and desirably, vice versa)) using electromagnetic interactions between the rotor and stator.

- Control Unit – Mounted onto the power converter and uses a combination of phase, position, speed, and/or torque data gathered from sensors to operate a control loop, which controls the machine by generating switching signals which are then sent between the Power Converter and Electrical Machine.

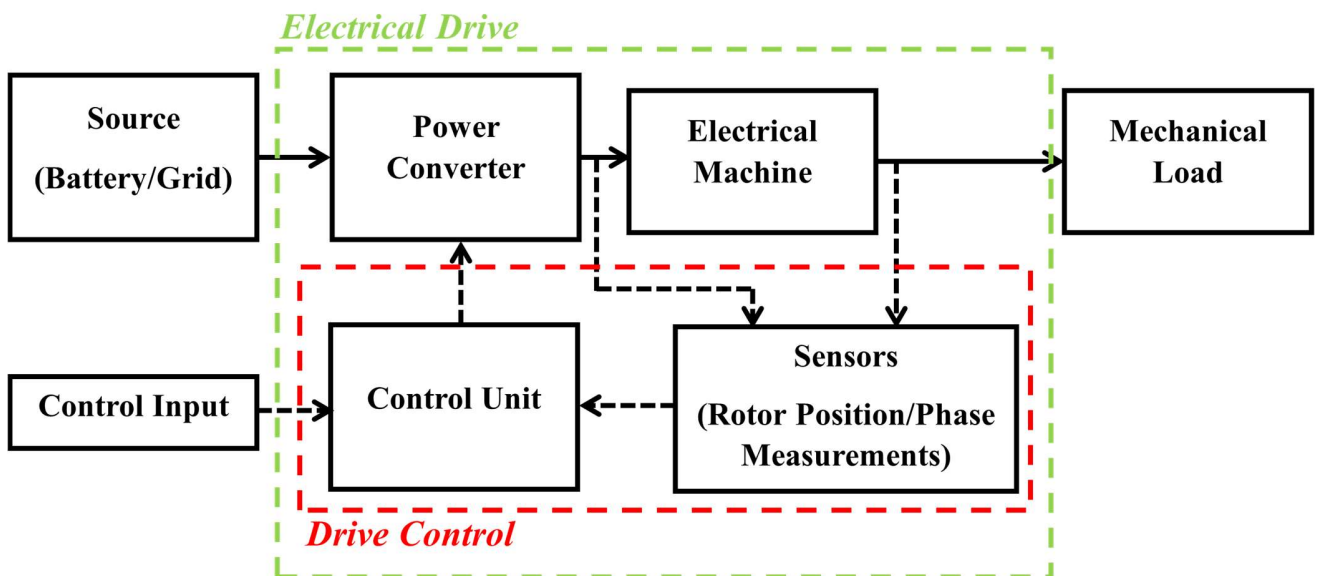


Fig 1.1 Generalised electrical drive system

In a drive system the electrical machine tends to cost less than the power converter, and dependent on the machine topology selected, heavily influences the converter design. The number of available machine topologies is expansive and depends on the application in question. Generally, some of the more popular machine topologies in use are the PMSM, induction machine (IM), brushless, synchronous reluctance machine (SynRM) and SRM. As it relates to the prior characteristics, PMSMs are superior in terms of base efficiency and overall power density. The downside is that they are expensive and environmentally unfriendly due to the permanent magnets embedded in the rotor [1-4], and there is interest in reducing the use of these materials. IMs are less efficient and have a lower power density than PMSMs but are currently the most popular machine topology in use [1-5], using no permanent magnets. They offer a good trade-off between cost, performance and are robust in operation. Two types of reluctance machines (SRM and SynRM) have seen increased use in recent times, particularly the SRM, where both offer a cheap, robust option which do not inherently use permanent magnets. SynRMs have mainly been proposed as promising candidates to replace PMSMs in EV applications [1-6], but this involves

the augmentation of the design with permanent magnets to provide comparable characteristics, which again increases cost and introduces the issue of high temperature demagnetization.

The differences between the topologies are summarised in Table 1.1, where the characteristics of each are weighted from 1 (worst) to 5 (best), as assessed in quantitative studies found in [1-2],[1-7]- [1-9]. When comparing the SRM as a candidate to other topologies, it measures closely to the PMSM in the factors considered. An increase to efficiency and or power/torque density would yield a competitive alternative to the PMSM , where PMSMs can typically operate at efficiencies of 90% [1-10] compared to 70-75% of SRMs [1-11]. Note that there are other factors which could be considered which relate to the engineering considerations such as the controllability where it is assumed that all possible topologies are viable for an electric drive across multiple applications.

Table 1.1 Analytical comparison between candidate machine topologies for an electrical drive

| | IM | PMSM | SRM | SynRM (PM- embedded) | BLDC |
|-------------------------|----|------|------|-------------------------|------|
| Cost | 4 | 2 | 4 | 2 | 2 |
| Reliability | 5 | 4 | 4.5 | 4 | 3 |
| Efficiency | 3 | 5 | 3.5 | 4 | 2 |
| Power/Torque Density | 3 | 5 | 3.5 | 4 | 2 |
| Total | 15 | 16 | 15.5 | 14 | 9 |

SRMs are cheaper and the simplest topology to manufacture compared to other candidates. Along with this, they do offer competitive, although inferior power density and efficiency compared to a PMSM of the same size, with the main drawback being the machines highly non-linear magnetic characteristics, which results in inherently large torque ripple (TR) and noise. TR is defined using (1.1), where $T_{ripple(max)}$ is torque error above torque demand T_{load} , and $T_{ripple(min)}$ is torque error below T_{load} .

$$\%TR = \frac{T_{ripple(max)} - T_{ripple(min)}}{T_{load}} \times 100 \quad (1.1)$$

Besides the advancement in design and control of electrical drive systems, an emerging interest has also been found in improving the drive development process [1-12]. When testing a drive

inverter software and hardware design, there are many methodologies that exist which provide varying levels of testing verification. Simulation based designs are typically the first step,

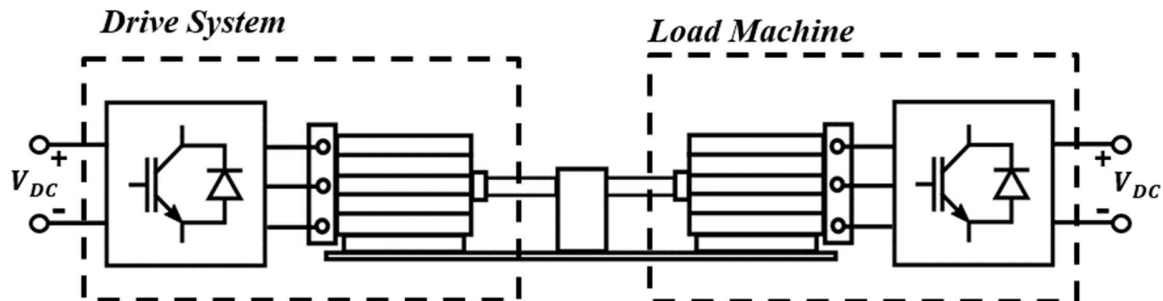


Fig 1.3 Generalised dynamometer testbench

simulating theoretical drive behaviour and involve control coding, but are purely computer based and contain no electrical testing elements, being referred to as model-in-the-loop and software-in-the-loop. The next level of verification is what is referred to generally Hardware-in-the-loop (HiL) testing [1-13]. This is where a control unit is programmed with the drive control software and connected to a simulation rig, which itself contains the model of the drive, providing the equivalent control responses to the control unit. While drive control is confirmed to some degree, there is still no electrical power or hardware component present, and therefore factors related to this cannot be considered, which greatly limits the extent of testing. Traditionally, drive testing that introduces the missing converter hardware that the prior methods lack is Dynamometer testing, usually abbreviated as “Dyno” testing. Fig 1.2 shows the layout of a Dyno testbench, where a full inverter hardware design is presented along with the machine for the application and required sensors. The drive is connected at the machine shaft to a second machine, which acts as a mechanical load and dissipates electrical energy from the conversion. This provides full verification of the drive system, where the only further step is testing the drive in its given application. Dyno testbenches are not without drawbacks; they are complex mechanically and electrically; therefore, they are difficult to construct and use correctly, along with being expensive. Once constructed they are also specific to only the given torque, speed and inertia of the application, where reconfiguring the Dyno requires a whole new process of replacing the load machine and drive etc.

An emerging alternative to dyno testbenches is what is known as power hardware-in-the-loop (PHiL) testing [1-14]. This method omits the use of any mechanical components but utilises the full drive converter and its control circuitry. It operates the converter by mimicking the back

electromotive force (EMF) that would be generated by the electrical machine when it is spun. Fig 1.3 illustrates a generalised PHiL testbench, with the mechanical element of the Dyno testbench being replaced by an inverter module and link inductance, where the inverter is programmed with a machine model control loop tasked of producing the emulated back EMF. This method can simplify the testing process, being simpler in nature than a dyno testbench, cheaper, quicker to construct and providing a near equal level of verification if the electrical machine is emulated

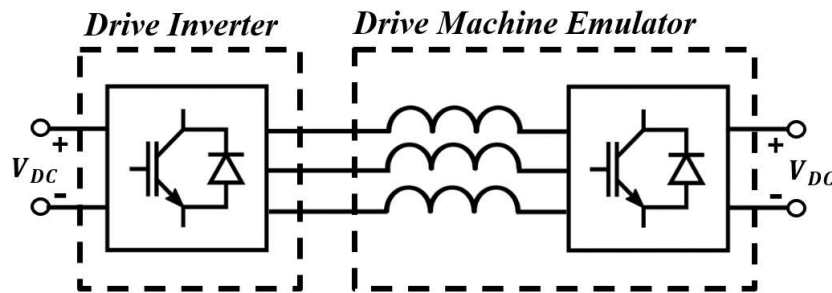


Fig 1.5 Generalised PHiL testbench

accurately [1-7].

1.2 Objectives of the thesis

The aim of this thesis is the optimisation of the cost and efficiency of electric drive systems and their development. The SRM and its respective drive converter has potential as a low cost, flexible candidate across multiple applications, but to be competitive against other machine topologies, its efficiency must be increased while also eliminating its inherent commutation TR. The drive converter switching device choice is first studied as it relates to drive efficiency. SRM control is then studied, where a control scheme is then proposed which eliminates TR and extends the zero TR speed range to match the SRM base speed. The proposed scheme also optimally minimises phase rms currents to increase machine efficiency by decreasing copper losses.

The design process of drive systems is examined in terms of the testing of three phase drive inverter designs using alternatives to dyno testbenches. A PHiL testbench design is proposed which aims to minimise the cost of the testbench while also maximising cost-efficiency along with a simple design, to be used in commercial testing applications. The testbench is designed to emulate a three phase PMSM, and verifies the operation of a commercial drive inverter module which is programmed with sensorless position control. Emulation of an SRM is not carried out in this work but is in theory possible, likely using an esoteric testbench design unlike the one presented in this

thesis. A possible design would likely require individual bidirectional DC converters for each phase of an SRM, with the discretised phase model programmed on each. The decision for the emulation of a PMSM is carried out in the interest of industrial partners.

1.3 Outline of the thesis

The thesis is composed of seven chapters, which are briefly summarized as follows:

- **Chapter 1** gives a short introduction on electrical machine topologies and the testing methodologies for the machines drive circuitry, highlighting the required characteristics for both, and the improvements that must be made to available topologies such as the SRM and PMSM to fulfil these requirements.
- **Chapter 2** details the fundamental construction of the SRM, including its doubly salient construction in how it contributes to its torque production and modelling. The operation of the SRM is then highlighted in terms of its unique drive converter designs and control methodology
- **Chapter 3** carries out an investigation into the power semiconductor devices which are commonly used in SRM drive converters. They are compared from an economic and loss perspective, being compared in theory from their characteristics and theoretical losses, and then experimentally using a non-discretised thermal superposition method to measure device losses.
- **Chapter 4** proposes a novel current profiling design for SRMs utilising a Genetic Algorithm, which incorporates theoretically optimal rms currents, delayed turn-on angle, two-phase overlap, and greater than two-phase overlap for optimally low rms currents across the full rated speed range of an SRM with zero torque ripple (ZTR) as it relates to commutation torque ripple. The algorithm design is validated using simulations, and the results are inserted into a simulated control scheme for a finite element analysis (FEA) modelled SRM.
- **Chapter 6** presents a novel PEBE testbench design aimed at commercial design processes for a PMSM, which utilises a microcontroller for emulator control and is fabricated from identical commercial inverter modules with a single DC supply. The testbench minimises cost in terms of hardware design, provides a simplified design and ease of use, and produces high efficiency and emulation quality. Firstly, the validation methods used for

drive systems at their various design stages are discussed. PHiL, more specifically power electronics based emulation (PEBE), is then examined in further detail. PEBE testbench design is then explored in terms of software and hardware components and the proposed testbench design is presented. To verify the testbench design, it is simulated and then verified experimentally by confirming the operation of commercial sensorless position control using the testbench.

- **Chapter 7** highlights the main conclusions and contributions of the thesis, and discusses the avenues for future research as it relates to this research.

References

- [1-1] S. Khalili and C. Breyer, "Review on 100% Renewable Energy System Analyses—A Bibliometric Perspective," in *IEEE Access*, vol. 10, pp. 125792-125834, 2022.
- [1-2] P. Ramesh and N. C. Lenin, "High Power Density Electrical Machines for Electric Vehicles—Comprehensive Review Based on Material Technology," in *IEEE Transactions on Magnetics*, vol. 55, no. 11, pp. 1-21, Nov. 2019.
- [1-3] E. Scolaro, M. Beligoj, M. P. Estevez, L. Alberti, M. Renzi and M. Mattetti, "Electrification of Agricultural Machinery: A Review," in *IEEE Access*, vol. 9, pp. 164520-164541, 2021
- [1-4] Z. Cao, A. Mahmoudi, S. Kahourzade and W. L. Soong, "An Overview of Electric Motors for Electric Vehicles," *2021 31st Australasian Universities Power Engineering Conference (AUPEC)*, Perth, Australia, 2021.
- [1-5] C. Gan, J. Wu, Q. Sun, W. Kong, H. Li and Y. Hu, "A Review on Machine Topologies and Control Techniques for Low-Noise Switched Reluctance Motors in Electric Vehicle Applications," in *IEEE Access*, vol. 6, pp. 31430-31443, 2018.
- [1-6] A. Credo, M. Villani, G. Fabri and M. Popescu, "Adoption of the Synchronous Reluctance Motor in Electric Vehicles: A Focus on the Flux Weakening Capability," in *IEEE Transactions on Transportation Electrification*, vol. 9, no. 1, pp. 805-818, March 2023.
- [1-7] Z. Cao, A. Mahmoudi, S. Kahourzade and W. L. Soong, "An Overview of Electric Motors for Electric Vehicles," *2021 31st Australasian Universities Power Engineering Conference (AUPEC)*, Perth, Australia, 2021

- [1-8] M. Zeraouila, M. E. H. Benbouzid and D. Diallo, "Electric motor drive selection issues for HEV propulsion systems: a comparative study," *2005 IEEE Vehicle Power and Propulsion Conference*, Chicago, IL, USA, 2005
- [1-9] W. Xu, J. Zhu, Y. Guo, S. Wang, Y. Wang and Z. Shi, "Survey on electrical machines in electrical vehicles," *2009 International Conference on Applied Superconductivity and Electromagnetic Devices*, Chengdu, China, 2009
- [1-10] G. Hong, T. Wei and X. Ding, "Multi-Objective Optimal Design of Permanent Magnet Synchronous Motor for High Efficiency and High Dynamic Performance," in *IEEE Access*, vol. 6, pp. 23568-23581, 2018
- [1-11] O. Rahmani, S. A. Sadrossadat, S. M. Mirimani, S. H. Mirimani "Optimization of efficiency and output power of 8/6 switched reluctance motor using new neural network-based adjoint Lp metric method" in *IET Electric Power Applications*, vol.15, pp. 769-783, 2021
- [1-12] K. Ma, S. Xia, Y. Qi, X. Cai, Y. Song and F. Blaabjerg, "Power-Electronics-Based Mission Profile Emulation and Test for Electric Machine Drive System—Concepts, Features, and Challenges," in *IEEE Transactions on Power Electronics*, vol. 37, no. 7, pp. 8526-8542, July 2022.
- [1-13] C. S. Edrington, M. Steurer, J. Langston, T. El-Mezyani and K. Schoder, "Role of Power Hardware in the Loop in Modeling and Simulation for Experimentation in Power and Energy Systems," in *Proceedings of the IEEE*, vol. 103, no. 12, pp. 2401-2409, Dec. 2015.
- [1-14] G. F. Lauss, M. O. Faruque, K. Schoder, C. Dufour, A. Viehweider and J. Langston, "Characteristics and Design of Power Hardware-in-the-Loop Simulations for Electrical Power Systems," in *IEEE Transactions on Industrial Electronics*, vol. 63, no. 1, pp. 406-417, Jan. 2016.

Chapter 2

Fundamentals of SRM Operation

This chapter will detail the theory behind the operation and control of SRMs and their respective drive circuits. The fundamental electrical characteristics are discussed along with how these relate to the torque production in the machine. Examples are then given of how the SRM can be controlled, along with introducing the machine modelling that is utilised in the process.

2.1 Introduction

The SRM is an electrical machine topology that can be categorised under the family of 'reluctance machines'. It is one of the oldest recorded designs of electrical machine and can be traced back to 1838. The 'reluctance' in the machine categorisation relates to its primary mode of torque production, which utilises magnetic reluctance. This differs from commonly used machine variants such as PMSMs or IMs which in a simple sense can be seen as using 'magnetic torque' as opposed to reluctance torque as the primary mode of torque production. The SRMs use of reluctance torque can be understood firstly by illustrating its design in Fig 2.1, showing a four phase 8/6 SRM topology. It is a doubly salient machine, meaning both rotor and stator poles protrude towards the airgap from their respective structures. The phase windings of the machines are wound round the stator poles and when excited correctly, the closest rotor poles will tend to align with the stator poles in order to attain a minimal reluctance flux path between rotor and stator. This desire to align will rotate the rotor and if the phases of the machine are sequentially excited; consistent rotational motion can be achieved.

In operation, the number of stator poles N_s and rotor poles N_r are significant. More importantly, the number of stator and rotor poles dictate the number of phases m the machine has as expressed in (2.1), and affects characteristics such as base TR, efficiency and radial forces [2-1][2-2]. While they offer benefits to these factors, there are associated drawbacks. With the general increase in poles (either stator or rotor) machining costs may increase in construction of the motor, along with the increases volume in copper required in windings also adding further. By increasing the number

of phases, converter costs also increase with the inclusion of further power electronics with each additional phase. Therefore for an SRM the percentage increase in cost must be weighed against the estimated percentage increase in efficiency and reduction in TR relative to designs with lower numbers of poles.

$$m = \frac{N_s}{|N_s - N_r|} \quad (2.1)$$

In general, there are numerous permutations of SRM that are available, where some examples expressed as N_s/N_r are:

Three Phase SRMs:

- 6/4
- 12/8
- 18/12

Four Phase SRMs:

- 8/6
- 8/10
- 24/18

Six Phase SRMs:

- 12/10

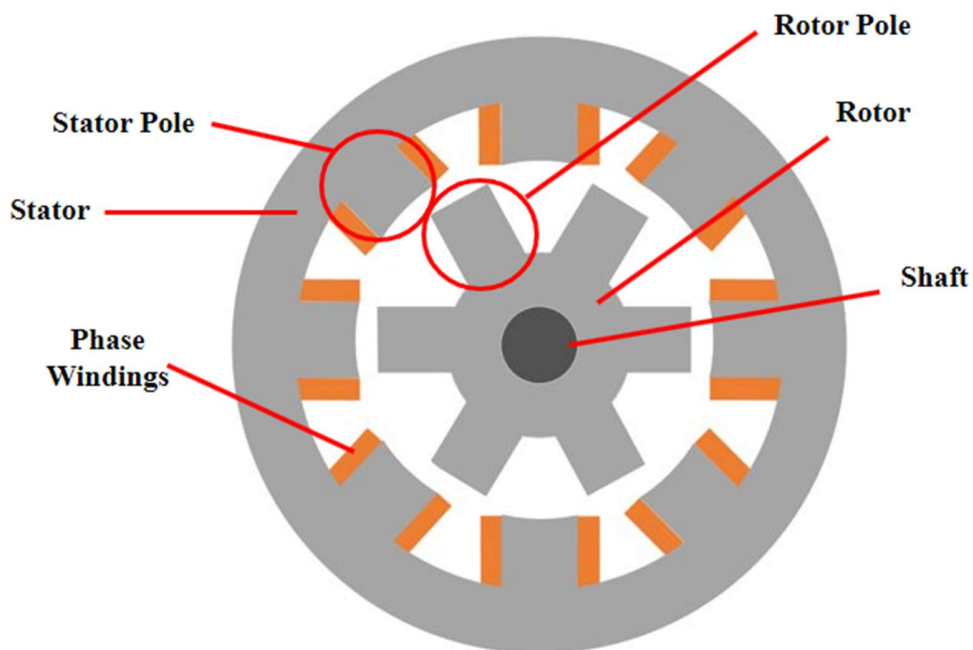


Fig 2.1 Axial view of a four phase, 8/6 SRM

2.2 SRM Torque Production

To establish the relationship between the electrical characteristics which drive the machine (current and voltage), and its magnetic characteristics as it relates to torque production, the inductance of an individual phase winding can be examined using basic electromechanical principles. Linearly, inductance, L can be considered as (2.2), a function of flux linkage λ (number of turns N multiplied by flux ϕ) over current, I . Fig 2.2 examines the non-linear characteristic of the phase inductance in an SRM as a function of λ and I .

$$L = \frac{\lambda}{I} \quad (2.2)$$

At the given unaligned position, θ_u the relationship for the inductance L_u is constant and is linear, with the increase in current providing an increase in flux linkage. As the rotor and stator poles reach the aligned position, θ_a , the inductance of the phase changes with changing reluctance as the rotor core is introduced. At alignment, the relationship between λ and I becomes non-linear with the magnetic saturation effects of the core now considered.

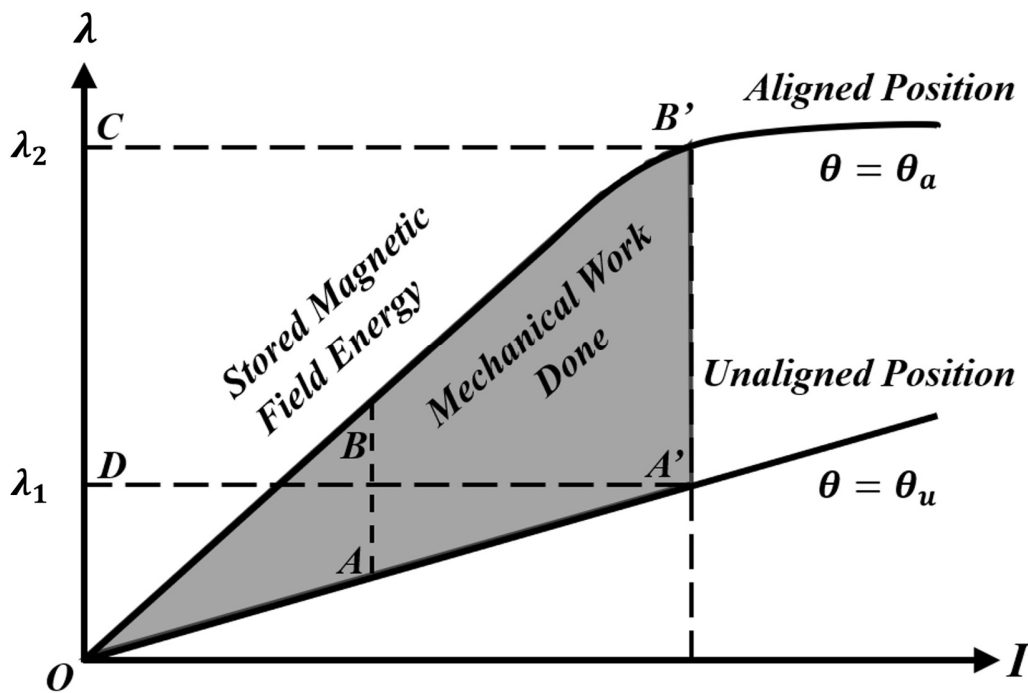


Fig 2.2 General SRM λ - I characteristic

Using points A and B from Fig 2.2, for a constant current, as the machine rotates from points θ_u to θ_a the stored magnetic field energy E at either point is given by (2.3), with the field energy, E_f , supplied in this transition given by (2.4), where dL is the change in inductance during the transition.

$$E = \frac{1}{2} \lambda I = \frac{1}{2} L I^2 \quad (2.3)$$

$$E_f = \frac{1}{2} I^2 dL \quad (2.4)$$

Converting (2.4) to field power P_f , the period of time for this transition dt is considered and (2.5) is produced.

$$P_f = \frac{E_f}{dt} = \frac{1}{2} I^2 \frac{dL}{dt} \quad (2.5)$$

Using the applied voltage V to the phase winding, the electrical power P_e applied during this period can be given by (2.6).

$$P_e = IV = I \times I \frac{dL}{dt} = I^2 \frac{dL}{dt} \quad (2.6)$$

It can be seen that between (2.5) and (2.6), half of the power applied in the phase electrically is missing, ignoring losses; this is converted to mechanical power P_m (2.7).

$$P_m = P_e - P_f = I^2 \frac{dL}{dt} - \frac{1}{2} I^2 \frac{dL}{dt} = \frac{1}{2} I^2 \frac{dL}{dt} \quad (2.7)$$

P_m can also be expressed as (2.8), being a product of net Torque T and mechanical speed, ω_m . Combining these equations yields (2.9), an expression for SRM torque production.

$$P_m = T \omega_m \quad (2.8)$$

$$T = \frac{1}{2} \frac{I^2}{\omega_m} \frac{dL}{dt} \quad (2.9)$$

It is more useful for T to be expressed in terms of the change in angle relative to the given phase. This is achieved by considering (2.10), where $d\theta/dt$ is alternative expression for ω_m . Substituting this into (2.9) yields (2.11).

$$\frac{dL}{dt} = \frac{dL}{d\theta} \frac{d\theta}{dt} \quad (2.10)$$

$$T = \frac{1}{2} I^2 \frac{dL}{d\theta} \quad (2.11)$$

Note that this equation is derived from the linear area of Fig 2.2, if points A' and B' are taken instead, saturation effects would need to be considered. The simplest gauge for this is replacing the energy equations in (2.4) to (2.7) with their equivalent areas in Fig 2.2, resulting in (2.12) to (2.14). In these equations, dE_e and dE_m are the respective changes in electrical and mechanical energy during the rotational transition.

$$dE_e = dE_m + dE_f \quad (2.12)$$

$$\text{area } A'B'CD = dE_m + \text{area } OB'C - \text{area } OA'D \quad (2.13)$$

$$dE_m = \text{area } OA'B' \quad (2.14)$$

Revisiting (2.11), it is established that this cannot describe the exact behaviour of the machine. It instead provides an approximation of the behaviour, from which insights into SRM operation can be gained. Given torque is proportional to current squared, the machine can be operated like a DC machine, where negative currents are not required, and similar to series DC machines, high starting torque can be achieved due this current square characteristic. Given current has no effect in terms of direction, to produce negative torque, it can be seen that the change in inductance with rotor angle dictates this. This gives the machine full four quadrant operational capability of motoring or generating. Due to this equation being an expression for a single phase of torque production in SRMs, torque production is discretised to its phases, which inherently causes detrimental TR. The discrete nature of torque production also means that there are little minimal mutual effects between the phases and they can be neglected without compromising any modelling of an SRM.

Fig 2.3 illustrates the changes in inductance typically observed when the SRM stator and rotor poles approach an aligned position, and then an unaligned position. As with Fig 2.2, the case examined here shows a linear relationship between inductance and rotor position, where saturation effects are not considered. The angular period that this profile is contained within is referred to as the rotor pole pitch, θ_r , being defined as (2.15).

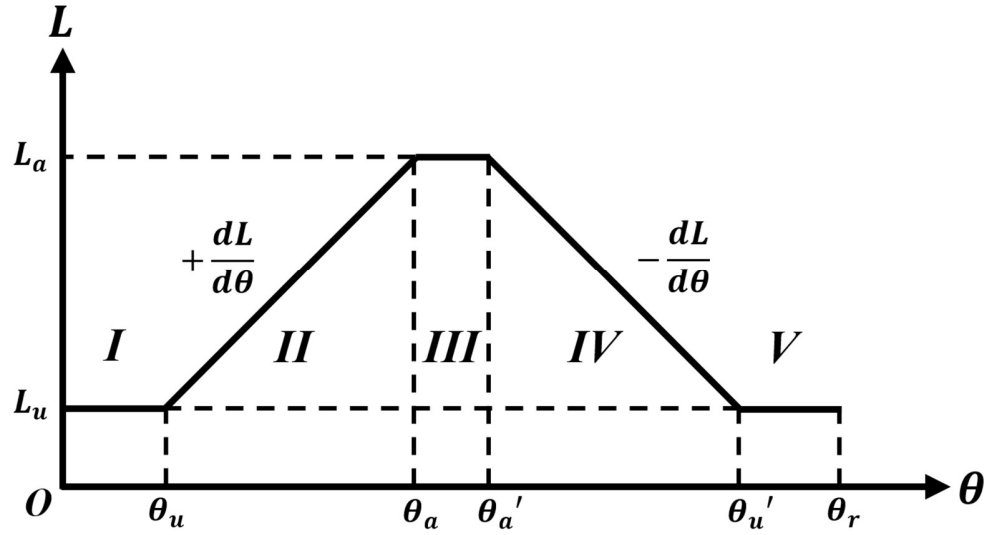


Fig 2.3 General SRM $L - \theta$ characteristic for a given phase

$$\theta_r = \frac{2\pi}{N_r} \quad (2.15)$$

In Fig 2.3, the stages of inductance are as follows:

- I. $0 - \theta_u$, The general unaligned region where relative to this phase, there is no interaction between stator and rotor pole, this therefore leads to a constant inductance of the airgap and no possible torque production since there is no $dL/d\theta$.
- II. $\theta_u - \theta_a$, Interaction between the stator and rotor pole as they align. Inductance changes from lower L_u to higher L_a inducing a positive $dL/d\theta$ and therefore positive torque production. If considering a realistic inductance profile, it would be observed that the rate of $dL/d\theta$ is not constant in this region, with it being largest approximately halfway through (greatest Nm/A efficiency) and being lower as it departs L_u or approaches L_a . Operationally, this region can be used for motoring with positive torque production.
- III. $\theta_a - \theta'_a$, The stator and rotor poles are now completely aligned and achieve a minimum path of magnetic reluctance. No change in inductance is present and therefore is another

region where no torque production is possible. This region can typically be fairly small in an angular sense and may even not exist, being dependent on the dimensions of the rotor and stator poles.

- IV. $\theta_a - \theta'_a$, Interaction between the stator and rotor pole as they unalign. It is the opposite region of II. where $dL/d\theta$ is now negative given $L_a > L_u$. This area will produce negative torque production if current is present in the winding, as effectively the rotor pole will have some desire to realign itself with the pole it has just departed.
- V. $\theta'_u - \theta_r$, Relative to the given phase, the stator and rotor poles are completely unaligned again, and no torque can be produced as in case in I.

The forces which compose SRM torque production can be separated into two components, which are related to the integral of flux density squared. The main component is tangential force, which acts in the rotational direction of the aligning stator and rotor poles, perpendicular to the rotor pole column. The other component is radial force, which acts in a parallel direction to the rotor pole column. Fig 2.4 gives an example of these forces at different states of alignment between stator and rotor pole. Before alignment in Fig 2.4a, the tangential force is at its largest, which coincides with the peak Nm/A efficiency regions of the machine. As the rotor pole aligns, tangential force begins to decrease until at alignment shown in Fig 2.4b, it is minimal. At alignment (60° for the four phase 8/6 SRM), the radial force is at a maximum, where to decrease the airgap and reduce

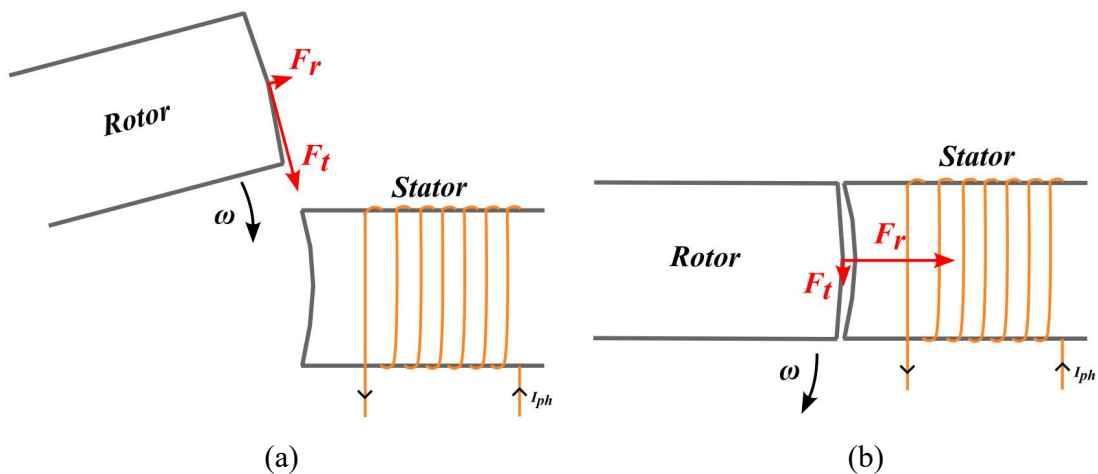


Fig 2.4 SRM rotor force production: (a) Near alignment of stator and rotor poles and (b) Alignment of rotor and stator poles

reluctance, the stator is pulled towards the rotor, which can cause stator deformation along with being the main source of vibrations and acoustic noise in the SRM [2-3] [2-4].

2.3 SRM Modelling

The equivalent per phase circuit of the SRM can be represented in Fig 2.5 by a series resistance and inductance, along with the back-emf produced by the interaction of the phase winding within the machine. This is obtained by expressing as the voltage equation of the phase as (2.16), where DC voltage demand V_{DC} is dictated by a resistive component which represents the SRMs windings, and demand required due to the rate of change in flux linkage $d\lambda/dt$.

$$V_{DC} = IR + \frac{d\lambda}{dt} \quad (2.16)$$

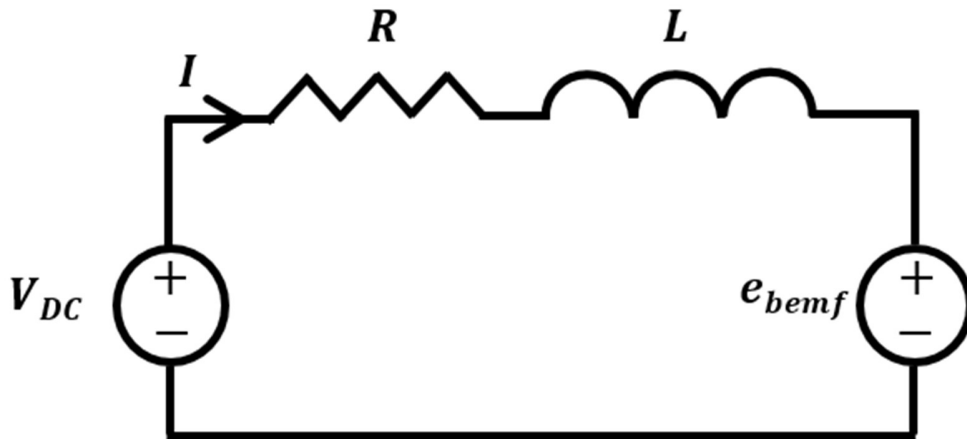


Fig 2.5 SRM per-phase equivalent circuit

$d\lambda/dt$ can be expressed in two components using (2.2) and further applying the product rule to express the components as (2.17).

$$V_{DC} = IR + L \frac{di}{dt} + I \frac{dL}{dt} \quad (2.17)$$

dL/dt can then be substituted for (2.10), where $d\theta/dt$ can be expressed as ω . This results in (2.18), where the components which compose the equivalent circuit can be seen.

$$V_{DC} = IR + L \frac{di}{dt} + I\omega \frac{dL}{d\theta} \quad (2.18)$$

With the expression for electrical equations established, the electrical torque T_e developed by the machine can be expressed as a summation of all discrete phase torques (2.19).

$$T_e = \sum_1^n T_{phase}(i, \theta) \quad (2.19)$$

The equation for mechanical motion is then expressed by (2.20).

$$J \frac{d\omega}{dt} = T_e - T_L - B_{fric}\omega \quad (2.20)$$

where J is the rotor inertia constant, B_{fric} is the friction coefficient and T_L is the machine load torque.

Given the non-linear nature of the SRM, equivalent circuit modelling of the machine can require a higher resolution than other commonly used machine topologies (PMSM, IM). To directly relate the characteristics of the machine operation, finite element analysis (FEA) can be utilised to obtain $\lambda - I - \theta$ and $T - I - \theta$ relationships as 2D Lookup Tables (LUTs). This provides a robust model, sufficient for simulation without including a complicated mathematical model. These tables are per-phase, and the equivalent phase SIMULINK model is illustrated in Fig 2.6.

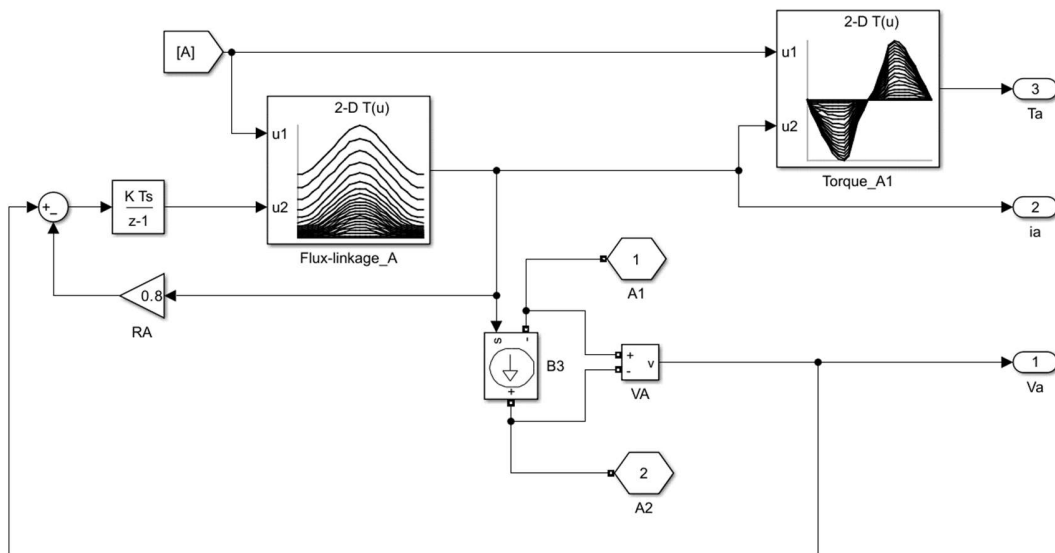


Fig 2.6 SIMULINK model of an SRM phase

2.4 SRM Control

Fig 2.7 highlights the typical torque-speed characteristic of an SRM. When operating the machine, control methods vary dependent on the speed of the machine speed [2-7]. At speeds within the machines constant torque region, current chopping control (CCC) is used. This involves the control of phase currents in the machine using either Hysteresis Band Current Control (HBCC) or Pulse Width Modulation (PWM). Beyond the constant torque region (above base speed ω_{rated}), the back electromotive force (BEMF) is pronounced due to high speed. Hence, the currents of the machine cannot be reliably controlled and instead, control of θ_{on} and θ_{off} is used; being referred to as advanced angle control (AAC). In this region, the constant power region ($P = T\omega$) rated torque can no longer be produced but by using AAC, power is still maintained with increasing speed. In the final region, speed has reached the peak value of the SRM ω_{peak} , where still using AAC, the SRM can no longer maintain its power output, whereas when speed increases torque will decrease rapidly in proportion to the square of said speed.

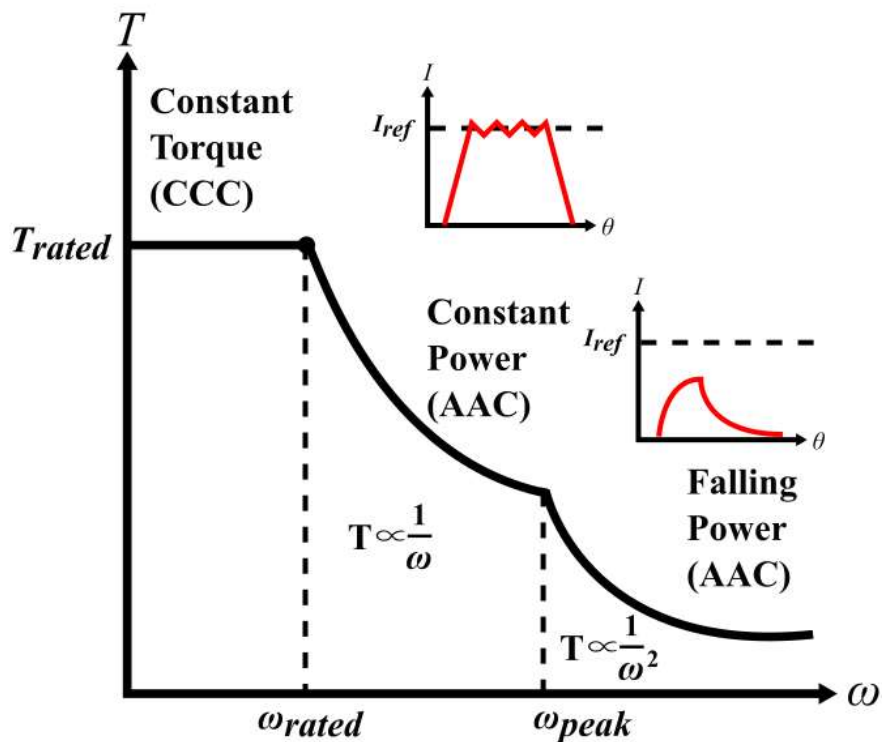


Fig 2.7 SRM torque speed characteristic

Aside from speed control, SRM control must consider the machines TR. Inherent in the SRMs doubly salient design, the resultant discrete torque production and nonlinear nature of the machine results in TR. This is the deviation of the machines output torque from a stable value as the machine shaft rotates. It is typically at its greatest during the commutation of phases [2-8]. Fig 2.8 shows operation an 8/6 SRM, with parameters given in Appendix A, at 500rpm. Fig2.8a shows the overlapping phase current waveforms with turn on and off angles of 35° and 50° respectively using basic CCC. Fig2.8b) illustrates the phase torques and significant TR that occurs at commutation with the reference full load torque of 25Nm.

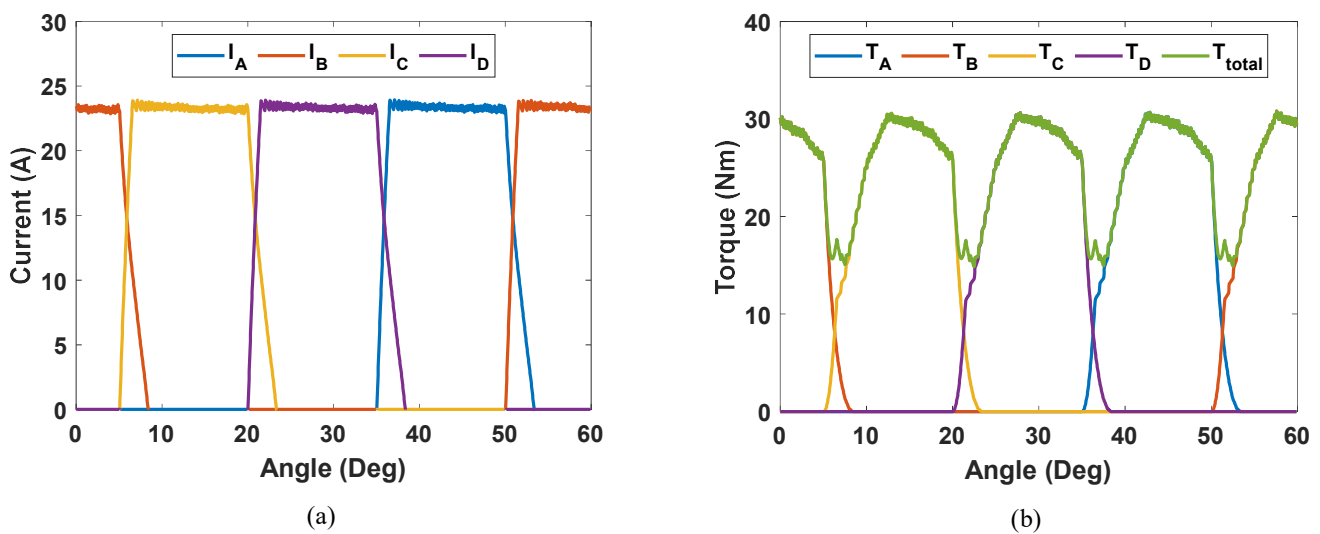


Fig 2.8 Constant speed SRM operation (a) Phase currents and (b) Phase and torques

Fig 2.9 illustrates the Nm/A efficiency across the conduction period of an 8/6 SRM, showing regions of positive and negative Nm/A efficiency, and zero at the aligned position. This is obtained using Ansys Maxwell FEA software, where firstly, the given SRM, which has no structural differences from the classical SRM design, is modelled in a 2D or 3D nodal mesh dependent on whether higher accuracy is desired. In the case of this work, the model is 3D and the characteristic is found by exciting a single discrete phase of the SRM which is electrically modelled in a circuit using the known parameters from Appendix A.1. At each respective rotor angle with a 0.1° resolution across the five current levels, the phase is excited, obtaining the output torque and flux linkage provided by the nodal model of the machine. This further highlights the nonlinear aspects of the machine, where although (2.10) states $T \propto I^2$ and $T \propto \frac{dL}{d\theta}$, $\frac{dL}{d\theta}$ is nonlinearly dependent on

rotor angle and injected current as shown in Fig 2.2. This is due to the relationship of $\lambda \propto L$, which results in change to Nm/A with I as θ changes.

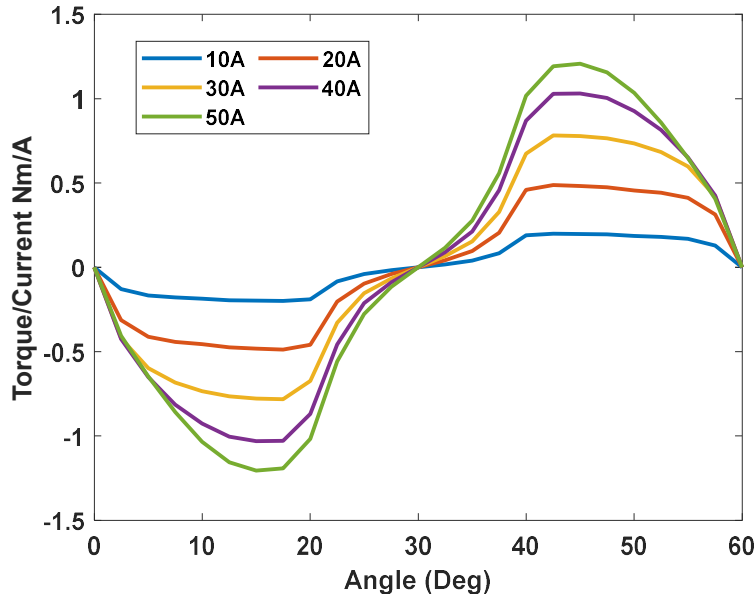


Fig 2.9 Nm/A efficiency across conduction period for an 8/6 SRM

To operate an electrical machine in most applications, four quadrant operations is required as a part of the machine function. In the SRM, both clockwise (+ve speed) rotation and anti-clockwise rotation (-ve speed) are both achievable in the rotor. To induce either positive or negative torque for motoring, generating (braking) or any other purpose, it is dependent on when a given SRM phase is excited relative to the conduction period. In the 8/6 SRM in this case, positive torque is produced in the first half of the conduction period ($0^\circ - 30^\circ$, motoring) while negative torque is produced in the second half of the conduction period for a given phase ($30^\circ - 60^\circ$, braking). At any given point if a braking motion is applied, the phases in said negative torque production regions will be excited as the machine slows in speed.

If controlling an SRM with single phases conducting sequentially, TR will occur as the phase approaches the zero Nm/A efficiency area at unaligned/aligned regions. Therefore, to address TR, the discussed strategies implement some form of multi-phase conduction, typically two phases, which allows the effective distribution of load torque. The reason why this is required can be found again when revisiting the SRMs torque production. It can be seen at two points Fig 2.9 (aligned at $0^\circ/60^\circ$ and unaligned at 30°), Nm/A efficiency is exactly 0, and near these points it remains low.

If using a single phase to conduct, mathematically there will be some form of commutation torque ripple due to these regions of no or low torque production. To rectify this, a range of strategies which exist to minimise or eliminate TR utilising multi-phase conduction. Commonly used methods include online direct torque control (DTC) and direct instantaneous torque control (DITC), Model predictive torque control (MPTC), online/offline torque sharing functions (TSFs) and offline current profiling.

DTC, first established in [2-7], functions as an online controller in the drive control loop. In its simplest form, it utilises a LUT derived from FEA analysis of machine parameters which relate Torque T , Current I and Rotor Angle θ , in order to estimate torque, where the rotor angle is obtained typically from an encoder or sensorless control. A vector for the rate of change of stator flux linkage is then created from another LUT relating Flux Linkage λ , Current I and Rotor Angle θ . Using the estimated torque and a vector created from the rate of change of flux linkage, optimal switching signals are then created to directly control machine torque production. DITC is a derivative of DTC and was first proposed in [2-8], where instead of a multi-step process to carry out the direct control of torque, it proposes taking measured terminal values to directly estimate torque. From the terminal values, it uses a $(T - I - \lambda)$ LUT where λ is found from terminal voltage and pre-measured winding resistance. It offers the same control benefits as DTC, with the added benefit of not requiring a high-resolution encoder given the absence of θ in the LUT. MPTC is a control method first applied to SRMs in [2-9], where it functions by calculating possible voltage vector values in the next control period (effectively current and torque values) form a model of the SRM. These voltage vector values and their respective torques and currents are then weighted using a cost function, and the optimal values are selected for torque control based upon an optimal cost function utilised in the scheme. TSFs are an extensively researched area of TR reduction in SRMs, first being proposed in some capacity by [2-10] and [2-11]. TSFs indirectly control torque production by controlling phase currents and managing these currents during phase commutation, when neither phase produces full load torque (FLT). Finally, current profiling, first presented in [2-11], employs indirect control of torque via the offline generation of current waveforms based upon some desired characteristic such as zero commutation TR. These profiles are stored in LUTs, and used as current references based upon rotor angle input accompanied by either desired torque or flux etc.

As it relates to control of the SRM and subsequent mitigation of TR, Table 2.2 highlights known advantages and disadvantages of the discussed control methodologies [2-7]-[2-14]. DTC and DITC are similar as expected and both offer dynamic control of torque while DITC offers more as it relates to TR mitigation. Both typically use a variable switching frequency, this can contribute to more switching ripple at higher frequencies. MPTC also offers control of torque and effective TR mitigation with a simple implementation, but requires a highly accurate model of the SRM to operate correctly.

Table 2. 1 Comparison of SRM control methods for TR mitigation and control

| | Advantages | Disadvantages |
|-------------------|---|--|
| DTC | <ul style="list-style-type: none"> - Torque control and some, but not complete TR mitigation across a speed range - Very fast dynamic response - Low computational burden | <ul style="list-style-type: none"> - Machine Parameters required beforehand - Increased TR at lower speeds - Variable switching frequency - |
| DITC | <ul style="list-style-type: none"> - Accurate torque control and reduced TR across a wider speed range than DTC - Fast dynamic response - Dependent on design, does not require an encoder | <ul style="list-style-type: none"> - Machine Parameters required beforehand - Variable switching frequency - |
| MPTC | <ul style="list-style-type: none"> - Accurate control and good TR mitigation - Effective at countering SRM non-linearities - Low complexity implementation once model is obtained | <ul style="list-style-type: none"> - Accurate and complex SRM model required beforehand - High CPU burden |
| TSF | <ul style="list-style-type: none"> - Torque control, with TR mitigation across a - Wide TR free speed range - Adaptable for optimization of Torque Sharing function | <ul style="list-style-type: none"> - High CPU burden and difficult implementation dependent on complexity of Torque Sharing Function. - Machine Parameters required beforehand |
| Current Profiling | <ul style="list-style-type: none"> - Simple control implementation, with complete commutation TR mitigation - Low computational burden - Highly customisable dependent on control parameters | <ul style="list-style-type: none"> - Machine Parameters required beforehand - Extensive pre-calculation of profiles required beforehand |

Examining TSFs further, they operate by sharing torque between SRM phases based upon some mathematical function, where Fig 2.10 gives examples of current waveforms using basic TSFs such as the linear function in Fig 2.10a, Cosine function in Fig 2.10b, Cubic function in Fig 2.10c and finally the exponential function in Fig 2.10d. Many advanced forms of TSF have been progressively developed, with examples such as [2-15], where some of the basic TSF functions shown in Fig 2.10 are optimised to propose a new family of TSFs which increase drive efficiency and maximal TR free speed range. When using TSFs, θ_{on} , θ_{off} and by extension the overlap angle θ_{ov} , can be adjusted in accordance with the general TSF equation (2.20). Within this function, T_d represents the demand torque required to fulfil load torque demand, and the $f_{rise/fall}(\theta)$ functions represent the given TSFs overlap equation which dictate the overlap shape as seen in Fig 2.10.

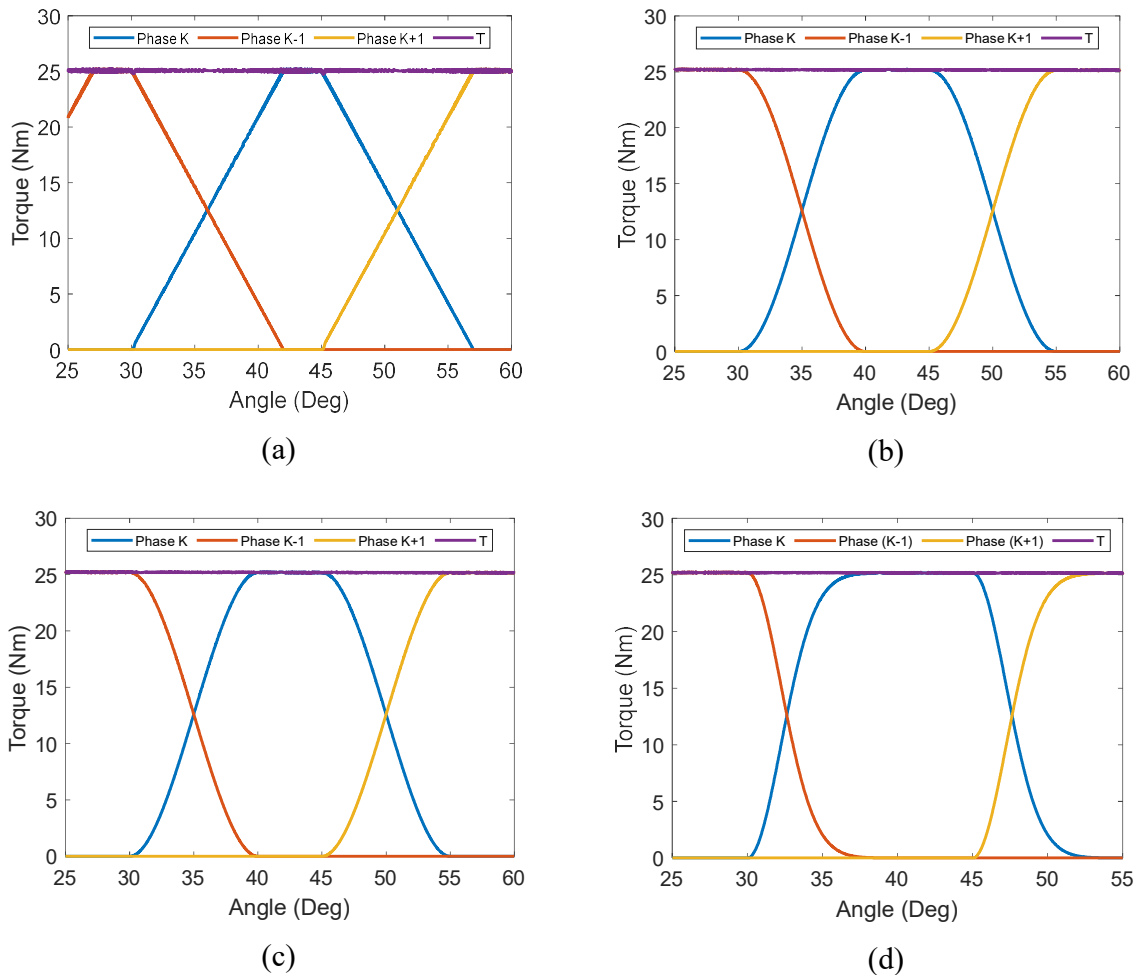


Fig 2.10 Torque sharing functions torque profiles (a) Linear (b) Cosine (c) Cubic, and (d) Exponential

$$T(\theta) = \begin{cases} 0, & 0 \leq \theta < \theta_{on} \\ T_d \cdot f_{rise}(\theta), & \theta_{on} \leq \theta < \theta_{on} + \theta_{ov} \\ T_d, & \theta_{on} + \theta_{ov} \leq \theta < \theta_{off} \\ T_d \cdot f_{fall}(\theta), & \theta_{off} \leq \theta < \theta_{off} + \theta_{ov} \\ 0, & \theta_{off} + \theta_{ov} \leq \theta < \theta_r \end{cases} \quad (2.20)$$

Along with the general equation, to operate an SRM using the same principles as TSFs, θ_{on} and θ_{off} must satisfy the constraints set forth in (2.21). θ_{on} must be equal to or greater than the unaligned angle θ_u to produce torque in the phase, θ_{off} must be less than or equal to θ_{ov} subtracted from the aligned angle θ_a .

$$\begin{cases} \theta_{on} \geq \theta_u \\ \theta_{off} \leq \theta_a - \theta_{ov} \end{cases} \quad (2.21)$$

The overlap angle θ_{ov} where torque is shared between phases is also constrained using (2.22), dependent on the aforementioned rotor pole pitch θ_r and stroke angle ε calculated from N_r and the number of machine phases m (2.23).

$$\theta_{ov} \leq 1/2 \theta_r - \varepsilon = \frac{60}{2} - 15 = 15^\circ \quad (2.22)$$

$$\varepsilon = \frac{360}{mN_r} = \frac{360}{4 \cdot 6} = 15^\circ \quad (\text{For an } 8/6 \text{ 4 phase SRM}) \quad (2.23)$$

For the conduction period of half a rotor pole pitch (30°), (2.24) represents the known torque sharing parameters for the 8/6 SRM.

$$T(\theta) = \begin{cases} 0, & 0 \leq \theta < 30^\circ \\ T_d \cdot f_{rise}(\theta), & 30^\circ \leq \theta < 45^\circ \\ T_d \cdot f_{fall}(\theta), & 45^\circ \leq \theta < 60^\circ \end{cases} \quad (2.24)$$

Using the Cosine TSF as an example, $f_{rise}(\theta)$ and $f_{fall}(\theta)$ can be defined using (2.25).

$$\text{cos:} \begin{cases} f_{rise} = 1/2 - 1/2 \cos 180^\circ \left(\frac{\theta - \theta_{on}}{\theta_{ov}} \right) \\ f_{fall} = 1/2 + 1/2 \cos 180^\circ \left(\frac{\theta - \theta_{off}}{\theta_{ov}} \right) \end{cases} \quad (2.25)$$

As a control scheme, TSFs can be implemented in the form illustrated in Fig 2.11, where torque is inferred from a $(T - I - \theta)$ LUT using phase current measurements, and an error torque is created from subtracting from the reference torque of the TSF. This error is then fed to a hysteresis band torque controller (HBTC), which functions by modulating the switching signals fed to the drive converter, to track torque within an upper and lower reference band. The calibration of the hysteresis band can influence torque ripple, for example if the band is wide, the reference torque will be tracked within the band with a larger torque ripple. In the other case where the band is narrow torque ripple, is now smaller within this band, but requires an increased switching frequency and therefore greater losses. As it relates to current profiling, the torque ‘sharing’ of TSFs is also utilised. Both control methodologies offer effective TR mitigation and control of the SRMs torque, Current profiling in particular is highly customisable in regard to further modifications that can be made for objectives beyond TR mitigation.

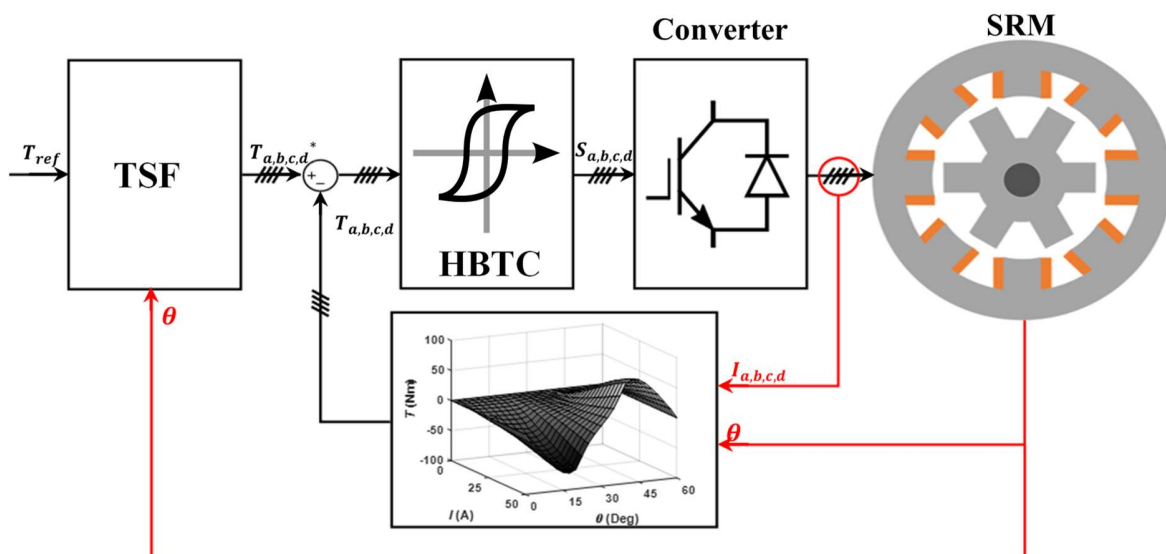


Fig 2.11 TSF torque control scheme for an 8/6 SRM

2.5 SRM Drive Converters

There are a range of power converter configurations that exist for the SRM, which play important role in the cost and efficiency of the drive system. From this range, the most commonly used family of converters are bridge type converters. Apart from these, there are also Capacitive, Magnetic, Dissipative and Self-Commutating converter families. Compared to other machine topologies,

SRMs cannot be operated with traditional converter designs, this is because the SRM differs greatly in its operating principles, using unidirectional current flow to produce torque as seen in (2.8), along with the presence of double the equivalent power connections per phase compared to machine topologies such as the PMSM.

For the optimal operation of the SRM, there are a set of requirements which must be met by the drive converter [2-16][2-17]:

- **Phase overlap capability:** To effectively reduce or eliminate TR through control, overlapping conduction in SRM phases must be possible in the converter, specifically at phase commutation.
- **High efficiency:** With any machine topology, efficiency is a crucial aspect which aims to be maximised. In SRM drive converters, the converter must efficiently energise and de-energise its phases with minimal losses, importantly being able to recycle phase energy instead of dissipating it.
- **Minimal Cost:** For a cost effective drive converter, any topology must be able to carry out the high efficiency, full operation of the SRM while utilising minimal amounts of circuit components, mainly power semiconductors, which require accompanying gate driving circuitry to accommodate their use.
- **Fast magnetisation and de-magnetisation:** To track current references with low error, the converter must be able to utilise its DC voltage supply effectively. This means quickly magnetising and reaching required current levels for torque production and then de-magnetise the phase without causing significant current error and therefore TR. Most converters can harness the full DC voltage value of their supply for operation, but some can also effectively ‘boost’ this voltage, which can boost base speed.
- **Fault tolerance:** For certain applications, the converter must be robust to either in-circuit failures or faults within the machine such as phase failures. For example, an SRM can typically operate with a phase failure in ‘limp home’ mode, the converter should be able to accommodate this.

Within the above stated converter families, an extensive amount of designs exist which can be suitable for an SRM dependent on the application. This has been studied and is exemplified in [2-16]-[2-18], where cases are made in general for the different families, highlighting various

advantages between them. These are graded as such with the inclusion of more complex converters such as multilevel and ones which utilise voltage boosting. Converters with high scoring due to their attractive features include the C-Dump, Sood, H-Bridge and the Asymmetric Half Bridge (ASHB). Both C-Dump and Sood converters belong in the ‘Capacitive’ families, where they both recover energy from the SRM via a capacitive element which charges during demagnetisation, and discharges during magnetisation to preserve energy in the converter. The C-Dump, illustrated in Fig 2.12, allows independent control of each of the SRMs phases, with a minimal amount of components, which attributes to a lower cost point but has decreased efficiency and reliability due its capacitive recovery method. The Sood converter, illustrated in Fig 2.13 can be seen as similar to the C-Dump, with the additional advantage of allowing either magnetization from the capacitive element or the DC supply rail, this is accompanied by a complex control requirement to implement the switching states which accomplish this. The remaining converters highlighted belong to the bridge converter family and are very similar in design. Compared to other converter types, bridge converters tend to have a slightly higher cost due to the number of components, but in terms of the benefits they offer, it is a beneficial trade off. They are simple,

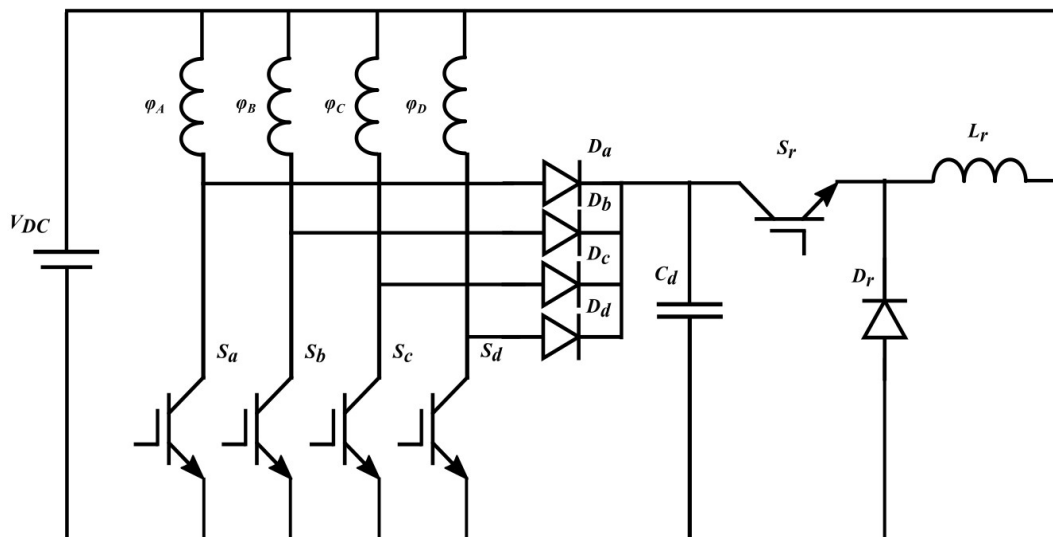


Fig 2.12 C-Dump Converter

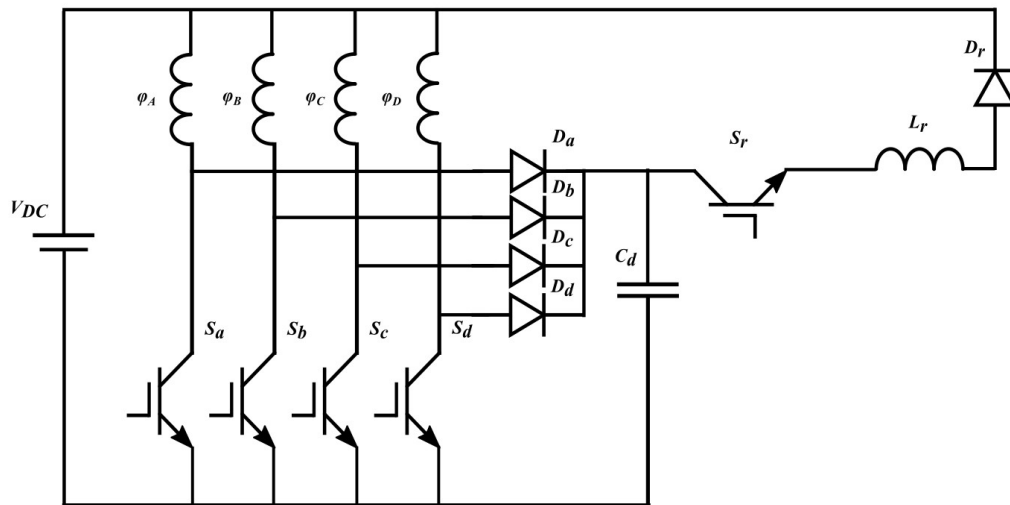


Fig 2.13 Sood Converter

robust converter designs which fulfil the above requirements of SRM operation by having the ability to quickly magnetise and demagnetise phases, allow multiphase conduction, all while operating at a high efficiency. Firstly, the H-Bridge which is shown in Fig 2.14, is the most flexible of these converters in terms of control, by allowing full control of the phase due to its number of switches. These extra switches offer an increased efficiency during freewheeling, but will increase cost significantly due to the cost of said switches and their respective gate driving circuitry.

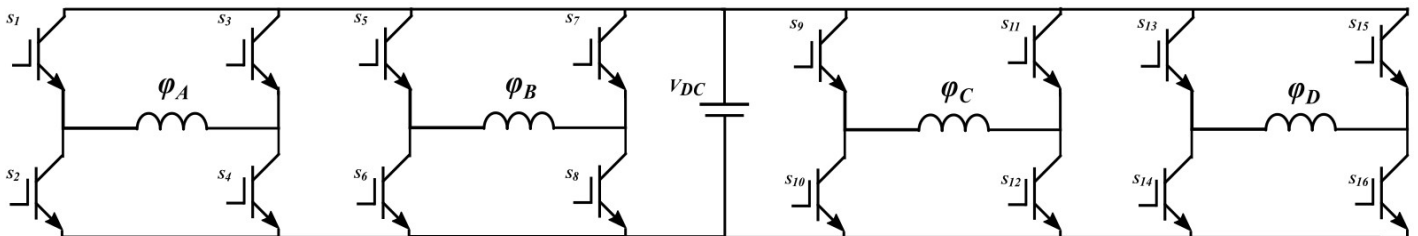


Fig 2.14 H-Bridge Converter

Finally, The ASHB is shown in Fig 2.15, being similar to the H-bridge but substituting two switches for freewheeling diodes which while offering great controllability, makes it slightly less flexible. The ASHB encapsulates the above characteristics of bridge converters, being efficient in operation, fault tolerant and cost efficient, which makes it an attractive candidate for a number of applications. It also offers full phase overlap capability, with no conflicts between the phases, and fast magnetisation/demagnetisation, by allowing the application of full DC link voltage and allowing the modification of the topology for voltage boosting. Compared to the other discussed converters, it offers superior reliability, while also being the cheapest option with near equal

efficiency [2-16]. This combination of factors along with its easy controllability results in it being the most deployed converter in an SRM drive, also being heavily modifiable to further improve its performance, where for example, voltage boosting can be implemented [2-19]. To address the number of components in the ASHB, another modification which can be utilised is the Common Phase ASHB shown in Fig 2.16. The main advantage of the common phase ASHB is its lower number of components, which therefore means a cheaper overall cost compared to the ASHB. The disadvantage of this is that it cannot operate with more than two phases conducting at the same time on the shared power semiconductor device, which also decreases fault tolerance slightly. For example, in a four phase, 8/6 SRM, three phase conduction cannot be properly achieved as one of

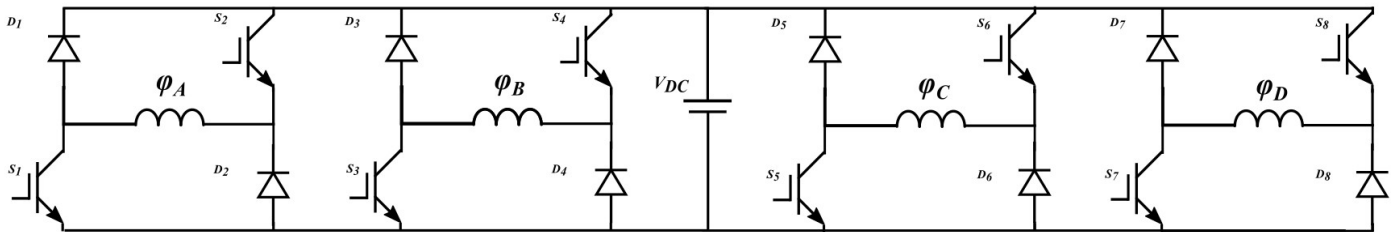


Fig 2.15 Four phase ASHB converter

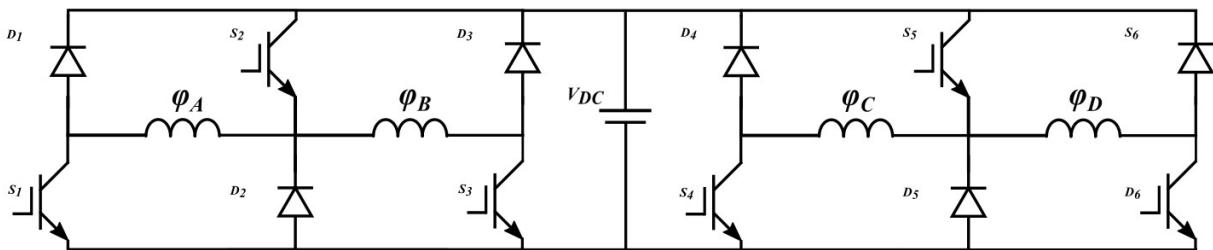


Fig 2.16 Four phase common phase ASHB converter

the phases will require a mutual power semiconductor which is already in use. Along with this, the converter can only be constructed for SRMs with an even number of phases, and it has a lower fault tolerance due to the commonly shared leg.

These converters switch and apply voltage in three different states when operating the drive system, being illustrated in Fig 2.17 and the three states are described as follows:

- i *Magnetization*: This is when positive DC link voltage V_{DC} is applied to the phase by switching both of the switching devices associated with the phase on. This is shown in Fig 2.14a, where the voltage energises the phase and injects current to induce torque in the rotor.

- ii *Free-wheeling*: In this state, displayed in Fig 2.17b), no voltage is effectively applied to the phase and current is circulated in a loop separate from the DC link with one switch enable. Losses due to the phase winding resistance along with the diode and power semiconductor device resistances actively cause the current in the phase to decay slowly in this state and it is useful for maintaining reference currents when they are not increasing or decreasing.
- iii *De-magnetization*: In this final state, shown in Fig 2.17c), V_{DC} is applied in the opposite polarity to the magnetization state when both switches are off. This causes current to decrease rapidly and leave the phase, returning to the DC source. This is utilised when reference current is decreasing or set to zero when the phase is required to be completely de-energised as other phases take over torque production.

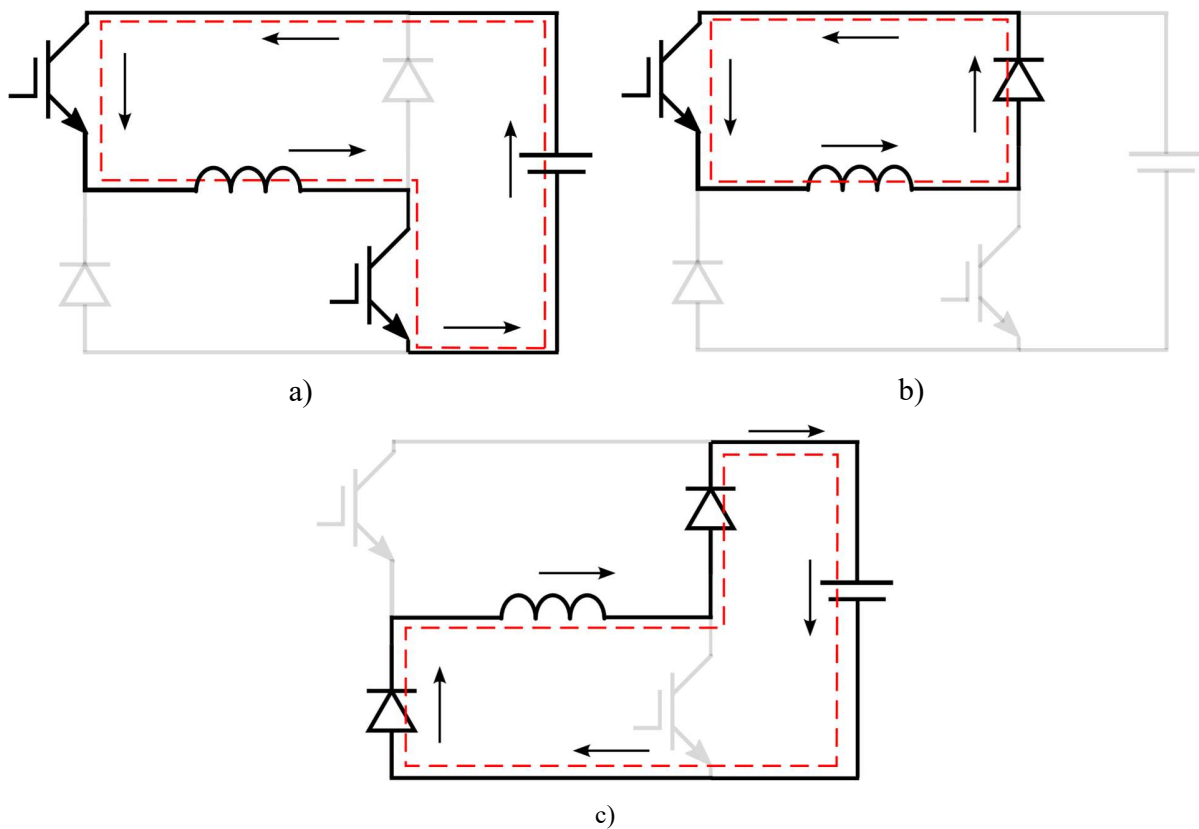


Fig 2.17 Bridge converter switching states: (a) Magnetization, (b) Free-wheeling and (c) De-magnetization

An example of these switching states when using basic CCC, like the waveforms in Fig 2. 8, is shown in Fig 2.18, where current is increased to the reference current for torque production, maintained at said current, and then returned to zero before the phase reaches negative torque production regions.

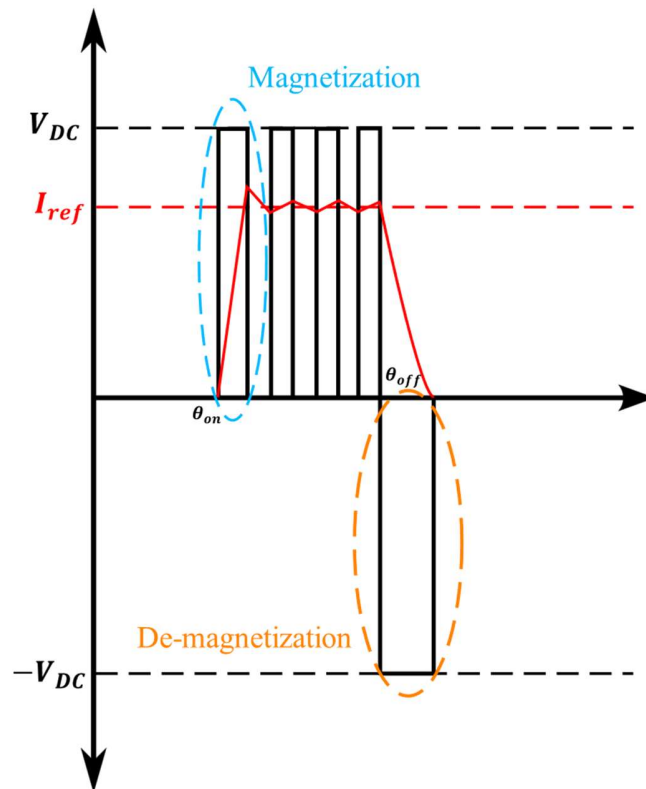


Fig 2.18 Typical phase current and voltage waveforms using CCC operation

Fig 2.14

2.6 Summary

This chapter presented the basic SRM structure in terms of its important characteristic of the ratio between the number of stator and rotor poles. Its mode of torque production is analysed, and from the resultant set of equations and equivalent circuit, the SRMs behaviour is established. Even with these equations, the non-linear nature of the SRM makes it necessary that for accurate modelling, LUTs are needed which can better quantify the relationship between torque, flux, current and rotor

position. The basic principles of how to operate an SRM are shown in terms of CCC and ACC dependent on constant torque or constant speed operation. From this, an overview of typical control techniques used for SRMs is discussed, with a more detailed view given on TSFs. Finally, the switching behaviour of SRM drive converters is illustrated in relation to the most popular drive topology, being the ASHB converter.

References

- [2-1] D. Mohanraj, J. Gopalakrishnan, B. Chokkalingam and L. Mihet-Popa, "Critical Aspects of Electric Motor Drive Controllers and Mitigation of Torque Ripple—Review," in *IEEE Access*, vol. 10, pp. 73635-73674, 2022,
- [2-2] J. -W. Ahn and G. F. Lukman, "Switched reluctance motor: Research trends and overview," in *CES Transactions on Electrical Machines and Systems*, vol. 2, no. 4, pp. 339-347, Dec. 2018,
- [2-3] A. Dorneles Callegaro, J. Liang, J. W. Jiang, B. Bilgin and A. Emadi, "Radial Force Density Analysis of Switched Reluctance Machines: The Source of Acoustic Noise," in *IEEE Transactions on Transportation Electrification*, vol. 5, no. 1, pp. 93-106, March 2019.
- [2-4] C. Gan, J. Wu, Q. Sun, W. Kong, H. Li and Y. Hu, "A Review on Machine Topologies and Control Techniques for Low-Noise Switched Reluctance Motors in Electric Vehicle Applications," in *IEEE Access*, vol. 6, pp. 31430-31443, 2018.
- [2-5] T. Husain, A. Elrayyah, Y. Sozer and I. Husain, "Unified Control for Switched Reluctance Motors for Wide Speed Operation," in *IEEE Transactions on Industrial Electronics*, vol. 66, no. 5, pp. 3401-3411, May 2019,
- [2-6] Z. Yang, F. Shang, I. P. Brown and M. Krishnamurthy, "Comparative Study of Interior Permanent Magnet, Induction, and Switched Reluctance Motor Drives for EV and HEV Applications," in *IEEE Transactions on Transportation Electrification*, vol. 1, no. 3, pp. 245-254, Oct. 2015.
- [2-7] A. D. Cheok and Y. Fukuda, "A new torque and flux control method for switched reluctance motor drives," in *IEEE Transactions on Power Electronics*, vol. 17, no. 4, pp. 543-557, July 2002,
- [2-8] R. B. Inderka and R. W. A. A. De Doncker, "DITC-direct instantaneous torque control of switched reluctance drives," in *IEEE Transactions on Industry Applications*, vol. 39, no. 4, pp. 1046-1051, July-Aug. 2003,
- [2-9] H. Peyrl, G. Papafotiou and M. Morari, "Model predictive torque control of a Switched Reluctance Motor," *2009 IEEE International Conference on Industrial Technology*, Churchill, VIC, Australia, 2009

- [2-10] M. Ilic-Spong, T. J. E. Miller, S. R. Macminn and J. S. Thorp, "Instantaneous Torque Control of Electric Motor Drives," in *IEEE Transactions on Power Electronics*, vol. PE-2, no. 1, pp. 55-61, Jan. 1987
- [2-11] D. S. Schramm, B. W. Williams and T. C. Green, "Torque ripple reduction of switched reluctance motors by phase current optimal profiling," *PESC '92 Record. 23rd Annual IEEE Power Electronics Specialists Conference*, June-July. 1992.
- [2-12] K. Sreeram, P. K. Preetha, J. Rodríguez-García and C. Álvarez-Bel, "A comprehensive review of torque and speed control strategies for switched reluctance motor drives," in *CES Transactions on Electrical Machines and Systems*, March 2025
- [2-13] O. Ellabban and H. Abu-Rub, "Torque control strategies for a high performance switched reluctance motor drive system," *2013 7th IEEE GCC Conference and Exhibition (GCC)*, Doha, Qatar, 2013
- [2-14] G. Fang, F. P. Scalcon, D. Xiao, R. P. Vieira, H. A. Gründling and A. Emadi, "Advanced Control of Switched Reluctance Motors (SRMs): A Review on Current Regulation, Torque Control and Vibration Suppression," in *IEEE Open Journal of the Industrial Electronics Society*, vol. 2, pp. 280-301, 2021
- [2-15] V. P. Vujičić, "Minimization of Torque Ripple and Copper Losses in Switched Reluctance Drive," in *IEEE Transactions on Power Electronics*, vol. 27, no. 1, pp. 388-399, Jan. 2012.
- [2-16] M. A. Gaafar, A. Abdelmaksoud, M. Orabi, H. Chen and M. Dardeer, "Switched Reluctance Motor Converters for Electric Vehicles Applications: Comparative Review," in *IEEE Transactions on Transportation Electrification*, vol. 9, no. 3, pp. 3526-3544, Sept. 2023.
- [2-17] O. Ellabban and H. Abu-Rub, "Switched reluctance motor converter topologies: A review," *2014 IEEE International Conference on Industrial Technology (ICIT)*, Busan, Korea (South), 2014
- [2-18] Abdel-Aziz, Ali, Mohamed Elgenedy, and Barry Williams. 2024. "Review of Switched Reluctance Motor Converters and Torque Ripple Minimisation Techniques for Electric Vehicle Applications" *Energies* 17, no. 13: 3263, July 2024
- [2-19] A. A. Abdel-Aziz, K. H. Ahmed, S. Wang, A. M. Massoud and B. W. Williams, "A Neutral-Point Diode-Clamped Converter With Inherent Voltage-Boosting for a Four-Phase SRM Drive," in *IEEE Transactions on Industrial Electronics*, vol. 67, no. 7, pp. 5313-5324, July 2020

Chapter 3

Experimental Efficiency Comparison of a Superjunction MOSFET, IGBT and SiC MOSFET for SRM Drives

This Chapter covers a comparison between three different power semiconductor device types for application in an SRM drive. The three (Si SJ MOSFET, Si IGBT and SiC MOSFET) are compared in theory in terms of device operation and from an economic perspective. Experimental analysis is then performed out on three chosen power semiconductor models with similar specifications, using device thermal analysis to gauge device efficiency in a rudimentary comparison.

3.1 Background

The switched reluctance machine (SRM) has attributes [3-1] - [3-4], which make it attractive for a range of applications. The SRM basic drive circuit is well established as discussed in Chapter 2, and the design choices are robust as they do not have conventional bridge-legs, which introduce the possibility of simultaneous conduction if power devices are erroneously signalled on at the same time, resulting in a short circuit of the DC supply. Furthermore, the power devices are not subjected to externally applied dv/dts , with the possibility of unwanted dv/dt -induced turn-on. For optimising the SRM as a candidate against other machine topologies, high efficiency is desirable in a machine's drive circuit which will reduce lifetime energy wastage and reduce cooling requirements. To this end, the relative losses of the silicon superjunction (SJ) MOSFET, IGBT and SiC MOSFET is investigated in this chapter, given as components, they will be responsible for the bulk of losses associated in a high efficiency drive. The comparison carried out is a general comparison of the devices accompanied with a rudimentary analysis of losses, and does not serve as a detailed analysis into the devices in application to an SRM, where a direct analysis would require a further experimental analysis of the devices applied in an SRM.

3.2 SRM Power devices and converter topologies

The IGBT and fast recovery diode are typically the preferred power semiconductor devices in machine drive power converters. High efficiency in the drive means less lifetime energy wastage, reduced cooling requirements and a consequent low converter mass, resulting in overall reduced cost. To attain high efficiencies, SiC devices are being considered for high-efficiency machine drives [3-5]-[3-10], particularly in automotive, aerospace, and railway applications. An example of a high-efficiency SRM drive using SiC devices is given in [3-11]. Another alternative to the IGBT is the silicon SJ MOSFET [3-12], which has attractive properties, including low on-state resistance, robust gate-drive requirements and good short-circuit behaviour [3-13], but is limited to voltage ratings of less than 850V. However, its highly non-linear output capacitance and poor performance of its intrinsic diode are problematic in the voltage source converter (VSC) topologies used for most AC machine drives. The SJ MOSFET therefore is not normally used in these drives without mitigating techniques and hardware to address these challenges [3-14] - [3-18]. Conversely, in simple hard-switched single-ended applications, the SJ MOSFET performs well. An example is in the boost converter [3-19] used for power factor correction. Unlike most machines, the winding currents drawn by the SRM can be unidirectional. Consequently, regardless of how sophisticated their power converter topologies are, the majority of SRM drives [3-20] - [3-22] essentially operate as single-ended converters in a manner similar to [3-19]. This means that their active switches only operate as forward switches, and never as fast-switching rectifiers. The SJ MOSFET performs well in the former mode, but poorly in the latter mode. Fig 3.1 presents the different circuit configuration for driving a standard electrical machine versus a converter leg for an SRM. In a standard VSC machine-drive topology, such as the bridge-leg in Fig 3.1a, a challenge is that the power devices have to perform both functions.

If the circuit in Fig 3.1a has a positive phase winding current I_{ph} , then S_1 is acting as the forward switch. Ideally, it would operate with D_2 acting as the freewheeling device. However, S_2 is also located in the freewheeling location. Similarly, if I_{ph} is negative, S_2 becomes the forward switch and, as well as D_1 , S_1 lies in the freewheeling location. The asymmetric half-bridge circuit is commonly used to drive SRM phase currents, and is shown in Fig 3.1b. Normally S_2 and D_2 operate as low-frequency steering devices at the machine's base frequency, and S_1 and D_1 operate as a buck converter when the machine is motoring, or as a boost converter when the machine is

generating. In each case, S_1 only ever operates as a fast-switching forward switch, and D_1 only ever operates as a fast-switching rectifier.

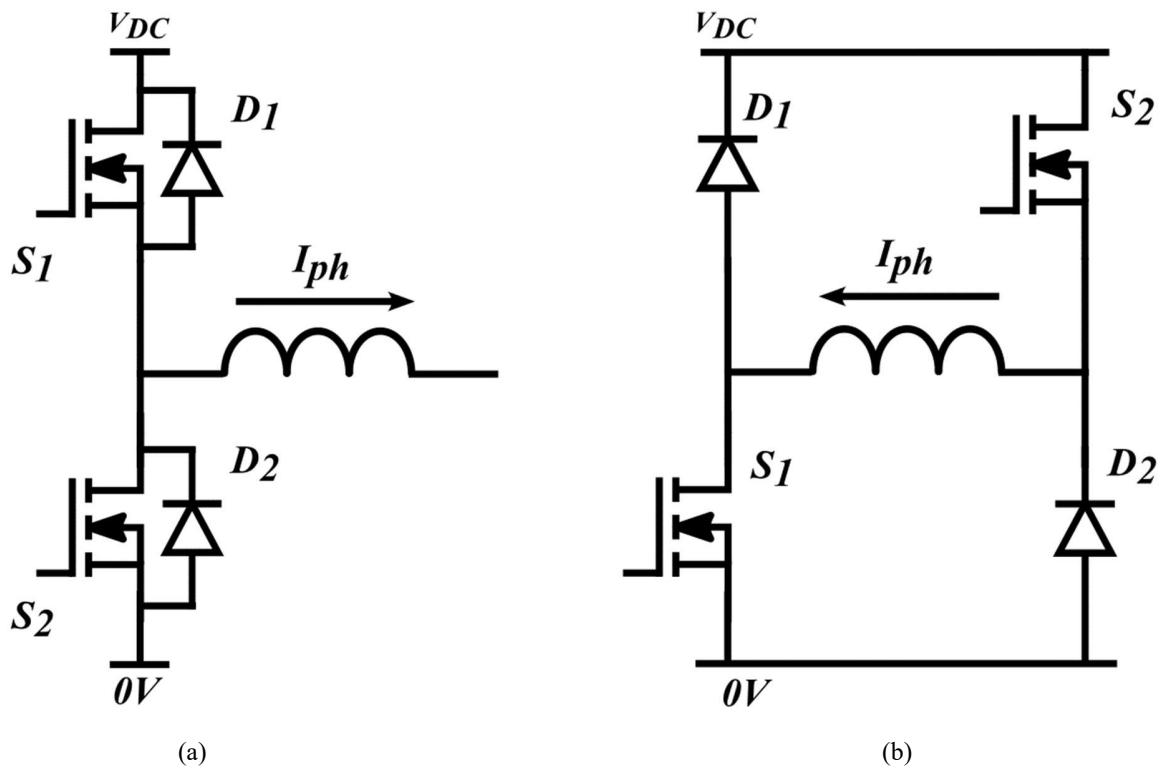


Fig 3.1 (a) Standard bridge-leg for driving one phase of a standard machine. (b) Typical driver circuit for driving one phase of a switched reluctance machine.

The problems with having a transistor, as in Fig 3.1a, instead of solely a purpose-designed diode in the freewheeling location, are summarised as follows:

- Simultaneous conduction occurs if the devices are erroneously switched on simultaneously.
- dv/dt -induced turn-on can be caused by rapid voltage changes across the device's output terminals causing current to flow through its Miller Capacitance.
- The device may have an intrinsic diode with poor performance, which therefore passes a large reverse recovery charge.
- The output capacitances of the transistor may present a high capacitive load to the incoming power device.

Apart from the avoidance of these problems, other potential advantages of the SRM drive topology are:

- As S_2 and D_2 only need to switch at the machine's base-frequency, then these devices can be different from S_1 and D_1 , and optimised for low-frequency operation. However, devices S_1 and S_2 may be identical for simplicity, along with D_1 and D_2 . Losses are not uniformly distributed.
- The reference electrode (emitter or source) of the device switching at high frequency, S_1 in Fig 3.1b here, is not subjected to high common mode dv/dts . These dv/dts inject currents through parasitic capacitances across the gate driver circuit's isolation barriers which can cause malfunctioning of the low-side gate driver circuitry, and the control circuitry generating the switching signal.

Instead of the switching arrangement described in this section, S_2 and D_2 could be driven at high frequency, with S_1 and D_1 switching at the base frequency. However, this means that a power device, S_2 , would be switching with a high dv/dt at its control electrode.

3.3 Output capacitances of the superjunction MOSFET and the SiC MOSFET

Fig 3.2a shows the QV characteristic of the output capacitance C_{oss} of an SJ MOSFET rated at 650 V with an on-state resistance $R_{DS(on)}$ of 60 m Ω . A major determinant of switching losses in the hard-switched SJ MOSFET is the stored energy in C_{oss} , which is dissipated as self-discharge energy at turn-on. This is small, and the turn-on losses are therefore small. The non-linear nature of C_{oss} also gives effective self-snubbing at turn-off, but without a large amount of associated self-discharge energy being stored in C_{oss} . Total switching losses are therefore low, provided the MOSFET is used with a freewheeling diode, which does not draw a large capacitive or reverse recovery charge, as in [3-19].

However, if the SJ MOSFET is used in a VSC bridge-leg its freewheeling behaviour is problematic. Even if its intrinsic diode recovery behaviour is addressed, its C_{oss} presents difficulties. Firstly, C_{oss} is very high at low voltage. When the incoming MOSFET initially turns on, it has this high capacitance in series with it and the supply rail, resulting in a large transient

current being drawn. Secondly, the co-energy, represented by the area under the QV curve, is large. This energy is dissipated in the incoming device when it turns on and charges the C_{oss} of the freewheeling MOSFET.

Fig 3.2b shows the QV characteristic of the output capacitance C_{oss} of a comparable SiC MOSFET, with the same voltage rating of 650 V, and the same $R_{DS(on)}$ of 60 m Ω . Key differences are that the co-energy is much smaller than that of the SJ MOSFET, and that the Q/V gradient (capacitance) is much lower near 0 V. Both of these factors favour the SiC MOSFET over the SJ MOSFET for applications in VSC bridge-legs.

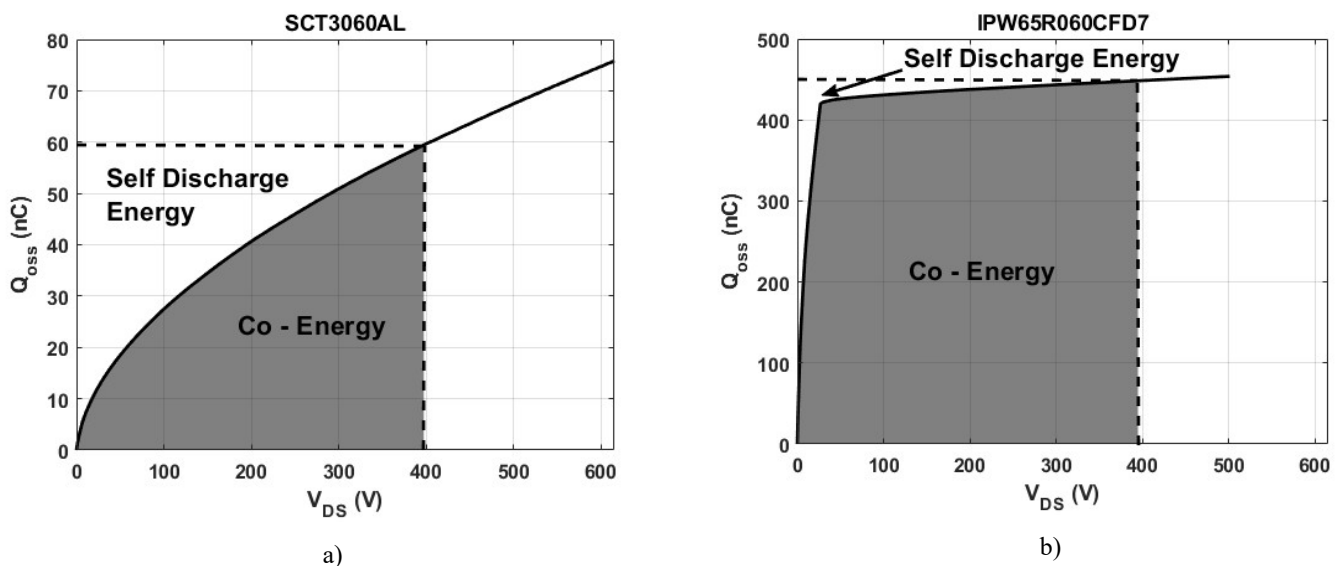


Fig 3.2 Power device output capacitance (C_{oss}) QV characteristics. (a) SJ MOSFET, and (b) SiC MOSFET. *note different vertical axis scales

Whilst the co-energy of the SJ MOSFET is much higher than that of the SiC MOSFET, it is observed that the self-discharge energy of each device is similar. For the SJ MOSFET, it is estimated at 8.4 μ J from Fig 3.2a when charged to 400 V, in rough agreement with the manufacturer's specified value of 9.5 μ J. For the SiC MOSFET, it is estimated at 8.1 μ J from Fig 3.2b when charged to 400 V, also in rough agreement with the manufacturer's data, in this case read from the graphical data provided, which gives approximately 9.0 μ J.

In applications where C_{oss} characteristics of a high co-energy and a high capacitance at low voltage are not problematic, as in Fig 3.1b, it is consequently expected that the SJ MOSFET is a feasible alternative to the SiC MOSFET. An estimation of losses is therefore carried out using the device

datasheets, followed by an experimental comparison of losses for an SJ MOSFET, a SiC MOSFET, and an IGBT.

3.4 Loss Estimation

Using the respective datasheets of the SI IGBT [3-23], SJ MOSFET [3-24] and SiC MOSFET [3-25], an approximation can be made of the general device losses, which mainly consist of switching and conduction losses. Estimating device losses without experimental aid can be complex if the best accuracy is desired, given the highly nonlinear relationships of device characteristics during operation. The modelling as such can vary greatly, where only a rudimentary method is applied in this scenario. The conduction losses can be represented using (3.1) for IGBT type devices, or (3.2) for MOSFETs. In each of these, I is the rms current flowing in the device, $V_{CE(sat)}$ is the IGBTs on state voltage drop and $R_{DS(ON)}$ is the equivalent drain source resistance of the MOSFET. Finally, δ represents the duty cycle of the device in operation as a percentage of the total that the device is effectively on for. Note that both $V_{CE(sat)}$ and $R_{DS(ON)}$ have nonlinear relationships with operating temperature, applied voltage across the device and also the current flowing in the device which would need to be considered in a complex model.

$$P = IV_{on}\delta \quad (3.1)$$

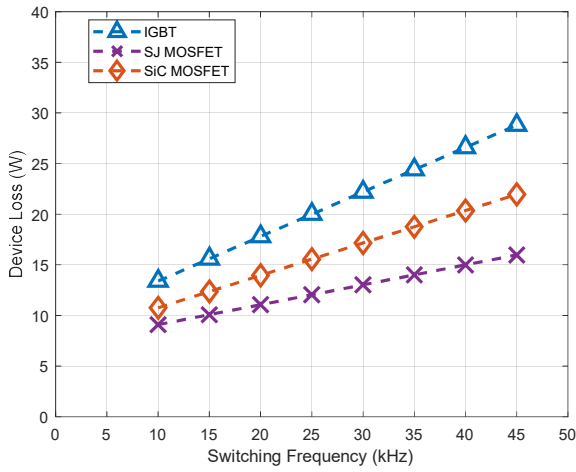
$$P = I^2R_{DS(ON)}\delta \quad (3.2)$$

Switching losses in the devices are caused by the energy consumed when either turning the device on or off. They are caused by the intrinsic parasitic capacitances created due to the layering of the device materials in construction. A simple estimation of switching losses can be given by (3.3), where the sum of device turn-on energy E_{on} and turn-off energy E_{off} is multiplied by switching frequency f_{sw} given the device will switch on and off once in a cycle at under 100% duty cycle. $E_{on/off}$ are typically provided in the device datasheet, but can also be estimated on other parameters such as rise and fall times t_{rise} and t_{fall} respectively using (3.4). Switching losses are more complex than conduction losses, and even with these two formulae, $E_{on/off}$ are dependent on many different factors in operation, and consist of different sub losses such as loss due to output capacitance or gate charge losses. These are all again non-linear and dependent on the state of the device at any given time where temperature, voltage and current can all vary.

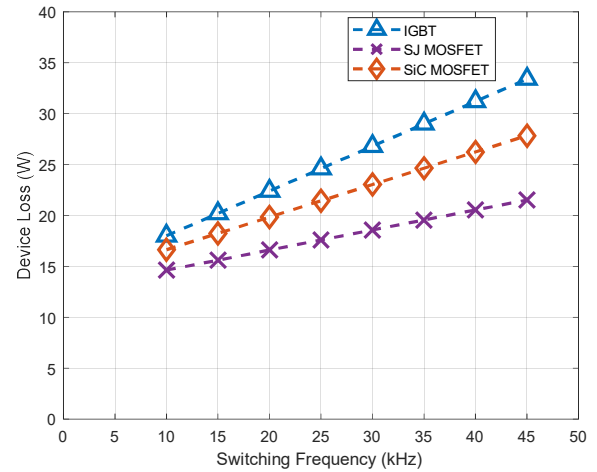
$$P = f_{sw}(E_{on} + E_{off}) \quad (3.3)$$

$$E_{on/off} = \frac{1}{2}IV \times t_{on/off} \quad (3.4)$$

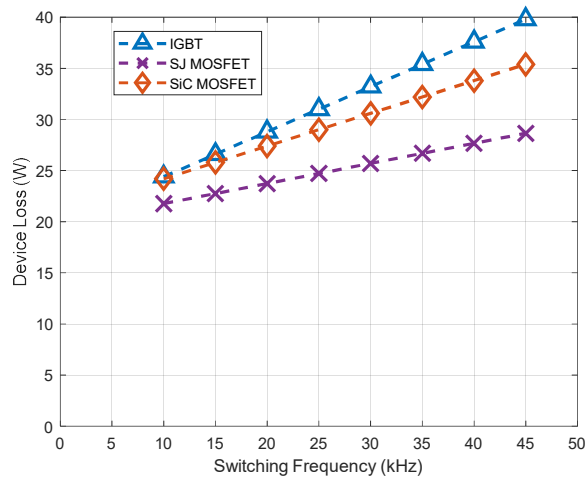
Using (3.1-3.4), a simple approximation from the device datasheets is performed, yielding the graphs shown in Fig 3.3 at three different rms current levels, being a) 6A, b) 8A and c) 10A. In this case, the voltage is taken as the supply voltage of the 8/6 SRM, which is 400V, and the assumed switching is the configuration in Fig 3.1a), where one switch acts as a fast switching rectifier at a flat 50% duty and variable f_{sw} ranging from 10-45kHz, while the other is on for the full duration of a switching period, attempting to mimic the switching patterns of an SRM



(a)



(b)



(c)

Fig 3.3 Experimental power loss vs switching frequency for (a) $I_{ph} = 6A$, (b) $I_{ph} = 8A$ and (c) $I_{ph} = 10A$

Table 3.1 Approximated device losses

| f_{sw} | | 10kHz | 15kHz | 20kHz | 25kHz | 30kHz | 35kHz | 40kHz | 45kHz | |
|------------|-----|------------|-------|-------|-------|-------|-------|-------|-------|-----|
| Si IGBT | 6A | P_{cond} | 67% | 58% | 51% | 45% | 41% | 37% | 34% | 31% |
| | | P_{sw} | 33% | 42% | 49% | 55% | 59% | 63% | 66% | 69% |
| | 8A | P_{cond} | 76% | 67% | 61% | 55% | 51% | 47% | 44% | 41% |
| | | P_{sw} | 24% | 33% | 39% | 45% | 49% | 53% | 56% | 59% |
| | 10A | P_{cond} | 82% | 75% | 69% | 65% | 60% | 56% | 53% | 50% |
| | | P_{sw} | 18% | 25% | 31% | 35% | 40% | 44% | 47% | 50% |
| SJ MOSFET | 6A | P_{cond} | 78% | 71% | 64% | 59% | 55% | 51% | 48% | 45% |
| | | P_{sw} | 22% | 29% | 36% | 41% | 45% | 49% | 52% | 55% |
| | 8A | P_{cond} | 87% | 81% | 76% | 72% | 68% | 65% | 62% | 59% |
| | | P_{sw} | 13% | 19% | 24% | 28% | 32% | 35% | 38% | 41% |
| | 10A | P_{cond} | 91% | 87% | 83% | 80% | 77% | 74% | 72% | 69% |
| | | P_{sw} | 9% | 13% | 17% | 20% | 23% | 26% | 28% | 31% |
| SiC MOSFET | 6A | P_{cond} | 70% | 61% | 54% | 49% | 44% | 40% | 37% | 34% |
| | | P_{sw} | 30% | 39% | 46% | 51% | 56% | 60% | 63% | 66% |
| | 8A | P_{cond} | 81% | 74% | 68% | 63% | 58% | 55% | 51% | 48% |
| | | P_{sw} | 19% | 26% | 32% | 37% | 42% | 45% | 49% | 52% |
| | 10A | P_{cond} | 87% | 81% | 77% | 72% | 69% | 65% | 62% | 59% |
| | | P_{sw} | 13% | 19% | 23% | 28% | 31% | 35% | 38% | 41% |

somewhat. Using this rudimentary approximation, the SJ MOSFET can be seen as the device with the lowest losses across the operational currents and frequencies, followed by the SiC MOSFET and finally the IGBT. Examining the losses of the devices further, Table 3.1 breaks down approximated losses along the lines of the percentage of total losses of the switching and conduction losses. From the three devices, the IGBT consistently has the highest share of switching losses proportional to its conduction losses, but as current increases with each of the devices, conduction losses begin to dominate, and with further increases in current, make up majority of the device losses.

3.5 Experimental Setup

The circuit shown in Fig 3.3 has been developed as a multipurpose demonstrator for four-phase SRM drive topologies [3-22]. In the comparison presented here, a single phase of this circuit is used, highlighted by the dashed box in Fig 3.3 and corresponding to Fig 3.1(b), where three versions, one each using IGBTs, SiC MOSFETs and SJ MOSFETs in locations S_1 and S_2 , are constructed as shown in Fig 3.4. Fig 3.5 shows the physical test circuits, which are all otherwise identical apart from the switching devices used.

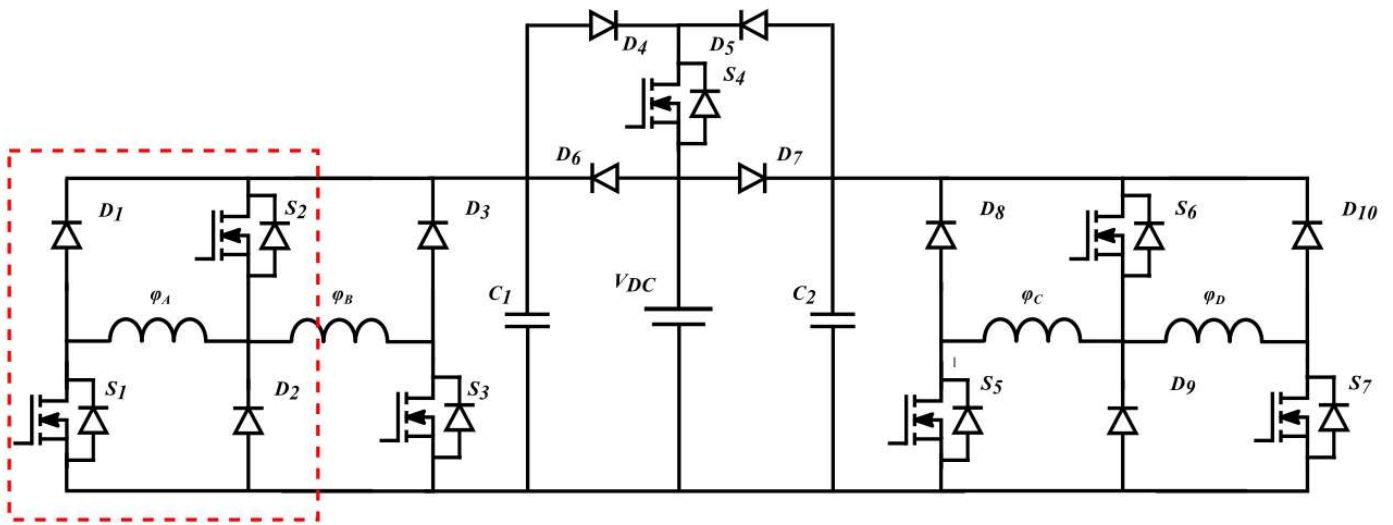


Fig 3.4 Reconfigurable test rig for SRM drive circuits.

The circuits in Fig 3.5 utilise isolated gate drivers. The local gate driver power is transmitted using transformers, and the switching signals are transmitted using UC21540DW gate driver ICs. The gate-source, or gate-emitter, voltages of the devices being tested are held at a negative potential when the devices are off. Fig 3.6 outlines the key gate driver components where $R_{G1} = 22 \Omega$ and $R_{G1} = 4.7 \Omega$, and D_1 is an MBRA340T3G Schottky diode.

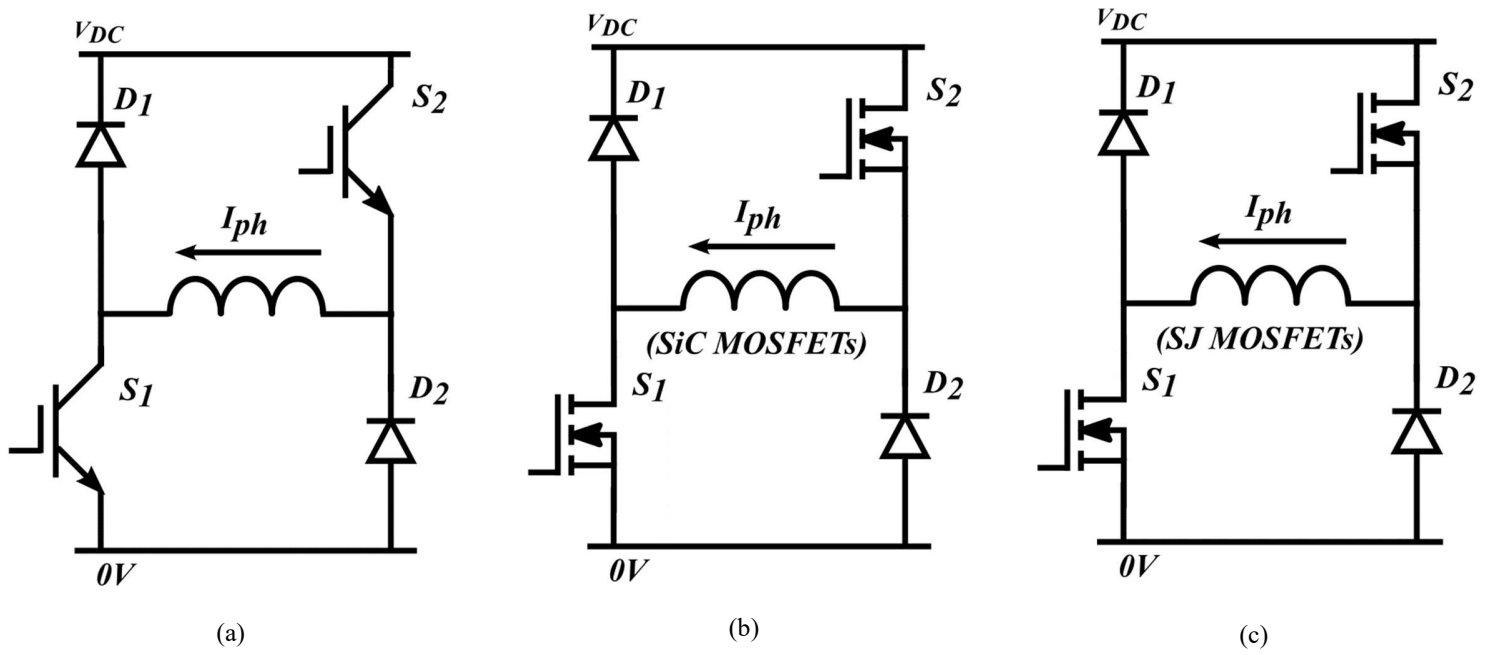


Fig 3.5 Experimental circuit configurations: (a) IGBT converter, (b) SiC MOSFET converter and (c) SJ MOSFET converter



Fig. 3.5 Physical experimental test circuits

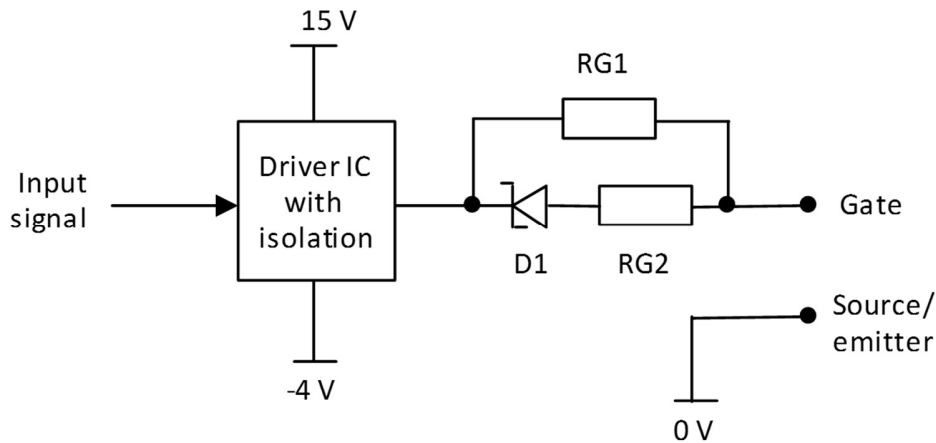


Fig 3.7 Schematic of gate drive circuits used in experimental test rig

Data for the power devices being evaluated are listed in Table 3.2 where all three devices are in TO247-3 packages and are rated at 650 V. The SJ and SiC MOSFETs both have an on-state resistance of 60m Ω . For simplicity, a C3D16065D SiC common-cathode diode-pair package is used in locations D_1 and D_2 in all the test circuits. Both diodes within the package are connected in parallel.

Table 3.2 Power semiconductor device data

| Device | Part Number | Rated V_{DSS} (V_{CES}) | Rated I_D (I_C) | $R_{DS(on)}$ ($V_{CE(sat)}$) | Cost (£) |
|---------------|-----------------|----------------------------------|--------------------------|-----------------------------------|-------------|
| SJ MOSFET | IPW65R060CFD7 | 650V | 36A | 60m Ω | 5.28 |
| SiC MOSFET | SCT3060AL | 650V | 39A | 60m Ω | 10.79 |
| IGBT | RGW60TK65DGVC11 | 650V | 33A | 1.5V | 3.54 |

3.6 Experimental Results

The circuits in Fig 3.5 are operated on a horizontal surface in free air (without forced cooling). Circuit power losses are measured using thermal superposition. To do this, the heatsink-to-ambient thermal resistance $R_{\theta_{hsa}}$ is determined to be approximately 1.03 $^{\circ}\text{C}/\text{W}$, by dissipating a known DC

power in the devices mounted on it and measuring the heatsink steady-state temperature rise T_{aa} above ambient.

The circuits are used to supply a series RL load and operated with a V_{DC} of 400 V, with phase currents I_{ph} of 6 A, 8 A and 10 A. S_2 is held on at a duty factor of 100%, and S_1 is switched at varying frequencies in 5 kHz increments. The load inductance is 5 mH, and the load resistance is set such that S_1 operated at a duty factor of 50%. This attempts somewhat to mimic the performance characteristics of an SRM drive, but is very limited in its extent compared to the

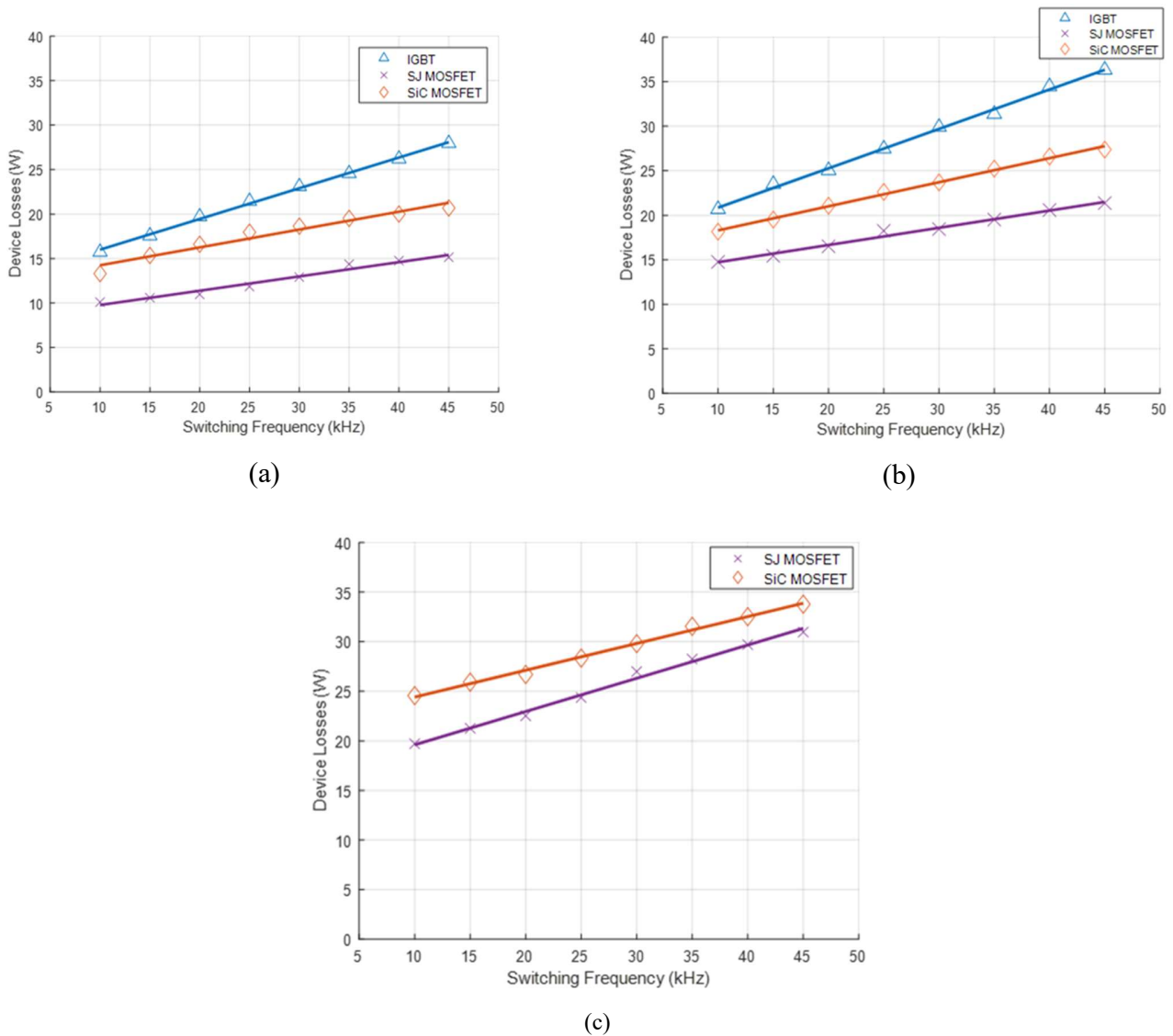


Fig 3.8 Experimental power loss vs switching frequency for (a) $I_{ph} = 6A$, (b) $I_{ph} = 8A$ and (c) $I_{ph} = 10A$

testing of a full SRM and its converter in operation. The measured losses are shown in Fig 3.7. T_{aa} is measured at each frequency and current, and the loss is calculated by dividing T_{aa} by $R_{\theta hsa}$.

When testing the circuit with IGBTs, losses are not recorded at 10 A. This is to avoid an excessive temperature rise of the IGBT in location S_2 , as observed/measured at the front of the IGBT's package.

3.6 Discussion

The approximations from datasheets and experimental results show that the SiC MOSFET and SJ MOSFET both exhibit lower power losses than the IGBT in this specific use case scenario, and for the selected models of said device types. For the particular devices and the gate driver arrangement used in this study, the measured losses in the SJ MOSFET were lower than those in the SiC MOSFET. Generally, the approximations of losses from the datasheets are lower than in experiment, which can be the case due to the limited resolution/complexity of the approximation, whereas discussed, losses in the device can be generally non-linear in their responses where extra losses can also occur in practical experimentation. The following should also be noted:

- Unlike the SJ MOSFET used here, SJ MOSFETs optimised for hard switching are available. These devices have lower self-discharge energies for a given $R_{DS(on)}$, and improved efficiency is consequently expected using these devices.
- For a given $R_{DS(on)}$ and V_{DSS} rating, the SJ MOSFET normally costs less than its SiC counterpart, but this is likely to change as SiC technology matures.
- A simple and identical gate driver arrangement, as shown in Fig 3.6, has been used for each device type tested. The driver circuit resistances R_{G1} and R_{G2} have not been adjusted to give similar voltage and current overshoot values at turn-off and turn-on respectively. The overall design of the drive circuitry is also not optimised for any of the devices, which may decrease losses in each of the devices by varying degrees.
- The EMI generated by each of the devices has not been assessed. Also, as with the voltage and current overshoots, the maximum dv/dts and di/dts occurring during switching have not been set by means of adjusting R_{G1} and R_{G2} .
- The power devices were tested when switching a voltage of 400 V DC. SJ MOSFET voltage rating limits of about 800 V, limit their applicability in many drive applications.

- While these three device types and the models chosen in this study are commonly used, other variations of SJ, Si and SiC devices exist, including experimental device designs which differ in their internal structure. There are also other device materials which could be examined, such as GaN power semiconductors.
- As it relates to the specificity of the comparison, it has been stated that the comparison is limited when assessing the direct application of the devices in an SRM drive compared to just general performance. For an SRM (with some of these factors also being applied to other motor types), many additional factors would need to be considered.
- Firstly, in any discrete instance, an SRM could be conducting with multiple phases, where more switching devices than in a singular phase are operating, and along with this possibly operating in different ways where for example, one phase is switching to demagnetise its phase, and the other to magnetise its phase.
- Secondly, the RL load used in this comparison does not accurately reflect a machine's inductance. In practicality, any electrical machine's apparent inductance at any given time is complex and dependent on its operational state with speed, torque etc. The load inductance connected to a switching device will impact its performance, which is why it must be considered for a comprehensive comparison.
- The losses in the experimental comparison have not been discretised due to the method of thermal analysis used. A more comprehensive comparison of the devices would attempt to separate the two as carried out from the datasheets, as factors could be differed to measure the optimal ratio of losses for the lowest overall loss.

3.7 Summary

This chapter presented a study comparing three different power electronics switches, namely the IGBT, SJ MOSFET and SiC MOSFET for consideration in an SRM drive theoretically, while carrying out a simplified experimental comparison. It is shown that, under this specific set of experimental conditions, both MOSFETs outperformed the IGBT, and that the efficiency of the SJ MOSFET exceeded that of the SiC MOSFET device. However, the gate driver circuits used were not optimised to give identical performance for each circuit configuration and there is a possibility

of different performances being obtained also by using internal variants of the devices. This is considering that higher performing SJ devices are available for hard switching applications, and that they can also provide a cost advantage when compared to similarly rated SiC devices. Other various factors have also been listed which limit this study, such as the lack of use of a full experimental drive setup for operation of a machine. This study, under the specified test conditions, has shown that a model of SJ MOSFET can be a viable alternative to an equivalent characteristic SiC MOSFET model in terms of generalised losses. Theoretical comparison is also given for direct application in SRM drive in terms of discussion of the two devices characteristics, but without a direct experimental comparison in an SRM application, the case cannot be conclusively made for either of the devices tested.

References

- [3-1] M. Krishnamurthy *et al.*, “Making the case for applications of switched reluctance motor technology in automotive products,” *IEEE Transactions on Power Electronics.*, vol. 21, no. 3, pp. 659-675, May 2006.
- [3-2] K. M. Rahman, B. Fahimi, G. Suresh, A. V. Rajarathnam, and M. Ehsani, “Advantages of switched reluctance motor applications to EV and HEV: design and control issues,” *IEEE Transactions on Industrial Applications.*, vol. 36, no. 1, pp. 111-121, Jan./Feb. 2000.
- [3-3] E. Sayed *et al.*, “Review of electric machines in more-/hybrid-/turbo-electric aircraft,” *IEEE Transactions on Transport. Electrification*, vol. 7, no. 4, pp. 2976-3005, Dec. 2021.
- [3-4] W. Cao, B. C. Mecrow, G. J. Atkinson, J. W. Bennett, and D. J. Atkinson, “Overview of electric motor technologies used for More Electric Aircraft (MEA),” *IEEE Trans. Ind. Electron.*, vol. 59, no. 9, pp. 3523-3531, Sep. 2012.
- [3-5] L. Dorn-Gomba, J. Ramoul, J. Reimers, and A. Emadi, “Power electronic converters in electric aircraft: current status, challenges, and emerging technologies,” *IEEE Transactions on Transport. Electrification*, vol. 6, no. 4, pp. 1648-1664, Dec. 2020.
- [3-6] K. Morya *et al.*, “Wide bandgap devices in AC electric drives: opportunities and challenges,” *IEEE Transactions on Transport. Electrification*, vol. 5, no. 1, pp. 3-20, Mar. 2019.
- [3-7] R. Wu, J. Ortiz-Gonzalez, Z. Davletzhanova, P. A. Mawby, and O. Alatise, “The potential of SiC cascode JFETs in electric vehicle traction inverters,” *IEEE Transactions on Transport. Electrification.*, vol. 5, no. 4, pp. 1349-1359, Dec. 2019.

- [3-8] S. O'Donnell, J.-L. Debauche, P. Wheeler, and A. Castellazzi, "Silicon carbide MOSFETs in more electric aircraft power converters: the performance and reliability benefits over silicon IGBTs for a specified flight mission profile," in *Proc., 21st European Conf. Power Electron. Appl.*, Genova, Italy, Sep. 2019.
- [3-9] T. Zhao, J. Wang, A. Q. Huang, and A. Agarwal, "Comparisons of SiC MOSFET and Si IGBT based motor drive systems," in *Proc., IEEE Ind. Appl. Annu. Meeting*, New Orleans, LA, USA, pp. 331-335, Sep. 2007.
- [3-10] M. Lindahl, E. Velandar, M. H. Johansson, A. Blomberg, and H.-P. Nee, "Silicon carbide MOSFET traction inverter operated in the Stockholm Metro system demonstrating customer values," in *Proc., IEEE Vehicle Power Propulsion Conf.*, Chicago, IL, USA, Aug. 2018.
- [3-11] S. S. Ahmad, C. Urabinahatti, K. N. V. Prasad, and G. Narayanan, "High-switching-frequency SiC power converter for high-speed switched reluctance machine," *IEEE Transactions on Industry Applications*, vol. 57, no. 6, pp. 6069-6082, Nov./Dec. 2021.
- [3-12] J.-S. Lai *et al.*, "Characteristics and utilization of a new class of low on-resistance MOS-gated power device," *IEEE Transactions on Industry Applications.*, vol. 37, no. 5, pp. 1282-1289, Sep./Oct. 2001.
- [3-13] M. Pfof *et al.*, "Short-circuit safe operating area of superjunction MOSFETs," in *Proc., 28th Int. Symp. Power Semiconductor Devices ICs*, Prague, Czech Republic, Jun. 2016.
- [3-14] J. Zhang and J.-S. Lai, "A synchronous rectification featured soft-switching inverter using CoolMOS", in *Proc., IEEE 21st Annu. Appl. Power Electron. Conf. Expo.*, Dallas, TX, USA, pp. 810-815, Mar. 2006.
- [3-15] N. McNeill, P. Anthony, and N. Oswald, "Ultra-high efficiency machine drive inverter using superjunction MOSFETs," in *Proc., IET 7th Power Electron., Machines Drives Conf.*, Manchester, UK, Apr. 2014.
- [3-16] Z. Feng, N. McNeill, and B. W. Williams, "A high-efficiency super-junction MOSFET based inverter-leg configuration using a dual-mode switching technique", in *Proc., IEEE 34th Appl. Power Electron. Specialist's Conf. Expo.*, Anaheim, CA, USA, pp. 2467-2474, Mar. 2019.
- [3-17] P. Sun, C. Liu, J.-S. Lai, C.-L. Chen, and N. Kees, "Three-phase dual-buck inverter with unified pulsewidth modulation," *IEEE Transactions on Power Electronics.*, vol. 27, no. 3, pp. 1159-1167, Mar. 2012.
- [3-18] Hopkins, N. Simpson, and N. McNeill, "Auxiliary resonant source charge extraction circuitry for enabling the use of super junction MOSFETs in high efficiency DC-DC converters," in *Proc., IEEE*

34th Appl. Power Electron. Specialist's Conf. Expo., Anaheim, CA, USA, pp. 2159-2166, Mar. 2019.

- [3-19] L. Lorenz, G. Deboy, and I. Zverev, "Matched pair of Coolmos transistor with SiC-Schottky diode - advantages in application," *IEEE Transactions on Industry Applications.*, vol. 40, no. 5, pp. 1265-1272, Sep./Oct. 2004.
- [3-20] M. Barnes and C. Pollock, "Power electronic converters for switched reluctance drives," *IEEE Transactions on Power Electronics.*, vol. 13, no. 6, pp. 1100-1111, Nov. 1998.
- [3-21] F. Peng, J. Ye, and A. Emadi, "An asymmetric three-level neutral point diode clamped converter for switched reluctance motor drives," *IEEE Transactions on Power Electronics.*, vol. 32, no. 32, pp. 8618-8631, Nov. 2017.
- [3-22] A. Abdel-Aziz, K. H. Ahmed, S. Wang, A. M. Massoud, and B. W. Williams, "A novel neutral point diode clamped converter with inherent voltage-boosting for a four-phase SRM drive," *IEEE Transactions on Industrial. Electronics.*, vol. 67, no. 7, pp. 5313-5324, Jul. 2020.
- [3-23] [RGW60TK65D : IGBT](#)
- [3-24] [Datasheet IPW65R060CFD7](#)
- [3-25] [SCT3060AL : SiC MOSFETs](#)

Chapter 4

Novel Genetic Algorithm Based Approach of Torque Control and Increased Efficiency Across an Optimised Speed Range in SRM Drives

This Chapter proposes a new torque control function approach for achieving zero TR operation in SRM Drives, based upon a genetic algorithm optimisation of machine phase currents. The function, at a given speed, produces the optimal current profile for ZTR along with delivering the minimal possible rms current, being applicable across an SRMs full rated speed range. The method is illustrated on a four phase 8/6 SRM in MATLAB/SIMULINK.

4.1 Introduction

As outlined in Chapter two, the SRM can be controlled in multiple ways, with the main goal being speed/torque control of the machine while also minimising, or removing, the TR inherent in the machine. The main mechanism for reduction of commutation torque ripple has been established as torque sharing between outgoing and incoming phases of the machine at commutation, where the majority of TR is concentrated when using basic non torque sharing control methods. To be competitive against topologies such as the PMSM, the SRMs drive control must also be optimal in terms of efficiency, while also eliminating commutation TR across its full operational speed range. Note that while commutation TR is aimed to be eliminated, the nature of this type of TR differs from TR caused by other sources such as radial TR, described in chapter two, or switching TR which is caused by the high frequency switching of the SRM drive. When TR is described in this chapter, it will explicitly be referring to commutation TR, i.e TR caused by the lack of, or overproduction of torque by the SRM when there is a lack of control of the SRMs ability to use overlapping phases for torque sharing.

Advanced control refinements from the traditional methods described in chapter two consistently aim at improving the machines control based upon multiple factors such as efficiency, speed range extension, flux-linkage usage, vibration reduction, etc [4-1]. Examining recent developments in

direct online methods, DTC and DITC have received extensive research in improving their ability as a control scheme. DTC has been improved in [4-2] in relation to increasing Nm/A efficiency, which inherently increases machine efficiency. This is done by removing hysteresis-loop control of flux and allowing a more flexible selection of voltage vectors to readily deal with negative torque production from the phases. TR in this method is reduced notably compared to traditional DTC along with an increase to Nm/A efficiency, but still has a TR >10% at low torque levels (<1Nm). Another example is [4-3], which takes the approach of only reducing TR further than conventional DTC by implementing a combination of a sliding mode controller with an antidisturbance sliding mode observer, for improved speed and torque control. This method provides improved TR reduction, while increasing Nm/A efficiency. Examples of refined DITC include [4-4] and [4-5], where in [4-4], θ_{on} and θ_{off} are controlled as well as conventional DITC, which gives greater control over commutation TR and therefore reduces overall TR. Reference [4-6] presents DITC with the inclusion of sliding mode control, which adjusts commutation angles based upon a steepest descent predictive TR tracking method. This reduces the TR compared to DITC, notably without excessive increases to current, but TR increases again with increasing speed and therefore does not obtain a consistent TR reduction. Along with these traditional methods, newer control techniques applied to other machines have also been applied to the SRM. This includes deadbeat predictive control (DPC) [4-7] or a combination of DPC and model predictive control (MPC) [4-8]. These aim at TR reduction and balancing other machine factors, where [4-8] also investigates four quadrant operation of the SRM.

Indirect methods of control have also been improved, mainly in the area of TSFs, with methods such as current profiling and commutation angle control receiving attention [4-1]. Examples of this include [4-9], which presents an offline TSF which uses FEA obtained flux linkage values to minimise TR and maintain lower copper I^2R losses, but does not aim to lower copper losses as much as practically possible. Another example is the online TSF in [4-10], which implements a predictive algorithm, calculating the required amount of torque sharing at commutation instantaneously based upon prior phase currents. It successfully lowers TR compared with basic TSFs and provides a consistent reduction across the speed range with some added improvement in Nm/A efficiency. An improved control scheme which is not TSF based is presented in [4-11], where commutation angles are constantly adjusted based upon an online calculation which uses the SRMs Nm/A characteristics to increase efficiency. While commutation angles are adjusted,

these are fed to a torque hysteresis controller which classifies the control scheme as technically being direct, while merging aspects of both.

The recent developments to SRM control all accomplish varying degrees of TR reduction, with typically reduced speed range, with some exceptions. This is usually accompanied with some secondary reduction of rms current, but it is difficult to gauge this reduction given there is not a readily available minimum rms current (which this thesis will now provide in section 4.2) for which to aim for, as opposed to comparing with other methods.

4.2 Theoretically minimum rms current with ZTR operation

This section presents a current profiling method which produces the theoretically lowest possible rms current achievable while maintaining ZTR at a given load torque. At low speed SRM operation, DC link voltage is not a limiting factor when considering phase commutation torque sharing, given the large $di/d\theta$ available when revisiting equation (2.15). This means profiles can be produced in effectively any desired shape which can be compared for minimal rms current. Along with this, two-phase torque sharing limits can be established using (2.19) and (2.20) for the maximum θ_{ov} which in the case of the 8/6 SRM, can be illustrated as Fig 4.1 for creating profiles in the positive torque production region. It can be seen when taking phase A, ϕ_A , as a reference, the first portion of any current profile will fulfil FLT from sharing torque from 30° to 45° with

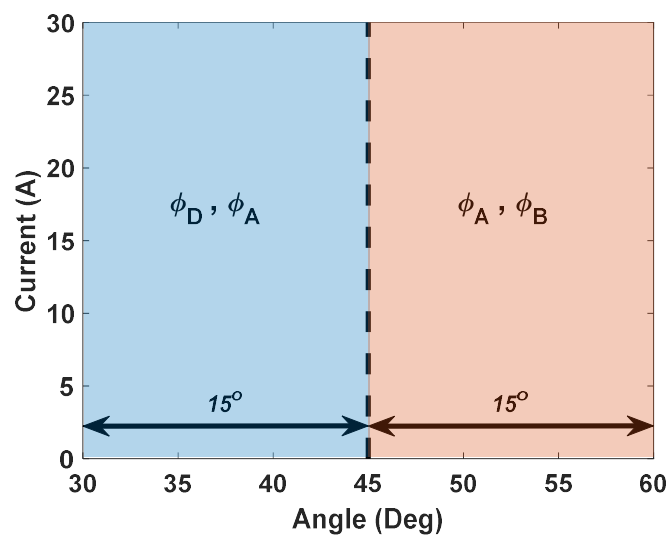


Fig 4.1 Two-phase overlap regions with maximum available θ_{ov}

outgoing phase D, ϕ_D , while the second portion will do the same but with the incoming Phase B, ϕ_B , from 45° to 60° .

As established, any point in the conduction period will generate FLT with a combination of each angular point along with an accompanying point in an overlapping phase that is separated by 15° . Given the large $di/d\theta$ available, each angular point and its overlapping phase can be considered as discrete currents. Therefore, each combination of currents which produces FLT can be evaluated at any angular point, based upon their rms current using a loss variable K_{Cu} which is calculated by (4.1) for Phases A and B, representing the magnitude of copper losses in the phases.

$$K_{Cu} = I_A^2 + I_B^2 \quad (4.1)$$

To obtain the currents which produce FLT at each angular point, a relationship is required between torque T , current I and rotor angle θ . This cannot be linearly obtained through equations, as established in Chapter 2. Instead, FEA can be used to create a LUT that relates these values, which is shown in Fig 4.2 for the 4kW 8/6 SRM, obtained using Ansys Maxwell with the modelling method discussed in Chapter 2.

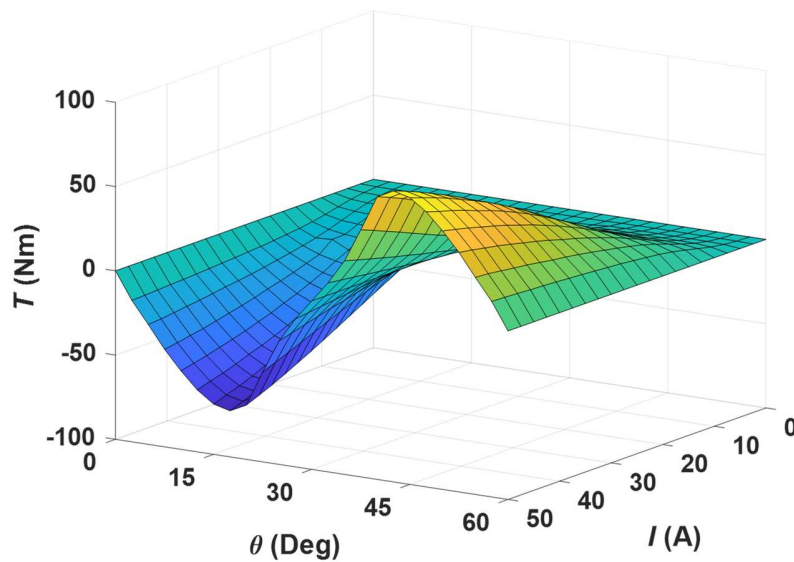
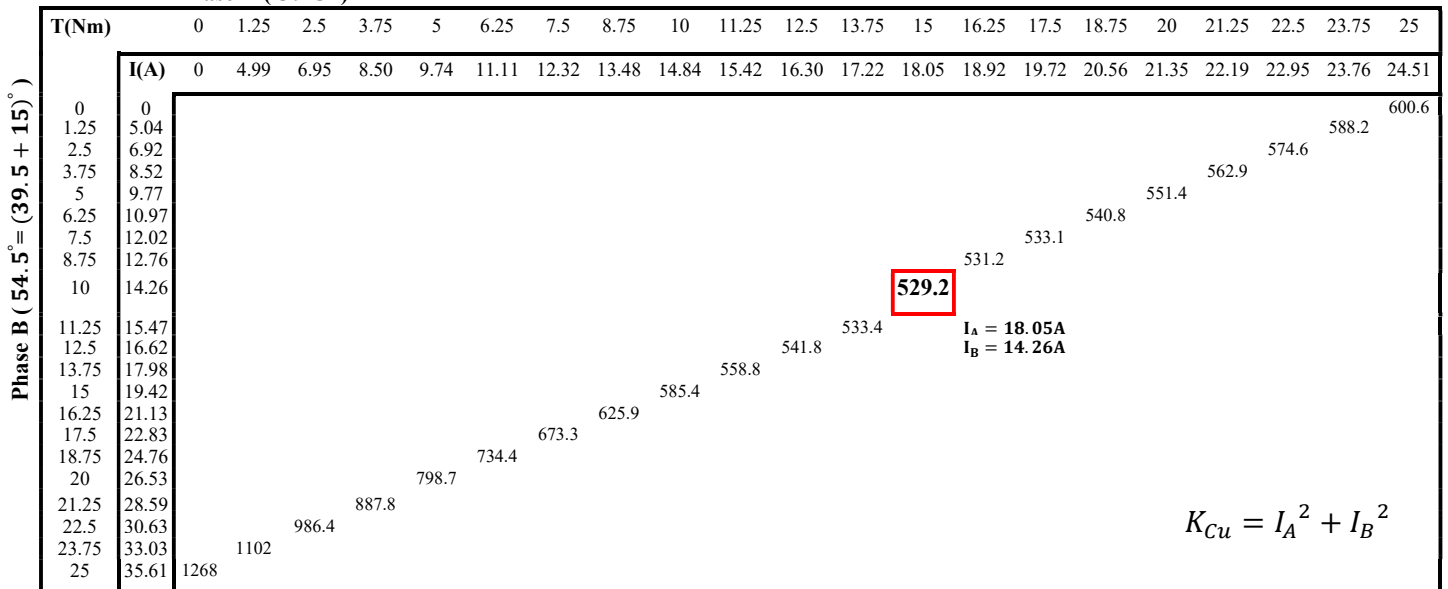


Fig 4.2 Ansys Maxwell FEA data relating $T - I - \theta$ for a 4kW 8/6 SRM

Table 4.1 shows an example of calculations for K_{Cu} , using the FEA data at the angular points of 39.5° and overlapping 54.5° , ($39.5^\circ + 15^\circ$) with a FLT of 25Nm which is presented in large increments of 1.25Nm for the purposes of the table. It can be seen that the range of K_{Cu} values are

calculated from FLT production purely in phase A at a K_{Cu} of 600.6 A^2 to FLT production purely in phase B with a K_{Cu} of 1268 A^2 . At these points, phase A is the more efficient phase as indicated by the K_{Cu} values for FLT production, but not efficient enough for the phase to optimally produce FLT. Instead, the combination of currents with the lowest values for copper losses (I^2) at 529.2 A^2 is found with a torque sharing combination of the two, where phase A produces 60% of FLT and the remaining 40% is produced by phase B. Around these levels of currents for both phases, the K_{Cu} are similar, with adjacent combinations in Table 4.1 only being 2-5 A^2 higher.

Table 4.1 Current Pairings selections at 39.5° and 54.5° for T_{Load} of 25Nm



This example is shown again but visually in Fig 4.3 (with K_{Cu} values in Table 4.1 plotted in the Z axis), where instead of large increments, the step size is reduced greatly to provide the best accuracy of what current combinations provide optimally low K_{Cu} values. From this the optimally low K_{Cu} value is now found to be 525.3 A^2 . Phase B produces slightly more torque, at 13.68Nm versus 11.32Nm for phase A. This indicates the optimal shift in the ratio of torque production from phase A to B as phase B enters optimal Nm/A regions and phase A approaches the aligned position with a Nm/A efficiency of 0.744Nm/A and 0.737Nm/A respectively. This is carried out for angular steps of 0.01° and using current steps of 0.01A across the 30° maximum conduction period and from 0A to the machines maximum allowable current of 30A respectively. The current pairings are chosen at each point and formed into a full profile for the positive torque production region,

where as established, any point in the two sequential phases in the machine are allowed to overlap but are not required to. The rms current I_{rms} of the profile is taken on a point-by-point basis using (4.2) for the profiles discrete currents I_N and sample points in the profile N.

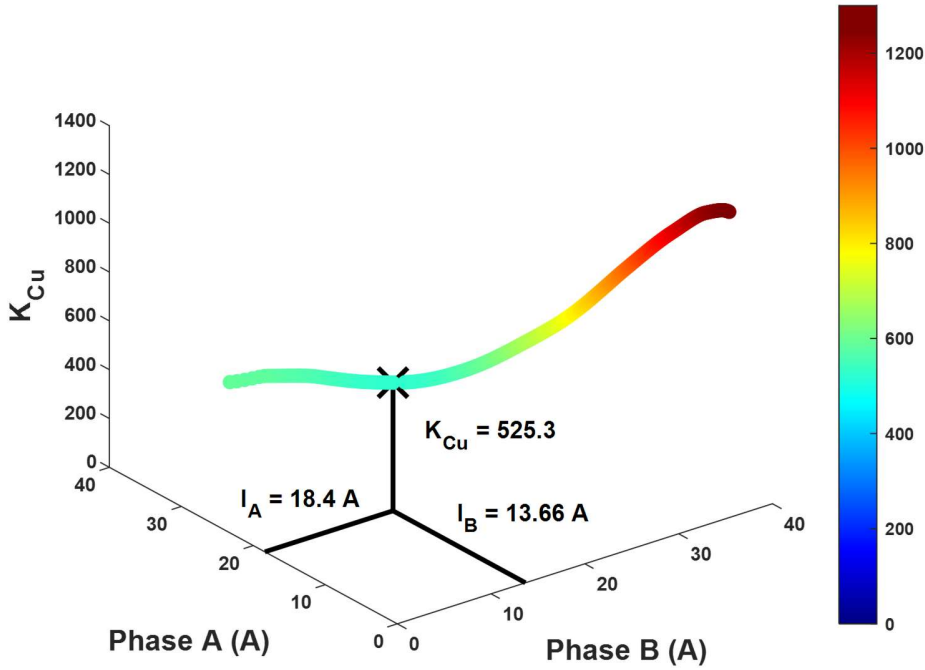
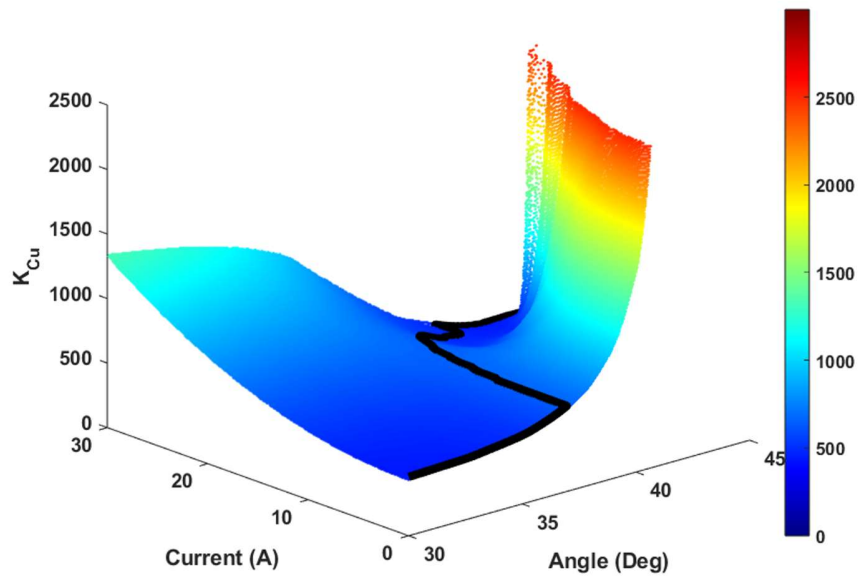


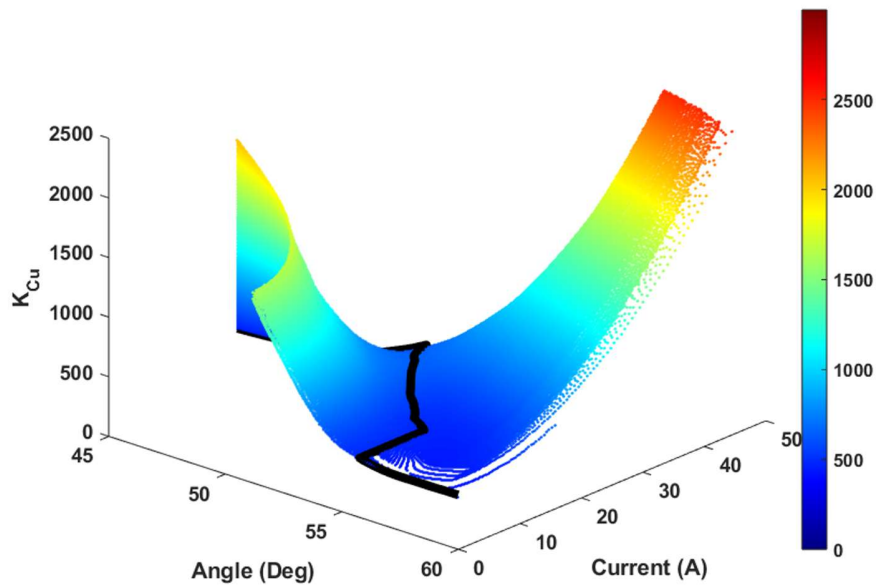
Fig 4.3 K_{Cu} values, Phase A and Phase B currents indicating the optimal overlapping current pairing at 39.5° and 54.5°

$$I_{rms} = \sqrt{\frac{1}{N} \sum_{n=1}^N |I_N|^2} \quad (4.2)$$

The method is now carried out across the full overlap period at a discrete angular step of 0.01° , as illustrated in Fig 4.4, where Fig 4.4a represents the first portion highlighted in blue in Fig 4.1, and Fig 4.4b represents the second portion in orange. Generally, a valley shape is formed from the current combinations at each angular step where, at valley the floor, the most efficient currents are present in black. The optimal K_{Cu} values follow an increase in current in the first portion as phase A becomes the dominant torque producing phase as phase D decays. In the second portion, phase A begins to decay as phase B takes over as the incoming phase. There are two situations that effectively sharp valley walls with high K_{Cu} . Firstly, near the aligned position (60°) inefficiency



(a)



(b)

Fig 4.4 Currents and K_{Cu} values across the full conduction period with optimal currents (with ZTR) highlighted from (a) 30° to 45° and (b) 45° to 60°

is found when large amounts of current in phase A is sourced to provide a small amount of torque (near zero Nm/A region) that fulfils FLT demand with phase B. In this scenario phase B is

producing most of the FLT demand at a much more efficient Nm/A angle and therefore lower current. Secondly on the other side of the valley, prevalent near the unaligned position (30°) is where the same scenario is applicable but with phase D instead of phase B.

Fig 4.5 presents the same data as before but from a 2-D perspective of the phase current and conduction angle. The two black traces ('river' at bottom of each valley) from both sets of data can now be combined into the single desired optimal profile, being connected at 45° .

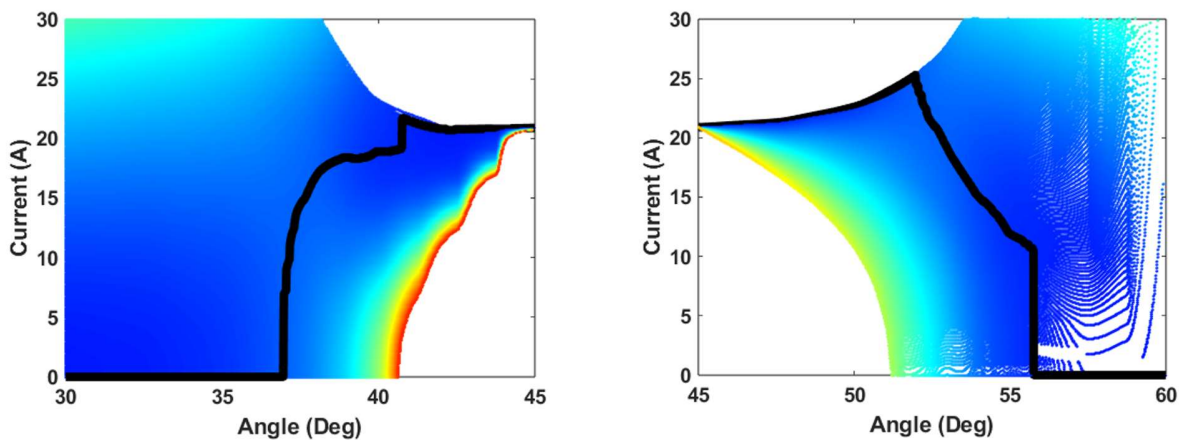


Fig 4.5 Currents across full conduction period with optimal currents highlighted from (a) 30° to 45° and (b) 45° to 60°

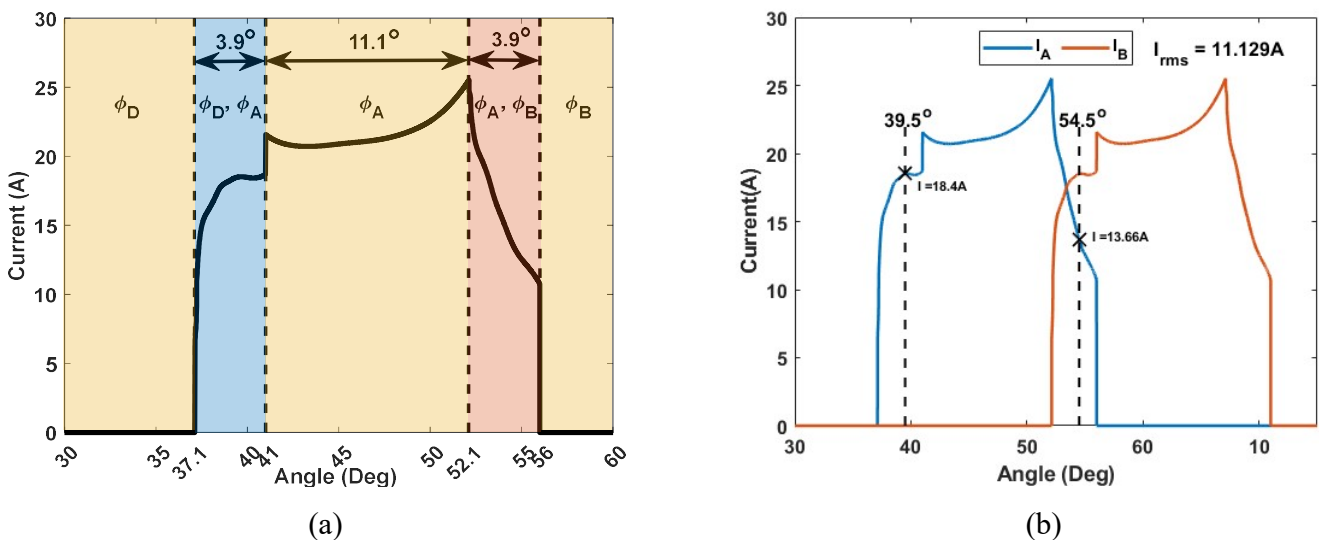


Fig 4.6 Theoretically optimal current profile: (a) Overlap and single phase conduction regions and (b) Phases A and B, visually overlapping and highlighting the optimal currents from Fig 4.3

Fig 4.6 presents the completed current profile, with an rms current of 11.129 A. This is theoretically (based on FEA results) the lowest achievable rms current for the given SRM configuration, at FLT demand with ZTR. The optimal points found in Fig 4.3 are displayed in Fig 4.6b at their respective points to highlight this overlap. When calculating the most efficient torque sharing between phases with the stated maximum θ_{ov} , conduction is not required in low Nm/A efficiency regions near the unaligned/aligned states of the phase (30° and 60° , respectively), (Zero current at alignment also results in no undesirable radial forces, where the radial Nm/A is the highest). Due to this, high efficiency Nm/A regions can conduct in a single phase for FLT with a small overlap (3.9°). During single phase conduction (41° to 52.1°), approaching the peak Nm/A position at 45° , the profiles current decreases with increasing Nm/A for given FLT, increasing current can then be observed for a further 7.1° as the phase Nm/A decreases as it approaches the aligned position. Near instantaneous $dI/d\theta$ is utilised at phase turn-on (37.1°) and turn-off (56°), along when the overlap between phases ends (41°).

Examining the other meaningful attributes of the optimal waveform, the fulfilment of ZTR is shown in Fig 4.7a, where phases A and B torque waveforms are superimposed in the same manner as Fig 4.6. As previously described, it can be seen that the torque waveforms consist of the overlap period where two-phase torque sharing is carried out and single phase FLT production. Fig 4.7b exhibits the change in flux linkage $d\lambda/d\theta$ in the profiles phases, which, as expected due to the

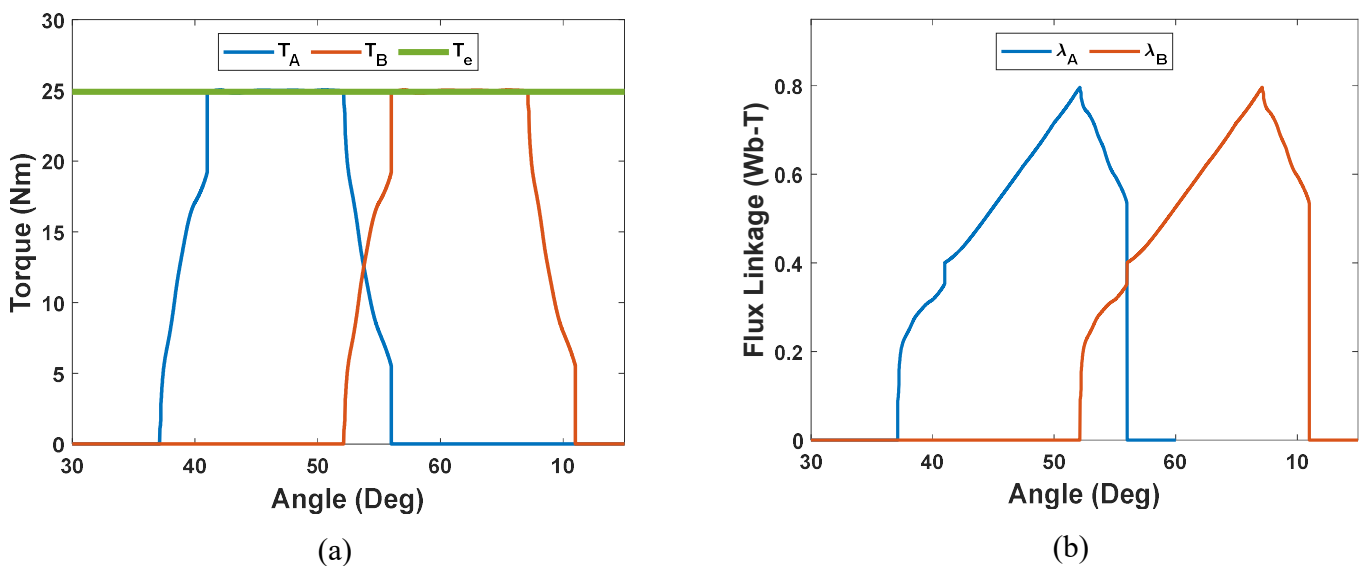
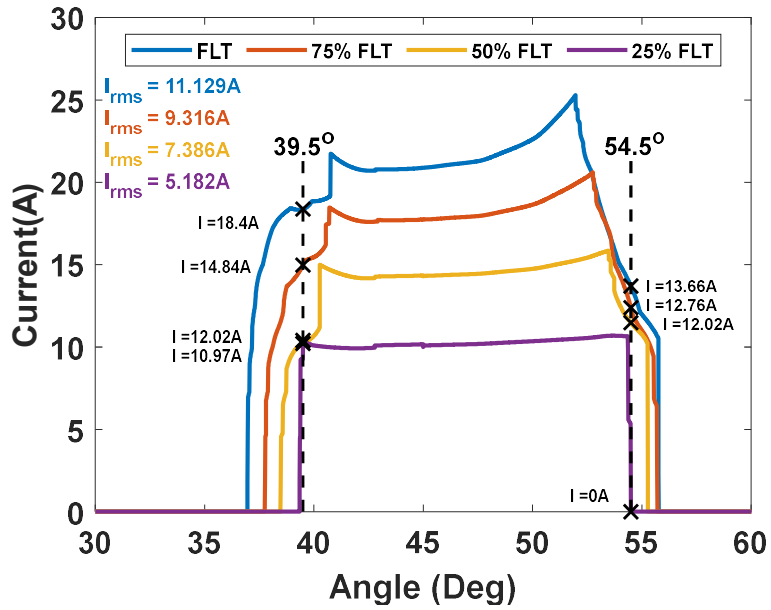


Fig 4. 7 Theoretically optimal current profile: (a) Torque waveforms (b) Flux linkage waveforms

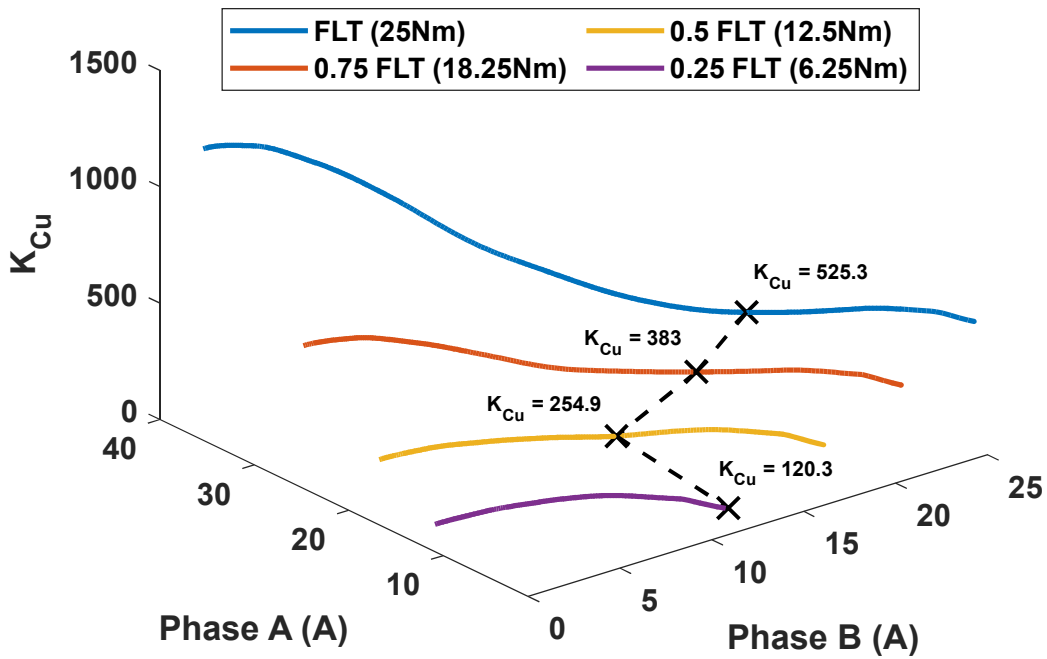
large $di/d\theta$, is large at the crossover points from two-phase to single phase conduction. It is also large at other points in the profile, which reiterates that a requirement for this profiles use is an impractically large DC link voltage supply for anything other than low speed operation. This method can be applied for any load torque, with minimal computational time required to produce theoretical profiles given each optimal current pairing can be calculated simultaneously, with no dependence on the rest of the waveform.

With the theoretically optimal current profiles found at the load torque of 25Nm, the methods used in Table 4.1 and Fig 4.4 can be applied to different values of load torque using the same FEA data. Fig 4.8 illustrates these theoretically optimal profiles produced when incrementally lowering this torque demand below 25Nm. Fig 4.8a presents this as a 2D plot, highlighting optimal current calculated in Fig 4.8b at the reference points of 39.5° and 54.5° . As the demand lowers, a respective decrease in conduction period is encountered until at 25% FLT, it can be seen that the profile conducts within only the highest efficiency Nm/A regions for 10A current flow in Fig 2.8 between approximately 39° to 55° . In terms of the peak current, the first of the two peaks (at 41°) for FLT represents the conducting phase being required to take full torque production as the overlapping phase ceases conduction. The second peak (at 52.1°) is the conducting phase reaching a point where the subsequent phase has not reached an angle of useful torque production while the conducting phase begins to unalign, resulting in the requirement for conduction at decreasing Nm/A efficiency. Decreasing FLT leads to these peaks becoming less pronounced due the lack of current demand with lower torque demand, until as discussed prior decreasing conduction period coupled with torque demand results in greatly diminished current peaks.

At FLT, K_{Cu} for the optimal currents lies at 529.1. Phase A produces 15Nm of torque versus 9.9Nm for Phase B. This indicates that phase A is still the optimal phase at torque production efficiency of 0.836Nm/A but becomes inefficient as it aligns. Phase B is at a less efficient angle relative to phase A with torque production efficiency of 0.694Nm/A but as it further approaches the aligned position it will become the dominant phase. Examining the optimal currents across the given torque range, it can be seen that as the torque demand decreases, requirement for conduction at the given angle of 39.5° decreases to minimal levels (50% FLT) until it is not required at all (25% FLT) as the lower torque demand can be efficiently produced by a single phase alone.



(a)



(b)

Fig 4.8 (a) Optimal profiles at different torque levels and (b) respective K_{Cu} values at 39.5° and 54.5° reference points

The final culmination of this method is illustrated in Fig 4.9 with a surf plot displaying a detailed view of the theoretically optimal current profiles as FLT decreases for the given SRM. As with Fig 4.8, the trend of decreasing conduction period towards a minimum level of single phase conduction as FLT decreases can be seen more gradually with increased torque resolution. Again, peak current and rms current is shown to decrease in more detail and the shape of the profiles begin to become undefined with very low load torques approaching zero, given the fewer possible options for the most efficient currents at each angular point.

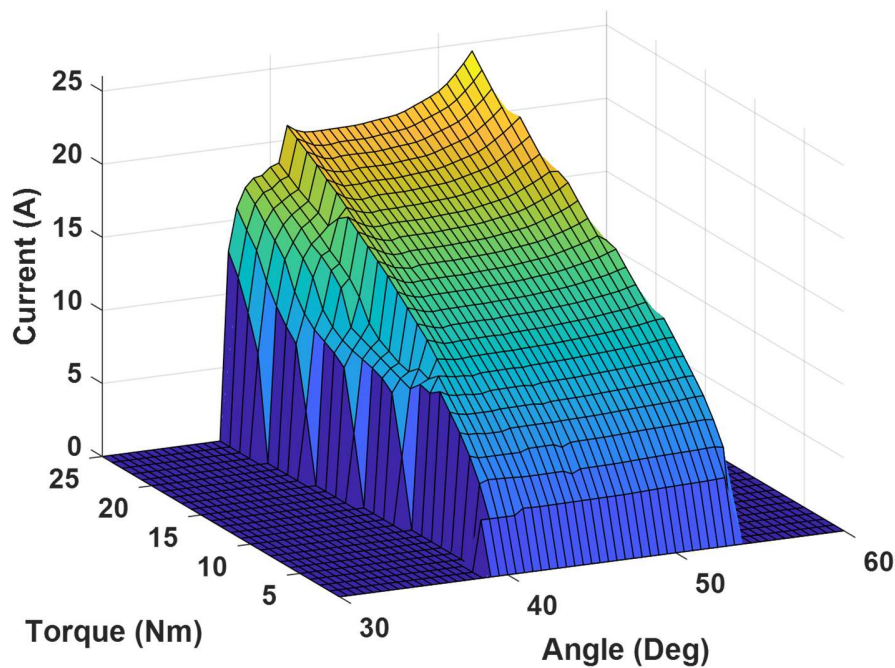


Fig 4.9 3D surf plot of optimal current profiles with decreasing load torques

With a mathematically reliable method for the calculation of optimal rms currents established, it can be used as a benchmark for any TR reduction method which desires to also judge its produced rms analytically to gauge its effectiveness. Applying the optimal current profiles at any practical speed to attain ZTR and optimally low rms currents encounters the aforementioned problem of the reintroduction of DC link voltage as a factor. For example, for FLT at 50rpm (3.3% of base speed), a DC link voltage of 400V in theory suffices, but rates of $d\lambda/d\theta$ at a speed of 500rpm (33% of base speed) require a peak V_{DC} of 2.8kV This is estimated using the FEA data in Fig 4.10 which relates flux linkage λ , current I and rotor angle θ , obtained using the method detailed in Chapter 2, where using this flux linkage with (4.2), which is derived from (2.9) and (2.15), V_{DC} is obtained.

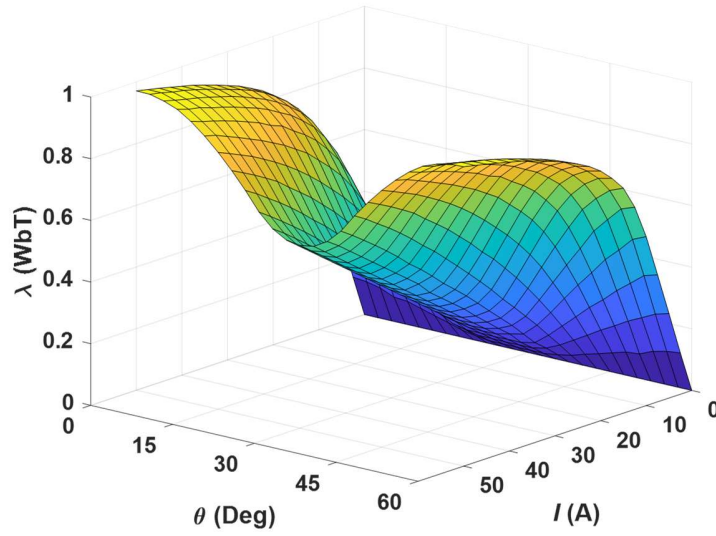


Fig 4.10 Ansys Maxwell FEA data relating $\lambda - I - \theta$ for a 4kW 8/6 SRM

As the torque demand decreases, DC link voltage requirement decreases, with the ZTR low speed limit increasing. At this point, another limit is present at standstill (holding torque), where the phase rms current limit must be observed.

$$V_{DC} - IR_{Cu} = \frac{d\lambda}{d\theta} \omega \quad (4.2)$$

Due to this, the deployment of this method for practically obtaining optimally minimised rms currents and ZTR is not feasible. A possibility that can be explored is the mitigation of any $dI/d\theta$ which require more than the supply voltage in the optimal profile and allowing the transitions to take place over longer angular periods. The problem that occurs with this is that this is not mathematically verifiable as the implementable profile with the lowest rms current due to the fact the profile is constructed procedurally and therefore does not explore every possible permutation of current profile that the given SRM can achieve. It also would compromise ZTR operation, given the new currents would not be the results of calculations based upon FLT production.

A new approach to exploit the theoretically optimal rms currents is therefore required which:

- Achieves optimally minimal rms current
- Eliminates commutation torque ripple and linearises torque control
- Maintains acceptable voltage demands at any operating speed, within a given V_{DC}

4.3 Application of minimal rms current torque control across an SRMs speed range

For the creation of profiles with two-phase overlap using current profiling, a set of mathematical limits must exist which can define the current boundaries in which a profile can be created within while maintaining ZTR and acceptable voltage requirements for a given speed. For a four phase, 8/6 SRM, the positive torque production region is within the 30° period shown in Fig 4.2. By utilising two-phase overlap, current profiles can therefore buildup and decay fully within this region without unintentionally introducing inefficient negative torque production which will also cause TR. As it relates to the drive converter, this overlap and operation at a given speed must be considered. For two-phase overlap, both bridge converter topologies can be used, but specific care must be taken with the common phase ASHB. Adjacent phases (phases A and B for example) must not share a power semiconductor device, where instead the sharing arrangement would be configured as phases A and C, and phases B and D.

4.3.1 Current profiling envelopes

Revisiting the concept of the limits that exist in current profiling to satisfy the mentioned requirements, Fig 4.11 illustrates an example of boundaries for a 4kW 8/6 SRM at 1000rpm (66.6% base speed), with a set θ_{on} of 30° and θ_{off} of 60° for a maximum conduction period θ_{cond} of 30° and θ_{ov} of 15° in the positive torque production region.

Examining these limits:

- **Blue** - the rated current of the SRM, this must not be exceeded.
- **Orange** – For two-phase overlap, any single phase must not produce torque above FLT demand at any time to satisfy ZTR requirements. If negative torque is introduced, this condition changes instead to include FLT plus any torque produced in the respective overlapping phase, which could include phase overlap greater than two phases.
- **Purple** - At turn on, the maximum current increase possible within V_{DC} limits must not be exceeded.
- **Yellow** – Approaching designated turn off, the profile must decay within a certain angular period in order to reach 0A at θ_{off} within $-V_{DC}$ limits.

- **Green-** Reverse limit, where to fulfil FLT with decay limit (yellow), this minimum level of torque must be produced
- **Cyan-** Reverse limit, where to fulfil FLT with the maximum amount of current from turn on, this minimum level of torque must be produced.

From Fig 4.11, these limits intersect at various points. The intersections create an enclosed area (shaded) within and can be formed into an upper and lower limit envelope as seen in Fig 4.12. The combination of these boundaries dictate the valid area for current profiles to be created within, where the limits widen at turn on and commutation (area of efficient two-phase overlap), and narrow at the most efficient Nm/A regions (single phase FLT production).

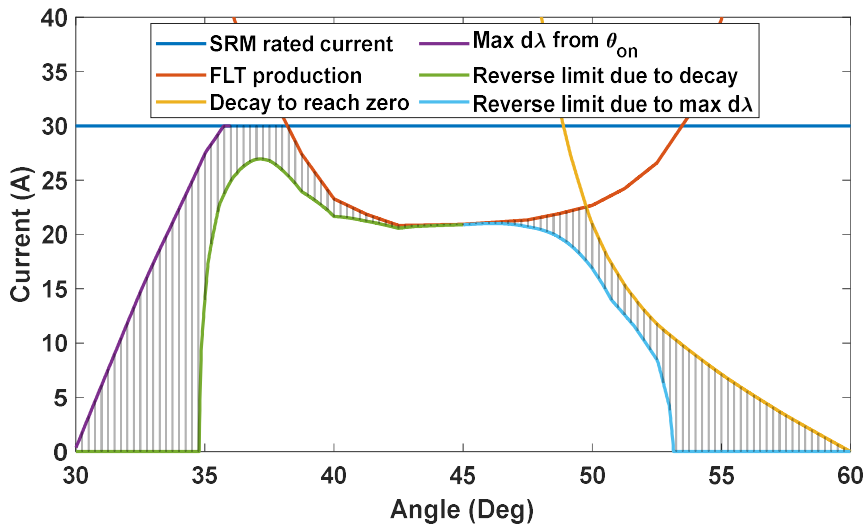


Fig 4. 11 Inherent limits on current profiles for FLT, ZTR and voltage constraints at 1000rpm

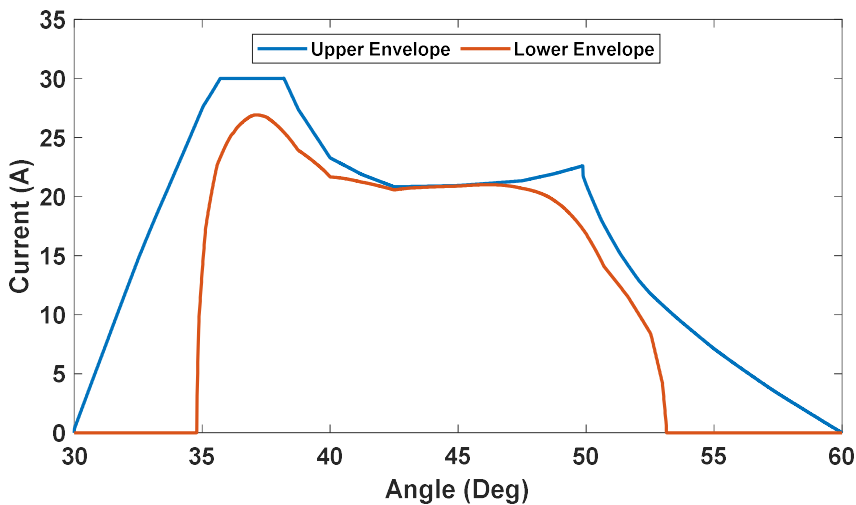


Fig 4.12 Upper and lower current limit envelopes at 1000rpm

At the given speed, a profile can be created with some flexibility in its shape, where the envelope will widen as speed decreases, given the greater available $di/d\theta$. As speed increases further the limits will narrow, where at 1080rpm, the upper and lower limit envelopes narrow to a point where any further increase will cause them to intercept as illustrated in Fig 4.13. When these envelopes intercept, it means that no current profile exists which satisfies all the requirements of FLT production with ZTR while respecting DC supply voltage constraints.

The limit for two-phase overlap at FLT with ZTR of the given SRM is therefore 1080rpm, which is 72% of the machine base speed, being 1500rpm. To attempt to increase this TR free speed range

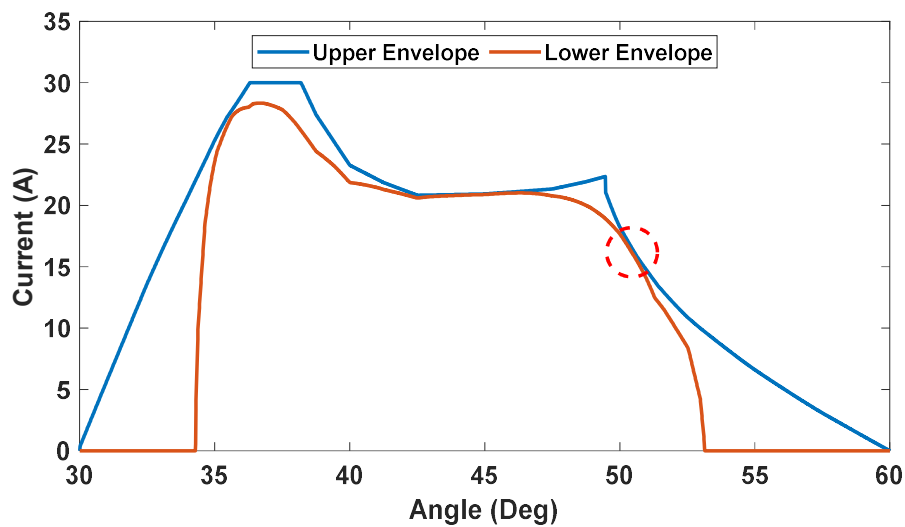


Fig 4.13 Upper and lower current limit envelopes at 1080rpm, illustrating two phase overlap boundary speed

to base speed, the only other variable readily available without changing the given SRMs characteristics or supply voltage are θ_{on} and θ_{off} . This must be done while maintaining two-phase overlap with a θ_{cond} of 30° or less, which will then alter the shape of the boundary envelopes. Fig 4.14 shows the speed limit when firstly advancing θ_{on} to 29° , while Fig 4.15 shows the same but with θ_{on} delayed to 31° . It can be seen that in advancing θ_{on} , the speed limit decreases to 1020rpm due to the increasing minimal currents in the 35° to 38° region reaching the machines maximum allowable current. In Fig 4.15, the speed limit does not decrease with delaying θ_{on} , but does not provide any further increase in ripple free speed range either. This means that for the

extension of the TR free speed range to the machines base speed, a method beyond two-phase torque sharing is required.

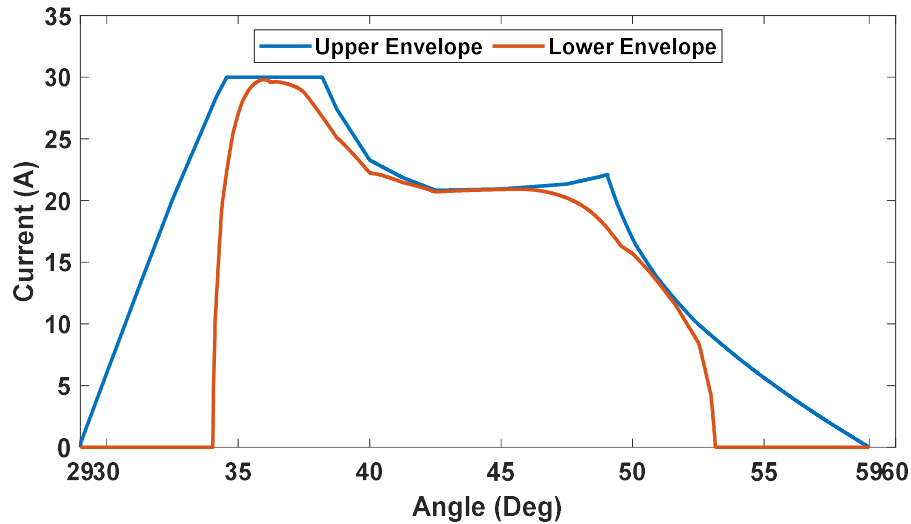


Fig 4.14 Upper and lower current limit envelopes at 1020rpm, illustrating boundary speed when θ_{on} is advanced

Revisiting the original limit envelope at 1000rpm (Fig 4.12), when approaching the efficient Nm/A regions of conduction, the lower envelope minimum currents increase substantially. Any profile requires at least more than 20A (66.6% maximum allowable current) from 35° to 42.5°, where at 35°, this produces only 4.8Nm of torque with a low Nm/A efficiency of 0.24Nm/A. This inherently leads to the creation of a profile with suboptimal rms current with the given limits. As established, the only other variable that can be altered without changing the given SRMs characteristics or

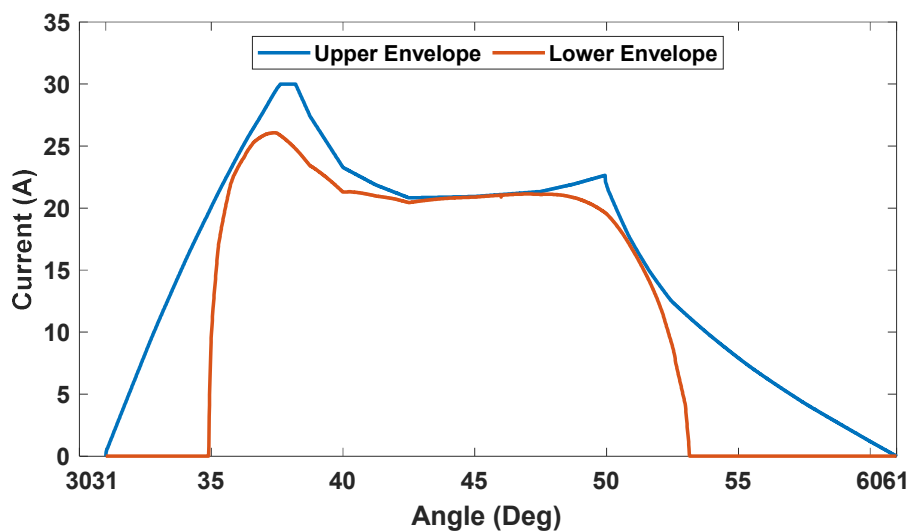


Fig 4.15 Upper and lower current limit envelopes at 1080rpm, illustrating boundary speed when θ_{on} is delayed

supply voltage, are θ_{on} and θ_{off} . Fig 4.16 shows the first case, where θ_{on} is advanced into the negative torque production region at 29° . This does not improve upon the prior θ_{on} , and actually exacerbates the minimum currents to over 25A (83.3% maximum allowable current) at 35° . Along with the fact that advancing θ_{on} also has been shown to decrease the TR free speed range due to these increasing minimal currents, it is not a suitable strategy. Fig 4.17 shows the second case, where θ_{on} is delayed to 31° , and θ_{off} now enters the negative torque production region at 1° . It can now be seen that the minimum rms currents begin to decrease in the 35° to 42.5° region,

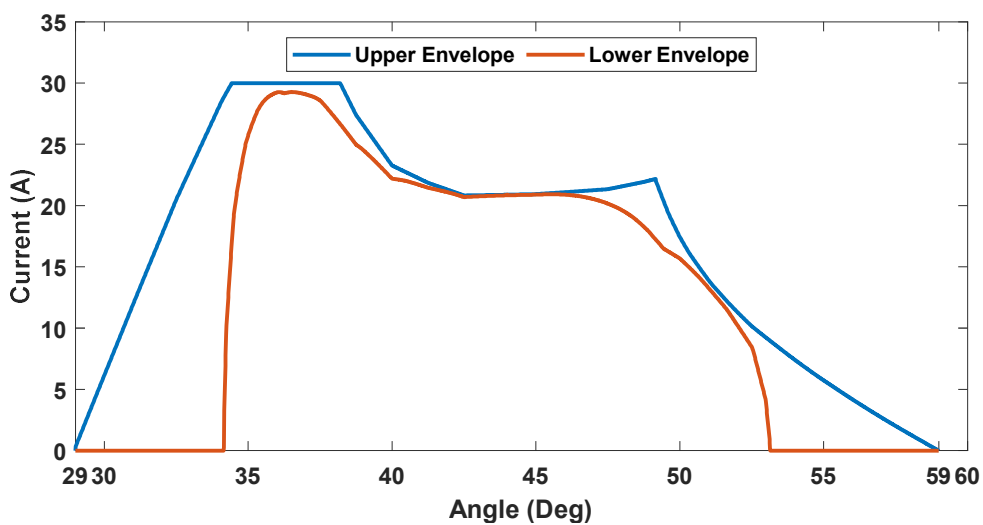


Fig 4.16 Upper and lower current limit envelopes at 1000rpm, when advancing θ_{on}

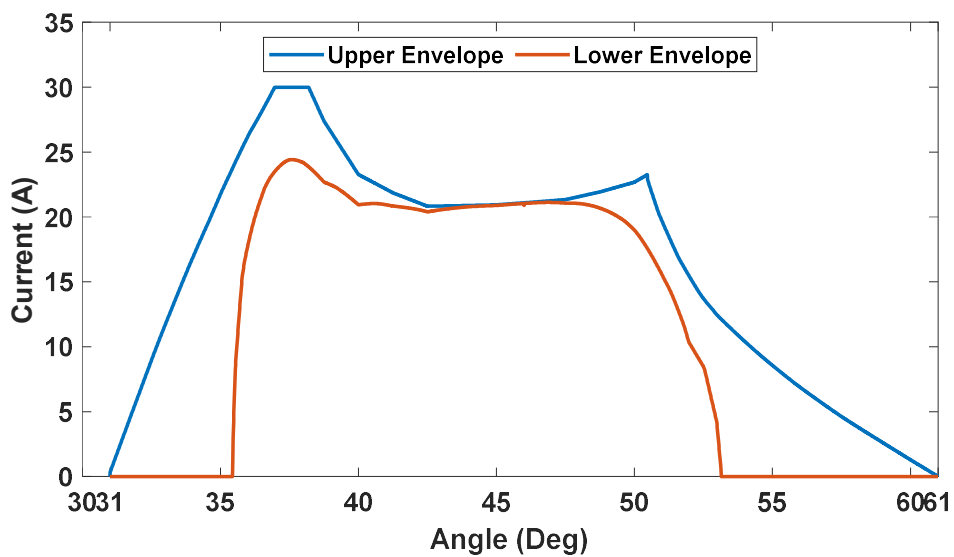


Fig 4.17 Upper and lower current limit envelopes at 1000rpm, when delaying θ_{on}

without major increases to minimal currents in the other areas of the envelope. This indicates a lower rms current is possible for constructed profiles when delaying θ_{on} which can be analysed by taking the average Nm/A efficiency from across the full lower limit envelopes currents and comparing across θ_{on} and speed.

Examining this, Fig 4.18 illustrates the result of carrying this out across speeds approaching the TR free speed limit from 700-1080rpm. The reasoning behind this is that at lower speeds, logically due to the low $d\lambda/dt$ requirements and therefore quick phase current buildup and decay, current profiles will not have difficulties in producing the majority of FLT torque production (single and two-phase overlap) in the most efficient Nm/A regions of the SRM. With higher speeds as the narrowing envelopes indicate, this becomes more difficult to accomplish, and therefore it is more warranted to delay θ_{on} to produce the majority of torque production in the 40° to 53° region. It can be seen that delaying θ_{on} as speed increases provides a benefit to average Nm/A efficiency, meaning that on average, a delayed θ_{on} should be pursued to for optimal Nm/A efficiency and logically minimal rms current. The effects of gradually delaying θ_{on} is shown in Fig 4.19 for 1000rpm. The delay in θ_{on} establishes a longer decay path which may be used to conduct for an extended period in the highest efficiency Nm/A regions, given the current build-up only requires a limited conduction period. As θ_{on} is delayed, the envelop for current build-up from turn-on to

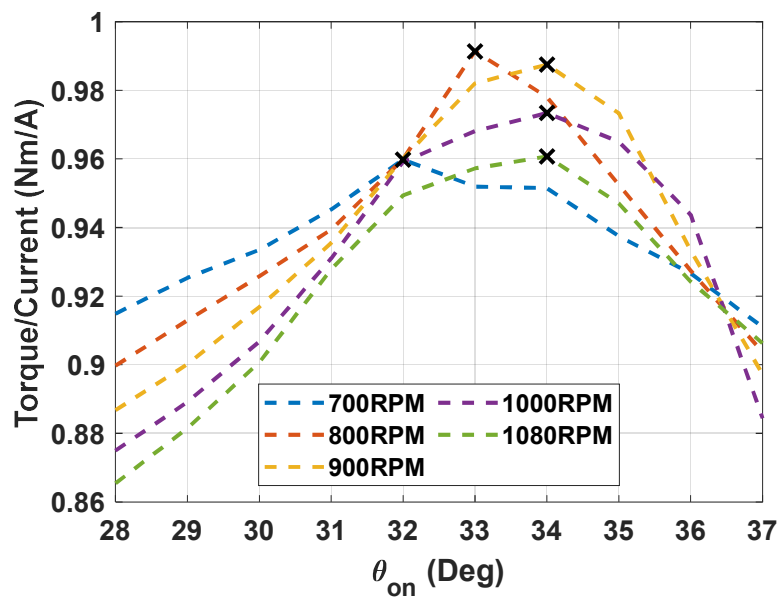


Fig 4.18 Average Nm/A efficiency with changing speeds and θ_{on}

overlap commutation becomes narrower while the latter half of the envelop from commutation to turn-off expands. The point of maximum commutation also shifts with a changing turn-on. This is Illustrated in Fig 4.19, where the lower envelope shifts and the reverse limit peak magnitude increases past the point of FLT production, due to the larger amount of retarding torque required when conduction extends past the aligned position.

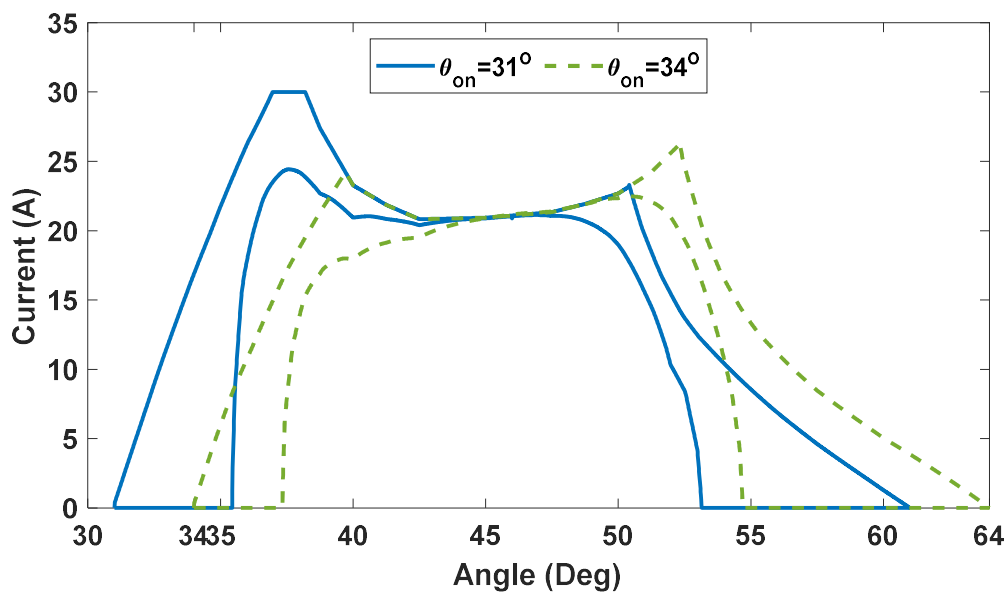


Fig 4.19 Effect of delaying θ_{on} to optimal value on current boundary limit envelopes

4.3.2 Exhaustive ‘branching’ method for current profiling

With the creation of the theoretically optimal current as a benchmark (11.129A rms at FLT), and the establishment of SRM current boundary envelopes, the requirements are now met for a method which can create optimal current profiles across the TR free speed range. To find the optimal current profile at each speed, a method can be used to theoretically create every possible profile, eliminating erroneous profiles that do not satisfy the voltage demand and produce ZTR for FLT production. The profile with the lowest rms current can then be extracted from the selection, where a large number of invalid profiles are already excluded by the boundary envelopes. To ensure the voltage constraints are met, all of the profiles must be generated on a discrete point-to-point basis with consideration to the $d\lambda/d\theta$ between currents, as it relates to $dI/d\theta$. It can be considered that all profiles are required to begin from the unity point at θ_{on} and $\theta_{on} + \theta_{ov(max)}$, proceeding to

then branch out across the conduction period. The profiles are able to ‘branch’ based upon the next angular steps range of ‘solution’ points between the maximum and minimum currents attainable. This is calculated using the maximum $d\lambda/d\theta$ transition at the given speed from the last current in each possible profile using (4.2). Once this range of currents is established, their torque values are calculated and subtracted from FLT, where currents are then calculated in the respective overlap that is shifted by θ_{ovmax} . These currents in the overlapping phase are then compared with the last current stored in overlapping phase, verifying if the voltage demand is acceptable by again calculating $d\lambda/d\theta$. If the overlapping phase is satisfied, the profile branches into new profiles with the amount of valid current solutions in each phase each forming a completely new profile. An example of a calculation between steps is illustrated in Fig 4.20 from $\theta_{on} = 36^\circ$.

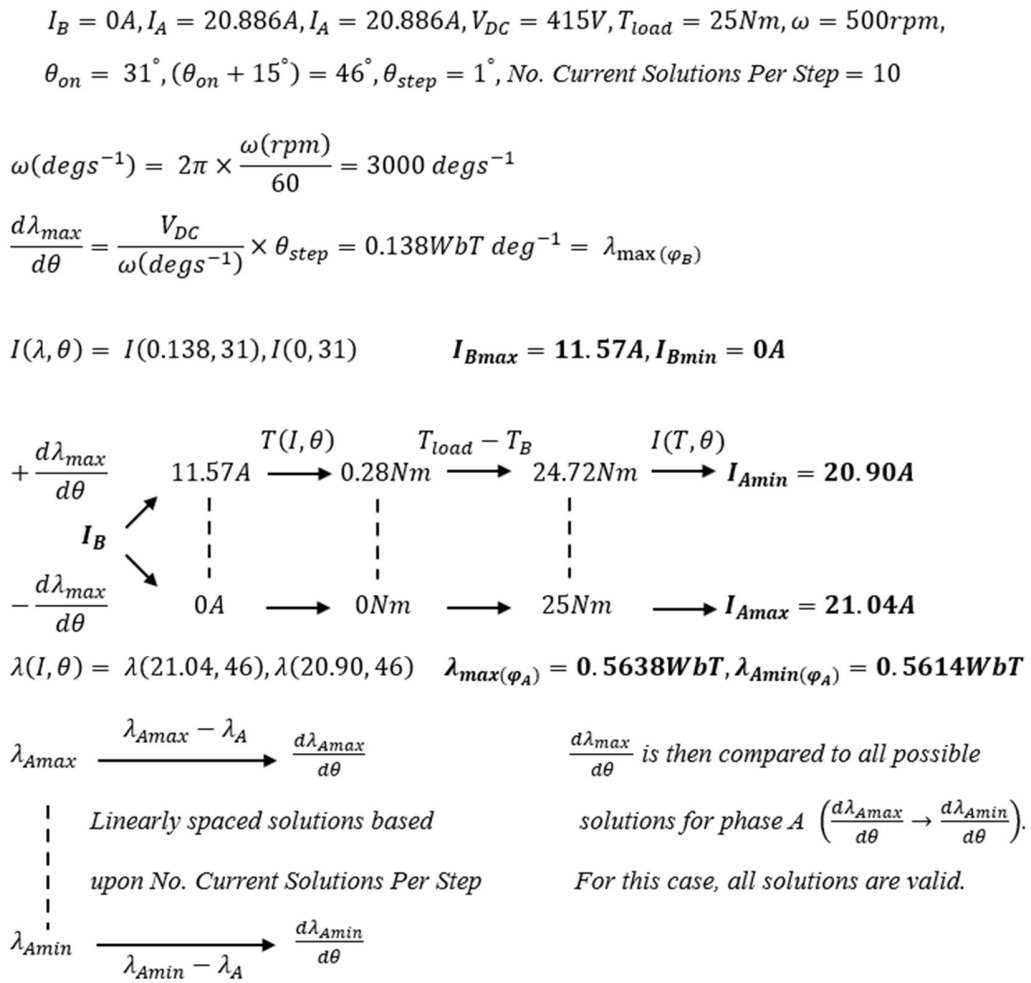


Fig 4.20 Visual explanation of the mathematical process of the branching method

When executing this method, the accuracy is determined by the parameters of the *No. of solutions per step* and the resolution of the profile with the given angular step θ_{step} . In ideal conditions, the *No. of solutions per step* would be very large and θ_{step} be small increments. This would provide a complete profile set to choose from which is likely to contain the optimal rms current at the given speed. In reality, computational limits are present, namely memory allocation and storage, and processing speed, when generating profiles on a sequential step-by-step basis. Given the large volume of profiles that are possible, even though a number of these will be invalid, the number of profiles that are valid will still be substantial even with a low resolution and number of solutions, where the total number of unique profiles can be expressed as (4.3). The issue of processing speed can be mitigated to some degree by employing parallel processing, where calculations for each profile at each angular step can be done in parallel given, they are only dependent on data from the prior angular step, which is available. Memory storage, more specifically the allocation of new profiles to a storage matrix cannot be avoided even with pre-allocation, where at a maximum, the size of this matrix is determined as (4.4).

$$\text{Angular Step} = 1^\circ, \text{No. Current solutions per step} = 10$$

$$\text{No. of Unique Profiles} = \left(\frac{\theta_{ov}}{\theta_{step}} \right)^{\text{No. Current solutions per step}} = 15^{10} \quad (4.3)$$

$$\text{matrix size} = \text{Rows} \times \text{Columns} = \text{No. of Unique Profiles} \times \frac{\theta_{ov}}{\theta_{step}} = 15^{10} \times 15 \quad (4.4)$$

Fig 4.21 presents the results of utilising the branching method at a θ_{step} of 1° , where an increase in rms current and some correlation in an increasing conduction period of the profiles with speed is present. Examining the profiles at low speeds, the shape of the profiles resembles that of the theoretical minimum in Fig 4.6. It can be seen that the profiles have a greater conduction period and therefore phase overlap, stemming from the voltage demand at commutation points compared the theoretical profile. As speed increases further, the profiles begin to lose resemblance to the theoretical minimum and take a different shape. RMS current is kept optimal by increasing conduction period at both turn-on and turn-off, to the extent that negative torque production is introduced as conduction extends beyond the aligned position above 600rpm. By using this extended conduction period, a higher peak current is avoided along with the majority of torque

production being in the efficient Nm/A regions, in a trade-off where minimal values of inefficient negative torque production are required.

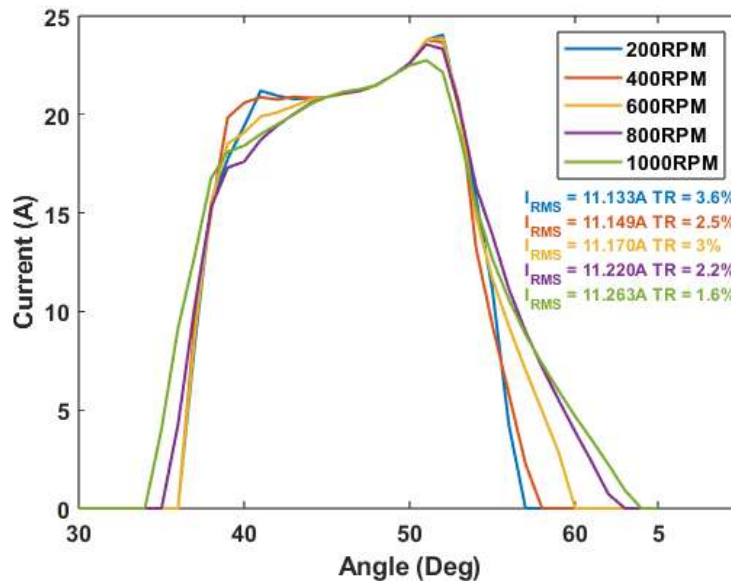
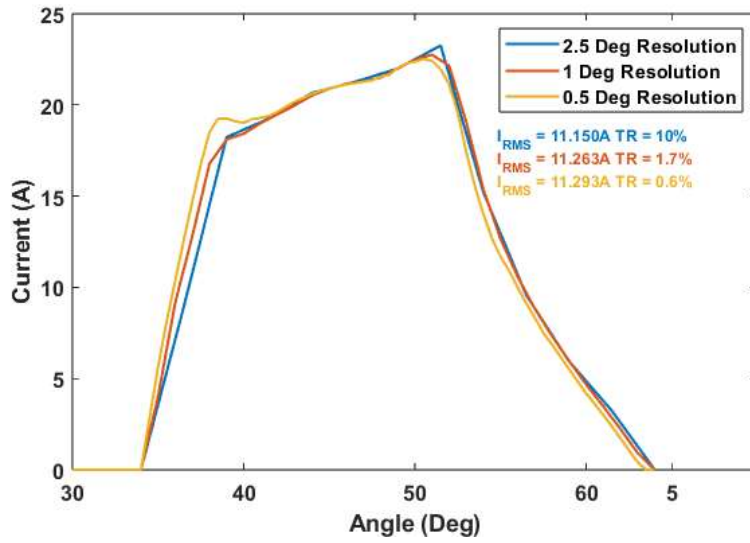


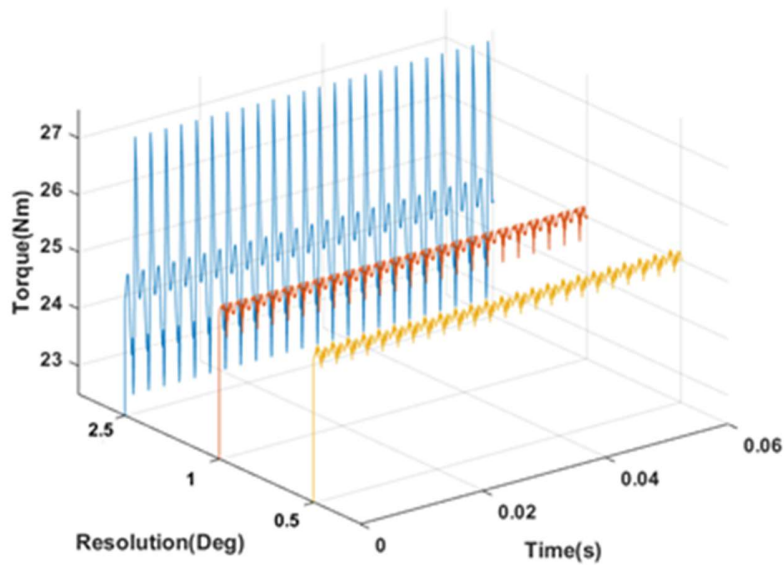
Fig 4.21 Optimal Profiles across 200-1000RPM using the branching method

The significant problem that is encountered is that all generated profiles generated at the given resolution produce TR above a 1% threshold while interpolating between discrete points in the profile. At low speeds this is more apparent, as the profiles follow a less linear shape resembling the theoretical minimum, where significant ripple occurs at or near phase commutation in Fig 4.6. At higher speeds, as the profile takes a linear shape, TR decreases but still is not at a suitable threshold.

Fig 4.22 presents an example of profiles created at 1000RPM at three resolutions of 2.5° , 1° , and 0.5° respectively, along with their torque profiles. The lowest rms current can be found with the profile with the lowest resolution in Fig.22a but suffers from significant torque ripple of 10% shown in Fig 4.23b. This TR is notably below FLT, which is likely why the rms current is lower. At the 1° resolution, an increase in rms current and decrease in TR is encountered, 1.7%, but as seen in Fig 4.21, as speed is decreased this ripple increases again. At 0.5° , a suitable TR value is achieved with the highest rms current.



(a)



(b)

Fig 4.22 (a) Optimal profiles generated at 1000rpm using the ‘Branching’ method at 2.5°, 1°, and 0.5° resolutions and (b) torque production of optimal profiles

This method while logical, is computationally arduous and time consuming when high resolution is required. Using any angular resolution of 0.5° or higher as suggested by Fig 4.22 becomes difficult as processing time increases in terms of memory allocation and storage adversely affecting simulation time, especially at low speed. Another reason for this apart from those

discussed prior is the fact that logically as the envelope opens up with decreasing speed and reduced $d\lambda/d\theta$ requirements, the number of solutions that are valid increase by a large amount.

At discrete points, the branching method can produce ZTR profiles at a given resolution. At high enough resolutions, this method can produce optimal current profiles which fulfil the conditions of <1% TR, where linear interpolation between small discrete angular steps will suffice. The problems encountered with this method is its inefficiency in producing the profiles. This is because it is based upon the concept that the optimal profile will be present if an exhaustive generation of all profiles within the envelope boundaries is carried out. Implementing this method with a suitable number of current solutions per angular step is computationally expensive, where using a suitable resolution paired with a number of solutions per step to ensure a profile with ZTR and the optimally low rms current is not practical. Therefore, another method must be found which can optimise the current profiling process and produce high resolution current profiles which satisfy the speed, torque demand, and TR requirements, while being in close proximity to the near standstill theoretically optimal rms current.

4.4 Optimisation techniques

Generating valid ‘optimal’ profiles which satisfy the criteria established in Section 4.2 has been shown to be computationally expensive and time consuming when aiming to exhaustively generate current profiles at a high enough resolution with optimally minimal rms current. The problem can be viewed as an optimisation problem, more specifically, a multi-objective optimisation problem, where the goal is to produce a current profile with minimal rms current, ZTR, and within the available DC supply voltage.

4.4.1 *Optimisation techniques in SRM control*

In literature, completely new methods for TR reduction or elimination have become rare. Instead, focus has tended to shift towards improving existing techniques from novel perspectives, where optimisation techniques have contributed significantly in this regard. TSFs for example have been modified with online, algorithm based approaches such as using an Ant Colony in [4-12] or an online exhaustive search [4-13], which is not dissimilar from the branching method, where switching angles are optimized to extend speed range and minimise rms current. An optimization is proposed in [4-14], where a multi objective problem is proposed to balance TR reduction with

other parameters in the SRM such as temperature. From this, a TSF is proposed which then uses an MPC controller. DTC is optimized in [4-15], which utilises a newer form of meta heuristic algorithm, the wolf and coyote. Using this approach, TR is reduced while also providing stable speed control as an alternative to using PI control. In [4-16], online particle swarm optimisation is utilised for TR reduction, which considers speed control and the integral squared errors of both speed and torque as optimisation objectives. As it relates to offline current profiling, optimisation techniques have not been explicitly applied, but the discrete nature of the current profiles is favourable. This is because it makes it simpler to format the current profile as a dataset to be optimised under some algorithmic process with a set of conditions. Heuristics are a subset of optimisation techniques which aim to provide a quick, approximate solution to a specific problem, which eliminates one of the issues facing current profiling in the processing time, but they cannot be used for every application. The goal of the optimisation problem here can be seen as obtaining the optimal rms current with a set of conditions, where a benchmark minimum rms current (from Section 4.2) as an optimisation goal, is known. Therefore, a more refined version of heuristics, known as meta-heuristic algorithms, are better suited. These algorithms again seek to provide an optimal solution, but they differ from heuristics in the sense that they require a set optimisation goal to start with, and compare results with only the optimisation objective in consideration, making them independent of the specific application and applicable across a broad range of fields. Overall metaheuristics can be considered as effective algorithms for solving diverse, complex problems, where more traditional algorithms may be inefficient, or fall short in finding solutions. While metaheuristics have these benefits, they are not without drawbacks. The main criticism of these algorithms is typically that they do not guarantee the global optima solution to a problem. Like many algorithm types, they run the risk of falling into a local optima, which is when the algorithm converges on a solution that may be near perfect or just of a good quality, but is not the absolute best, known as the global optima. This factor can vary dependent on design, where metaheuristic algorithms with a well-designed process may be able to avoid local minima, or be able to navigate out of them if that is where they converge. The other main drawback for specific applications is the speed of these algorithms. They are not typically suited for problems which require quick solutions, where the processes often need a long time to converge on an optimal solution and can also mean they are computationally intense. An example of a case where they may not be suitable is the online control of an electrical machine, where the control loop must be

able to respond within the time of the PWM generation cycle, which in reality is a very short time dependent on switching frequency that a standard processor could not respond to with any form of complex metaheuristic.

4.4.2 Genetic Algorithms

The Genetic Algorithm (GA) is a population-based metaheuristic, meaning an initial population of data is generated, and from this, the data is manipulated through the optimisation process towards the objective. In this process each individual piece of data is evaluated and can be discarded to be replaced, or manipulated depending on the algorithm method used. For the case of the SRM, the discrete nature of the current profiles lend themselves to the design format of a GA compared to other algorithms, where each profile is effectively a one dimensional sequential data set. Along with this, GAs are known to produce high quality results to non-linear problems and in finding global optima in sets of solutions, where the SRMs non-linear magnetics and torque production characteristics can be considered as such. The GA is an ‘evolutionary’ algorithm, modelled on the process of natural selection. Firstly, a base population is generated with its simplest form being in a binary encoding of a number, representing the solution to the problem, but this varies based upon the application of the methodology. From this, the population is optimised over a series of iterative generations. In each generation, member ‘genes’ of the population are chosen to be ‘bred’ together using a ‘crossover’ function, while other genes are then chosen, either being the offspring of the crossover or the existing population, to be altered using a ‘mutation’ function. Once this is carried out, the new population is then evaluated by the algorithm with a ‘fitness’ score that is based upon the objective function of the algorithm i.e. the single or multiple parameters that are desired to be optimised in the given problem. With each member of the population now holding a value of fitness, a selection process then occurs which can vary greatly in method, but in general, increases the likelihood of the fittest members of the population surviving, mimicking natural selection. Finally with the new population, the algorithm then advances to the next generation and repeats the process until a candidate optimal solution forms, the population converges, or it reaches the set number of generations.

4.4.3 Crossover Stage

As a general overview using binary string, the crossover stage carries out a form of ‘breeding’ between two population members. Figure 4.23 offers a visual representation of this where a random cutting point is chosen within the bit length of the population genes binary. From this, two parent genes are selected per number of times crossover is carried out in a generation, and split in half at the cutting point. From this, two ‘offspring’ genes of the parents are then created by



Fig 4.24 Mutation using binary string population genes

swapping the latter half past the cutting point of the two parents with each other. This generates new unique solutions to the problem that may either have a greater or lesser fitness than the parent members.

4.4.4 Mutation Stage

In the mutation stage, a singular population gene is picked per number of times the stage is carried out in a generation. This gene is then randomly ‘mutated’ dependent on the design, where in the example shown in Fig 4.24, one random segment of the genes is binary is flipped to the opposite value. In general, any random alteration of the population gene can suffice as a mutation, with the main stipulation being that it is completely randomised to not compromise the algorithm to bias.

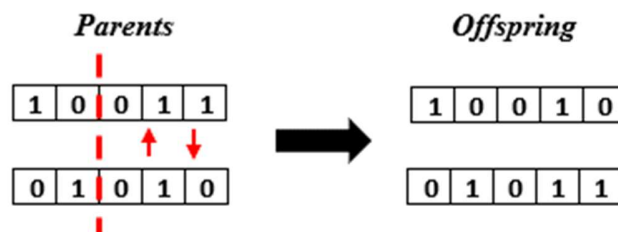


Fig 4.23 Crossover using binary string population genes

4.4.5 Fitness and objective function

The fitness of a population member is measured by the objective function of the algorithm. For optimisation problems these functions can take almost any mathematical form based upon what optimisation is desired by the algorithm designer. The algorithm itself is not limited to a single objective function, GAs can be programmed to interchange the use of multiple objective functions dependent on other parameters, such as if a certain level of fitness is reached then another function is introduced to further optimise the solution in a different direction. The objective function is the most consequential section of the algorithm design, as it must be defined precisely so that the algorithm will achieve the desired optimisation and be able to increase fitness to a global optimum. When defining an objective function, it can be stated as single or multi-parameter, becoming more sensitive to failure in a local optimum or biasing, when more parameters are present without a proper design. Care needs to be taken upon weighting these multi-parameter problems, especially if increasing fitness from one parameter is detrimental to another. This can cause either the algorithm to not converge on any one solution or completely disregard one parameter in favour of the best fitness it can attain with a single other.

4.4.6 Selection Stage

When selecting the new population to carry on to the next generation of the GA, many forms of selection are available to achieve an increase in fitness as the algorithm progresses. Methods for selection consider the level of fitness of the population, where the format will favour higher levels of fitness for progression to the next generation. The two forms explored in this section are the commonly used formats of ‘Roulette Wheel’ and ‘Tournament’ style.

Roulette Wheel selection operates from visualising the population as a collective fitness value created from summing all fitness values in the population representing the ‘wheel’. The probability of selection of each population member is then taken by dividing the individual fitness values by this summed fitness, creating segments in the roulette wheel where members with larger fitness values have a larger segment based upon the cumulative probability of selection out of the whole population. With these values set, the wheel is then spun for how many members that are desired in the new population, with the remainder that were not chosen regardless of what fitness value they hold being discarded.

Tournament style is a simpler method that operates by holding selection ‘tournaments’ between members of the population chosen at random and selecting a winner. The size and style of the tournaments can be variable based upon the designer’s choice, such as the number of concurrent competitors, tiers of tournament where a single member may have multiple competitions before it is selected and also what determines the winner of a tournament. When determining winners of competitions, judgement must be carried with either an absolute consideration to fitness, that is, the higher fitness wins or with some weighting towards fitness which introduces more of an element of randomness where a population member with a lesser fitness may prevail against a competitor with a higher fitness. If neither of these are implemented, the algorithm will typically fail given there is no attempt to increase fitness by this selection method.

Finally, an augment to any selection method chosen by the designer can be made which guarantees fitness does not decrease with successive generations. Variations of ‘Elitism’ effectively are added to these methods before they are carried out, where a segment of the population with the highest fitness values are extracted and stored for the next generation. This is done to promote better results in the algorithm, where these best population members contribute to constantly increasing fitness but can be replaced once better solutions are found. This again poses the risk of guiding the algorithm into a local optimum, given increases in fitness at any point in the algorithms process does not necessarily indicate that the algorithm is on the right path to the global optimum solution.

4.5 Genetic algorithm approach to current profiling for torque control and minimal rms current across TR free speed range

Approaching the design of a GA for SRM current profiling, its objective can be considered as a multi objective problem, with the three main goals; Stipulated as:

- Minimized rms current
- Zero Commutation Torque Ripple
- Voltage demand less than $\pm V_{DC}$

This design could prove to be difficult to implement when balancing the three objectives to ensure the algorithm with no biasing, where for example if the GA ignored the third condition, the theoretical minimum profile would be the result. The second and third objectives of this optimisation instead of being considered in this way, could be viewed as prerequisite conditions

for each profile. This is because ZTR ($TR < 1\%$) is necessary for the profiles and can be actively maintained, while voltage demand is similar in being maintained and is only required to be less than a set value. If through the GAs design, these two can be consistently maintained, the algorithm can be simplified to a single objective optimisation which improves its ability to function. In generating a population, a valid voltage demand and production of the FLT at ZTR for every discrete phase pairing in the current profile can be maintained. TR as a variable can be eliminated by ensuring every ‘gene’ of a population current profile, which are the overlapping currents at each angular point, collectively produce FLT (with ZTR). DC voltage usage can be solved by ensuring that population members at generation already are within DC voltage limits, and any stage of the GA must also consider the available $di/d\theta$ between any two genes in a population member if one is altered. With this, the GA can solely optimise rms current. The GA functions as follows: population generation is carried out once and proceeding from this, crossover, mutation, evaluation, and selection stages are performed for 2000 ‘Generations’. An illustration of the algorithms flow is in Fig 4.25. At the selection stage of each generation, 250 candidate current profiles are chosen from a pool of 750 created by crossover and mutation, where candidates with an rms current closer to the theoretically optimal rms current $I_{rmsOptimal}$, is favoured. The number of generations are chosen as a reasonable estimation for the number of iterations that the algorithm takes to converge on an optimal solution while in the design phase. The number of crossovers and mutations provide a good pool of current profile variations, given the actual available range of practical solutions is not large when considering Fig 4.20, compared to other possible applications of a GA.

The algorithm itself, is ran from MATLAB script, generating a population and running in a set loop of 'generations' where each iteration will carry out a set number of crossovers, mutations and then proceed to weigh fitness and select profiles for the next generation.

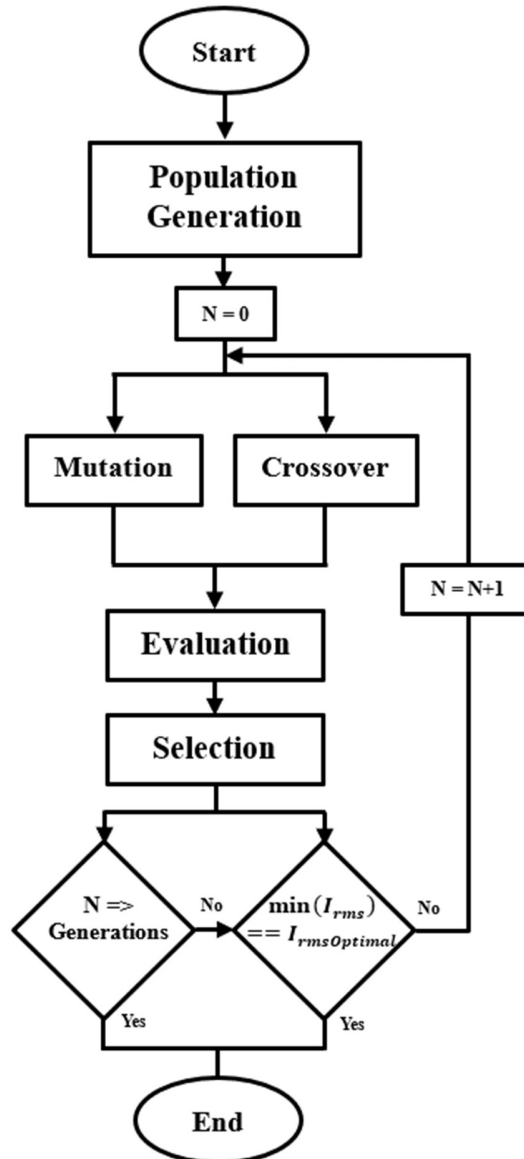


Fig 4.25 Overview of proposed GA process

4.5.1 Population Generation

In generating a population for the algorithm, the limit envelopes introduced in Section 4.3 are used to procedurally create random current profiles with a chosen resolution θ_{step} of 0.1° , with an

example of a population generated at 200rpm given in Fig 4.26. Firstly, a linearly spaced grid of current solutions is created from the currents between the upper and lower envelopes for the first half of the phases conduction period (30° to 45°), and the second half overlapping (45° to 60°). This is expressed as (4.5) for both currents and their respective flux linkages.

$$\phi_{1,2} = \begin{bmatrix} \lambda, I_{\text{Upper}}(30^\circ, 45^\circ) & \cdots & \lambda, I_{\text{Upper}}(45^\circ, 60^\circ) \\ \vdots & \ddots & \vdots \\ \lambda, I_{\text{Lower}}(30^\circ, 45^\circ) & \cdots & \lambda, I_{\text{Lower}}(45^\circ, 60^\circ) \end{bmatrix} \quad (4.5)$$

This is done with 500 current solutions per angular increment of 0.1° across the conduction period to provide a wide variety of choice for the random generation while not compromising processing time. Each phase pairing that is generated will produce ZTR FLT, where the first period (30° to 45°) are linearly spaced solutions, and the second (45° to 60°) is generated to produce the remaining amount of torque required to produce FLT, which will correspond to the envelope boundaries. To ensure voltage limits are not exceeded, each current is converted into flux linkage and stored along with the currents, where the maximum allowed $d\lambda/d\theta$ for the given speed is

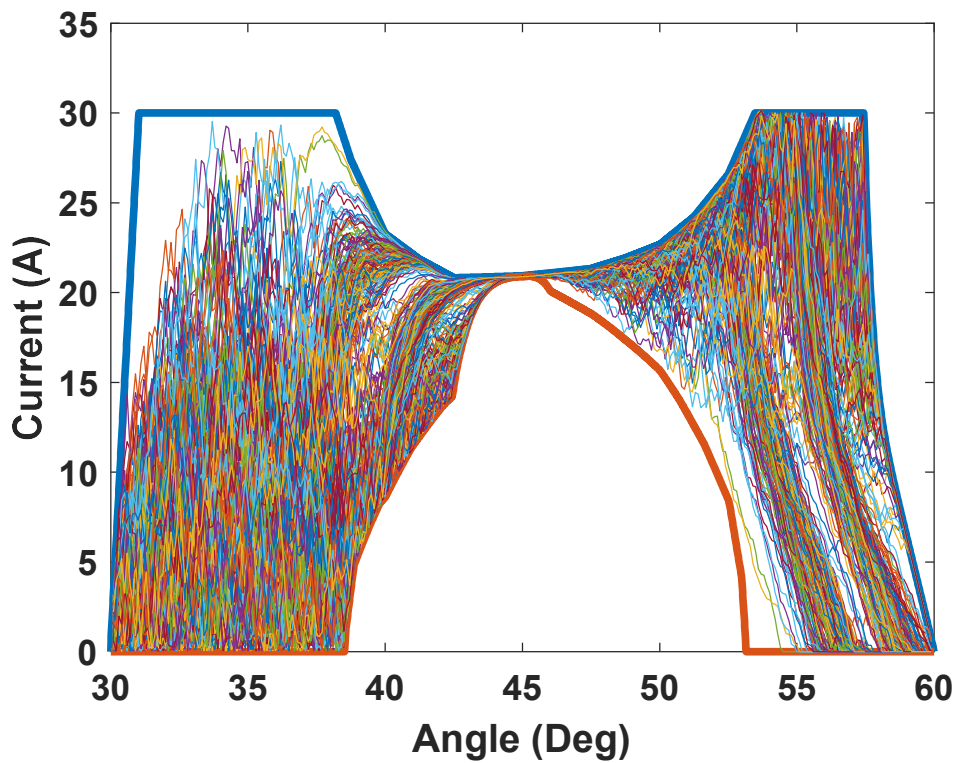


Fig 4.26 Population generation for the GA at 200rpm

found using (4.2). The profiles are then generated randomly from the beginning point of 0A at 30°, and 21.89A (25Nm) at 45°, where the next valid range of current solutions is dictated by (4.6), which ensures voltage limits are respected by finding the maximum $\lambda_{\max(\phi_k, \theta_n + \theta_{step})}$, and minimum $\lambda_{\min(\phi_k, \theta_n + \theta_{step})}$ flux linkage values from the given profiles flux linkage $\lambda_{\phi_k \theta_n}$ from the prior increment. Once this range is found, $\lambda_{\max/\min(\phi_k, \theta_n + \theta_{step})}$ are reverted back to currents and matched with the closest pairings to each flux linkage limit. From this, a current can then be selected between these indexes randomly.

$$\begin{aligned}\lambda_{\max(\phi_k, \theta_n + \theta_{step})} &= \lambda_{\phi_k \theta_n} + \frac{d\lambda_{max}}{d\theta} \\ \lambda_{\min(\phi_k, \theta_n + \theta_{step})} &= \lambda_{\phi_k \theta_n} - \frac{d\lambda_{max}}{d\theta}\end{aligned}\quad (4.6)$$

In the case where any partially constructed profiles path reaches a point where no valid solutions exist for its next angular increment, the profile is discarded, and the process is restarted. Revisiting Fig 4.26, it can be seen at low speed that the envelope limits are wide and because of this, a great variety of profiles can be constructed which do not resemble a typical SRM current profile. When comparing this to Fig 4.20, higher speeds offer much less variance in the shape of the profile, given $d\lambda/d\theta$ is large, and consequentially possible $dI/d\theta$ between angular points is small. At low speeds the opposite is true, and a large $dI/d\theta$ is available between points, where this allows much greater random jumps as can be seen in Fig 4.26. The initial population is generated with 250 candidates, and this stage is now no longer repeated until a new speed is chosen to generate an optimal profile for, in a separate iteration of the GA.

4.5.2 Population Crossover

In each iteration of the crossover stage of the GA, two population profiles are randomly selected. A crossover point is then selected, which corresponds to two angular points in each profile, with one in the first segment of the profile (30° to 45° in this case), and the other being the same point shifted by θ_{ov} into the second segment of the profile (45° to 60°). ZTR and FLT production in this stage does not need to be checked as each discrete current pairing is not altered, therefore each will still produce FLT. Voltage demand is required to be checked, as at the crossover point in for each profile currents that are adjacent to each other are changed and the resultant $d\lambda/d\theta$ could exceed DC supply voltage. In the case that the voltage demand is too high, a new crossover point

is selected. If the voltage demand in each of the profiles is valid, the crossover can occur, where each profiles form the crossover point to the end of each segment is swapped between the profiles and new profiles are formed to be carried to the selection stage. An example of this is given in Fig 4.27 at 200rpm. A crossover point is selected at 35.6° and 50.6° ($35.6^\circ + \theta_{ov}$) respectively, where at this low speed, voltage demand is low and the crossover points are valid. The first offspring

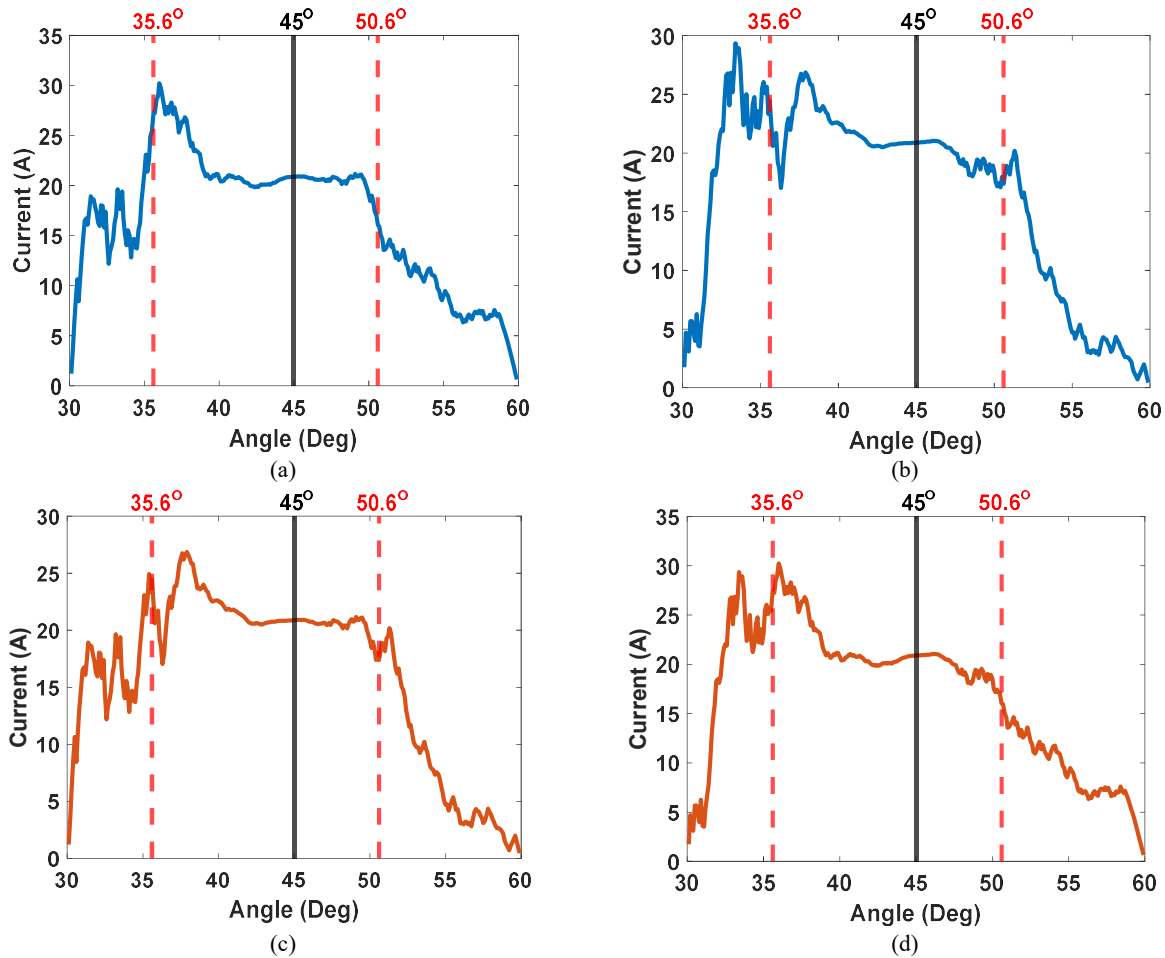


Fig 4.27 Crossover Stage carried out at 200rpm for two population members: (a) Parent 1, (b) Parent 2, (c) Offspring 1, and (d) Offspring 2.

profile in Fig 4.27c is composed of Fig 4.27a before the crossover and Fig 4.27b after the crossover. The second offspring profile in Fig 4.27d is instead composed of Fig 4.27b before the crossover, and Fig 4.27a after the crossover.

4.5.3 Population Mutation

In each iteration of the mutation stage, a single profile is selected. A mutation point θ_{Mu} is then randomly selected in the profile, which corresponds to an angular point in the first section of the

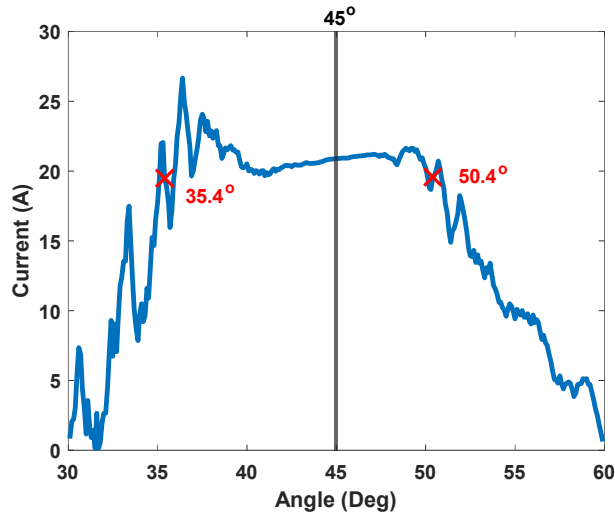
profile ϕ_k (30° to 45°), with another in the second segment ϕ_{k+1} (45° to 60°), shifted by θ_{ov} . From this, the selection is ‘mutated’ randomly where in the GA design this is randomly changing the values of the selected currents. To successfully perform the mutation, both the conditions of FLT ZTR and supply voltage must be respected, which in the mutation stage takes the form of the range of acceptable mutation for either condition. An example of the mutation stage is given in Fig 4.28 at 200rpm which highlights these ranges with a θ_{Mu} of 35.4° and 50.4° ($\theta_{Mu} + \theta_{ov}$). Examining the mutation range due to flux-linkage demand, $\lambda_{max/min}$ for each point in the two overlapping phases is found using (4.6) for the prior and next currents in the profiles, creating four values. This establishes the valid range of mutation when at least one point from the prior step ($\theta_{Mu} - \theta_{Step}$), and one point from the following step ($\theta_{Mu} + \theta_{Step}$) overlap, expressed in (4.7).

$$\begin{aligned}
\lambda_{\max(\theta_{Mu}-\theta_{Step})} &\geq \lambda_{\max(\theta_{Mu}-\theta_{Step})}, \lambda_{\max(\theta_{Mu}-\theta_{Step})} \leq \lambda_{\max(\theta_{Mu}-\theta_{Step})} \\
&or \\
\lambda_{\min(\theta_{Mu}-\theta_{Step})} &\geq \lambda_{\min(\theta_{Mu}-\theta_{Step})}, \lambda_{\min(\theta_{Mu}-\theta_{Step})} \leq \lambda_{\max(\theta_{Mu}-\theta_{Step})} \\
&or \\
\lambda_{\max(\theta_{Mu}+\theta_{Step})} &\geq \lambda_{\max(\theta_{Mu}-\theta_{Step})}, \lambda_{\max(\theta_{Mu}-\theta_{Step})} \leq \lambda_{\max(\theta_{Mu}-\theta_{Step})} \\
&or \\
\lambda_{\min(\theta_{Mu}+\theta_{Step})} &\geq \lambda_{\min(\theta_{Mu}-\theta_{Step})}, \lambda_{\min(\theta_{Mu}-\theta_{Step})} \leq \lambda_{\max(\theta_{Mu}-\theta_{Step})}
\end{aligned} \tag{4.7}$$

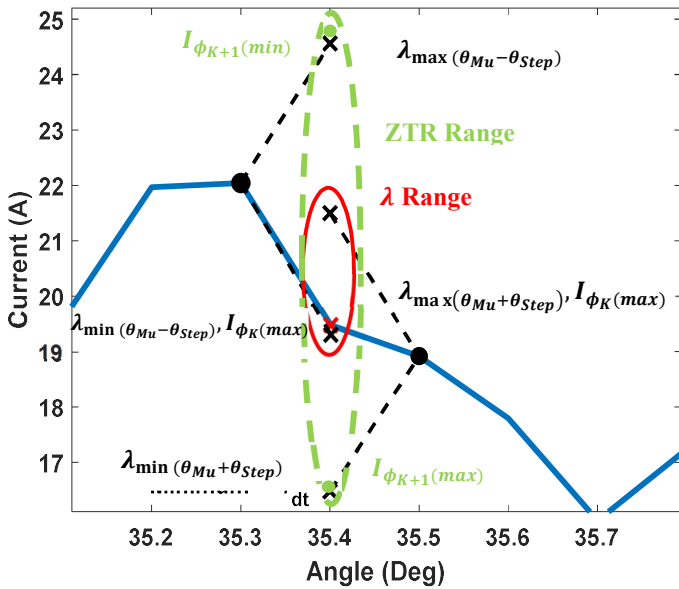
In the case where no points overlap, it means that no valid mutation is possible, and another mutation point is chosen. For the condition of ZTR at FLT, a range must be established from the prior range created to respect flux-linkage demand. Examining the range highlighted in red in Fig4.28b, each of these points will represent a respective current pairing in Fig4.28c which will fulfil FLT. Using FEA data to calculate the respective currents as shown in (4.8) and (4.9), a ZTR range in green is established in Fig4.28c.

$$I_{\phi_{k+1}(Max/Min)} = I(T_{\phi_{k+1}(Max/Min)}, \theta_{Mu} + 15^\circ) \tag{4.8}$$

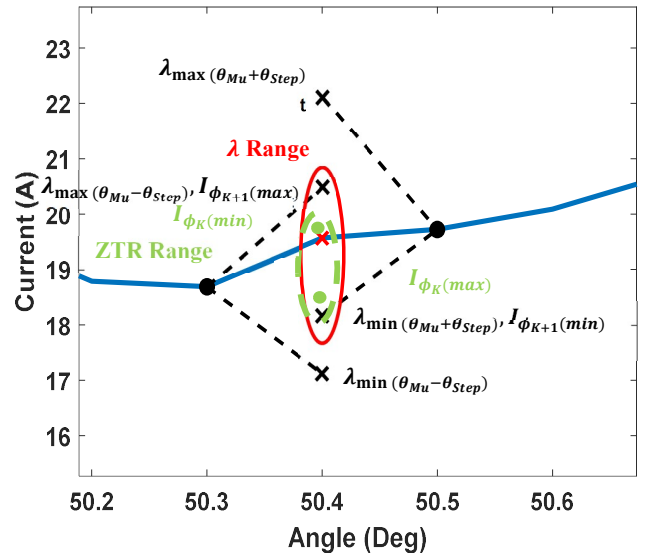
$$T_{\phi_{k+1}(Max/Min)} = T_{\theta_{Mu}} - T(I_{Mu(Max/Min)}, \theta_{Mu}) \tag{4.9}$$



(a)



(b)



(c)

Fig 4.28 Mutation Stage carried out at 200rpm: (a) The population member, (b) Incoming Phase Mutation, and (c) Outgoing Phase Mutation

It can be seen that this range is smaller than the flux-linkage demand range established for the point at $\theta_{Mu} + \theta_{ov}$, therefore it will dictate the true valid range of mutation for this point. Revisiting Fig4.28b, the ZTR range is also established for the respective phases flux-linkage demand range. In this case, the ZTR range is wide due to the low Nm/A efficiency at θ_{Mu} compared to the high Nm/A efficiency at $\theta_{Mu} + \theta_{ov}$, meaning that the flux-linkage demand range θ_{Mu} and its corresponding ZTR range are the dominant limits for mutation.

4.5.4 Population Evaluation

To evaluate current profiles fitness, the GA only takes into consideration rms current, where each current profile will already produce FLT with ZTR and be applicable at the given speed. This provides a simple, single problem objective function which is given in (4.10). The objective function takes a measure of the absolute proximity of a given profiles rms current I_{rms} to the theoretical optimal current $I_{rmsOptimal}$ found in Section 4.2.

$$Fitness = \left(1 - \frac{|I_{rmsOptimal} - I_{rms}|}{I_{rmsOptimal}} \right) \quad (4.10)$$

Two examples of the representative calculation can be seen an initial profile and the final result of the GA at 200rpm in Fig 4.29 and Fig 4.30 respectively. In Fig 4.29 its final fitness is gauged at 0.966, with a rms current 3.3% higher than the theoretical optimal being 0.37A at an rms current of 11.499A. In the second example, the profile has been optimised, now holding a fitness value of 0.999, with an rms current which is 0.05% above the theoretical optimum, being 0.06A higher at 11.135A

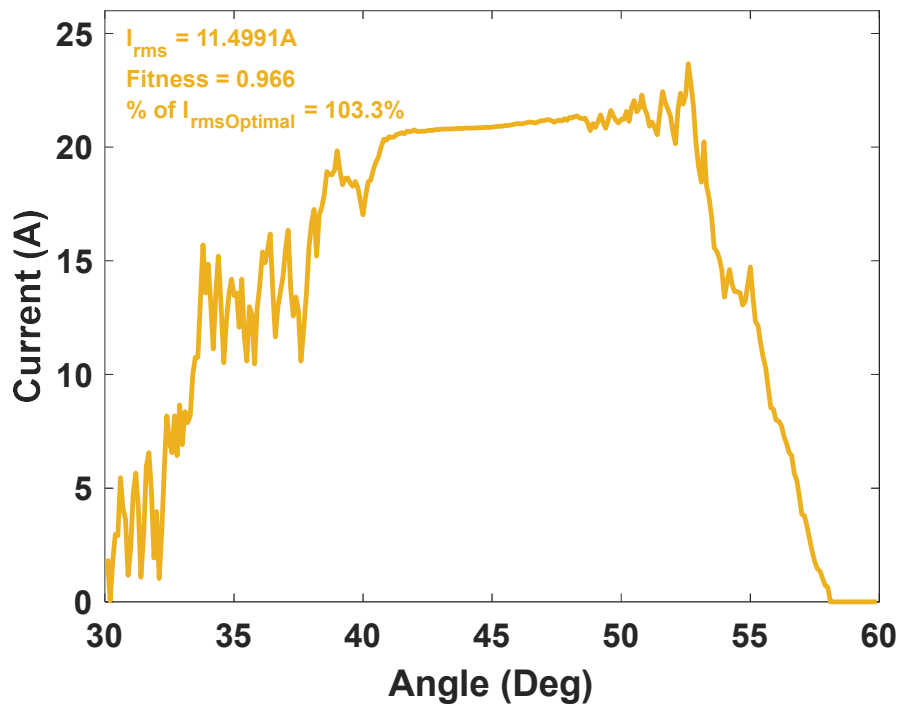


Fig 4.29 Initial GA generated profile at 200rpm

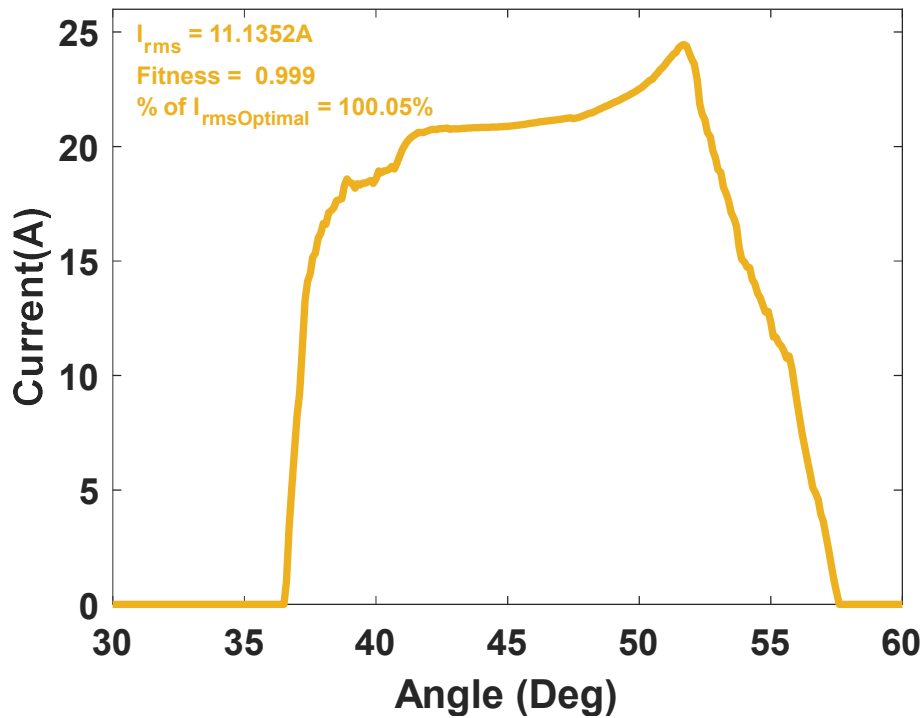


Fig 4.30 GA generated optimal profile at 200rpm

4.5.5 Population Selection

For selection of the profiles that pass to the next generation, a roulette style was chosen. Roulette Wheel selection operates from visualising the population as a collective fitness value created from summing fitness values of the population representing the wheel. The probability of selection is then taken by dividing the individual fitness values by this summation. This creates segments in the roulette wheel where members with larger fitness values have a larger segment based upon the cumulative probability of selection from the population. With these values set, the wheel is spun for how many members that are desired in the new population, with the remainder not chosen, are discarded as the GA progresses. The selection stage for this GA is provided with 750 profiles, which include the initial population of the generation, the crossover profiles, and the mutated profiles. From this it is then given the discretion to carry out a generic roulette wheel selection with no alterations.

4.5.6 Simulation Results

The designed GA is run with the configurations stated prior for increments of 100rpm from 0 to 1000rpm, with an average calculation time of 1.04 second per generation meaning 34.7 minutes per process. This speed was obtained with MATLAB utilising an average of 4.9% of a 4.7GHz central processing unit (CPU). The results from the first part of the chosen speed range are shown in Fig 4.31 with the given V_{DC} of 415V and FLT of 25Nm. The profiles shown from 0 to 500rpm, including the theoretically minimum profile introduced in Section 4.2. At the low end of the speed range at 100 to 200rpm, the algorithm produces profiles that tend to resemble the theoretically optimal profile. The profiles begin to lose this shape from 300rpm onwards as the increased $d\lambda/d\theta$ begins to extend the decay path of the profiles closer to the aligned position at 60° . This gradually increases the realised θ_{ov} in order to maintain the optimal single and two-phase conduction in the most efficient Nm/A regions of the machine, for either the whole or majority of FLT production respectively. This likely contributes the slow increasing rms current of the profiles at this stage (from 11.129A to 11.150A).

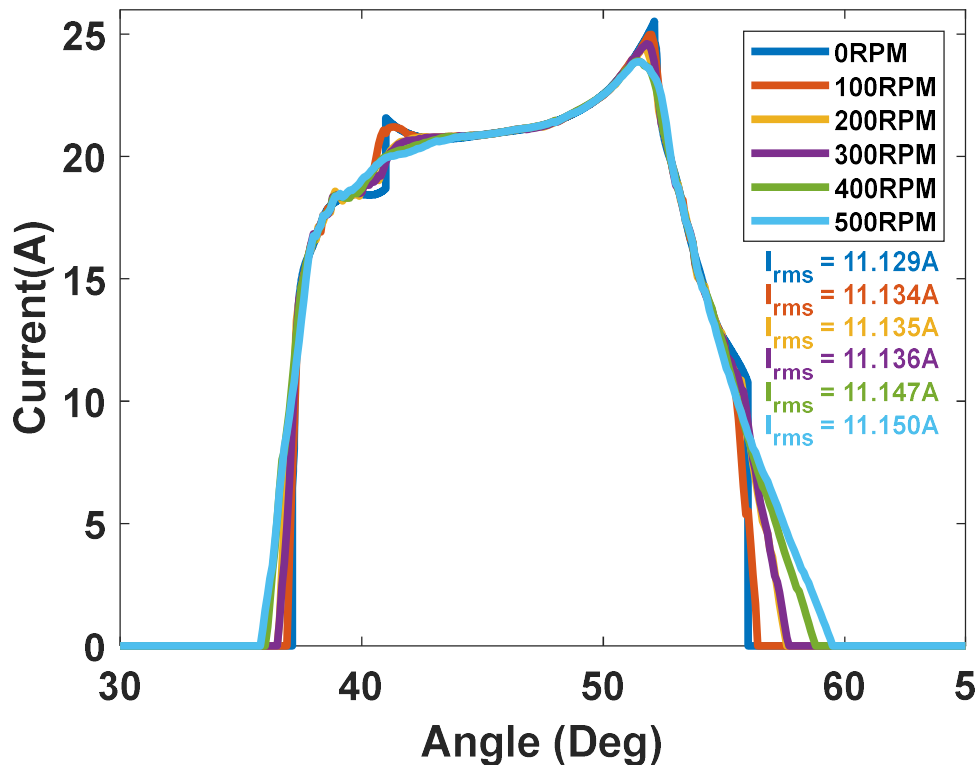


Fig 4.31 GA optimal profile from 0-500rpm

As profiles approach 500rpm, the θ_{on} of the profiles begins to advance notably as the optimal buildup to single phase conduction requires a wider conduction period as $d\lambda/d\theta$ increases further. This accompanies the further delayed θ_{off} , notably increasing θ_{ov} and realised θ_{cond} . This leads to lower peak current overall but contributes to a small rise in rms current as two-phase overlap conduction is increasingly required in less efficient Nm/A regions.

Fig 4.32 shows the algorithm results over the second half of the given speed range given from 600 to 1000rpm in 100rpm increments. In this speed region, the optimal profiles shapes are dependent on maintaining the build-up and decay paths required for the given speed to produce optimal levels of torque production, again in the most efficient Nm/A regions from 40° to 55° . In this range, the trend continues of an increasing θ_{ov} coupled with an increasing conduction period. 600rpm highlights the profiles reaching the limit of the positive torque production region for decay, where higher speeds introduce negative torque production during decay. Above 800rpm marks a larger disparity in rms current as the profiles advance θ_{on} into more inefficient regions for buildup while requiring larger currents and conduction within inefficient negative torque production regions.

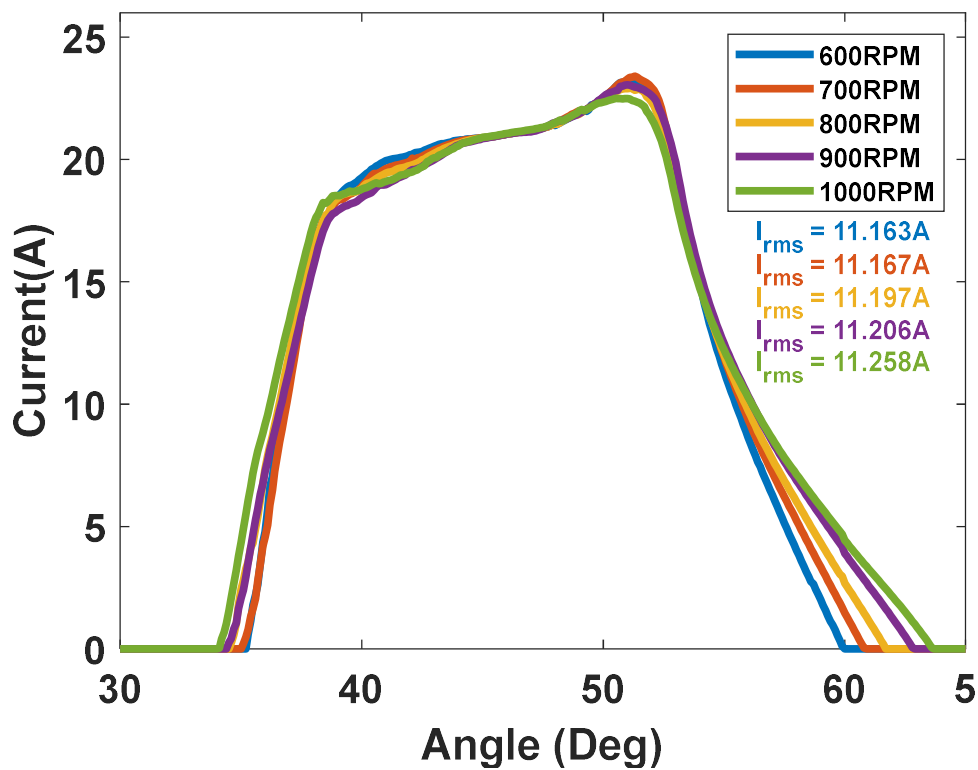


Fig 4.32 GA optimal profile from 500-1000rpm

While the peak current is consistent in still decreasing, it does not contribute to any decrease in rms current, as more current is required to compensate for the negative torque production of the now notable tail off current. The main characteristics of the profiles produced by the GA are presented in Table 4.2 where the trends described can be observed. Across this ripple free speed range, it can be seen that an increase of only 1.17% in rms current above the theoretically optimal current is produced, reinforcing the case of the GA to produce high quality solutions to the challenge of current profiling of the SRM.

Table 4.2 Characteristics of GA produced optimal profiles from 0-1000rpm

| ω (rpm) | I_{rms} (A) | % $I_{rmsOptimal}$ | I_{pk} (A) | P_{Cu} (W) | % $P_{CuOptimal}$ | θ_{on} (°) | θ_{off} (°) | θ_{ov} (°) | θ_{cond} (°) |
|----------------|---------------|--------------------|--------------|--------------|-------------------|-------------------|--------------------|-------------------|---------------------|
| 0 | 11.129 | 100 | 25.52 | 99.08 | 100 | 37.1 | 56 | 3.9 | 18.9 |
| 100 | 11.134 | 100.04 | 24.99 | 99.17 | 100.09 | 37 | 56.4 | 4 | 19.4 |
| 200 | 11.135 | 100.05 | 24.46 | 99.19 | 100.11 | 36.7 | 57.6 | 5.9 | 20.9 |
| 300 | 11.136 | 100.06 | 24.62 | 99.21 | 100.13 | 36.5 | 57.7 | 6.2 | 21.2 |
| 400 | 11.147 | 100.16 | 23.91 | 99.40 | 100.32 | 36.5 | 58.9 | 7.4 | 22.4 |
| 500 | 11.150 | 100.19 | 23.88 | 99.46 | 100.38 | 36 | 59.5 | 8.5 | 23.5 |
| 600 | 11.163 | 100.31 | 23.33 | 99.69 | 100.62 | 35 | 60 | 10 | 25 |
| 700 | 11.167 | 100.34 | 23.11 | 99.76 | 100.69 | 35 | 0.9 | 10.9 | 25.9 |
| 800 | 11.197 | 100.61 | 22.91 | 100.30 | 101.23 | 34.5 | 1.7 | 12.2 | 27.2 |
| 900 | 11.206 | 100.69 | 23.05 | 100.46 | 101.39 | 34.5 | 2.9 | 13.4 | 28.4 |
| 1000 | 11.259 | 101.17 | 22.51 | 101.41 | 102.35 | 34.2 | 3.7 | 14.5 | 29.5 |

Fig 4.33 shows the results of comparing the profile produced at a speed of 1000rpm with a commonly used Cosine TSF. It can be seen that the GA profile produces a notably smaller rms current of 11.259A compared to the 12.464A of the TSF, which when comparing to the benchmark of the theoretically optimal rms current, is 101.17% of the value compared to 111.99% of the TSF (10.83% increase). This is due to the ability of the GA design to utilise minimal negative torque production in its profiling to allow this optimal concentration of torque production in the highest Nm/A regions. In the profile produced by the Cos TSF, it can be seen that excessive current can be found in the inefficient Nm/A regions before 40°. Examining Fig 4.32 parts b and c, the Cosine TSF is unable to maintain ZTR at the given speed and switching angles, entering unintentional

three phase conduction which gives rise to a TR of 3.2% compared to the GAs <1% TR objective. This is due to the profile not being able to decay within the maximum overlap period, as the TSF cannot account for this in its calculation.

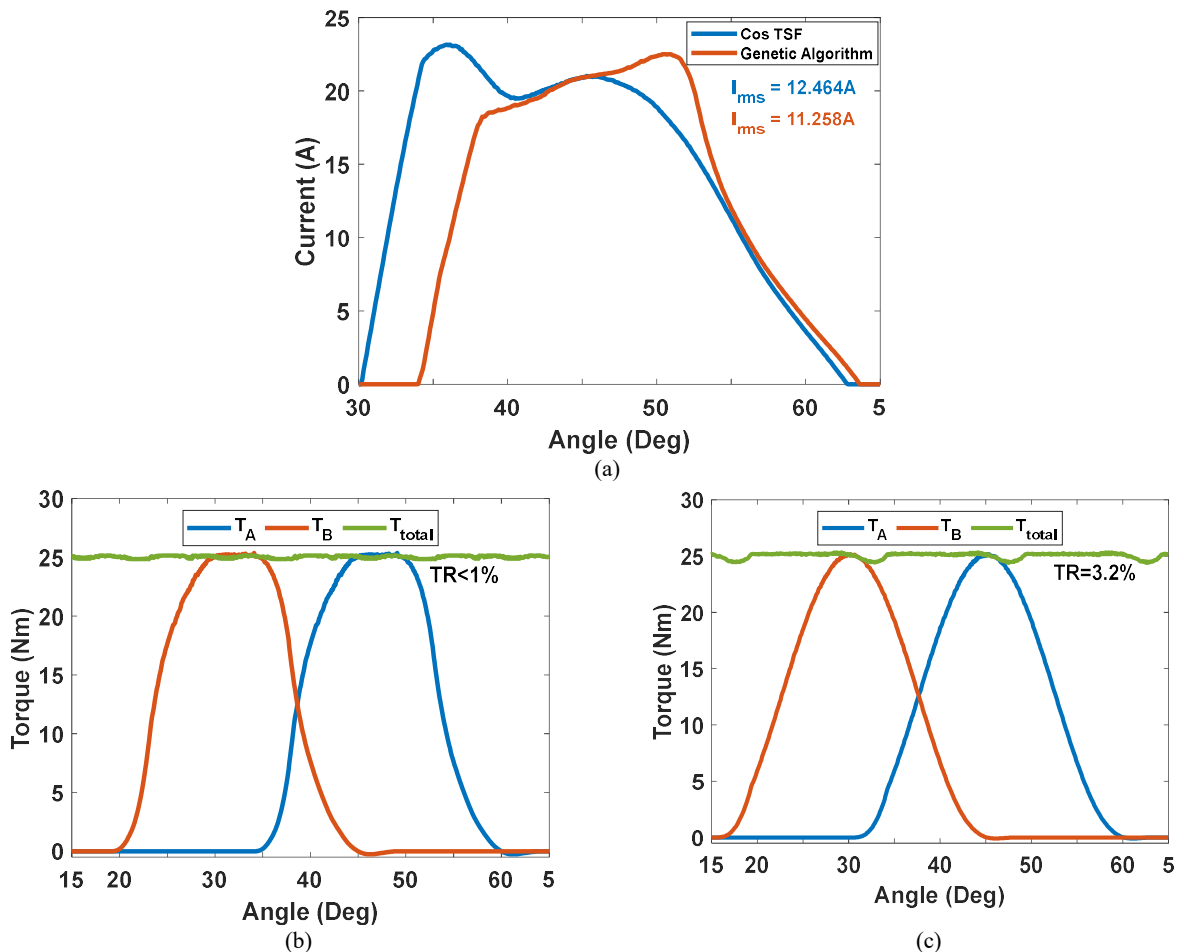


Fig 4.33 Comparison between the GA and the Cos TSF at 1000rpm: (a) Current profiles, (b) GA torque waveforms, and (c) Cos TSF torque waveforms.

Fig 4.34 shows the results operational torque speed curve of the GA method with two-phase overlap. It also illustrates the corresponding theoretical optimal currents for the varying torque levels, accompanied by the rms current of GA produced optimal profiles at maximum speeds. While this method has produced optimal currents across the ripple free speed range for two-phase overlap in the 8/6 SRM, it is limited to only 72% of the machines based speed at 1080rpm compared to 1500rpm. At higher speeds and lower torques, closer to the common operating points in applications of the machine this difference becomes greater, where at 50% of FLT the two-phase overlap can only operate less than 50% of the machines rating in the constant power region. Therefore, an augmentation of the methodology that the current profiling used so far must be made.

This is given that in Section 4.3, it is established that no variables can effectively increase the machines TR free speed range bar altering machine characteristics such as increasing the supply voltage rating or changing the design. For the production of optimal current profiles, it can be seen that the profiles correlate in terms of maintaining the majority of torque production in the most efficient Nm/A region, while accommodating for this with the rest of the profile in an optimally fast current buildup and decay. Logically this can be continued at higher speeds, but the problem that is encountered in the case of the four phase, 8/6, SRM is exceeding the maximum two-phase θ_{cond} , introducing unintentional three phase conduction. This will cause TR as the new torque production is not accounted for within the boundaries of the two-phase framework.

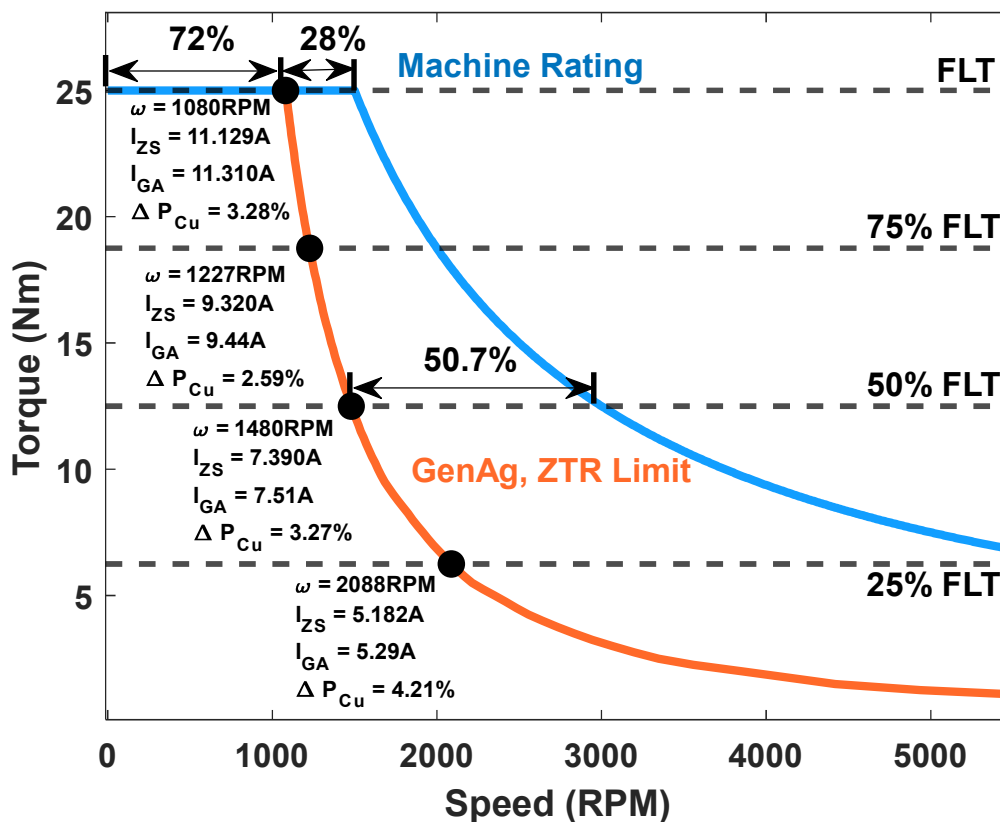


Fig 4.34 GA ripple free speed range and rated $T - \omega$ curve

The profiles at the two-phase GAs ripple free speed limits for the four highlighted torque levels are presented in Fig 4.35, with their characteristics summarised in Table 4.3. It can be seen that as these are at the maximum speeds, the full available two-phase conduction period of 30° is used. A delayed θ_{on} is not utilised for these speeds, as it is found that at the absolute speed limits, but not

near maximal speeds, the delay of θ_{on} can compromise the decay path of profiles, as more of the profiles tail-off occurs much closer to the aligned position, where the machine cannot decay efficiently without causing unintentional three phase overlap. At maximum speeds, the profiles correlate in shape, where the only possibility for fulfilling load torque demands are producing significant amounts of torque in inefficient regions (35° to 38°), resulting in significant peak currents and then proceeding to decay at 50° . Compared to each of their respective theoretically optimal profiles, these profiles maintain an rms current of 1% to 2% above the theoretically optimal rms current.

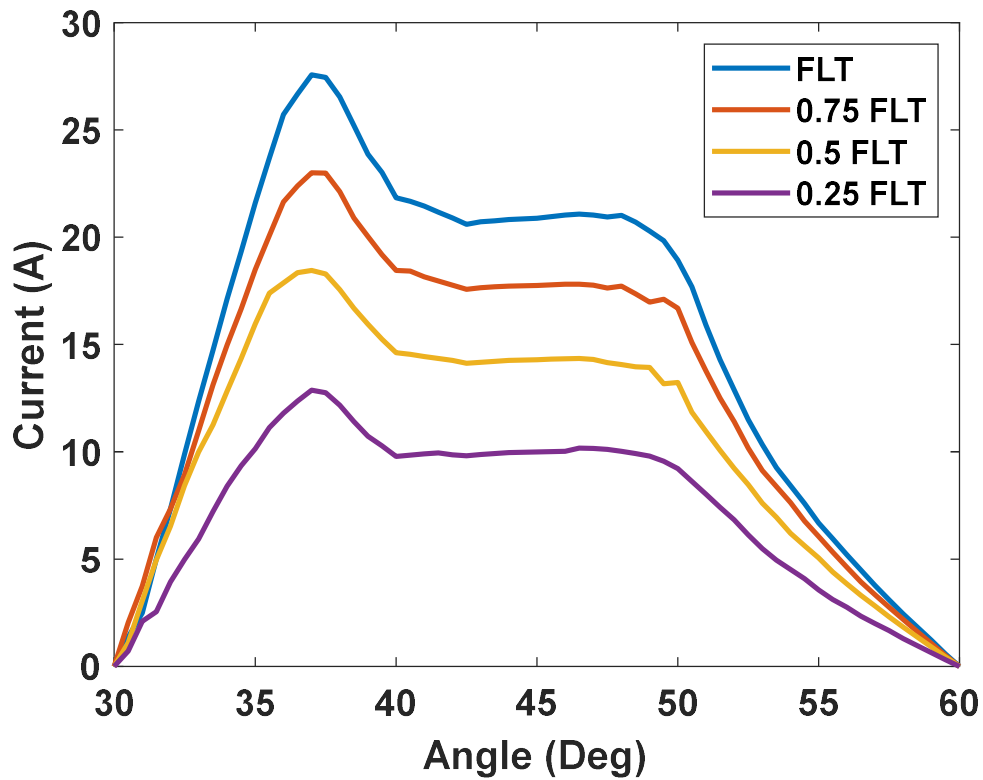


Fig 4.35 GA optimal profiles at highlighted torque levels

Table 4.3 Characteristics of GA produced optimal profiles from 0-1000rpm

| $T(Nm)$ | I_{rms} (A) | $I_{rmsOptimal}$ | $\% I_{rmsOptimal}$ | I_{pk} (A) | P_{Cu} (W) | $\% P_{CuOptimal}$ | θ_{on} ($^\circ$) | θ_{off} ($^\circ$) | θ_{ov} ($^\circ$) | θ_{cond} ($^\circ$) |
|---------|---------------|------------------|---------------------|--------------|--------------|--------------------|----------------------------|-----------------------------|----------------------------|------------------------------|
| 25 | 11.310 | 11.129 | 101.63 | 27.56 | 102.33 | 103.28 | 30 | 60 | 15 | 30 |
| 18.25 | 9.44 | 9.320 | 101.29 | 23 | 71.29 | 102.59 | 30 | 60 | 15 | 30 |
| 12.5 | 7.51 | 7.390 | 101.62 | 18.44 | 45.12 | 103.27 | 30 | 60 | 15 | 30 |
| 6.25 | 5.29 | 5.182 | 102.08 | 12.87 | 22.39 | 104.21 | 30 | 60 | 15 | 30 |

4.6 Torque ripple free speed range extension using greater than two-phase conduction

Two-phase torque sharing in principle allows successive SRM phases to overlap their conduction for a maximum period $\theta_{ov(2\phi)}$, being established as θ_{ov} in prior sections at 15° for a four phase, 8/6 SRM. Using two-phase overlap the FLT TR free speed range is limited to 1080rpm as seen in Fig 4.36, due to the profile not being able to buildup and decay (due to insufficient V_{DC}) in an appropriate conduction period while still fulfilling FLT torque demand. By introducing another phase into the overlap, the problem of decay and buildup can be alleviated, as this allows a conduction period greater than 30° in the case of the four phase, 8/6 SRM. Fig 4.36 illustrates the concept of this intentional three-phase overlap using a reference turn on $\theta_{on_{ref}}$ of 30° and turn off $\theta_{off_{ref}}$ of 60° and phase A as a reference. Similar to two-phase overlap, the maximum three phase overlap period $\theta_{ov(3\phi)_{max}}$ can be expressed as (4.11), where the $\theta_{ov(3\phi)_{max}}$ in the four phase, 8/6 SRM is 15° before four phase overlap is introduced. The realised three-phase overlap can be calculated using (4.12), where it is the sum of the shifted turn on $\theta_{on(3\phi)}$ before or after $\theta_{on_{ref}}$ and shifted turn off $\theta_{off(3\phi)}$ before or after $\theta_{off_{ref}}$.

$$\theta_{ov(3\phi)} \leq \frac{1}{2}\theta_r - \varepsilon = \frac{1}{2} \times 60^\circ - 15^\circ = 15^\circ \quad (4.11)$$

$$\theta_{ov(3\phi)} = \left(\theta_{on(3\phi)} - \theta_{on_{ref}} \right) + \left(\theta_{off(3\phi)} - \theta_{off_{ref}} \right) \quad (4.12)$$

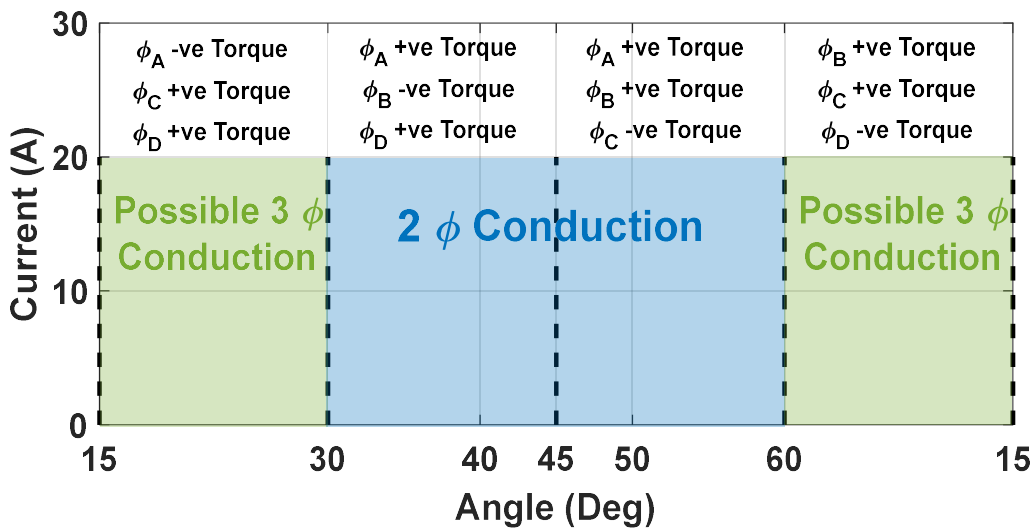


Fig 4.36 Three-phase conduction boundaries with reference to two-phase torque sharing.

Fig 4.37 illustrates the use of this method with $\theta_{on(3\phi)} = 30^\circ$, $\theta_{off(3\phi)} = 2^\circ$ and therefore $\theta_{ov(3\phi)} = 2^\circ$ using the current profiling limit envelopes. Now the maximum ZTR speed at FLT is extended to 1230rpm (from 1080rpm) by allowing a longer decay path with a delayed $\theta_{off(3\phi)}$, and a small overall conduction period increase to $\theta_{cond} = 32^\circ$.

Fig 4.38 presents the use of this method again, this time using $\theta_{on(3\phi)} = 28^\circ$, $\theta_{off(3\phi)} = 60^\circ$ providing a $\theta_{ov(3\phi)} = 2^\circ$ but at a different angular position. Allowing a longer buildup by advancing $\theta_{on(3\phi)}$ provides an increase in speed range to 1130rpm. This is notably less than the equivalent $\theta_{ov(3\phi)}$ in Fig 3.37 due to the requirements of excessive peak currents to produce the majority of FLT in the 35° - 38° region above the SRMs current limit. Note that due to this extension of conduction into the negative torque production region, compensation of the small amount of additional negative torque must be considered. This is done by allowing the main control phase to produce torque greater than FLT, as highlighted in red where the upper envelope boundary is increased slightly by the maximum amount of compensation it may need to provide during three-phase conduction in both Figs 4.37 and 4.38.

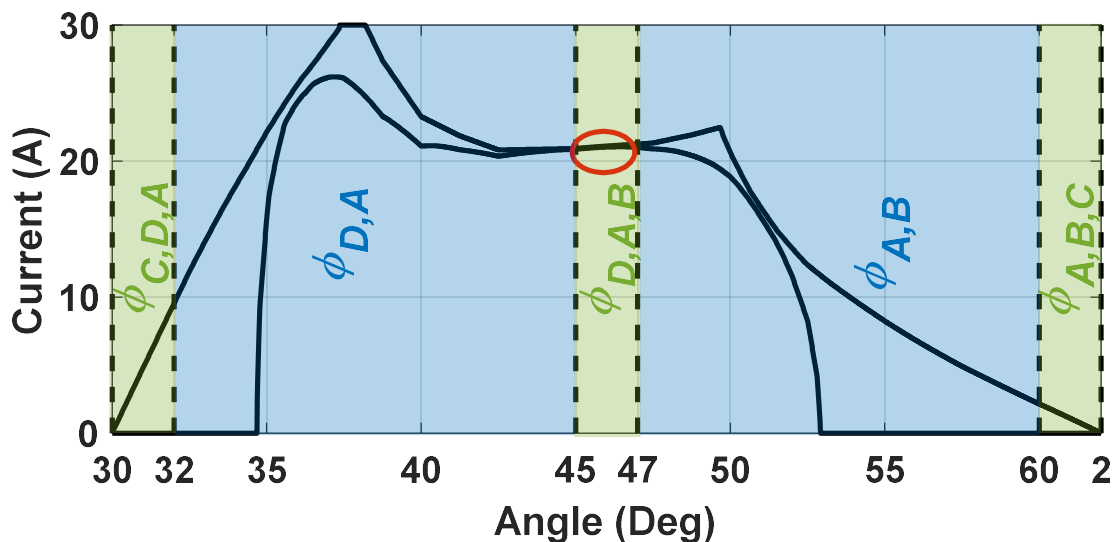


Fig 4.37 Three-phase FLT Speed limit envelopes at 1230rpm by delaying $\theta_{off(3\phi)}$

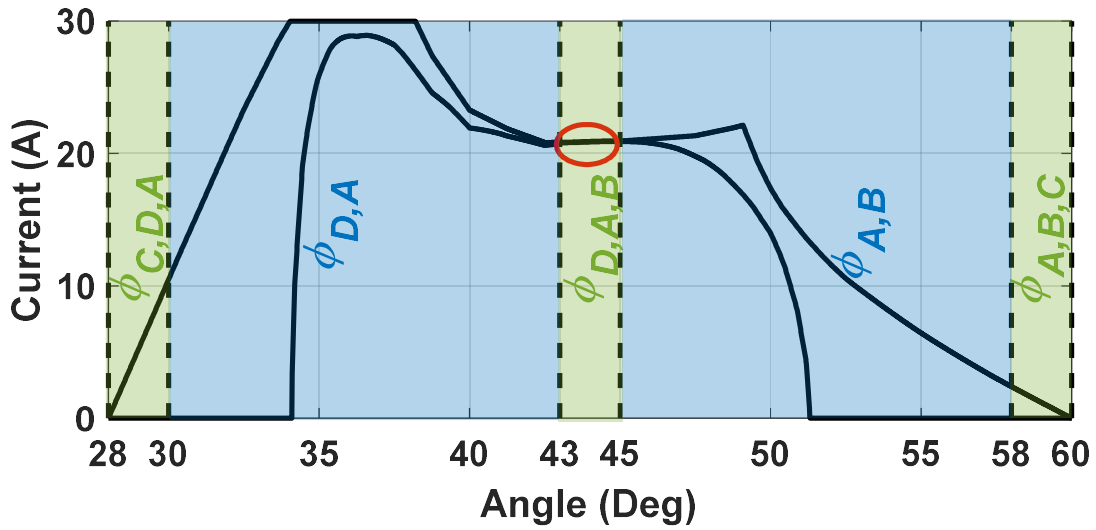


Fig 4.38 Three-phase FLT Speed limit envelopes at 1130rpm by advancing $\theta_{on(3\phi)}$.

Fig 4.39 shows an example of a three-phase profiling envelope for the SRM peak power point at the base speed of 1500rpm with FLT. This example makes use of both an advanced $\theta_{on(3\phi)} = 28^\circ$ and delayed $\theta_{off(3\phi)} = 4^\circ$, collectively resulting in an $\theta_{ov(3\phi)} = 6^\circ$. This is only an example of a combination of $\theta_{on/off(3\phi)}$ that can yield feasible current profiles at the given speed; as it has been established that the alteration of the combinations of switching angles yields different shapes and notably more efficient current profiles.

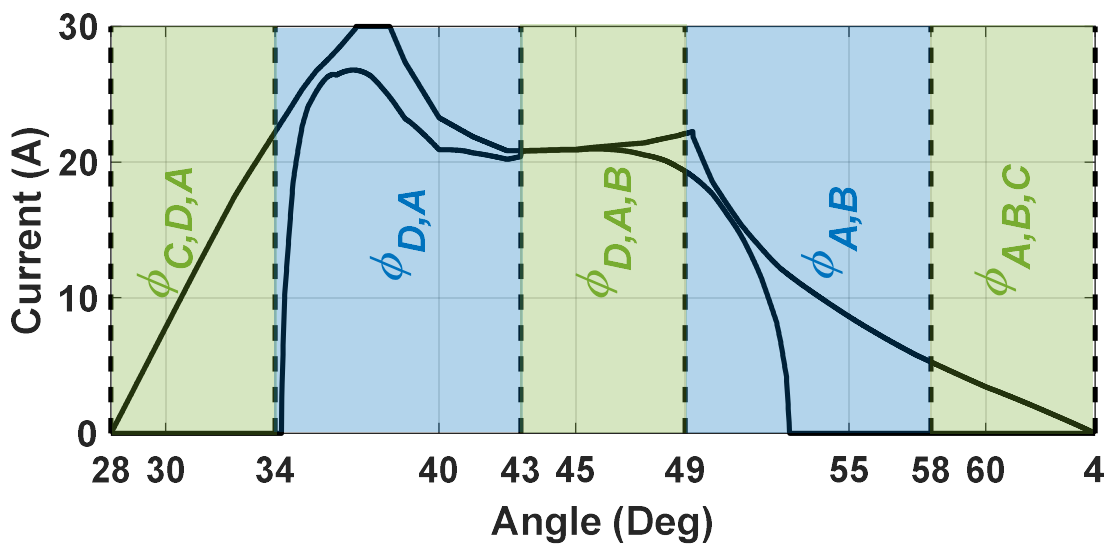


Fig 4.39 Three-phase FLT Speed limit envelopes at 1500rpm.

An added benefit of this method is that it can be proven that ZTR operation at FLT can be achieved above the rated speed and power of the machine as illustrated in Fig 4.40 at 1600rpm with $\theta_{ov(3\phi)} = 7^\circ$. The limitation on achieving this operating point for a prolonged period though may not be associated with the machine electrical parameters but external factors such as thermal or mechanical limitations.

With the concept of utilising more than two-phase conduction in an SRM to harness the full speed range and power of the machine with ZTR, the GA current profiling-based approach can now be augmented to obtain current profiles which satisfy the ZTR and V_{DC} limits while optimising rms current from 0-1500rpm. While this section focuses on the use of three-phase overlap, in the case of any SRMs where three phase overlap does not suffice to fulfil the rated speed range of the machine, the method is expandable, for example with four phase overlap, or above.

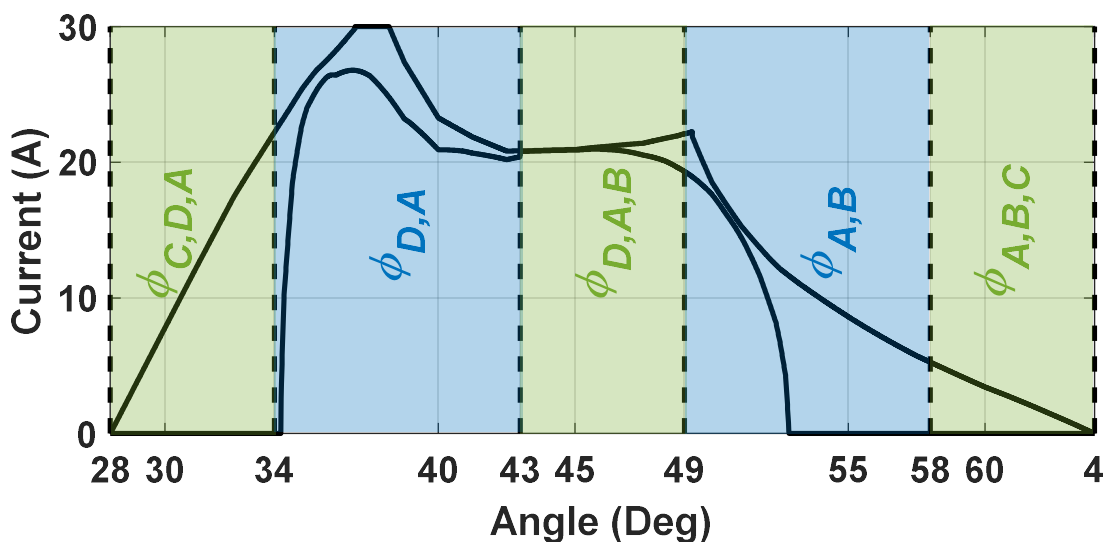


Fig 4.40 Three-phase FLT Speed limit envelopes at 1600rpm.

4.7 Genetic algorithm approach to current profiling for torque control and minimal rms current across an optimised speed range

The proposed GA design is limited to two-phase torque sharing for any multiphase SRM. By altering the design at the population generation, crossover and mutation stages, the GA can be both utilised for two and three-phase overlap. Three phase overlap in this case (and any case where the third phase produces negative torque) should only be used for TR-free speed range extension due

to the inefficiency as it relates to rms current, that three phase overlap implies. This is because when considering optimally minimal rms currents, any θ_{cond} that is greater than 30° (three-phases) includes the production of negative torque in one additional phase along with the two other phases conducting. This is opposed to two-phase torque sharing where at most one phase will produce negative torque while the other is producing positive torque.

With alterations to the design, the augmented GA functions as shown in Fig 4.41, where if the reference speed which the profiles are being created for is above the two-phase speed limit of the given SRM, a three-phase version of the algorithm is deployed.

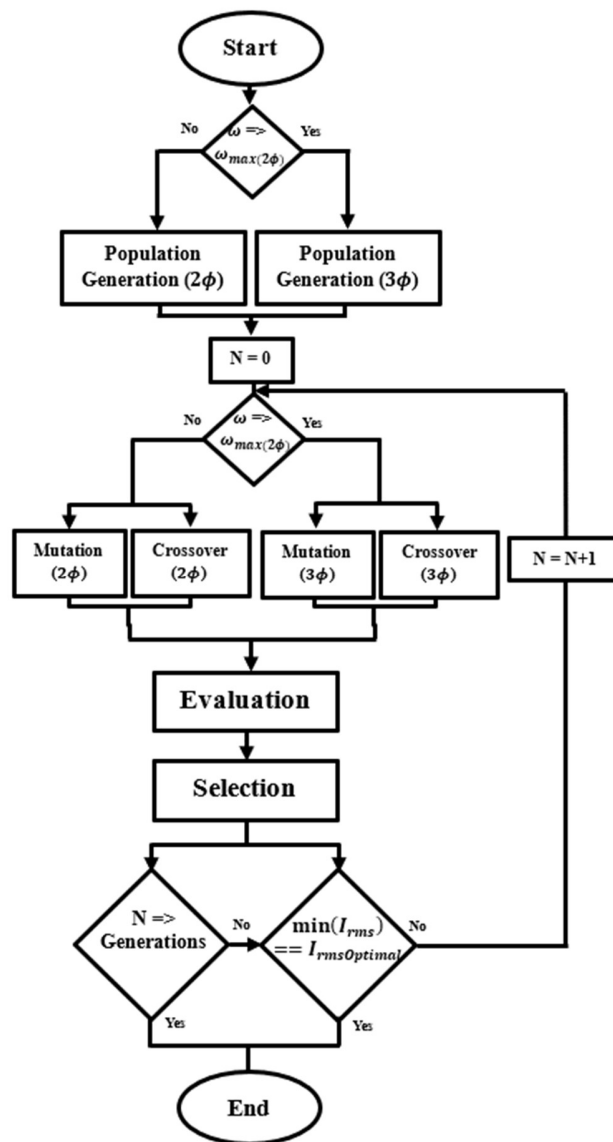


Fig 4.41 Overview of augmented GA process

The augmented GA is simulated with the same characteristics as in the original, where 250 initial population profiles are generated, where 250 profiles are carried over for each of 2000 generations from a pool of 750 profiles generated from the augmented crossover and mutation. The same theoretically optimal profile is used as an optimisation target, and the augmented GA is ran from a MATLAB script.

4.7.1 Augmented Population Generation

An example of population generation at 1200rpm is presented in Fig 4.42, with a $\theta_{on(3\phi)}$ of 33° , $\theta_{off(3\phi)}$ of 6° and θ_{step} of 0.1° . The function of this stage is similar to the two-phase equivalent in subsection 4.5.1, where within the current profiling envelopes, random current profiles are procedurally generated based upon a procedural grid of currents created from the upper and lower envelope limits. This is expressed for the current pairings, or in the case of three phase overlap in the highlighted regions, current trios in (4.13).

$$\phi_{1,2} = \begin{bmatrix} \lambda, I_{Upper}(33^\circ, 48^\circ) & \cdots & \lambda, I_{Upper}(48^\circ, 63^\circ) \\ \vdots & \ddots & \vdots \\ \lambda, I_{Lower}(33^\circ, 48^\circ) & \cdots & \lambda, I_{Lower}(48^\circ, 63^\circ) \end{bmatrix} \quad \phi_3 = \begin{bmatrix} \lambda, I_{Upper}(63^\circ) & \cdots & \lambda, I_{Upper}(66^\circ) \\ \vdots & \ddots & \vdots \\ \lambda, I_{Lower}(63^\circ) & \cdots & \lambda, I_{Lower}(66^\circ) \end{bmatrix} \quad (4.13)$$

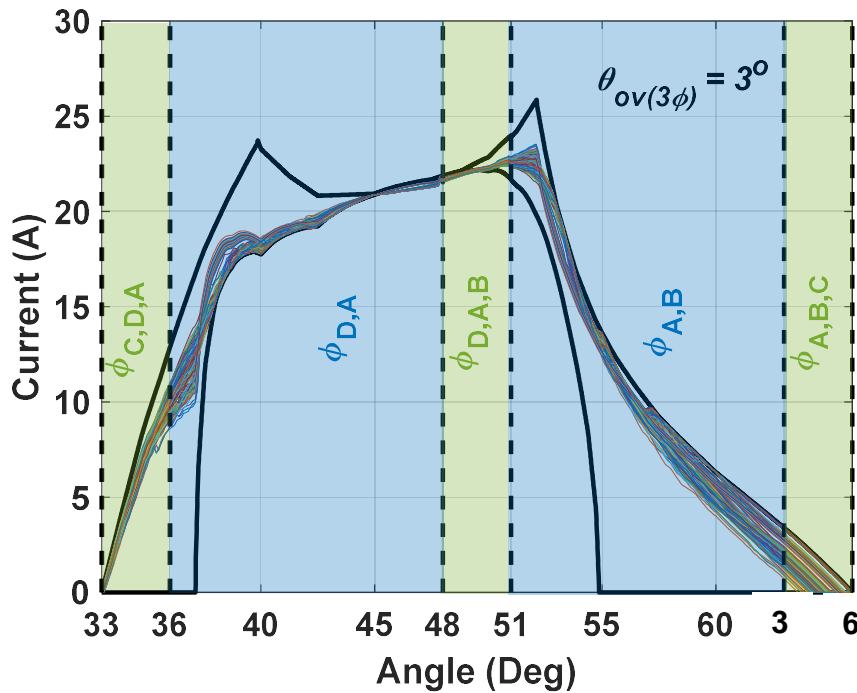


Fig 4.42 Three phase GA population generation at 1200rpm.

The main difference with this stage is the generation of these current trios in the three-phase region, where the consideration is first taken for the first two phases, which the main purpose is current buildup, decay and the production of FLT. The third phase is purely used for decay or buildup, where the first two phases are calculated to produce FLT plus the required compensation for the third phase negative torque in combination while respecting supply voltage limits. In the case where this is not possible, the profiles are discarded and restarted. Examining the generated population, the effects of higher speed (relative to base speed) operation can be seen where the profiles are limited in the shapes they can take while fulfilling all of the requirements. This is not only due to the envelope limits, but also the drastically increased $d\lambda_{max}/d\theta$ and therefore smaller increases or decreases of current between angular points, requiring an exact buildup, bulk torque production and decay to stay within DC supply voltage.

4.7.2 Augmented Population Crossover

An example of the augmented crossover stage is illustrated in Fig 4.43 with the same parameters as the augmented population generation. Compared to two-phase crossover, three phase crossover can be carried out in the same way with a random cutting point in the profile (41° and 56°) within the boundaries of θ_{on/off_ref} , which in this case is 33° and 3° respectively, and another spaced by θ_{ov} . With the same checks made for $d\lambda/d\theta$ at the cutting points, a new one is selected if any chosen cutting point is invalid. The new consideration must be now made for ZTR in the three phase region, given the crossover will create a new set of three phase current trios. In the likely case there is TR, the dominant torque producing phase (highest Nm/A efficiency) is adjusted to restore ZTR within supply voltage limits. This adjustment is likely to always be minor given that any profile at speeds using three phase overlap will have relatively small amounts of negative torque production to begin with in the three phase region. Along with this, these profiles will also have a relatively similar decay path to the profile it is being crossed over with, meaning negative torque production values will be similar. This can be seen when examining the high Nm/A three phase region in Fig 4.42 (48° to 51°), where the offspring profile has a very small ($<0.2A$) amount of current adjustment to compensate for the new values of currents introduced for the new current trio.

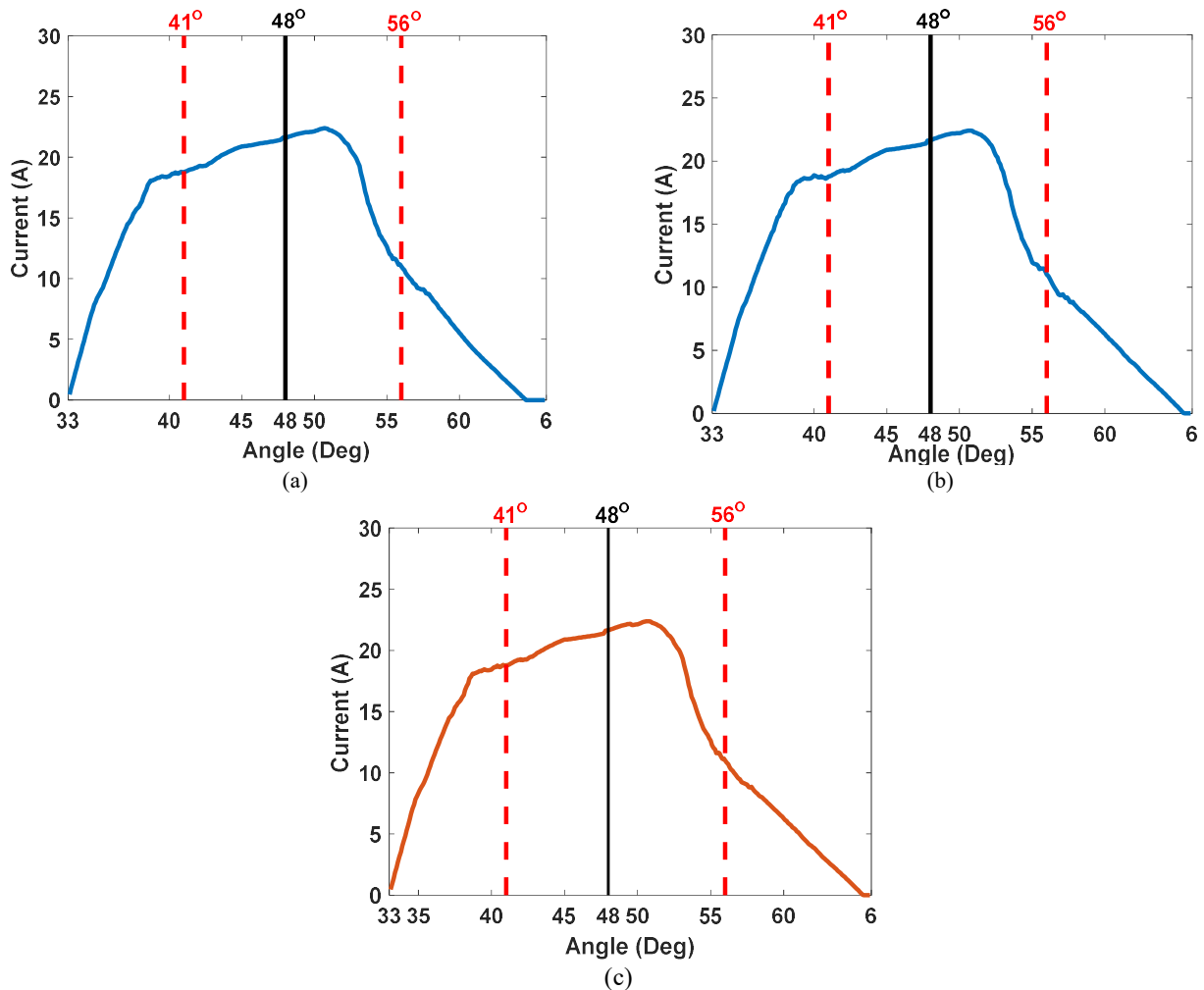


Fig 4.43 Three phase crossover stage performed at 1200rpm for two population members: (a) Parent 1, (b) Parent 2, and (c) Offspring.

4.7.3 Augmented Population Mutation

An example of the augmented mutation stage is given in Fig 4.44, with the same parameters as the prior stages. For mutation, a random θ_{Mu} and $(\theta_{Mu} + 15^\circ)$ is selected and can be situated at any point in the profiles reference θ_{on/off_ref} conduction period which again is 33° and 3° in Fig 4.42. In this case it is 36.6° and 51.6° , and the same ranges (ZTR, supply voltage) established prior are created over a much smaller range of values due to the increase in $d\lambda/d\theta$ at high speed. This can be seen particularly in the buildup at 36.6° , where the supply voltage mutation range is very small, being less than 0.5A between λ_{max} and λ_{min} , dominating the overall range of mutation. For mutation points selected within the three phase conduction range, the two primary phases overlapping are mutated, given the third phase will be in a rigid decay or buildup path. When

mutating these points, the ZTR FLT range is altered, to consider not only FLT but FLT plus the compensation required for the negative torque production in the third phase.

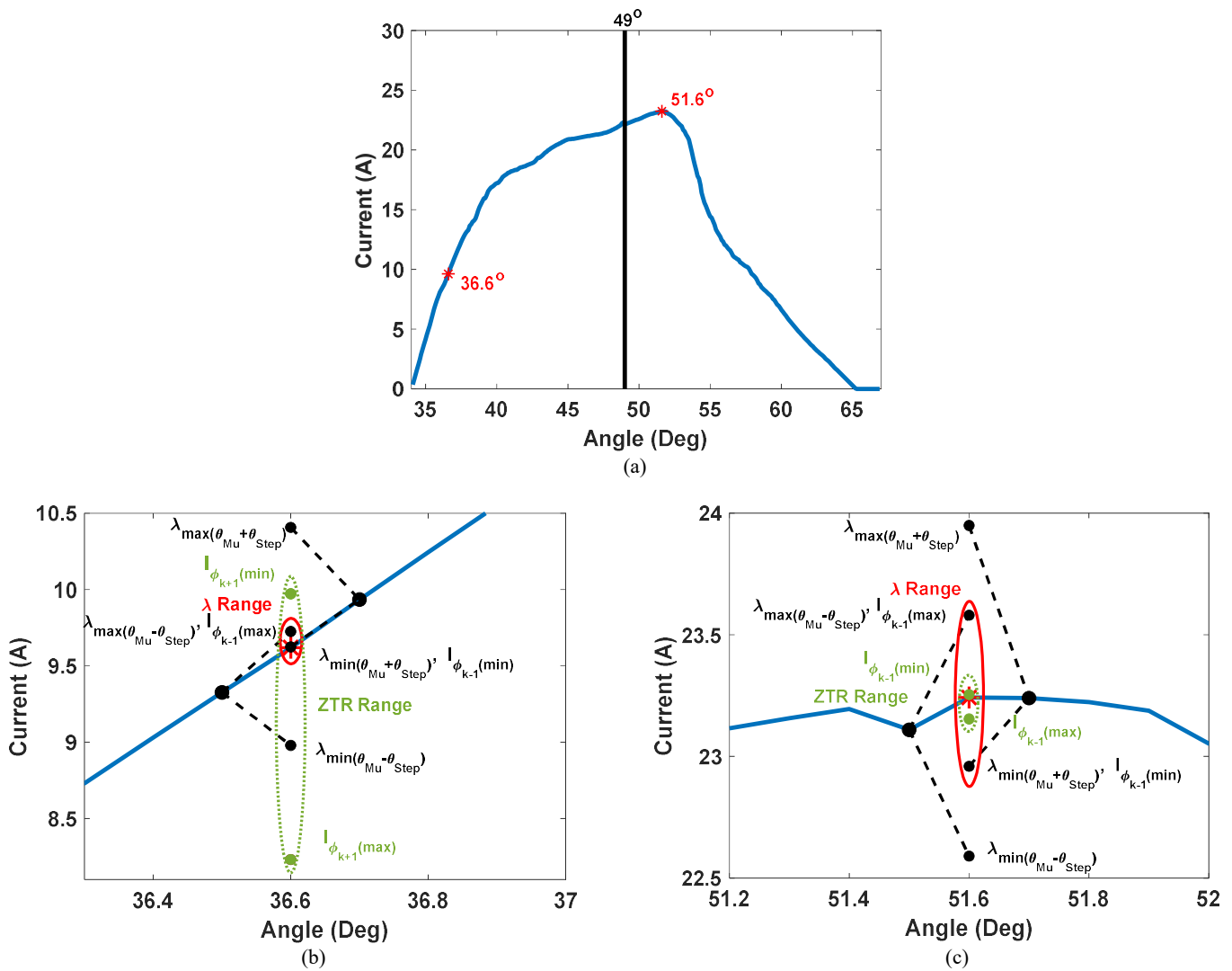


Fig 4. 44 Three phase mutation stage carried out at 1200rpm: (a) The population member, (b) Incoming phase mutation, and (c) Outgoing phase mutation

4.7.4 Simulation Results

The augmented GA script is run for the speeds of 1100rpm to the base speed of the SRM under test at 1500rpm for FLT and a V_{DC} of 415V, in 100rpm increments. The performance in MATLAB maintains the same characteristics as the original GA, with the adjustments to the GA providing minimal additional computational load, along with MATLABs in built limitations in computer usage. Fig 4.45 presents the results of augmented GA along with the respective rms current of the

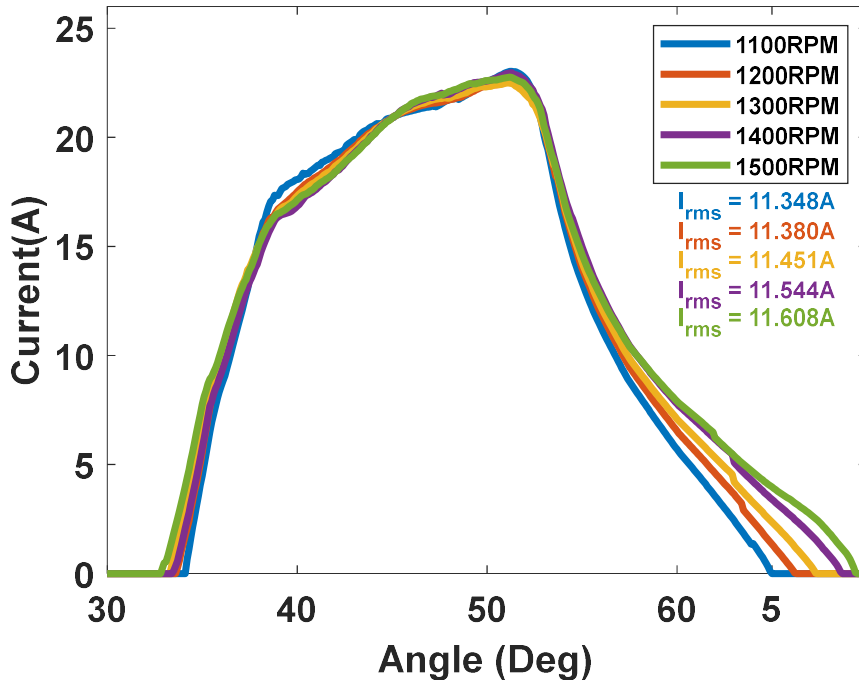


Fig 4.45 GA Current profiles from 1100 to 1500rpm.

profiles. In this speed range, three phase overlap is necessary to allow the build-up and decay of enough current for FLT production and $\theta_{ov(3\phi)}$ increases with speed. This overlap is seen more in the decay path of the profiles, where to maintain the majority of FLT production in the most efficient Nm/A regions shown in Fig 2.8 (40° to 55°), decay typically begins after 53° . θ_{on} also begins to advance for the same reasons, where buildup is limited by the increased $d\lambda/d\theta$ and needs a longer conduction period in lower Nm/A regions to reach the same current levels. As speed increases, the decay path becomes notably longer (further delayed θ_{off}) for the same advanced θ_{on} , introducing more efficient regions of negative torque production for greater periods of the conduction period. This contributes to an rms current increase but is an acceptable trade to avoid excessive peak currents on the initial profile build-up. Table 4.4 presents the characteristics of the GA profiles across the full speed range of the machine, with the values of currents in the aligned position added. Across the full SRM speed range from 0 to 1500rpm, rms current is maintained below the I_{rated} given in Appendix A, and overall is only 4.3% above the theoretically optimal current at the machines maximum power point. This represents a maximum copper loss P_{Cu} of 107.8W, being 8.8% higher than the theoretically optimal value of 99.08W. At the aligned position (60°), current begins increase from 700rpm onwards, reaching a peak of 7.89A at 1500rpm. These

are required for optimal efficiency of the profiles with the requirements for a larger decay path. In general, they are required to some degree for any profile operating at speeds which use three phase overlap. At alignment, tangential force Nm/A efficiency is zero but radial force Nm/A efficiency is a maximum. The tail current produced radial force causes stator deformation resulting in acoustic noise and vibration in the machine. The aligned current approaching base speed is not significant, and below 700rpm, zero current (radial force) exists at alignment.

Table 4.4 Characteristics of GA produced optimal profiles from 0-1500rpm

| ω (rpm) | I_{rms} (A) | % $I_{rmsOptimal}$ | I_{pk} (A) | $I_{aligned}$ (A) | P_{Cu} (W) | % $P_{CuOptimal}$ | θ_{on} (°) | θ_{off} (°) | $\theta_{ov(2\phi)}$ (°) | $\theta_{ov(3\phi)}$ (°) | θ_{cond} (°) |
|-------------------|---------------|--------------------|--------------|-------------------|--------------|-------------------|-------------------|--------------------|--------------------------|--------------------------|---------------------|
| 0 | 11.129 | 100 | 25.52 | 0 | 99.08 | 100 | 37.1 | 56 | 3.9 | 0 | 18.9 |
| 100 | 11.134 | 100.04 | 24.99 | 0 | 99.17 | 100.09 | 37 | 56.4 | 4 | 0 | 19.4 |
| 200 | 11.135 | 100.05 | 24.46 | 0 | 99.19 | 100.11 | 36.7 | 57.6 | 5.9 | 0 | 20.9 |
| 300 | 11.136 | 100.06 | 24.62 | 0 | 99.21 | 100.13 | 36.5 | 57.7 | 6.2 | 0 | 21.2 |
| 400 | 11.147 | 100.16 | 23.91 | 0 | 99.40 | 100.32 | 36.5 | 58.9 | 7.4 | 0 | 22.4 |
| 500 | 11.150 | 100.19 | 23.88 | 0 | 99.46 | 100.38 | 36 | 59.5 | 8.5 | 0 | 23.5 |
| 600 | 11.163 | 100.31 | 23.33 | 0 | 99.69 | 100.62 | 35 | 60 | 10 | 0 | 25 |
| 700 | 11.167 | 100.34 | 23.11 | 1.46 | 99.76 | 100.69 | 35 | 0.9 | 10.9 | 0 | 25.9 |
| 800 | 11.197 | 100.61 | 22.91 | 2.68 | 100.30 | 101.23 | 34.5 | 1.7 | 12.2 | 0 | 27.2 |
| 900 | 11.206 | 100.69 | 23.05 | 3.89 | 100.46 | 101.39 | 34.5 | 2.9 | 13.4 | 0 | 28.4 |
| 1000 | 11.259 | 101.17 | 22.51 | 4.43 | 101.41 | 102.35 | 34.2 | 3.7 | 14.5 | 0 | 29.5 |
| 1100 | 11.348 | 101.98 | 23.02 | 5.69 | 103.02 | 103.98 | 34.2 | 5.1 | 15.9 | 0.9 | 30.9 |
| 1200 | 11.380 | 102.26 | 22.57 | 6.53 | 103.60 | 104.56 | 33.7 | 6.4 | 17.7 | 2.7 | 32.7 |
| 1300 | 11.451 | 102.89 | 22.50 | 7.08 | 104.90 | 105.87 | 33.4 | 7.5 | 19.1 | 4.1 | 34.1 |
| 1400 | 11.544 | 103.73 | 22.96 | 7.77 | 106.61 | 107.60 | 33.4 | 8.6 | 20.2 | 5.2 | 35.2 |
| 1500 | 11.608 | 104.30 | 22.76 | 7.89 | 107.80 | 108.8 | 32.9 | 9.6 | 21.7 | 6.7 | 36.7 |

4.8 Application of GA optimal profiles in an SRM control scheme

With the results set provided by the GA, an offline control scheme which can provide speed and linear torque control of the SRM can be created. As a control scheme, the current profiles can be stored in a 3D LUT relating inputs T_{ref} reference speed ω_{ref} , reference torque T_{ref} and rotor angle θ to the output of reference current I_{ref} . This LUT is shown in Fig 4.46, highlighting the structure

of every profile at FLT as speed increases, where the trend of increasing conduction period and the generalised form of the profiles are visualised. The LUT is placed within the control scheme shown in Fig 4.47, where using the speed obtained from the encoder a speed error, ω_{err} is generated which corresponds to T_{ref} , after being fed through a PI controller. In terms of tuning, the PI controller in the scheme is tuned to provide a stable overdamped response which is able to control the machine. Dependent on the controller tuning, the overall control of the SRMs torque can be affected. If overtuned to the point of instability when tracking a steady state, the PI controller may cause irregular spikes in torque production as it oscillates around the reference due to the excessive control response. The scheme is therefore tuned to avoid any interference of the PI

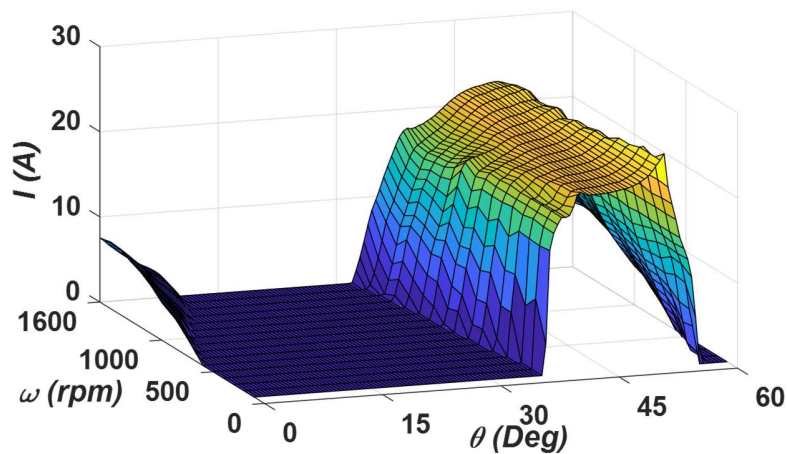


Fig 4.46 GA produced profiles from 0 to 1500rpm

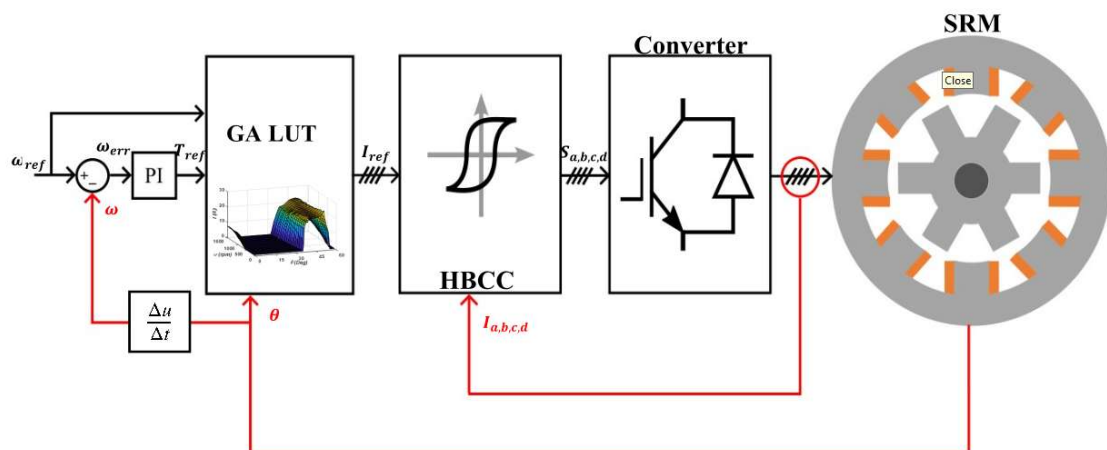
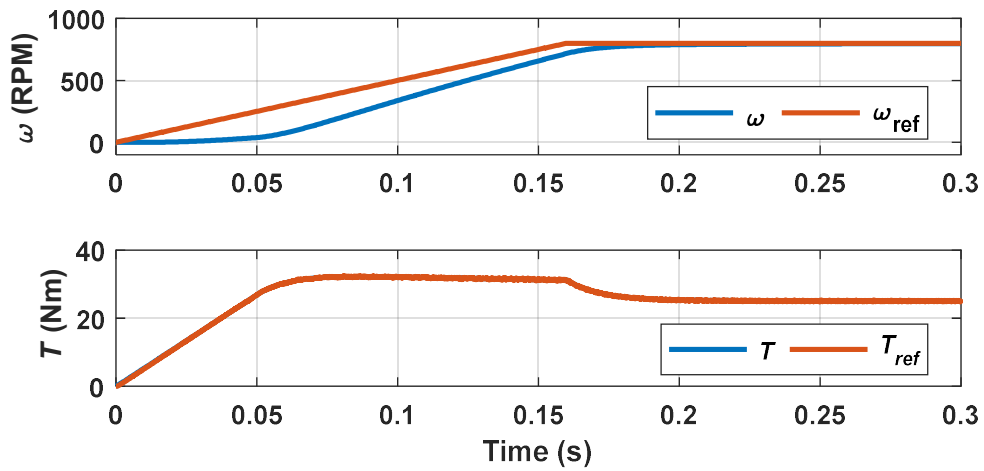


Fig 4.47 GA current profiling linear control scheme

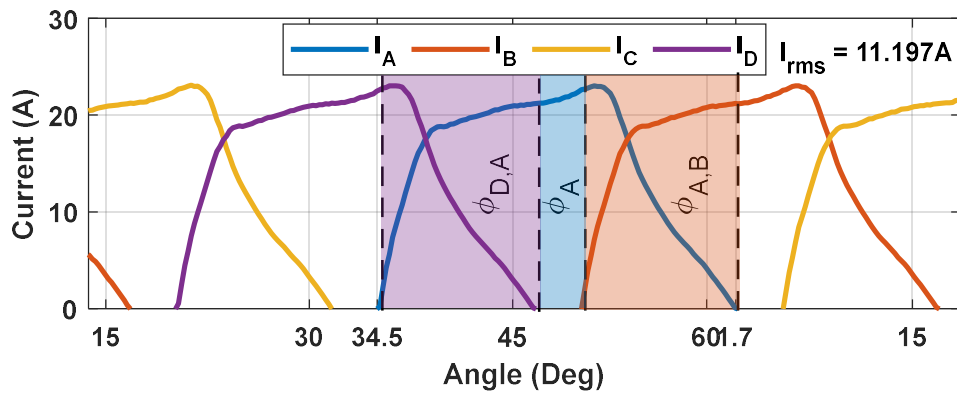
controller with the SRM bar its purposes of being able to track the speed reference correctly. The variables T_{ref} , ω_{ref} and θ , also obtained from the encoder, are then fed to the GA LUT from the PI controller, which in turn produces the respective I_{ref} for each phase. This LUT linearises the torque production of the machine, inherently eliminating commutation TR and allowing discrete torque values to be generated based upon speed requirements. To generate switching signals for the converter, I_{ref} is then fed to a hysteresis band current controller (HBCC), where the hysteresis bands size and resultant tracking is a trade-off between a small band, which will decrease tracking error and therefore any possible commutation torque error but will increase switching frequency and therefore switching TR. The opposite is then true for a large band, which is low frequency and therefore low switching TR, but likely will result in a larger tracking error and commutation TR. For this scheme, to demonstrate the elimination of commutation TR, a relatively narrow band is chosen, but in further application, this would be reconsidered. From this, the HBCC will proceed to generate and feed switching signals to an ASHB drive converter with individual bridge legs as shown in Fig 2.15.

This is required due the use of three phase overlap in the given four phase, 8/6 SRM configuration, where to prevent potential mutual conduction of a single switching device, the no shared switch configuration of the ASHB can be utilised. Using MATLAB/SIMULINK, the control scheme is implemented with a sampling time of $1\mu s$.

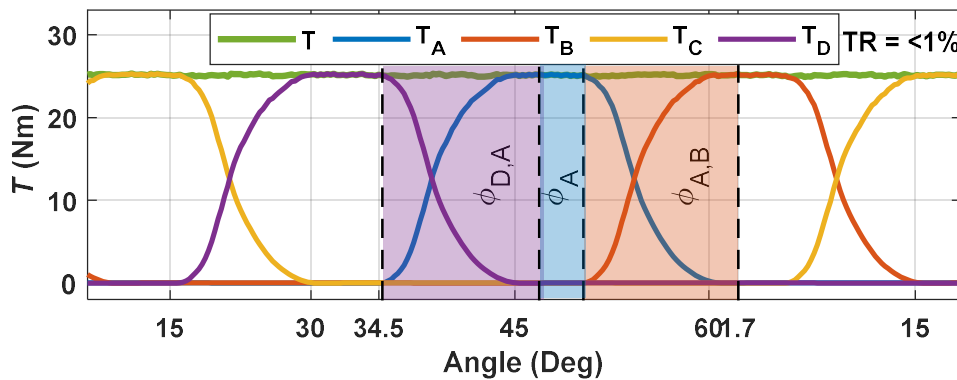
Fig 4.48 shows the simulated response for 0.3 seconds simulation time of the control scheme in the two-phase operation region of 800rpm at FLT, with a linear acceleration using a V_{DC} of 415V. The scheme demonstrates the ability to reliably accelerate from startup in Fig 4.48a) with no commutation TR, where the LUT does not utilise any form of advanced interpolation methods and contains data for only the FLT, 0.75, 0.5, and 0.25 FLT levels for efficient memory usage. Once at 800rpm, the control scheme operates in steady state, where the shape of the current waveforms produced in in Section 4.5 can be seen in Fig 4.48b). The waveforms are accurately reproduced from the stored profile within the given V_{DC} , where overlapping phases are highlighted in their respective colours, showing the transition to full two-phase overlap as speed increases. Fig 4.48c) illustrates the torque waveforms at steady state, where commutation TR is completely eliminated and a torque just above FLT is produced to compensate for frictional losses.



(a)



(b)



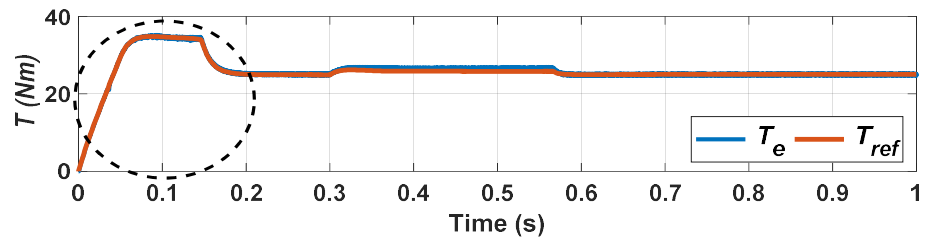
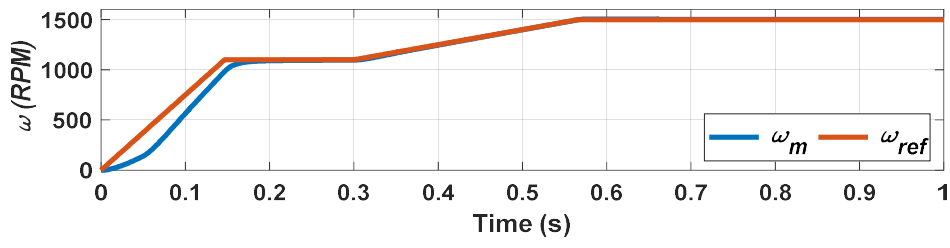
(c)

Fig 4.48 Results of control scheme in two-phase overlap regions at 800 rpm:
 (a) Speed and torque responses, (b) Steady state currents, and (c) Total and phase torques

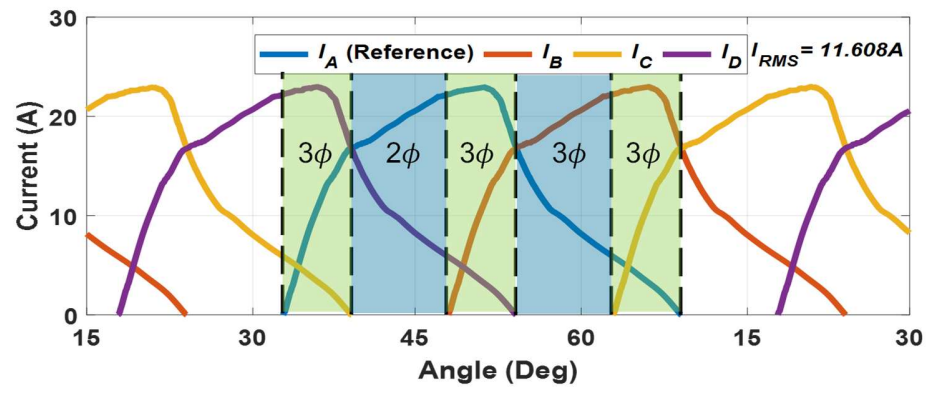
Fig 4.49 presents the operation of the SRM within the three phase speed region of the machine. Fig 4.49a) shows the SRMs speed response over one second, first accelerating from 0 to 1100 rpm,

reaching steady state operation, and proceeding to then accelerate to the maximum power operating point at 1500rpm with FLT loading. The proposed scheme's speed control performance is demonstrated to its full capabilities, controlling the SRM across its speed range using the GA current profiles, also without notable TR during dynamic portions of the SRMs response (and near ZTR during steady state periods).

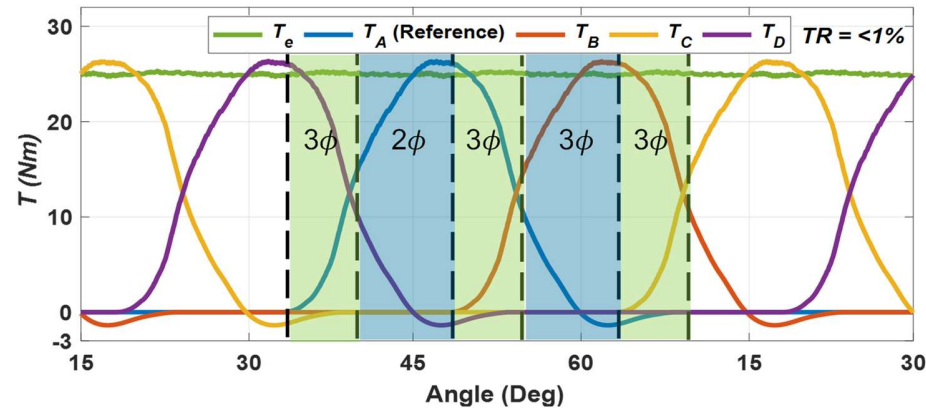
Shown in Fig 4.49 parts b) and c) are the steady state current and torque waveforms respectively for the SRM operating at 1500rpm and FLT from 0.6 to 1 seconds in Fig 4.49a). Phase A is taken as a reference in this case for the rotor position where the profile has a realised θ_{cond} of 36° in Fig 4.49b), displaying a significant $\theta_{ov(3\phi)}$ of 6° . ZTR is maintained at this speed and overlap, where Fig 4.49c) shows a resultant TR of less than 1% of the FLT value. This is while also producing a peak negative torque value of -1.45Nm approaching θ_{off} , requiring a peak two-phase positive torque production of 26.45Nm.



(a)



(b)



(c)

Fig 4.49 Results of SRM Drive: (a) Speed and torque, and 1500rpm steady state, (b) Currents and (c) Torques

The waveform rms current values are again maintained at the value established in Fig 4.40, accomplishing the objectives of ZTR and minimal rms currents below the SRMs rating, where it shown that while maintaining these two, the profiles are produced within the V_{DC} limits that have been outlined.

The control scheme is operated again in Fig 4.51, but now, the SRM is accelerated to peak power, and two different torque steps are applied in Fig 4.51a). Firstly, a negative torque step is applied to reduce the load torque to 10Nm from 25Nm, a positive step is then applied to bring the SRM above peak power to 1500rpm, 27.5Nm. During both steps, the control scheme exhibits the ability to stably recover speed with the torque loading, while still maintaining no commutation torque

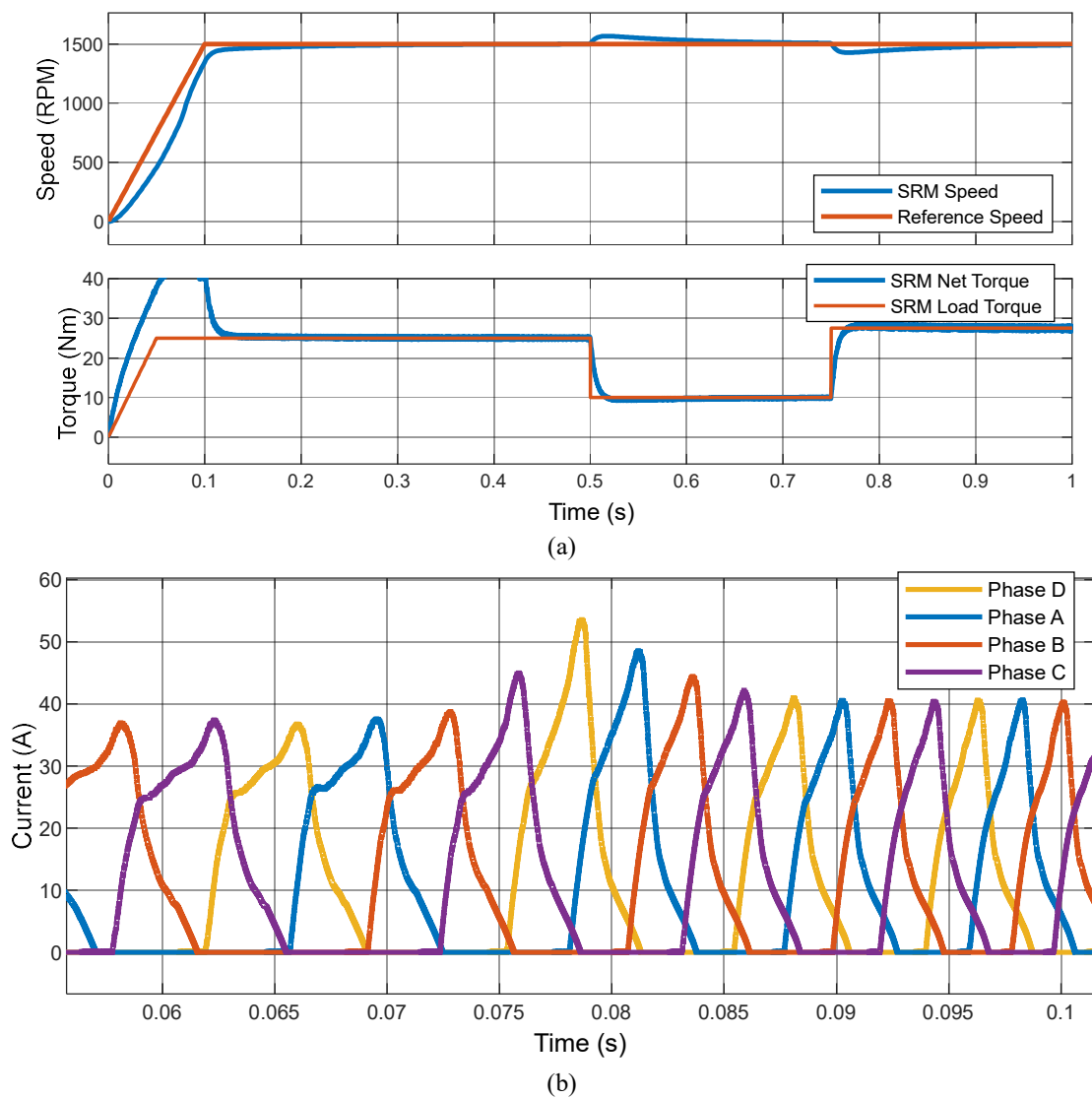


Fig 4.50 Results of SRM Drive (a) with torque steps and (b) with two to three phase overlap transition highlighted

ripple. Examining the acceleration further, the point at which the control scheme transfers from two, to three phase overlap can also be observed in Fig 4.51b). This can be seen firstly on the left hand side of the plot, where the waveforms are producing much greater than 25Nm torque but are still in the area of operational 2 phase conduction. Following the plot with time at 0.08 seconds, it can be seen at the tail end of each phases waveform, a gradual three phase overlap begins to occur, until at the end of the figure at 0.1 seconds, a notable three phase overlap is occurring due to the machine being well above the two phase conduction boundary of 1080rpm. This highlights the aforementioned features of the control scheme, along with demonstrating its full dynamic capabilities in operation as a control scheme.

Revisiting the Cosine TSF from Section 2 and Section 4.5, it is simulated again, but with a steady state speed of 1500rpm and FLT in Fig 4.50. It can be seen here that the rms current of the TSF is notably higher than the GA at this speed, being 110.6% (122.35% P_{Cu}) of $I_{rmsOptimal}$, compared

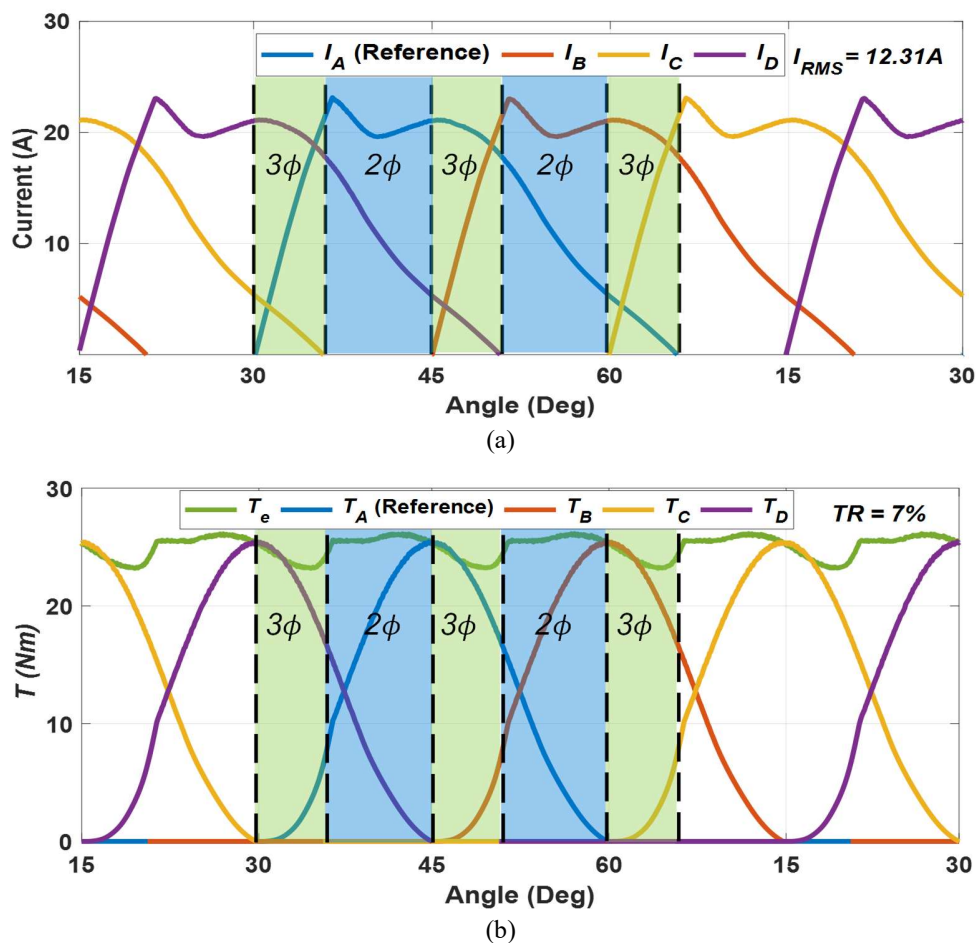


Fig 4.51 Results of Cos TSF at 1500rpm: (a) Currents and (b) Torques.

to the GAs 104.3%. Notably, the rms current of the Cosine TSF is lower than when it is operated at 1000rpm, where it is 111.99% of $I_{rmsOptimal}$. This likely due to the torque production at 1500rpm, where significantly more TR is present being 7% compared to 3.2% at 1000rpm, where the GA produces <1% at both of these speeds. By having significantly increased TR, the net torque production of the TSF is inherently lower when comparing to the same function at a lower speed with the same switching angles and other characteristics, meaning it would have a lower rms current accompanying it. Comparing the torque waveforms in Fig 4.49c) and Fig 4.50b), it can be seen that the GA demonstrates firstly the ability to delay θ_{on} and utilise negative torque production to decrease rms current, and secondly intentionally use three phase overlap to maintain ZTR with the given V_{DC} . The TSF in both cases does not do this, where firstly rms current is increased by not utilising the optimal torque production regions for high Nm/A efficiency, which can be seen with the excessive currents before 40° . Secondly, the TSF suffers from commutation TR in the three phase overlap region, where it cannot effectively compensate for the third phase and produce FLT. While the proposed controller has been shown to outperform the Cosine TSF, many more advanced control schemes have been proposed for the SRM which aim to reduce or eliminate commutation TR which may also seek to reduce RMS current, peak current, or extend speed range. These can be compared, on these factors and can also be compared using the benchmark current established in Section 4.3. Table 4.5 presents a comparison between the GA based control scheme and five control schemes proposed in recent literature [4-18]-[4-22]. Examining the contents of Table IV, recent publications include adaptations of TSFs [25][29], DTC [26], model predictive control [27] or hysteresis control [28]. References [25] and [29] demonstrate the full speed range capability of their control schemes where [25] reduces TR compared to other DTCs and [29] lowers TR greatly. The other schemes do not present results at SRM rated speed. This does not mean that the control cannot function at this speed and all schemes do reduce TR comparatively to similar methods but do not eliminate it. The main goal of the GA is the absolute minimisation of the rms current across a given SRMs operational torque and speed range. Notably, the GA at peak power operates at lower than the machines rated rms and peak current, at 92.8% and 91% respectively. The closest comparison in terms of a percentage of rated power is [26] which exhibits 49.9% of rated rms current and 60% peak current at 50% rated power. Reference [29] presents

operation of an improved TSF function above the machines rated power of 120.8% but does not provide the machine rated currents they use to provide a percentage usage for comparison.

Table 4.5 Performance Comparison of Recent SRM Publications

| | GA | [25] | [26] | [27] | [28] | [29] |
|---------------------------------------|--------------|--------------|-------------|-------------|-----------------------|--------------|
| Control | T | I | T, ψ | T | T | T |
| Parameter | | | | | | |
| SRM Config. Used | 8/6 | 12/8 | 8/6 | 12/8 | 12/8 | 8/6 |
| Zero TR Speed | $\geq 100\%$ | $\geq 100\%$ | $\geq 53\%$ | $\geq 50\%$ | $\geq 1000\text{rpm}$ | $\geq 100\%$ |
| Range | @<1%TR | @<56.6% | @<13.5% | @<18.7% | @<8.7% TR | @<9.5% |
| (%ω_{rated}) | | TR | TR | TR | | TR |
| RMS Current | | | | | | |
| (%I_{rated}) | 92.8% | 63.1% | 49.9% | N/A | N/A | 15.22A |
| (%P_{rated}) | 100% | 38.1% | 50.4% | | | 120.8% |
| Peak Current | | | | | | |
| (%$I_{pk rated}$) | 91% | 73.4% | 60% | ~19A | N/A | ~34A |
| (%P_{rated}) | 100% | 38.1% | 50.4% | 10.5% | | 120.8% |
| Online/Offline | Offline | Online | Online | Online | Online | Offline |

Fig 4.52 presents the updated operational torque speed of the 8/6 SRM, including both the three phase, and two-phase variations of the GA profiling method. Using current profiling envelopes, it can be confirmed that using three phase overlap, current profiles are possible at the rated constant power speeds of 2000rpm at 0.75FLT and 2990rpm at 0.5FLT. As speed becomes significantly higher and torque decreases, four phase conduction could be considered if three phase conduction can no longer suffice. Compared to the two-phase overlap, the GA utilising three phase overlap allows the full capability of the SRM to be harnessed while maintaining ZTR operation.

As it relates to this high speed operation, an example application of the SRM in applications such as EVs, where maximum speed operation may occur at in excess of three times base speed. This means that with constant speed cruising, which requires torque proportional to speed, squared, far less than FLT is required. Figure 4.52 shows that the ZTR speed limit increases significantly with reducing torques and therefore torques close to the rated values at the given speeds are likely not

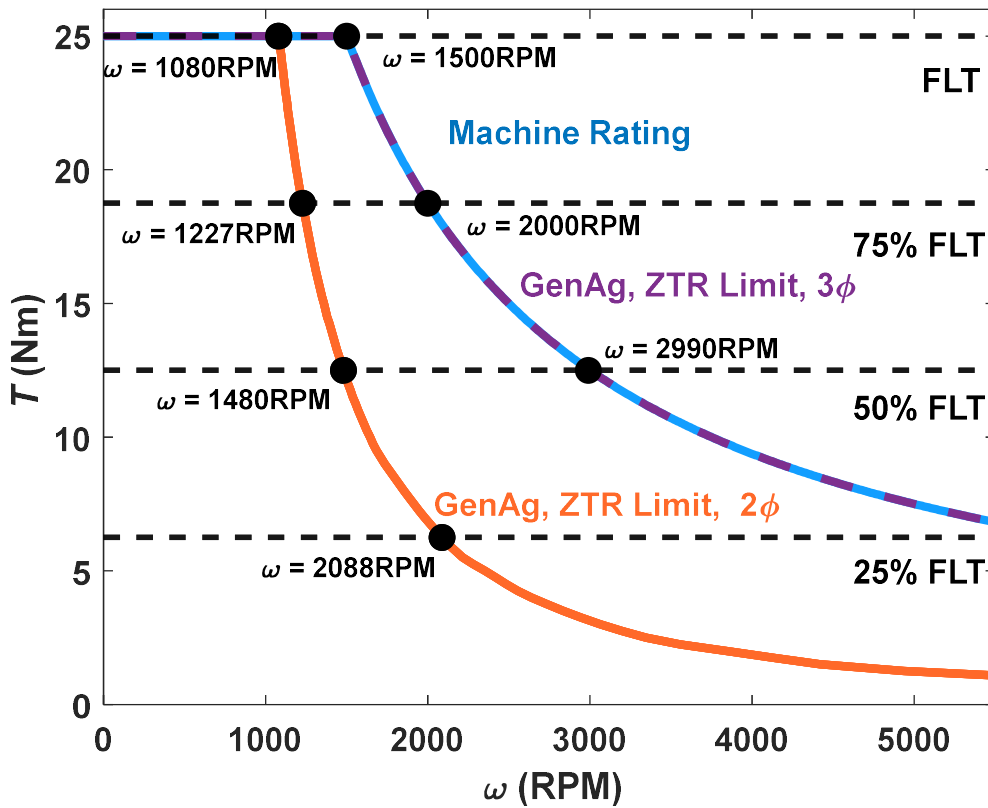


Fig 4. 52 GA ZTR speed range and machine $T-\omega$ curve.

required or are well within the established two-phase and three phase overlap limits. Higher torque in excess of this cruising requirement is available for acceleration (non-steady state, where defining and quantifying TR is problematic), hill climbing, towing, etc. Additionally, with the use of DC link voltage boosting with the converter topology in Fig 3.3, base speed can be extended (hence machine power rating), along with the ZTR speed range for both two and three-phase conduction across all torque levels in conjunction with the proposed control scheme [17].

4.9 Summary

A method for finding the theoretically (FEA based) lowest possible rms current for any given torque value in an SRM is proposed and implemented as a benchmark for any control scheme seeking to evaluate produced rms currents in the machine. From this, a new method of torque control is proposed and investigated based upon the use of novel intentional multiphase (two-phase and greater than two phases) overlap. It is deployed in a genetic algorithm based current profiling

design which also utilises delayed turn on and consequentially negative torque production to deliver current profiles which are optimised for minimal rms currents, zero commutation torque ripple and applicable across the machines full rated speed range.

References

- [4-1] G. Fang, F. P. Scalcon, D. Xiao, R. P. Vieira, H. A. Gründling and A. Emadi, "Advanced Control of Switched Reluctance Motors (SRMs): A Review on Current Regulation, Torque Control and Vibration Suppression," in *IEEE Open Journal of the Industrial Electronics Society*, vol. 2, pp. 280-301, 2021,
- [4-2] N. Yan, X. Cao and Z. Deng, "Direct Torque Control for Switched Reluctance Motor to Obtain High Torque–Ampere Ratio," in *IEEE Transactions on Industrial Electronics*, vol. 66, no. 7, pp. 5144-5152, July 2019,
- [4-3] X. Sun, J. Wu, G. Lei, Y. Guo and J. Zhu, "Torque Ripple Reduction of SRM Drive Using Improved Direct Torque Control With Sliding Mode Controller and Observer," in *IEEE Transactions on Industrial Electronics*, vol. 68, no. 10, pp. 9334-9345, Oct. 2021,
- [4-4] Q. Sun, J. Wu and C. Gan, "Optimized Direct Instantaneous Torque Control for SRMs With Efficiency Improvement," in *IEEE Transactions on Industrial Electronics*, vol. 68, no. 3, pp. 2072-2082, March 2021,
- [4-5] D. Ronanki, K. R. Pittam, A. Dekka, P. Perumal and A. R. Beig, "Phase Current Reconstruction Method With an Improved Direct Torque Control of SRM Drive for Electric Transportation Applications," in *IEEE Transactions on Industry Applications*, vol. 58, no. 6, pp. 7648-7657, Nov.-Dec. 2022
- [4-6] M. V. de Paula and T. A. d. S. Barros, "A Sliding Mode DITC Cruise Control for SRM With Steepest Descent Minimum Torque Ripple Point Tracking," in *IEEE Transactions on Industrial Electronics*, vol. 69, no. 1, pp. 151-159, Jan. 2022,
- [4-7] M. Ma, Q. Yang, X. Zhang, F. Li, and Z. Lin, "A switched reluctance motor torque ripple reduction strategy with deadbeat current control," in *Proc. 14th IEEE Conf. Ind. Electron. Appl.*, 2019, pp. 25–30.
- [4-8] S. Song, J. Liu, Y. Zhao, L. Ge, R. Ma and W. Liu, "High-Dynamic Four-Quadrant Speed Adjustment of Switched Reluctance Machine With Torque Predictive Control," in *IEEE Transactions on Industrial Electronics*, vol. 69, no. 8, pp. 7733-7743, Aug. 2022,

- [4-9] H. Li, B. Bilgin and A. Emadi, "An Improved Torque Sharing Function for Torque Ripple Reduction in Switched Reluctance Machines," in *IEEE Transactions on Power Electronics*, vol. 34, no. 2, pp. 1635-1644, Feb. 2019,
- [4-10] A. K. Rana and A. V. R. Teja, "A Mathematical Torque Ripple Minimization Technique Based on a Nonlinear Modulating Factor for Switched Reluctance Motor Drives," in *IEEE Transactions on Industrial Electronics*, vol. 69, no. 2, pp. 1356-1366, Feb. 2022,
- [4-11] S. Song, G. Fang, R. Hei, J. Jiang, R. Ma and W. Liu, "Torque Ripple and Efficiency Online Optimization of Switched Reluctance Machine Based on Torque per Ampere Characteristics," in *IEEE Transactions on Power Electronics*, vol. 35, no. 9, pp. 9608-9616, Sept. 2020,
- [4-12] J. Ye, B. Bilgin and A. Emadi, "An Extended-Speed Low-Ripple Torque Control of Switched Reluctance Motor Drives," in *IEEE Transactions on Power Electronics*, vol. 30, no. 3, pp. 1457-1470, March 2015,
- [4-13] R. Abraham and S. Ashok, "Data-Driven Optimization of Torque Distribution Function for Torque Ripple Minimization of Switched Reluctance Motor," *2020 International Conference for Emerging Technology (INCET)*, Belgaum, India, 2020,
- [4-14] S. Song, R. Hei, R. Ma and W. Liu, "Model Predictive Control of Switched Reluctance Starter/Generator With Torque Sharing and Compensation," in *IEEE Transactions on Transportation Electrification*, vol. 6, no. 4, pp. 1519-1527, Dec. 2020,
- [4-15] L. Feng, X. Sun, X. Tian and K. Diao, "Direct Torque Control With Variable Flux for an SRM Based on Hybrid Optimization Algorithm," in *IEEE Transactions on Power Electronics*, vol. 37, no. 6, pp. 6688-6697, June 2022,
- [4-16] M. Mansouri Borujeni, A. Rashidi and S. M. Saghaeian Nejad, "Optimal four quadrant speed control of switched reluctance motor with torque ripple reduction based on EM-MOPSO," *The 6th Power Electronics, Drive Systems & Technologies Conference (PEDSTC2015)*, Tehran, Iran, 2015,
- [4-17] A. Abdel-Aziz, K. H. Ahmed, S. Wang, A. M. Massoud, and B. W. Williams, "A novel neutral point diode clamped converter with inherent voltage-boosting for a four-phase SRM drive," in *IEEE Transactions on Industrial Electronics*, vol. 67, no. 7, pp. 5313-5324, Jul. 2020.

- [4-18] Z. Xia, B. Bilgin, S. Nalakath and A. Emadi, "A New Torque Sharing Function Method for Switched Reluctance Machines With Lower Current Tracking Error," in *IEEE Transactions on Industrial Electronics*, vol. 68, no. 11, pp. 10612-10622, Nov. 2021.
- [4-19] D. Ronanki, K. R. Pittam, A. Dekka, P. Perumal and A. R. Beig, "Phase Current Reconstruction Method With an Improved Direct Torque Control of SRM Drive for Electric Transportation Applications," in *IEEE Transactions on Industry Applications*, vol. 58, no. 6, pp. 7648-7657, Nov.-Dec. 2022.
- [4-20] S. Song, J. Liu, Y. Zhao, L. Ge, R. Ma and W. Liu, "High-Dynamic Four-Quadrant Speed Adjustment of Switched Reluctance Machine With Torque Predictive Control," in *IEEE Transactions on Industrial Electronics*, vol. 69, no. 8, pp. 7733-7743, Aug. 2022,
- [4-21] S. Song, G. Fang, R. Hei, J. Jiang, R. Ma and W. Liu, "Torque Ripple and Efficiency Online Optimization of Switched Reluctance Machine Based on Torque per Ampere Characteristics," in *IEEE Transactions on Power Electronics*, vol. 35, no. 9, pp. 9608-9616, Sept. 2020,
- [4-22] H. Li, B. Bilgin and A. Emadi, "An Improved Torque Sharing Function for Torque Ripple Reduction in Switched Reluctance Machines," in *IEEE Transactions on Power Electronics*, vol. 34, no. 2, pp. 1635-1644, Feb. 2019
- [4-23]
- [4-24]

Chapter 5

Electronic Machine Emulation for Inverters with Sensorless Position

Control

This Chapter discusses the basic structure of electrical machine emulators and their operating principles. This includes hardware and software features, along with the modelling of PMSMs that are emulated by the testbench. A novel power electronics based emulator testbench is then proposed. The testbench is aimed for use in the verification of commercial drives, and is therefore designed with cost, efficiency, ease of use and fabrication as the main factors. The testbench concept is simulated using MATLAB/SIMULINK and then confirmed experimentally, with results being compared with a dynamometer testbench.

5.1 Introduction

In the electrical drive system design process, many methods exist for varying levels of verification of the drive inverter. With recent trends in the electrification of society, mainly transportation [5-2], [5-3] and the widespread adoption of renewables [5-4], the demand for differing specifications of machine topologies such as the PMSM, IM and SRM have all increased in demand. Due to this demand, the desire for a streamlined, full power verification testing process of the inverter component which can also emulate the mission profile of the machines application, is desired. Traditionally, drive inverter and electrical machine full power verification has been carried out using a dyno testbench which can be seen in Fig 5.1. This testbench consists of the full drive system connected to a load machine at the rotor shaft, which generates a load torque to operate the drive. These setups are expensive, time consuming, mechanically complex and difficult to construct and use. Along with this, they also tend to be specific to the drive systems inertia for the intended application, making them inflexible due to the difficulty in reconfiguring the testbench, while also being limited in the dynamism of the load behaviour that can be performed.

Due to these factors, there is an interest in alternative forms of verification which can provide comparable results to a dyno. PHiL verification, also referred to as PEBE, has received significant levels of interest as an alternative to Dynos compared other verification methods such as model, software or hardware-in-the-loop, which lack the full power component of testing [5-5].

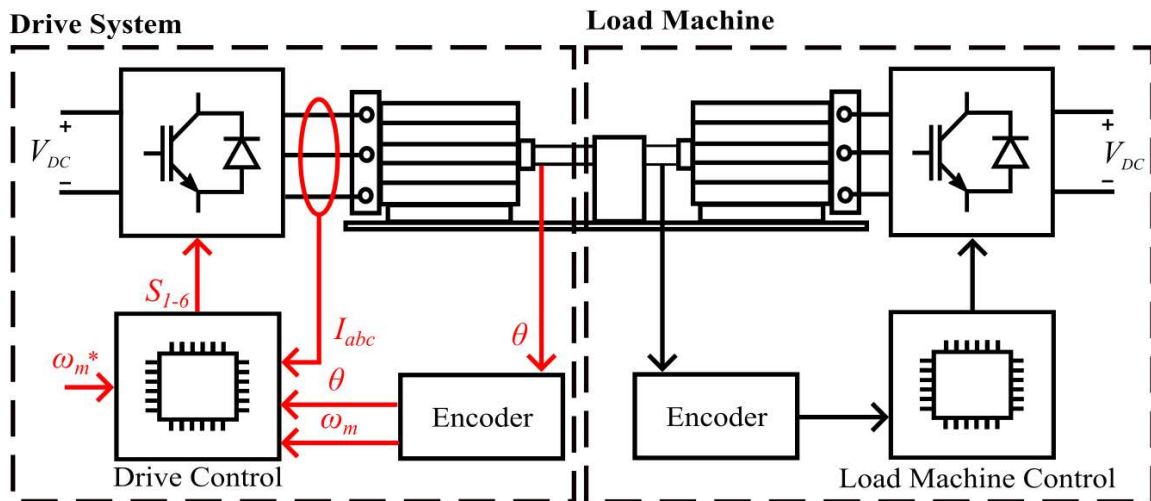


Fig 5.1 Dynamometer testbench

5.2 Drive inverter verification methods

5.2.1 Model based methods

Before any hardware is introduced, some level of verification of drive inverter design and control can be carried out virtually. These methods can be referred to as model-in-the-loop and software-in-the-loop. As a part of any design process, it is almost guaranteed that model-in-the-loop is implemented. Both methods first involve the use of a virtual plant model, which can be contained on the host PC. The plant model contains the dynamics of the system, which in the case of the drive, will be the modelled converter and electrical machine. Model-in-the-loop uses a modelled controller to control the plant model, which will mirror the control to be utilised in the real drive but will not include the code that would be utilised in the drive. At this point, software-in-the-loop can be implemented, by code generation from the model, which will provide some evidence at the simulation stage if the controller is feasible from the software perspective. It involves running the same virtual plant model but instead with the aforementioned code version of the controller, which can be generated from the model or manually coded. These both in conjunction or just model-in-the-loop can be useful in the early stages of the drive design process and can be considered

separately from other verification methodologies as they aim at only a certain level of testing which does not involve any hardware.

5.2.2 Processor-in-the-loop and Hardware-in-the-loop

The next level of verification involves the introduction of hardware, in the form of the control unit used in the actual commercial drive. This can be a microcontroller or FPGA, where the device is connected typically via communication bus to the Host PC, while being programmed with the controller code. The virtual plant model is then ran again, but this time with the physical control unit present in the loop. It allows the introduction of the dynamics of the control unit, mainly its processing times and limitations in software such as a lack of parallel processing dependent on the device. To fully implement the electrical control dynamics that is experienced by the controller connected to the wider electrical system, HiL is then implemented. HiL verification is a well-established concept for high power applications [5-6] - [5-9], for the testing of converter and drive control, also being applied to lower power electrical drives [5-7]. . An example of a HiL setup is illustrated in Fig 5.2, where the controller, programmed with the machine control software, is typically connected to a real time simulator unit and fed equivalent control signals of phase and machine measurements. The controller then proceeds to output PWM control signals, which are then converted and fed back to the RTS as reference commands in a control loop. Internally within the RTS, the machine equivalent network model is programmed in a real plant model. This allows further verification of control behaviour in the machine controller, with flexibility in the behaviour that can be emulated, and introduces control delays experienced when using of ADC circuitry that will be present in the real drive when converting phase measurements and propagating control

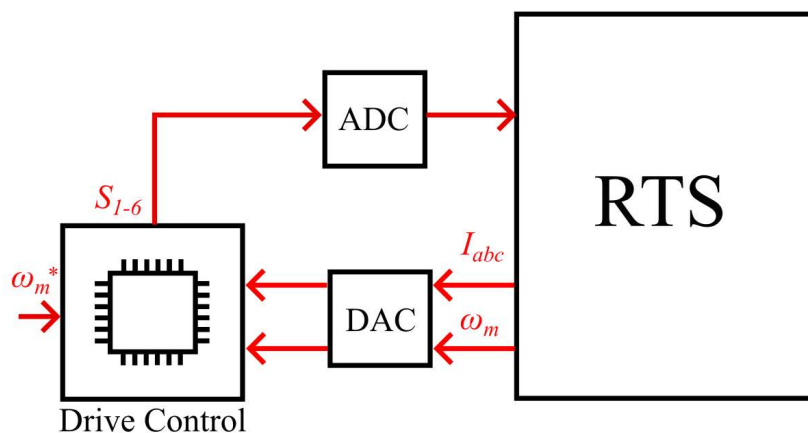


Fig 5.2 HiL testbench

signals. The main limitation with this method is the lack of any form of power in the inverter phases, which means only partial verification of the inverter control can only ever be performed.

5.2.3 Power-hardware-in-the-loop

PHiL refers to an advancement on HiL, where the power stage is introduced into the testbench, and the full drive inverter hardware is utilised. The concept involves the mimicking of the electrical response and mechanical measurements of a machine, taking the form of the electrical BEMF and rotor angle θ respectively. These can be generated through two differing configurations of testbench. The first of these, illustrated in Fig 5.3, is implemented by utilising a power amplifier connected to the drive inverter which generates the BEMF [5-10]-[5-12]. In this configuration, phase measurements are taken and fed to an RTS unit, which then proceeds to feed the reference BEMF value to the power amplifier. The other configuration which can be utilised is where instead of a power amplifier, power electronics are used to generate the BEMF, mutually connecting the drive inverter to another inverter at their phase outputs [5-13]-[5-15]. This configuration is illustrated in Fig 5.4, where phase measurements are taken at the output of the BEMF emulating inverter (EMU) and fed to a control unit, commonly being an RTS. Programmed onto the control unit is an equivalent mechanical model for the electrical machine that the drive inverter is intended

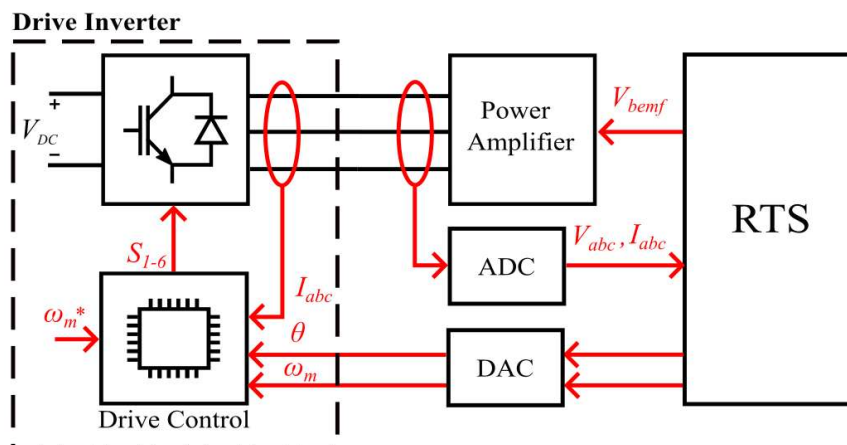


Fig 5.3 Power amplifier based PHiL testbench

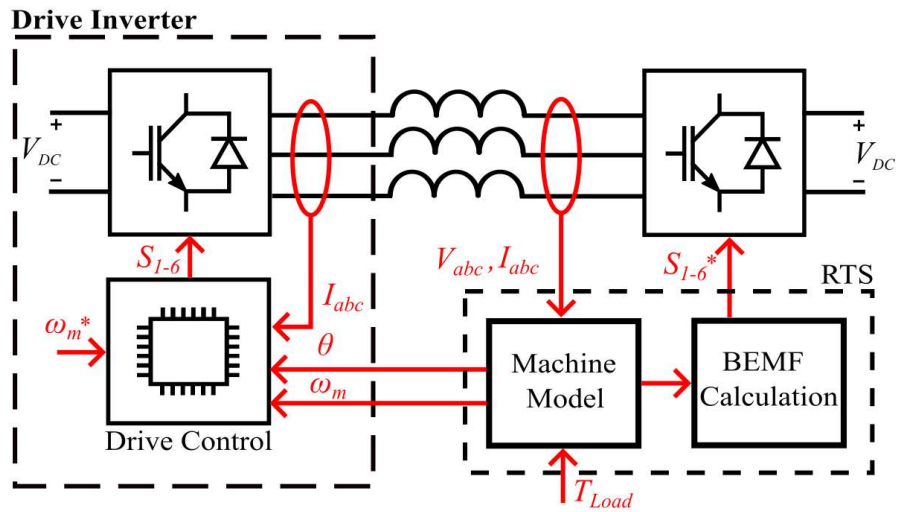


Fig 5.4 Power electronics based PHiL testbench

for. This produces the mechanical values of θ and the machines mechanical speed ω_m , which are then fed to the drive inverter and the machine electrical model which then produces the reference BEMF. Both the power amplifier and the power electronics based (PEB) testbench are capable of carrying out full power testing with detailed electrical characteristics [5-5]. The main difference that can be drawn between the two is the control unit, where the power amplifier based testbench requires some form of RTS to function. The PEB testbench in theory does not require this, instead being possible to use on board controller units such as microcontrollers or field programmable gate arrays (FPGAs) to operate the EMU. This means that the main benefits to would be a significantly reduced cost and removal of the control delays introduced by an RTS.

5.3 Power electronics based emulator testbenches

While Fig 5.4 illustrates an example of a PEBE, variations can be made in hardware and software which can affect the performance of the testbench, and also other factors such as cost, size and efficiency.

5.3.1 Inverter coupling

Differing from the power amplifier based testbench, it can be seen that there is a form of coupling between the inverters in a PEB testbench. This coupling is required for filtering purposes between the inverter and can vary in its components. The most common coupling choice is an inductive L filter [5-13] - [5-16]. Other choices include the use of LC filters [5-17],[5-18], and LCL [5-19]

filters which are both shown in Fig 5.5 parts a) and b) respectively. These two filtering arrangements provide suppression of high frequency harmonic components produced by the mutual connection of the two switching arrangements of the inverters but can affect the higher frequency response of the emulated machine and limit bandwidth. A purely inductive filter instead can provide a sufficient filtering performance without adverse effects to the emulator bandwidth, but this is also dependent on the chosen value of inductance relative to the characteristics of the emulated machine, as investigated in [5-20].

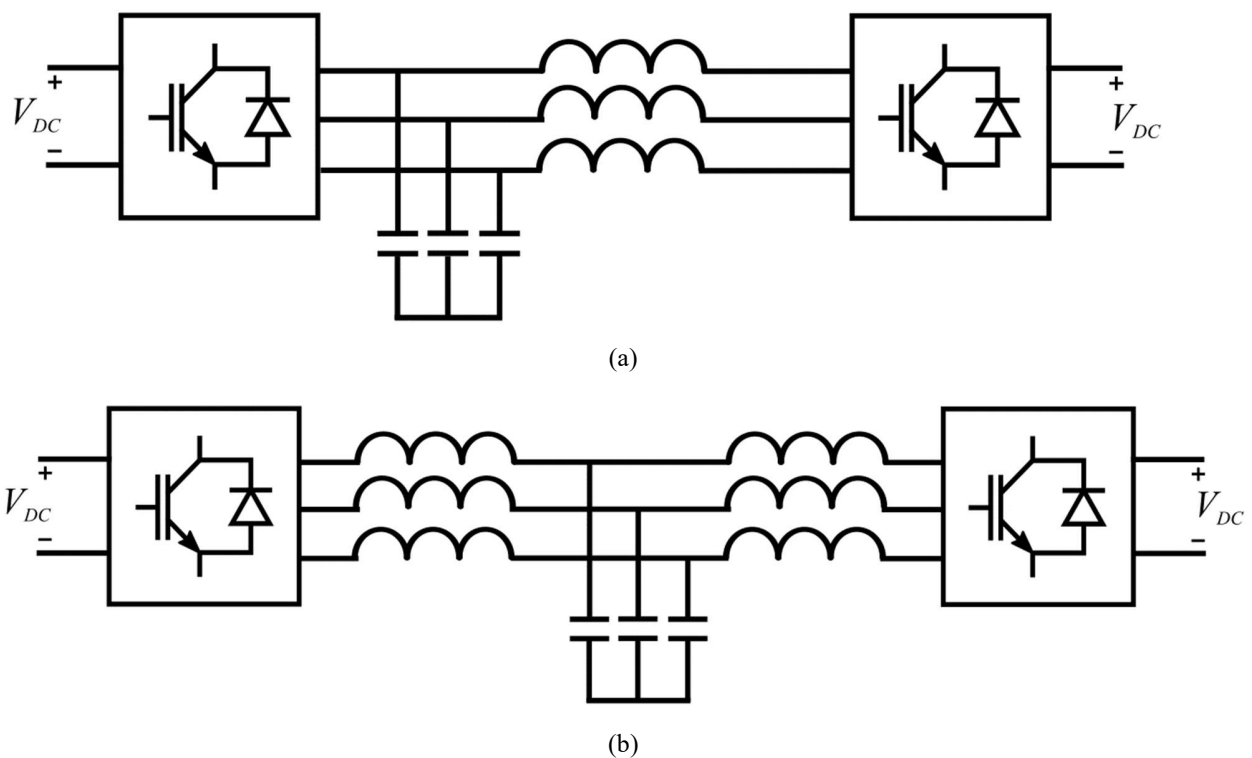


Fig 5.5 PEB testbench filtering arrangements (a) LC and (b) LCL

5.3.2 Power supply

The power supply arrangement of the testbench can factor heavily as it relates to the cost and efficiency of the testbench. In Fig 5.6a), two separate DC sources are shown, where each inverter is powered by its own independent supply. This means that power will flow through the system in one direction and exit through the other source. The alternative to this is mutually connecting the DC inputs of the inverters together, allowing them to effectively share one DC supply as shown in

Fig 5.6b). This allows one of the supplies to be removed, providing a significant cost saving. Along with this, power is now available to be recycled within the system which provides an increase in efficiency as the supply now only needs to supply the systems losses. The downside to this is that with the connection of the DC inputs, a low impedance circulating current path is formed, which introduces a varying degree of zero sequence current dependent on the characteristics of the testbench to the emulator phases [5-5], [5-14].

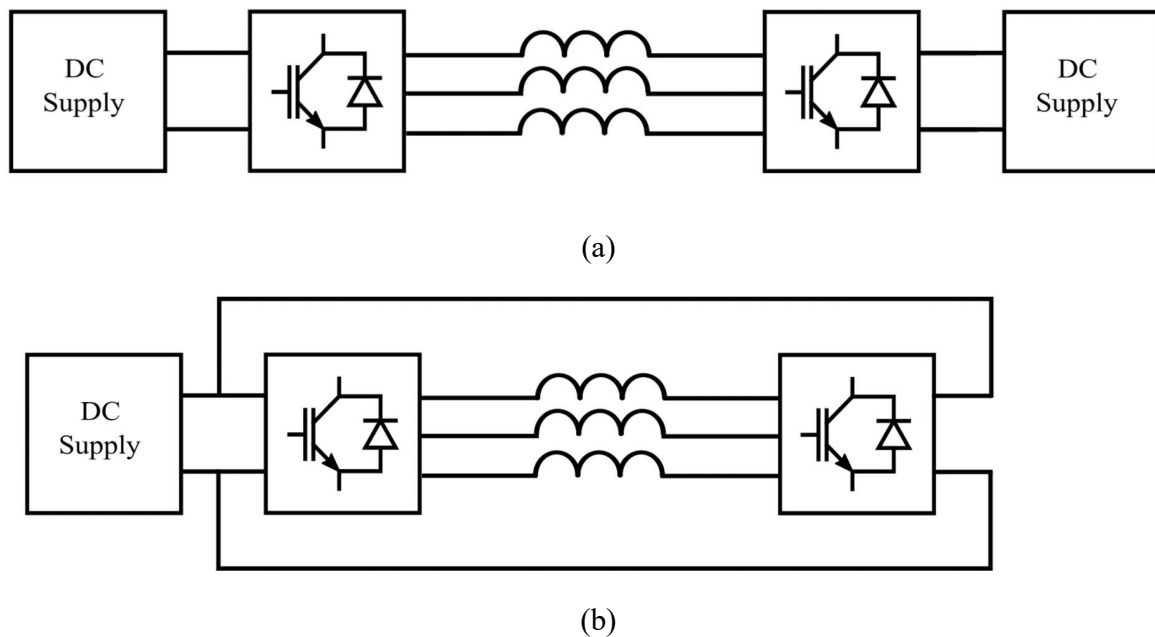


Fig 5.6 Testbench power supply arrangements (a) Individual supply and (b) Shared supply

Attempts resolve this zero sequence current have been made by the introduction of filtering components to the testbench such as common mode inductances [5-14], [5-21] or transformers [5-18], [5-19] to introduce galvanic isolation. Similar to the coupling arrangement, the introduction of these components can successfully suppress the zero sequence current but come with the added cost to the testbench, along with the restriction of its bandwidth and therefore quality of emulation at certain operating points. An attempt to suppress zero sequence current without hardware adjustments is made in [5-22], where the common mode voltage is directly compensated through an space vector modulation control strategy in the converter algorithm. While not suppressing it to the degree of hardware adjustments, this strategy does suppress the zero sequence current to 3.7% of the AC phase current amplitude.

5.3.3 Machine modelling

Regarding the software implemented for PEBE, the given electrical machine is required to be modelled in both its mechanical and electrical aspects. The two most common emulated machine topologies are the IM and the PMSM, which have well established equations which can describe their behaviours in the commonly used dq framework [5-23]. The PMSMs behaviour can be expressed in multiple forms, with the simplest electrical model being expressed as a set of dq voltages with V_d in (5.1) and V_q in (5.2), where flux linkages λ_{dq} are simplified using (5.3).

$$V_d = I_d R_s + L_d \frac{dI_d}{dt} - \omega_e L_q I_q \quad (5.1)$$

$$V_q = I_q R_s + L_q \frac{dI_q}{dt} + \omega_e L_d I_d + \omega_e \lambda_f \quad (5.2)$$

$$\lambda_{dq} = I_{dq} L_{dq} \quad (5.3)$$

In this model, I_{dq} represent the d and q axis currents, obtained via conversion of phase currents I_{abc} to the dq frame using the Clark and Park transforms. L_{dq} represent static expressions of the machines inductance in the dq frame, while R_s is machines equivalent resistance. ω_e is the machines electrical speed and finally, λ_f is known as the flux constant, which approximates the flux linkage contribution by the permanent magnets embedded in the PMSMs rotor. This model excludes complex behaviours in the machine such as the dynamic flux linkage behaviour, magnetic saturation and harmonics due to machine slotting in exchange for a simplified model, while also omitting losses. To refine the model of the PMSM to encapsulate these behaviours, FEA analysis can be introduced which can factor in all of these non-linearities dependent on the complexity of the FEA model. Introducing non-linear FEA acquired flux linkages to the model, V_{dq} can now be expressed as (5.4) and (5.5) respectively, where λ_{dq} are the flux linkage values stored in LUTs relating $\lambda_d - I_d - I_q$ and $\lambda_q - I_d - I_q$.

$$V_d = I_d R_s + \frac{d\lambda_d}{dt} - \omega_e \lambda_q \quad (5.4)$$

$$V_q = I_q R_s + \frac{d\lambda_q}{dt} + \omega_e \lambda_d \quad (5.5)$$

Comparing this to the prior model, the simplified expressions of λ_{dq} (5.5) are now substituted for the more accurate FEA modelled values. This model provides a superior expression of the

behaviour of a PMSM but can be more computationally expensive to utilise given the required storage space and processing time when using LUTs.

To model the mechanical behaviours of the PMSM, the mechanical swing equation (5.6) can be used, where the rate of change of mechanical speed ω_m of the rotor shaft is a result of the load torque T_L and friction constant F , subtracted from electromagnetic torque T_e , then divided the rotor inertia constant J , which approximates the rotors inertial behaviours based upon its structural design.

$$\frac{d\omega_m}{dt} = \frac{T_e - T_L - F\omega_m}{J} \quad (5.6)$$

The expression for T_e varies dependent on the electrical model that is utilised, where (5.7) is used for the simplified non-FEA model. In this expression, torque production is composed of two components, the first is reluctance torque $((L_d - L_q)i_d i_q)$, and the second is the torque produced from the interaction between the stator field and the magnetic field produced by the rotors embedded permanent magnets $(\lambda_f I_q)$. The second model used when FEA is introduced is expressed as (5.8), where the torque components are represented instead by the LUT flux linkage values. Both models are multiplied by $\frac{3}{2}p$, where p are the machines pole pairs.

$$T_e = \frac{3}{2}p \left((L_d - L_q)i_d i_q + \lambda_f I_q \right) \quad (5.7)$$

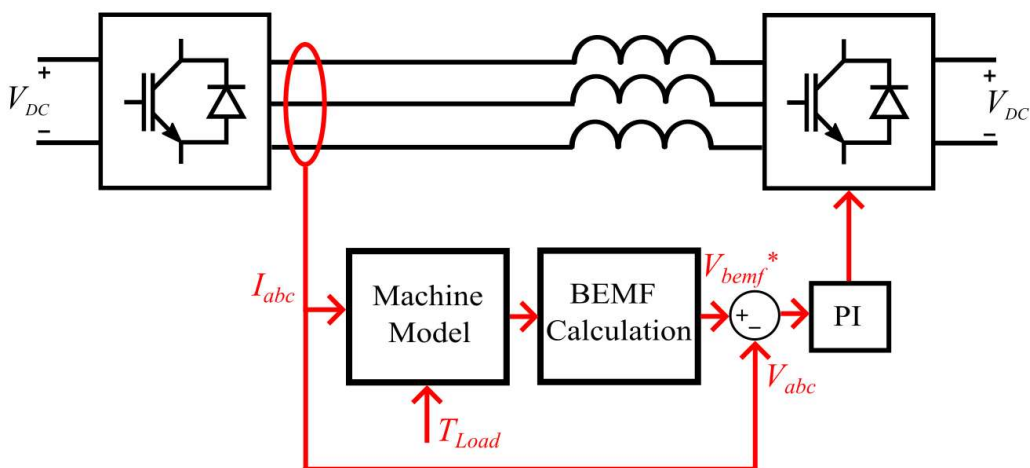
$$T_e = \frac{3}{2}p (\lambda_d I_q - \lambda_q I_d) \quad (5.8)$$

5.3.4 Emulator control

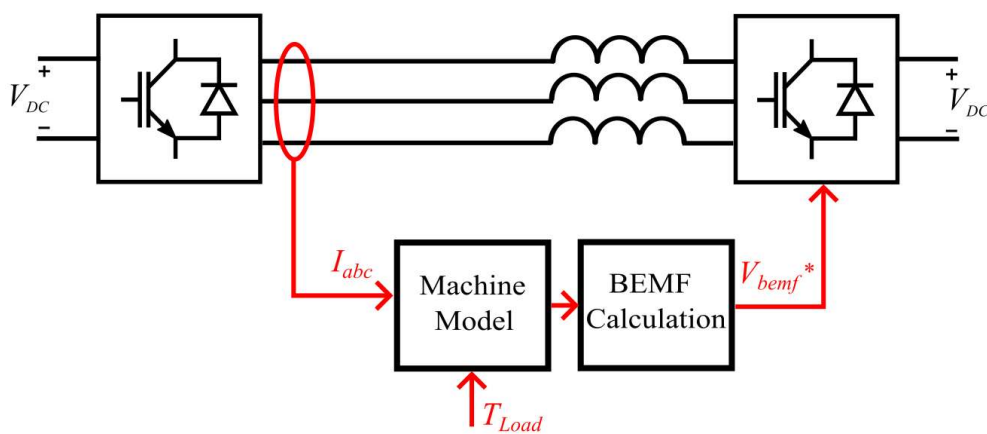
To operate a PEBE testbench, a control algorithm is required which combines the machine model in the prior subsection with an overarching BEMF calculation algorithm. This overall model takes the measured phase values at the input of the EMU, and produces a response in the EMU which mimics the equivalent BEMF for the given terminal characteristics. This model can exist in three broad forms, dependent on the availability of phase values. The first of these is a voltage-in model [5-19], [5-24] which takes phase voltage measurements as an input to produce the reference BEMF. Another is a current-in model, which uses phase current measurements instead to then

calculate the reference [5-14], [5-22], [5-25]. The final most common option is to use both values in the control algorithm, requiring both voltage and current phase measurements [5-12], [5-13], [5-17], [5-26], [5-27].

To control the EMU, the BEMF calculation model can be implemented using a closed or open loop approach. In the closed loop approach [5-10], [5-13], [5-25], [5-28], voltage and/or current measurements are required to produce error values from the reference BEMF of the model, where an example of this is shown in Fig 5.7a. This provides a finer emulation of the machine behaviour such as ripple current, but limits emulator bandwidth for its operation. An open loop approach shown in Fig 5.7b provides the opposite characteristics, where emulation bandwidth is not limited



(a)



(b)

Fig 5.7 Emulating inverter utilising (a) Closed loop control and (b) Open loop control

and voltage sensors are not strictly required, but instead the accuracy of the emulation is decreased [5-14], [5-15], [5-20], [5-21].

The other consideration that must be made with these approaches is how they relate to the control of the drive inverter. Given the way the inverters are coupled, possible control conflicts can occur. For example, if both inverters are operating as VSCs and are closed loop, a control conflict between the inverters will arise. This can be avoided by ensuring the control bandwidths of the two are sufficiently spaced, where typically the bandwidth of the EMU needs to be significantly larger. The other way to avoid this conflict is the use of open loop control for the EMU, or another option is ensuring both inverters use differing modes of control, which is uncommon.

5.4 PEBE testbench for the verification of position sensor and sensorless control based commercial drives

PEBE testbenches are a promising candidate for streamlining the commercial drive verification process, by either replacing fully or undertaking a portion of the testing typically carried out by a dynamometer. In the commercial context, any candidate testbench must be cost effective, efficient and straightforward to use, and easily fabricated from its base components. Prior proposals of testbenches beyond experimental verification has been limited, and therefore there has not been direct consideration towards designs which focus on the prior objectives while also preserving the quality of emulation. Along with this, it is desired that a commercial testbench should demonstrate the capability of verifying drive inverters programmed with firstly position sensor based control [5-16],[5-20],[5-29], and secondly, sensorless position based control which is absent from literature. Many applications of drive systems including E-Mobility use sensorless position control for a variety of reasons, such as cost saving from the removal of precision sensors or geometric limitations in the drive not allowing the placement of a sensor [5-30]. Therefore, there is a need for a testbench which can provide emulation for a drive inverter programmed with production ready sensorless position control which is unaltered for the testbench.

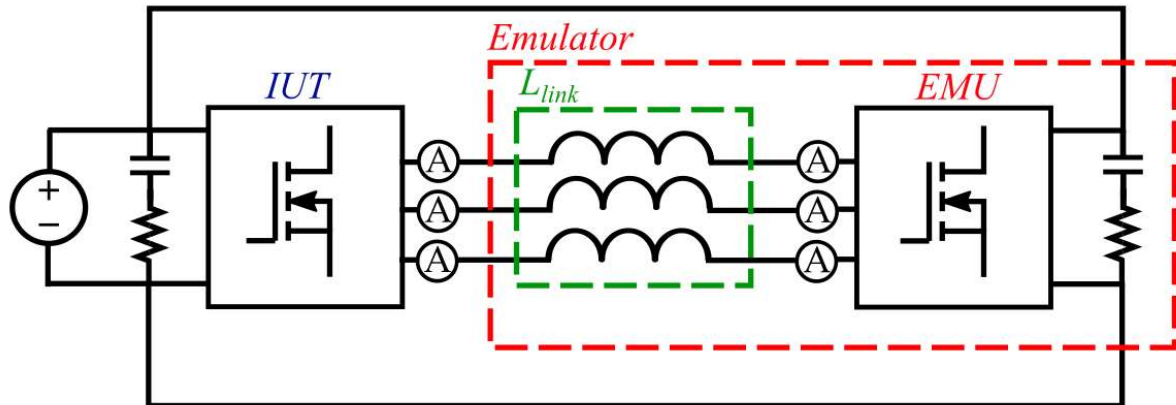


Fig 5.8 Proposed PEBE testbench

5.4.1 Testbench Hardware Design

Fig 5.8 illustrates the design of the proposed PEBE testbench from the hardware perspective. The testbench is designed for a modular setup, where it can be fabricated from two separate identical inverters, the inverter under test (IUT) and EMU, connected at both AC and DC ends in the common DC supply configuration. The use of this common DC supply provides minimal cost by reducing the number of supplies, and increase efficiency by introducing the circulation of current in the testbench. Fig 5.9 illustrates the internal design of both the IUT and EMU, which are implemented as standard three phase inverters using Si MOSFETs. The other main components of the testbench are firstly the sensing circuitry seen in Fig 5.9, which are a separate set of current sensors supporting each inverter. This is because in commercial drive systems, the inverter is often configured to operate as a current source inverter while being constructed as a voltage source converter, and is designed with non-invasive current sensors. Along with this, PEB emulators require current measurements for all control formats, voltage sensing is optional dependent on the control scheme and therefore cost can be minimised by not using it. Given the sensors are two separate sets, this allow the testbenches inverters to operate as isolated, modular control systems, where the IUT and EMU can effectively be ‘plug and play’ with the testbench as either can be swapped out. The second major component remaining is the coupling between the AC sides of the inverters, which are chosen as a purely inductive coupling L_{link} to provide filtering without bandwidth limitation, also minimising the number of required components for the testbench.

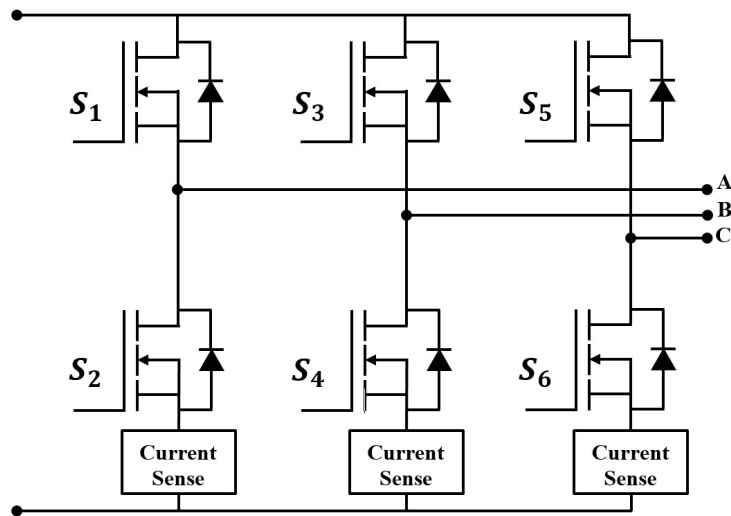


Fig 5.9 Implemented three phase inverter with current sense circuitry

5.4.2 Emulator Control Unit

When designing a PEBE testbench, it is well known that the EMU is typically controlled using an RTS unit [5-31]-[5-35]. These controllers allow models to be designed in programs such as MATLAB/SIMULINK or other methods of code generation, which can then be used as control for the system. RTSs offer a computationally powerful, user-friendly option that meets the demands of a PEBE testbench, however, they are not without disadvantages. They are very expensive, power consumption is sizeable, and they require specific circuit design in the inverter to accommodate. Another consideration with the RTS is that experimental setups will often have the IUT control also programmed onto the same unit for convenience (RTS controls both IUT and EMU), which is reasonable when seeking to validate the functionality of a designed PHiL testbench. The problem with this is that the purpose of a PHiL testbench is to carry out inverter control and/or hardware testing. Using an RTS does not necessarily validate control software of the IUT to a full commercial level, and does not give an accurate hardware representation of a practical inverter design. In commercial inverter design, control is implemented using a microcontroller or less commonly, an FPGA. Both units differ in how they function internally from an RTS and need to be mounted on the inverter. Therefore, necessary considerations need to be made towards thermal testing of the inverter along with other factors such as EMI in the surrounding control circuitry. By using a standard inverter module containing either of these units instead of an RTS, control software intended for the machine drive can be verified, along with the added full operational testing of the inverter as a complete electrical system.

Comparing Microcontrollers and FPGAs for the EMU, they are similar in principle, and both are widely implemented in inverters. In literature, PHiL testbenches can be found using FPGAs [5-31],[5-34]-[5-35]. A PEBE testbench which uses a microcontroller for the EMU control unit has not been demonstrated in literature. Basing the software of the EMU on code that is compatible for a microcontroller carries its own benefits, and is necessary for the EMU to be a commercial inverter module with no modification as proposed in this testbench. In a more general sense, this allows a testbench which is simpler to fabricate and reproduce as it maintains its modularity, but this can also be true if an FPGA is used. FPGAs tend to have more processing power than microcontrollers, accompanied with a higher cost and a customisable software architecture that allows greater freedom in design. The customisation makes FPGAs difficult to utilise correctly but can be suited for higher precision applications where more processing power is required. Notably though, machine drive systems with greater computational demands are still likely to opt for higher power (and cost) microcontrollers with multiple cores. Contributing to the FPGAs processing speed is its parallel processing capability, which is only found again on more expensive microcontrollers with multiple execution units. To exemplify these features, a comparison is shown between these three control unit types in Table 5.1. Firstly, the microcontroller used in this work is presented which is from the Microcontroller DSPic family. Two FPGA modules used for PHiL in [5-31] and [5-35], which are the Zynq 7020 and Xilinx 6. Finally, there are many RTS units which can fulfil the purposes of PHiL testing given their exceptional performance characteristics, such as DSpace, Opal-RT and Speedgoat amongst others. In this case, two Opal RT RTS units, the OP5033XG and the OP4610XG are shown along with the Speedgoat IO334-325K, which exemplify the typical performance capacity and cost of an RTS. These examples highlight the points made about the different control units. The DSPic is significantly cheaper than all of its counterparts, but as expected is significantly less powerful, and with less memory space. While FPGAs may be available closer to these ratings that would be feasible at a price more comparable to a microcontroller, they have not been demonstrated in existing PHiL testbenches. The RTS units shown here are significantly more powerful, but are staggeringly more expensive than either a microcontroller or FPGA, averaging a price point of £19500 for similar total characteristics, where the main differences come in processor choice, storage and RAM. While microcontrollers may lack pure performance versus FPGAs, functioning EMU control software is

feasible using a microcontroller at a reduced cost compared to an FPGA, which is important for the proposed PEBE testbench which aims for minimal cost using a commercial drive.

Table 5.1 Comparison of PHIL Testbench controller units

| | DSPicMP508 | Zynq 7020 | Xilinx 6 | OP5033XG | OP4610XG | IO334-325K |
|----------------------------|-------------------|---------------------|-----------------|-----------------|-----------------|-------------------|
| Size | Negligible | Negligible | Negligible | Medium | Medium | Small |
| Typical Cost Per Unit | £3 | £147 | £820 | £18900 | £20300 | £19400 |
| Processing Power | 100MHz | 766MHz | 1.6GHz | 2.1GHz | 3.8GHz | 4.2GHz |
| Random Access Memory | 24kB | 256kB | 1.05MB | 32GB | 16GB | 32GB |
| Memory | 128kB | 256kB (RAM only) | 5.5MB | 500GB | 250GB | 250GB |
| No. of Cores | 1 | 2 | - | 44 | 6 | 4 |
| Parallel Processing | No | Yes | Yes | Yes | Yes | Yes |

5.4.3 Emulator Software Design

Fig 5.10 illustrates the control design of the EMU for the proposed PEBE testbench. As discussed in the prior subsection, the decision for the inclusion of only current sensing circuitry means that a current-in model is utilised for voltage control. Due to the current sensor polarity when using identical commercial inverters, the measured currents in the EMU are required to be inverted to maintain unaltered circuitry in the drive. To avoid a conflict with any control configuration of a potential IUT, and to avoid the use of voltage sensors, the EMU control is configured as an open loop voltage control. This reinforces the ‘plug and play’ aspect of the testbench, where the goal is to ensure that minimal changes apart from the reprogramming of machine parameters are required, where any prospective drive inverter can be easily inserted into the testbench. The trade-off here is that some more complex details of the BEMF voltage cannot be emulated, but from a control perspective it also means that the operating bandwidth of the proposed testbench is not limited by the presence of the closed loop. For the machine model of the emulator, the more refined FEA

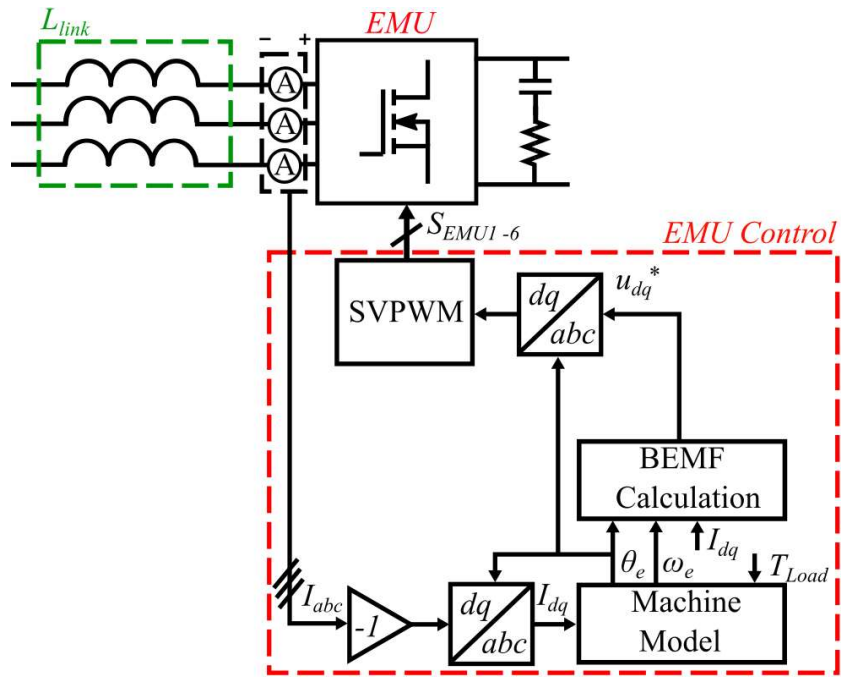


Fig 5.11 Proposed PEBE control

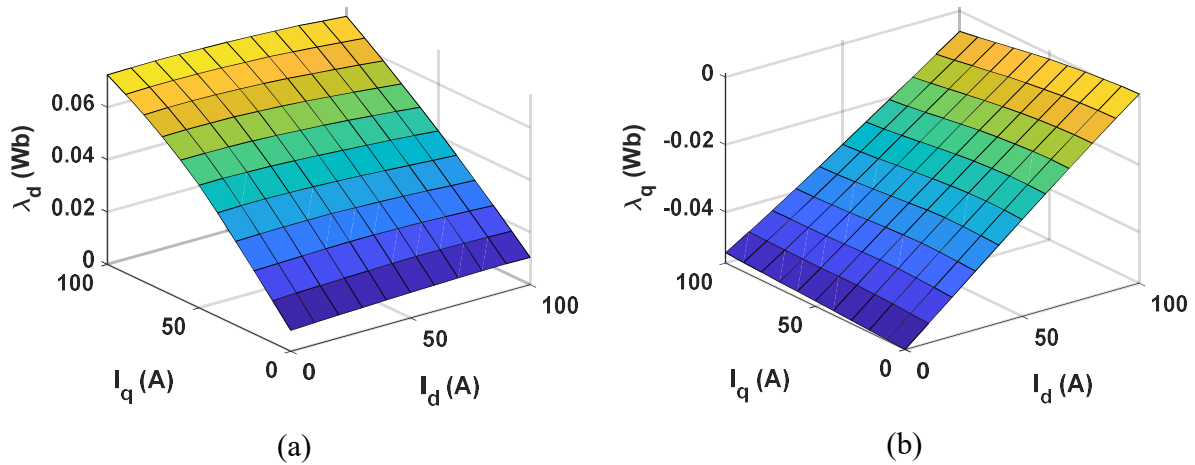


Fig 5.10 JMAG data relating dq axis current to: (a) d-axis flux linkage, and (b) q-axis flux linkage for 1.2kW PMSM

based model expressed in (5.4), (5.5) and (5.8) is utilised with the swing equation in (5.6). This will provide a higher quality of emulation of the machines behaviour without significant drawbacks. The machine emulated on the testbench is a 1.2kW PMSM machine designed for E-mobility applications, where its specifications are given in Appendix B. The FEA data used in the

machine model is acquired from JMAG for the given machine, and is shown in Fig 5.11, where the LUTs relate $I_d - I_q - \lambda_d$ in Fig 5.11a) and $I_d - I_q - \lambda_q$ in Fig 5.11b).

In an idealised setup, the machine model in (5.4) and (5.5) would suffice for accurate emulation of the machines equivalent BEMF. In the practical testbench this is not the case as L_{link} is present between the inverters AC outputs. This will contribute a voltage drop in the circuit, which can be accounted for in the machine modelling by altering (5.4) and (5.5) to (5.9) and (5.10) respectively for reference BEMF values u_{dq}^* . In the altered model, the resistive voltage drop is subtracted in the first section of the equations using link resistance R_{link} , the inductive voltage drop is then accounted for with each of the flux linkage values using L_{link} and I_{dq} .

$$u_d^* = I_d(R_s - R_{link}) + \frac{d(\lambda_d - L_{link}I_d)}{dt} - \omega_e(\lambda_q - L_{link}I_q) \quad (5.9)$$

$$u_q^* = I_q(R_s - R_{link}) + \frac{d(\lambda_q - L_{link}I_q)}{dt} + \omega_e(\lambda_d - L_{link}I_d) \quad (5.10)$$

5.5 Inverter sensorless control

Fig 5.12 illustrates the control configuration of the IUT used for verification of the proposed testbench design. The control is a form of BEMF based sensorless position control which is proposed in [5-36], requiring current measurements from the inverter AC output and estimation of the emf of the load machine. Firstly, the currents are converted into the rotating dq frame, and are then used to generate the components of the BEMF in terms of voltages in the dq frame referred to as E_{s_re} and E_{s_im} for the d-axis and q-axis respectively. Fig 5.13 illustrates a vector diagram of the stator rotating reference frame of a given PMSM aligned with the stator voltage vector V applied by the inverter. In the equivalent circuit of a PMSM shown in Fig 5.14, these vector values present themselves as the applied stator current I_s in the dq frame, and BEMF E_s and can be given as follows for a PMSM in (5.11).

$$\bar{V}_s = \bar{E}_s + j\bar{I}_s X_s + \bar{I}_s R_s \quad (5.11)$$

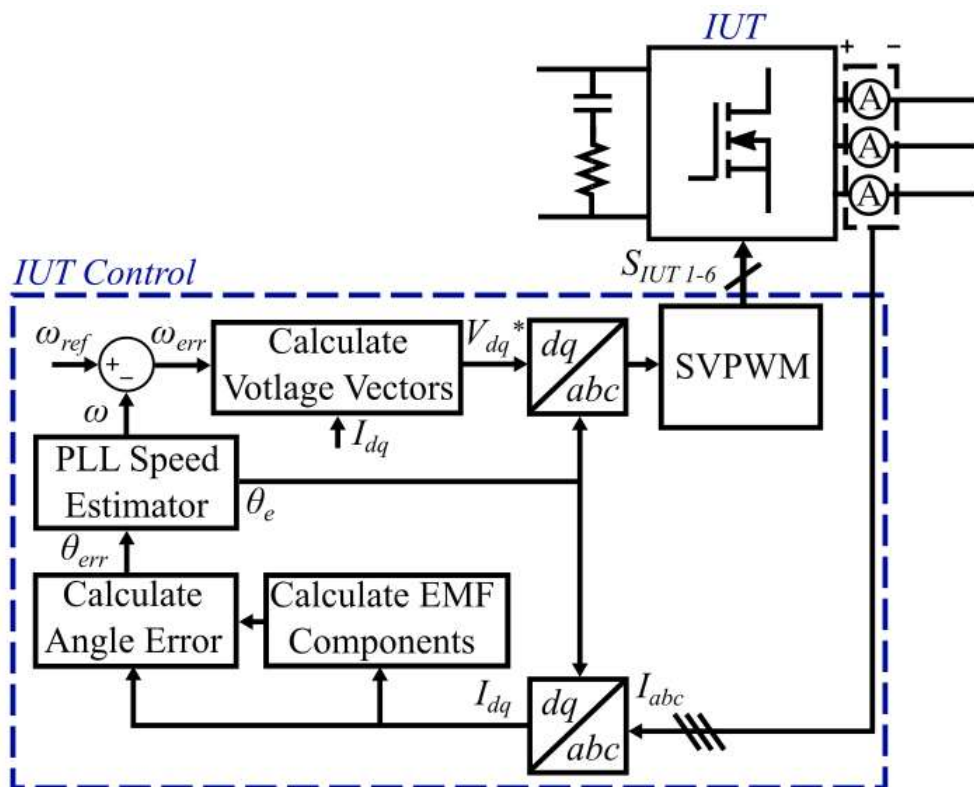


Fig 5.12 Proposed PEBC control

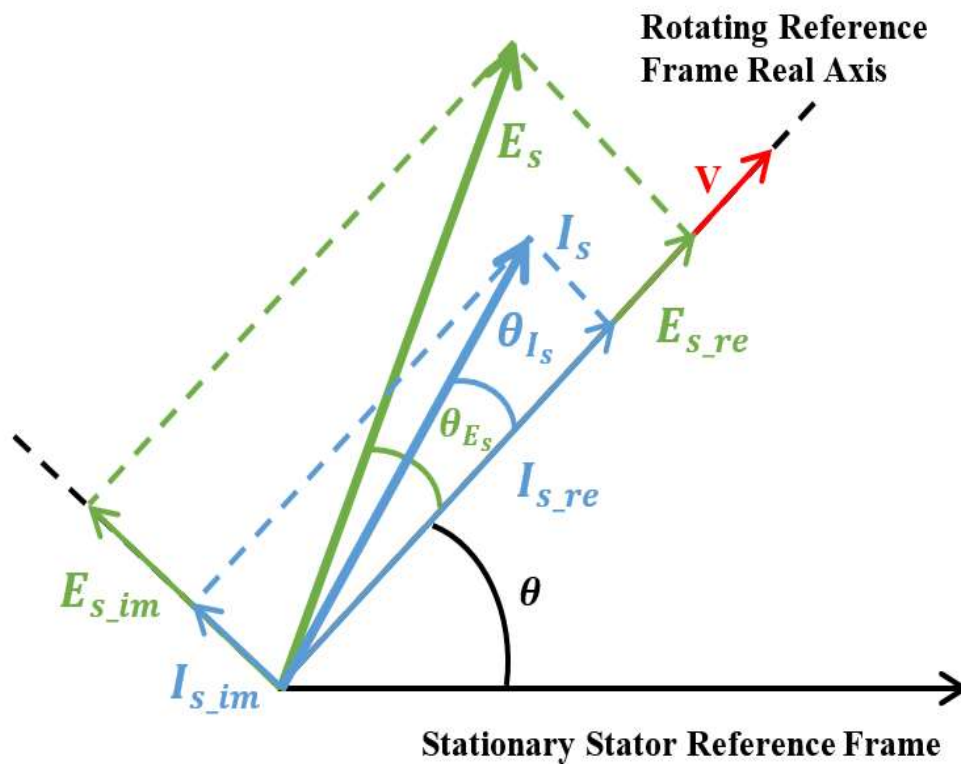


Fig 5.13 Diagram of stator rotating reference frame

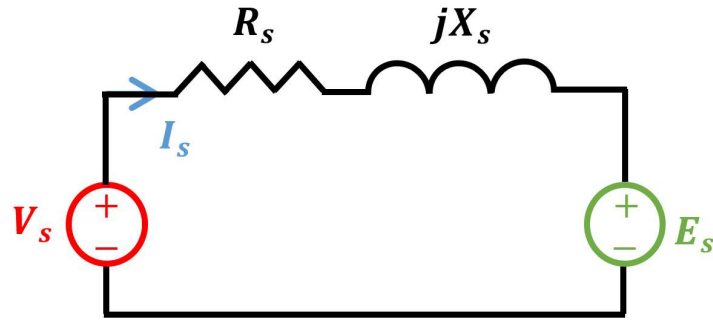


Fig 5.14 PMSM stator equivalent circuit

Where, X_s represents the stator phase winding reactance and R_s the resistance. Separating these vectors into real and imaginary components in (5.12) and (5.13) yields the values in Fig 5.14. Notably, X_s may differ between equations as it is dependent on the type of PMSM that is being controlled, where d and q axis inductances may not be identical and variable reluctance is present in the PMSM structure.

$$V_{s_re} = E_{s_re} + I_{s_re} R_s - I_{s_im} X_s \quad (5.12)$$

$$V_{s_im} = E_{s_im} + I_{s_im} R_s - I_{s_re} X_s \quad (5.13)$$

Given the alignment of Fig 5.13 with vector V , the equations will become (5.14) and (5.15), where the imaginary component of V is given as zero and can be rearranged to represent the BEMF vector.

$$E_{s_re} = V - I_{s_re} R_s + I_{s_im} X_s \quad (5.14)$$

$$E_{s_im} = -I_{s_im} R_s + I_{s_re} X_s \quad (5.15)$$

With these values available in this form, E_s can be calculated and using this and the aforementioned dq currents I_s , the angle between I_s and the rotating reference frame, θ_{I_s} , and angle between E_s and the rotating reference frame, θ_{E_s} , can be calculated. This accomplished by revisiting Fig 5.10 and using trigonometry in (5.16) and (5.17) for θ_{I_s} and θ_{E_s} respectively. The angular difference between the two vectors, θ_{diff} is given by subtracting the two from each other (5.18).

$$\theta_{I_s} = \tan^{-1} \left(\frac{I_{s_im}}{I_{s_re}} \right) \quad (5.16)$$

$$\theta_{E_s} = \tan^{-1} \left(\frac{E_{sim}}{E_{sre}} \right) \quad (5.17)$$

$$\theta_{diff} = \theta_{I_s} - \theta_{E_s} \quad (5.18)$$

This difference can be managed based on an angular control loop that produces the angular error θ_{err} (5.19) from the desired angular difference θ_{ref} , but is typically desired to be zero and is minimised as such. As the frame rotates, given these angles are in reference to the rotating voltage vector, which itself is in the rotating reference frame, the control loop can be kept in synchronism with the machine and the position of the back emf can be estimated quickly in each pulse width modulation (PWM) cycle using a phase locked loop (PLL) estimator which along with the BEMF position will produce the estimated speed ω for the speed control of the IUT.

$$\theta_{err} = \theta_{ref} - \theta_{diff} \quad (5.19)$$

5.6 Simulation results

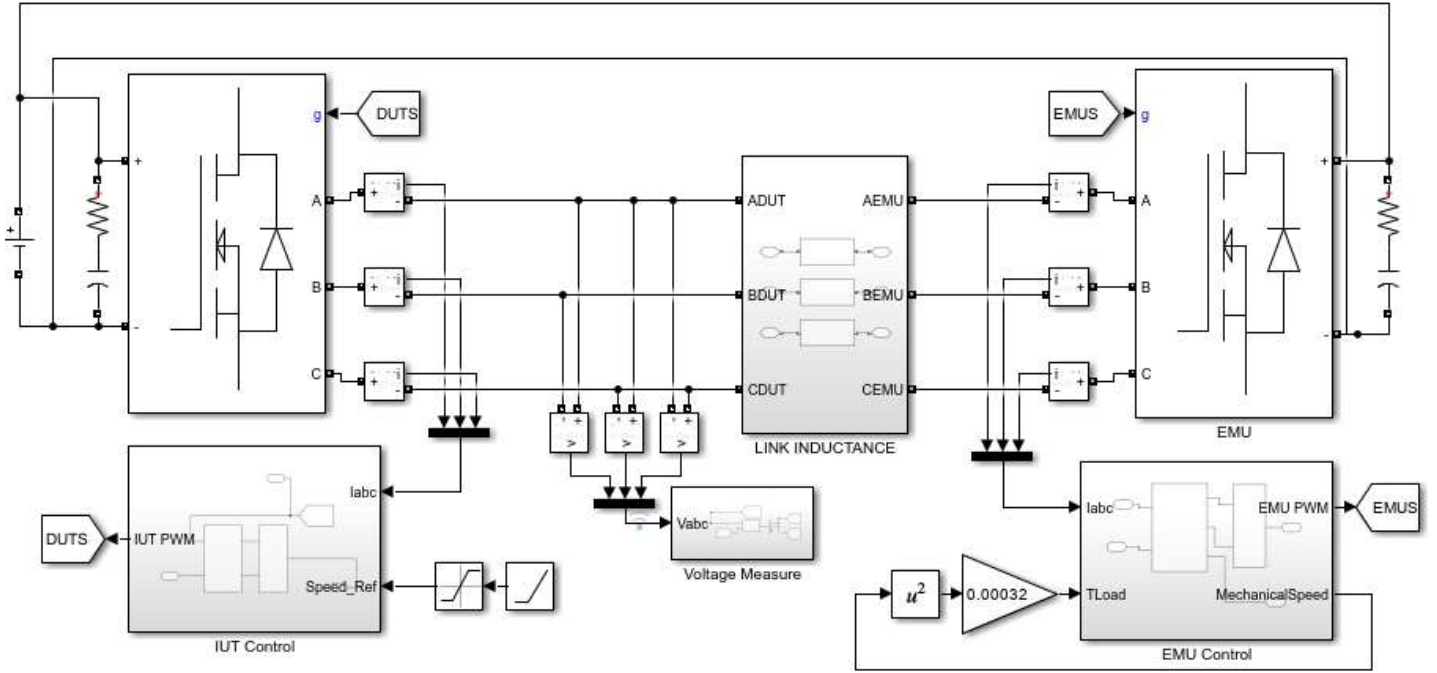


Fig 5.15 Modelled emulator testbench

To evaluate the proposed testbench in theory, it is modelled in MATLAB/SIMULINK, shown in Fig 5.15. This is compared with a Simscape electrical model of a PMSM with an identical drive inverter, modelled with the FEA data shown in Fig 5.10 and the characteristics in Appendix B. For the load torque of the machine, a torque profile is utilised, which is gathered experimentally from the intended fan application of the machine, expressed as (5.20). This results in a squared characteristic dependent on the mechanical speed ω_m .

$$T_{Load} = 0.00032\omega_m^2 \quad (5.20)$$

The testbench is simulated with a switching frequency f_{sw} of 16kHz and sample time T of $1\mu s$, and given a speed command of 1500rpm, near the peak power point of the machine with the given torque characteristic. The speed response and torque of this simulation are presented in Fig 5.16. It can be seen that the proposed emulators speed response mirrors the modelled PMSM, exhibiting a near identical control response with the same parameters.

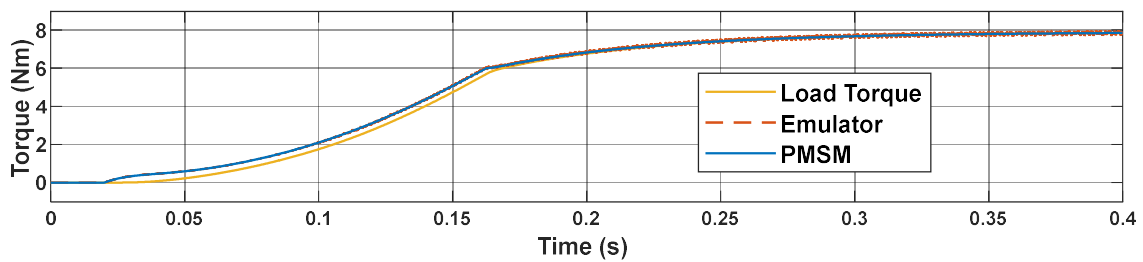
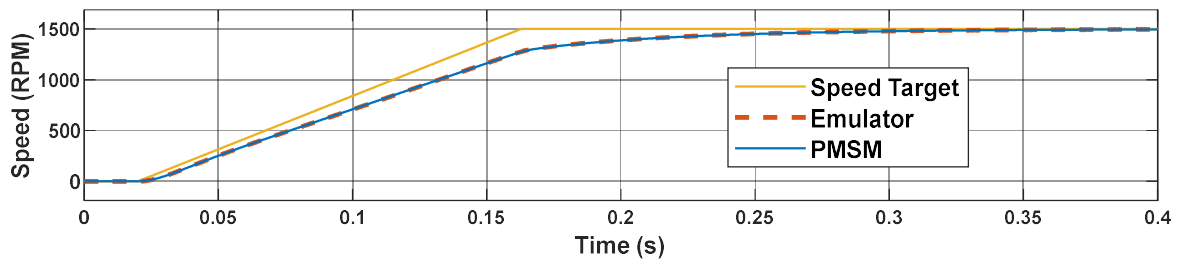


Fig 5.17 Simulated control response with a command of 1500rpm

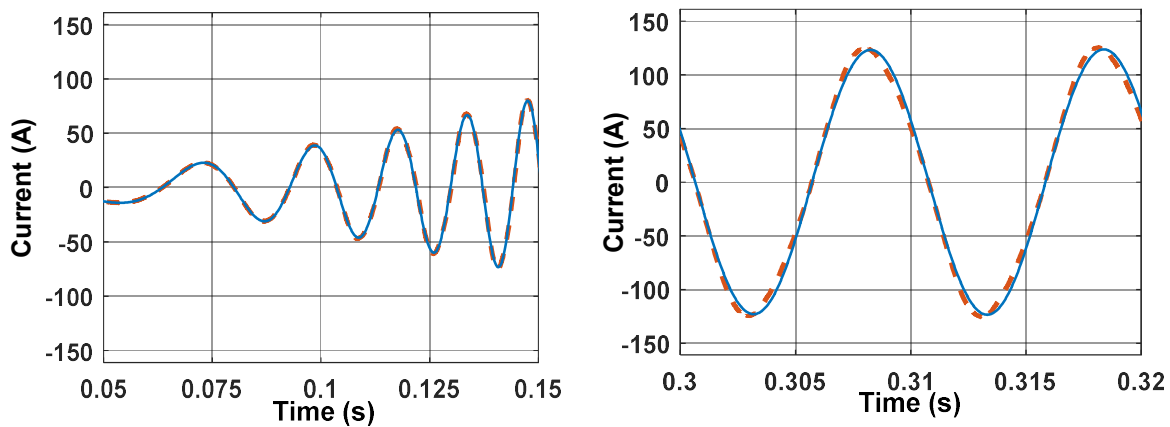
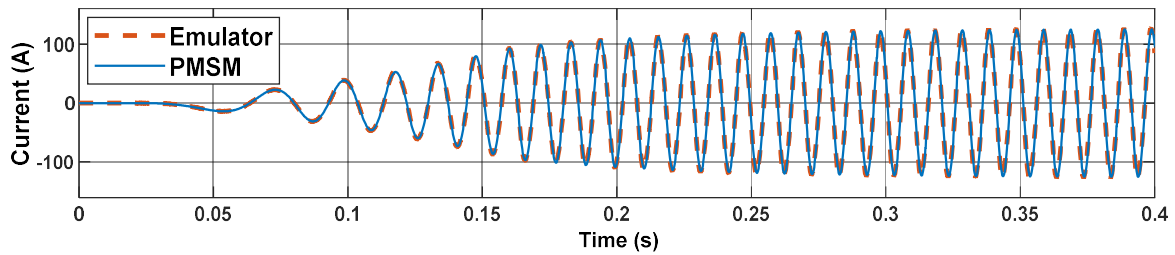


Fig 5.16 Simulated phase A current with a command of 1500rpm

Fig 5.17 presents the current waveforms taken from Phase A of the testbench and modelled PMSM. A good correlation is found in the current waveforms generated by the emulator, being almost identical across the full acceleration and steady state. At low speed, the currents agree, and as

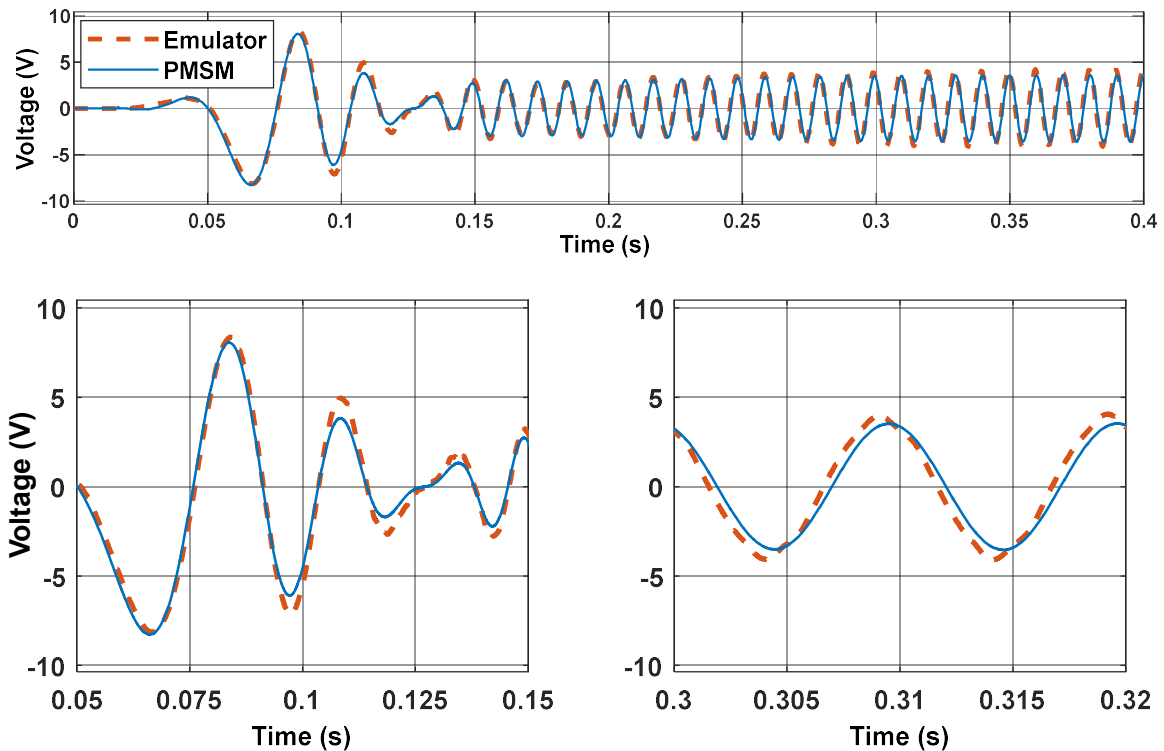


Fig 5.18 Simulated phase A voltages with a command of 1500rpm

steady state speed is achieved, there is a minor difference in shape between the two accompanied with a difference in frequency of 0.017Hz (1rpm) contributing a slight phase shift. It is expected that with the given choices in control of the emulator, that a high quality emulation of the currents should be achieved, and differences in emulation quality versus the electrical machine would occur with the voltages. Fig 5.18 presents the resultant voltage waveforms from the same phase between the proposed testbench and the modelled PMSM.

It can be seen here that the proposed testbench is able to achieve a relatively good quality of emulation, but notable differences in voltage emulation begin to occur due to the open loop control implementation. It can be seen that while the important factor of the same relative shape between the voltage waveforms is maintained, amplitude differences in voltage occurs at different points in the simulation such as at 0.11 seconds where there is a maximum difference of 1V between emulation and modelled PMSM. Overall, this confirms that the testbench can in theory provide a sufficient level of emulation to mimic the BEMF of the PMSM in question.

5.7 Experimental setup and results

With the simulation modelling of the proposed PEBE testbench confirmed, the testbench is constructed experimentally for full verification. Fig 5.19 illustrates the proposed testbench from a top down view, highlighting the cabling to a 60V/60A DC supply, the link inductance used for each phase, and the two inverter components. The inverters used for the proposed testbench are designed for E-mobility, rated from 24V to 48V, utilising Si MOSFETs and are designed with the configuration shown in Fig 5.9. The IUT is programmed with the sensorless position control detailed in Section 5.5, with the EMU programmed with the control configuration in Subsection 5.4.3. Both inverters utilise Microchip dsPIC33C 16-bit microcontrollers detailed in Appendix C where the proposed testbench omits the use of RTSs entirely, providing a significant cost saving. The inverters are operated at a switching frequency of 16kHz, and the supply voltage is configured to 36V. The proposed testbench is firstly operated at a steady state speed of 1500rpm. Fig 5.20 shows a scope view of this steady state operation, where phase currents can be observed with an RMS current of 70A with a scaling of 10mV/100A. These illustrate the balanced steady state operation of the emulator with minimal distortion to the sinusoidal AC waveforms.

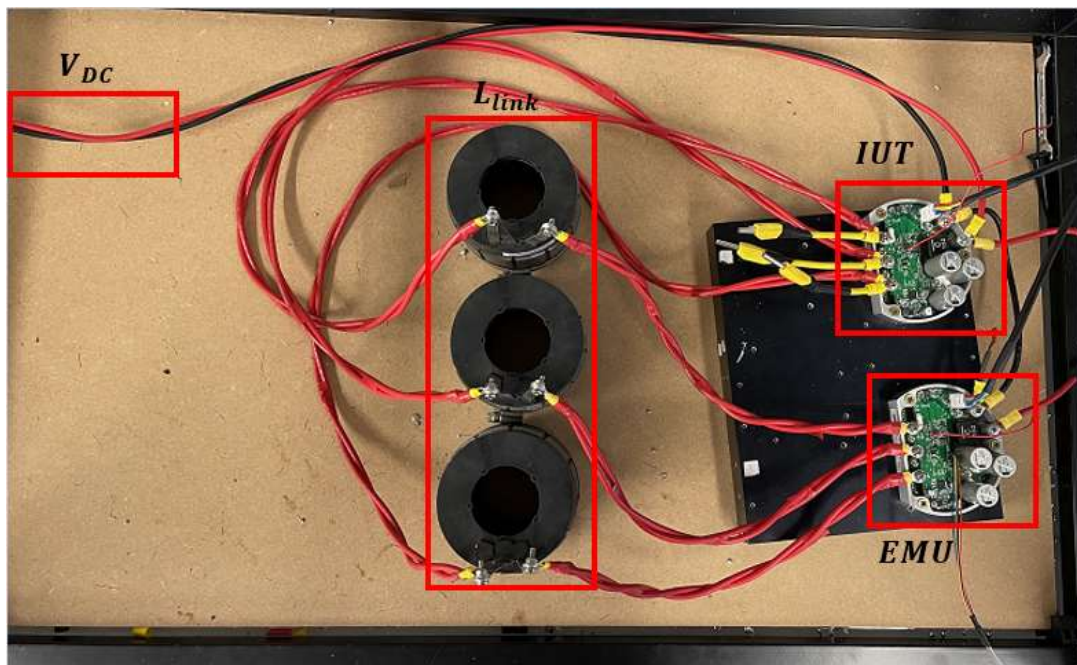


Fig 5.19 Experimental sensorless emulator testbench

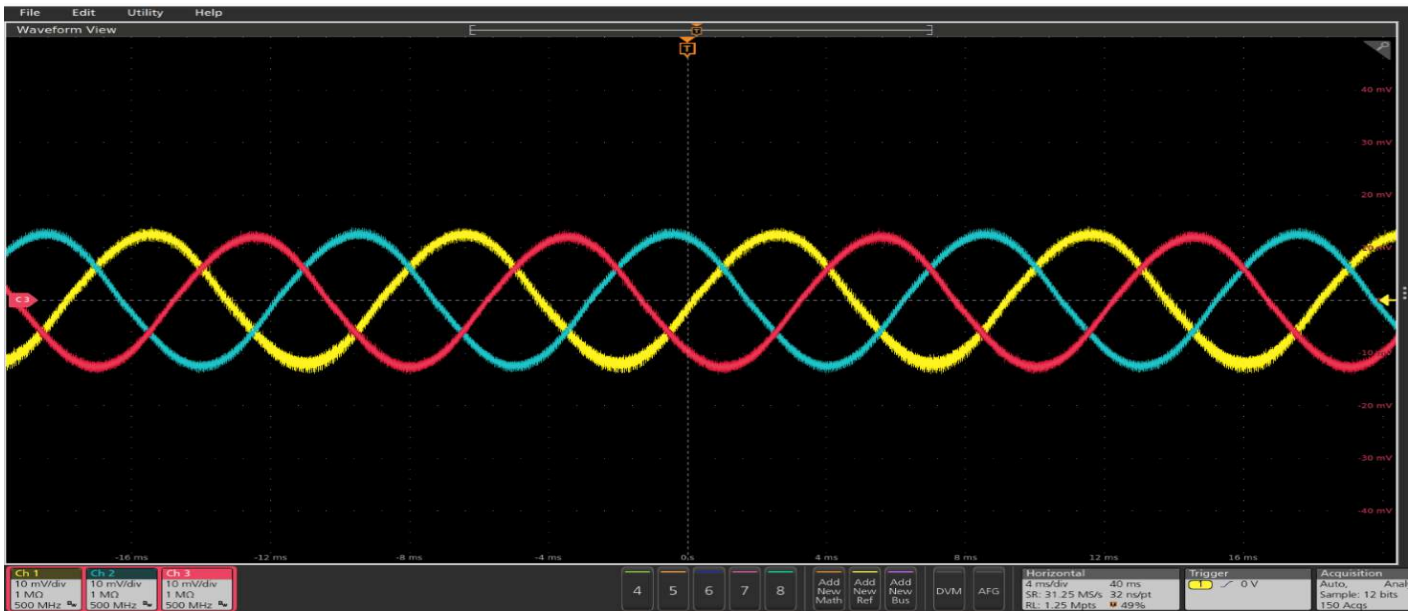


Fig 5. 20 Proposed PEBE testbench three phase currents through oscilloscope view with resolution of 100A/div and 4ms/div

The testbench is now programmed with the torque characteristic in (5.20) and given a speed command of 1500rpm. Fig 5.21 illustrates the speed response of the experimental proposed testbench, where it exhibits a similar control response as in simulations. Compared to the simulation, the constructed testbenches sensorless control programmed on the microcontroller exhibits a slight delay in buildup at low speed. This occurs typically when sensorless position controls are applied at low speeds, where the BEMF is small, and the control is not fully synchronised yet. The currents from this test are shown in Fig 5.22, where it can be seen that while the control cannot exactly estimate the position of the BEMF, current is applied and speed increases. Examining the phase current, it can be seen that the proposed testbench produces stable sinusoidal AC with minimal harmonic disruption. It can be seen that at steady state, there is a mismatch in current amplitudes of 2.22A (2.9% of RMS Current) due to the circulating zero sequence current introduced by the common DC supply connection. At steady state, the power output reaches of 1.23kW while drawing 12A from the supply at 36V, resulting in a power draw of 432.5W.

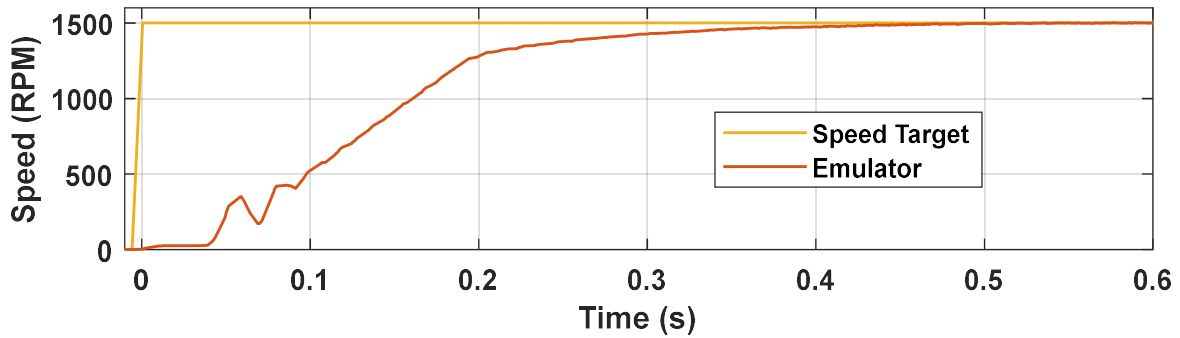


Fig 5.22 Speed response of emulator from startup with application torque profile

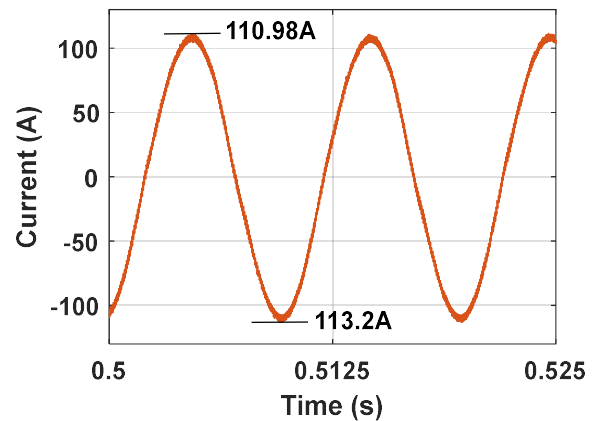
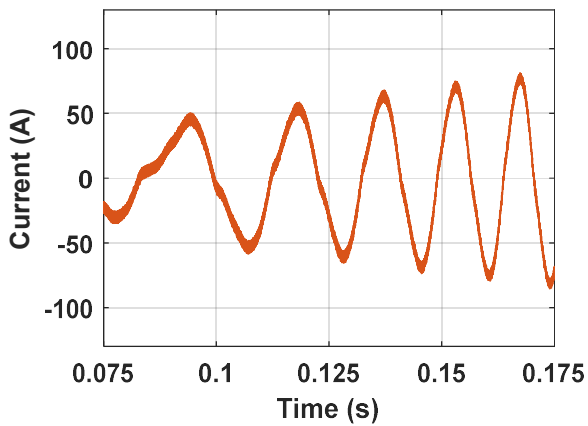
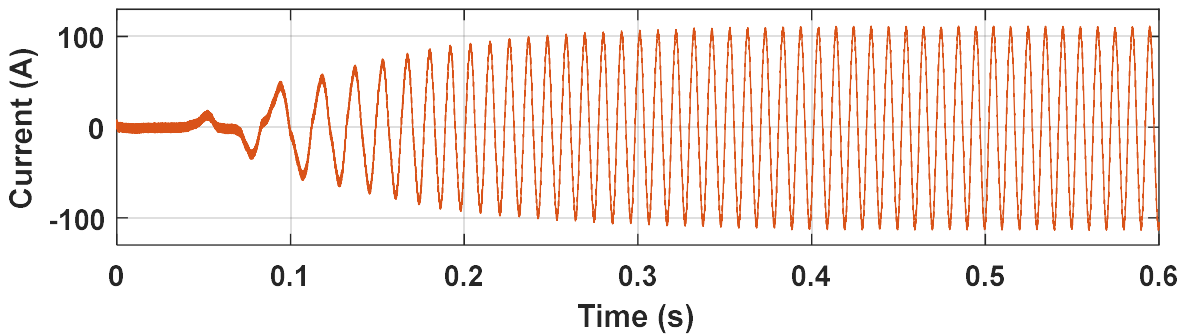


Fig 5. 21 Experimental phase A current with a command of 1500rpm and application torque profile

The PEBE testbench is now evaluated against a dyno testbench, which is configured with the application PMSM and an identical drive inverter with sensorless position control. This can be seen in Fig 5.23, where the differences can be seen in size and mechanical complexity as opposed to the proposed PEBE testbench. A step command of 1500 RPM is given with 4 Nm of load torque at startup where Fig 5.24 is the speed response and Fig 5.25 is phase A currents between dynamometer and emulator. At low speed, the response of the emulator does not fully mirror the

dynamometer but exhibits the same control behaviour of the real dynamometer which is important especially given the challenges of operating sensorless position control at low speeds. The emulator creates the back-emf of the real dynamometer and accelerates the emulated inertia to the speed target. The differences at low speed likely can be attributed to the differences in modelling inertia when it comes to comparison with a dynamometer. As it approaches the reference speed, the control responses of the two begin to closely mirror each other and reach steady state in similar times with near identical amplitudes in terms of peak and steady state currents.

Figs 5.26 and 5.27 shows the response of the two systems to a torque step of 8 Nm from no-load steady state, where Fig 5.26 is the speed response and Fig 5.27 is current from phase A. The torque is loaded on the dynamometer as fast as the setup can safely, where the emulator can approximately match the response of the dynamometer, exhibiting a smaller peak current in the acceleration and slight difference in speed response. Given the dynamometer is limited in the rate at which it can mechanically load torque, the emulator is at an advantage. This is given its ability to step torque

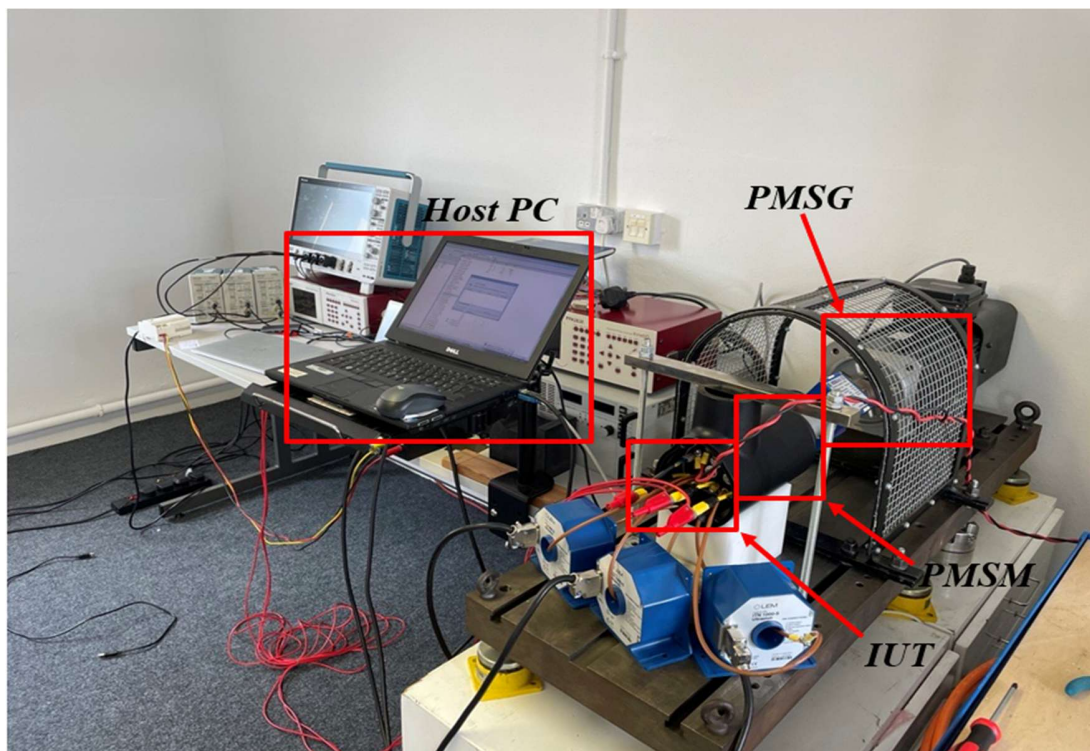


Fig 5. 23 Experimental dynamometer testbench

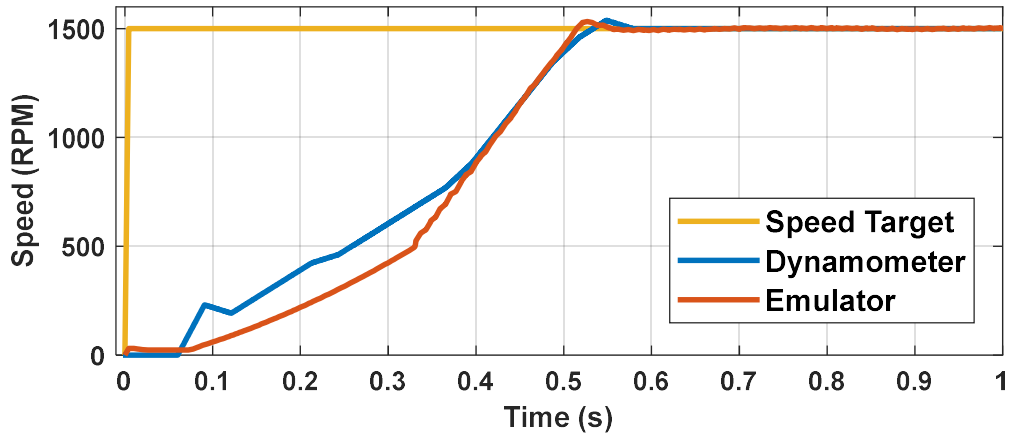


Fig 5. 24 Speed response of PEBE and dyno from startup with 1500rpm and 4Nm of load torque

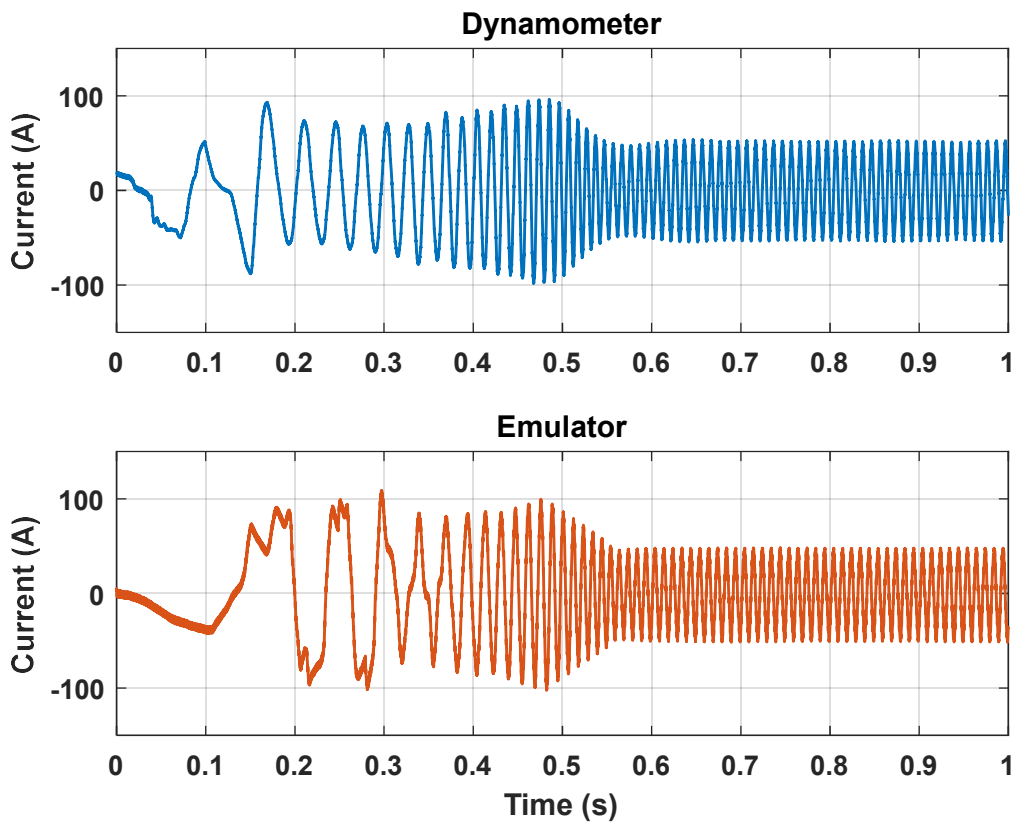


Fig 5.25 Phase A currents of PEBE and dyno from startup with 1500rpm and 4Nm of load torque

or speed instantly, which gives it a wide range of possibilities when it comes to testing faults that require extreme or irregular changes in torque, where the dyno is limited in terms of inertia.

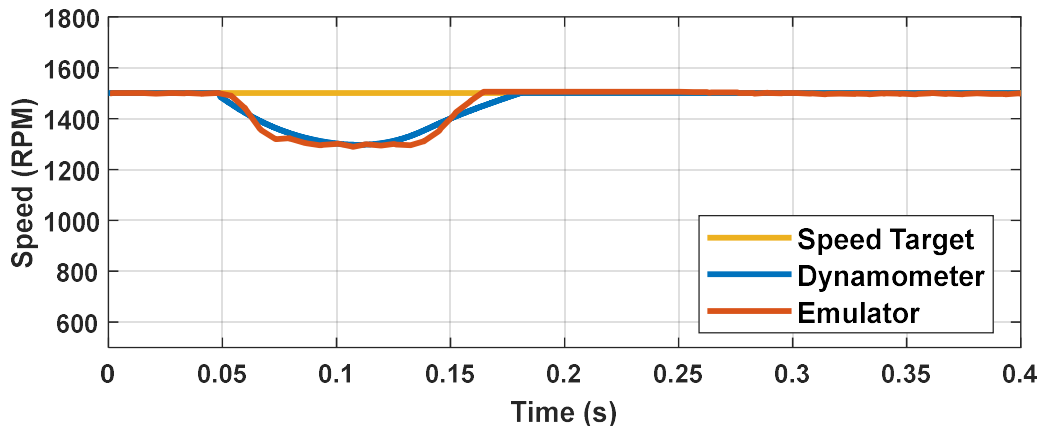


Fig 5.26 Speed response of PEBE and dyno at steady state 1500rpm and torque step of 8Nm

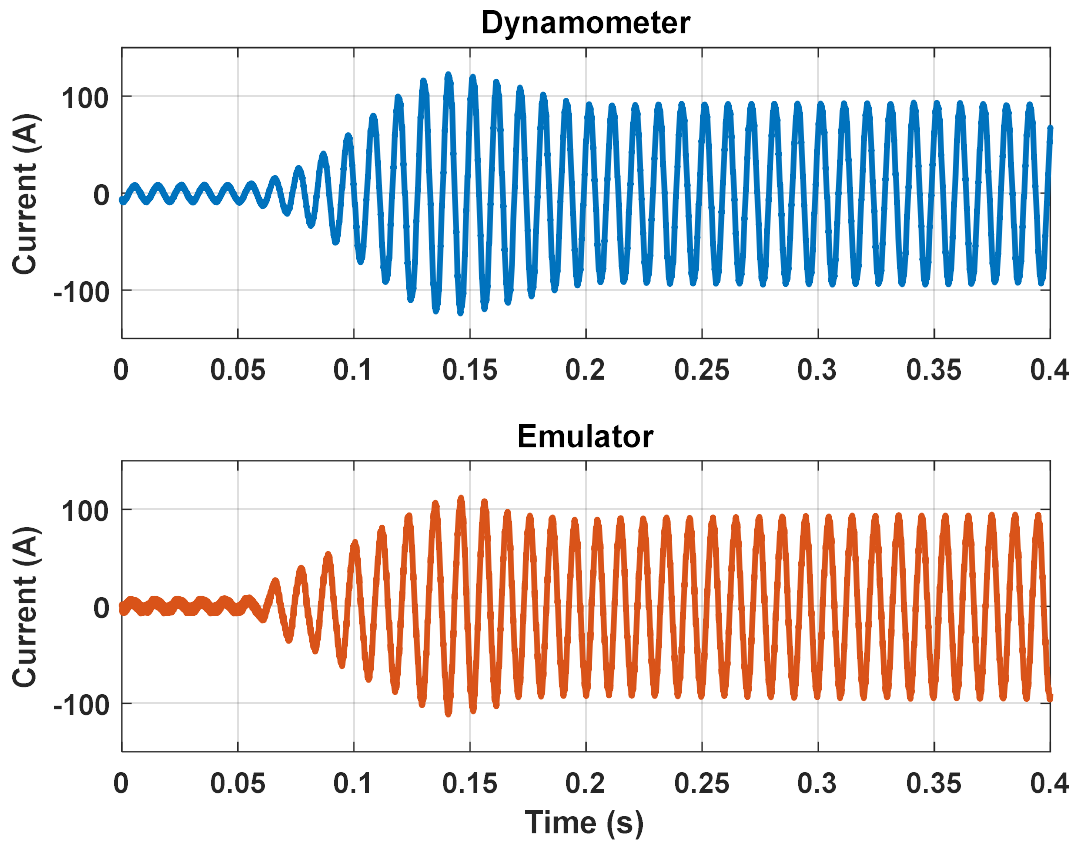


Fig 5.27 Phase A currents of PEBE and dyno at steady state 1500rpm and torque step of 8Nm

5.8 Discussion

This chapter presented the concepts of control, and electrical machine emulation for drive inverter systems. The main testing concept of HIL, PHiL, and dyno testing are discussed. PHiL is given more examination, discussing the subsets of this testing in the forms of PA based testbenches and PEBE testbenches. Finally, the software and hardware aspects of PEBE testbenches are discussed in terms of control and machine modelling in the software, along with power supply configuration and AC filtering in the hardware.

The proposed PEBE testbench has been shown that it can provide an effective response compared to a dyno in terms of control and in-the-loop power levels. Sensorless position control is also verified as functional, even with the physical PMSM being replaced with the proposed testbenches fully electrical configuration. Small differences are exhibited between startup, and the response of the emulator produces tend to be more linear when examining di/dt gradients due to the lack of inertia modelled into the electrical system to directly attempt to mimic the dyno. Behavioural differences such as current error between the two could be caused by the value of L_{link} , which has been shown to affect the operating bandwidth of emulators as it relates to torque (current), speed, and acceleration [5-20]. Using the torque characteristic expressed in (5.20), an evaluation of operating points in terms steady state torque and speed operating points of the machine is performed, with respective power draws from the DC sources of each testbench being measured. The power consumption of the proposed testbench is an important factor after its emulation performance, where optimally low power consumption contributes to a much cheaper, environmentally friendly testbench while using the single DC supply. While the dyno used in this case does not actively recirculate power, dyno testbenches are capable of doing so. Regardless of this, a recirculating dyno will have greater losses compared to the proposed emulator testbench given the additional machine losses along with converter losses that will be present, whereas the emulators losses will mainly be just its converter losses.

Fig 5.28 illustrates the operational torque-speed characteristic of the machine with test points highlighted in 100 RPM increments. These represent steady state operating points of the machine emulated in this work. Fig 5.29 illustrates the comparison between power consumption of the two setups at these steady state points. The proposed testbench has notably smaller power consumption, consistently drawing at least three times less power than the dynamometer while emulating the

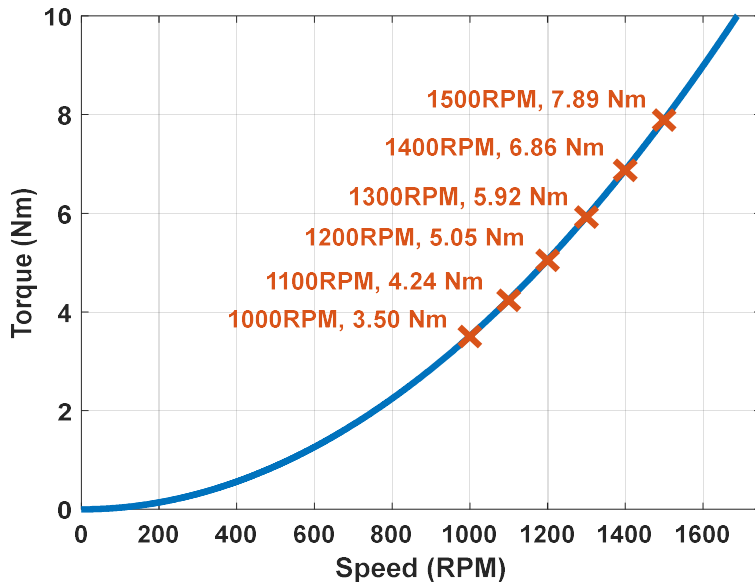


Fig 5.28 Operational torque-speed characteristic with test points highlighted

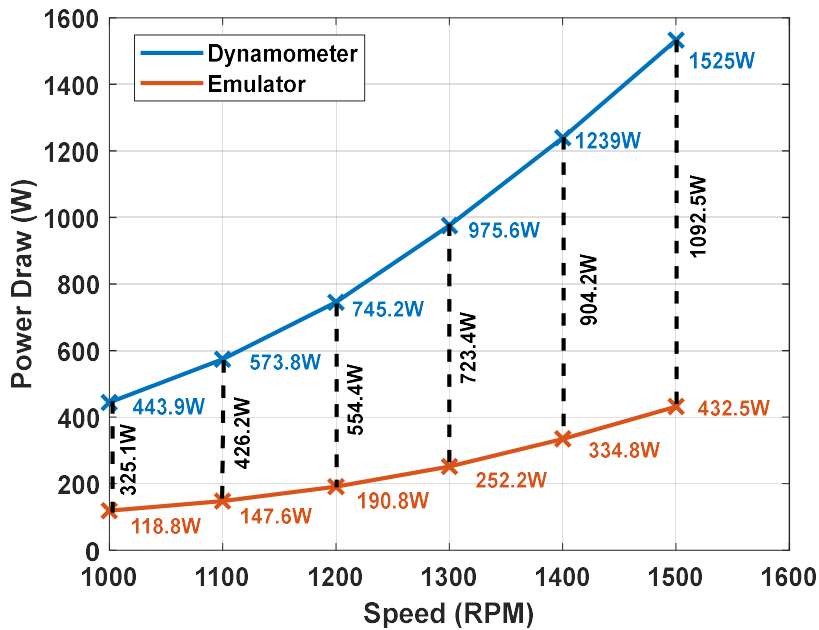


Fig 5.29 Power consumption at test points between dynamometer and emulator

same AC power levels. This is due to the presence of the mutual DC connection discussed in Section I, where current from the emulators DC end supplies the IUTs DC input and the DC supply only needs to supply the proposed testbenches losses. If circulating zero-sequence current is addressed, this is a superior choice as compared to a multiple DC source emulator, which will consume a closer amount of power to a dynamometer and require extra costs in hardware.

Regardless, an absolute analysis of the power consumption of the dynamometer would give an even greater power draw than any emulator configuration given in this case, the generator side source could not be accessed.

Drive system testing is typically carried out on a dynamometer testbench at some point in the development cycle, but it is well documented that this setup has limitations in mimicking the full dynamic behaviour of drive applications. The goal of an emulator testbench while providing a comparable response to a dynamometer should be to emulate the electrical machines behaviour in its given application. An example of this is torque characteristic demonstrated in the prior section but can extend to emulating expected load profiles in the application. While data for the application may not be available at the point of initial inverter/machine testing, commercial drive designs in many applications go through multiple design iterations over time, and it would be beneficial to have available an easily reconfigurable test setup. A point of future work could be further verification of the proposed test bench against data gathered from the operation of a machine in its application, emulating the behaviour on the proposed testbench and comparing the two datasets. Considering the testing capabilities of the proposed testbench, the implementation of electrical and/or mechanical faults could be considered in future. Literature has covered to a degree the emulation of electrical faults and potential failings in machine windings etc. on RTS systems, but there has been limited consideration beyond this. A comprehensive practical verification of a range of faults using the proposed testbench could be developed for use in inverter application safety testing in the design stage or End-of-Line full power testing. This could include faults which present themselves as highly non-linear changes in load torque which cannot be emulated by a dynamometer or electrical faults such as short or open circuits.

Overall, the design and verification of a compact, economical, commercially attractive machine emulating PHiL testbench capable of verifying position sensor and sensorless position based inverter control methods is proposed. It can be an important addition to the hardware and software testing of inverters across a range of applications. It is shown to be superior in many aspects to a dyno testbench, which is expensive, takes significant time to construct and is difficult to utilise, being limited testing a single machine specification without reconstructing the dynamometer. The

proposed testbench is also designed to optimize cost compared to other PHiL and PEBE testbench designs. The setup is composed of two identical commercial inverter modules. They are connected at DC inputs to a mutual DC source and connected at AC outputs through a link inductance, creating an easily reproducible setup which is efficient, by circulating current and only supplying losses in the system. The use of a microcontroller for control programming omits the cost of an RTS unit and allows an easily reprogrammable, simplified testbench setup which is assembled from a commercially designed inverter module without modification to circuitry. The proposed testbench has exhibited that it can provide near identical dynamic results to the dynamometer with the degree of detail in the system. While further refinement could be performed, challenging areas of operation for sensorless position control such as machine startup and dynamic behaviours are successfully emulated, and full rated power operation is achieved. It is also demonstrated that the proposed testbench consumes significantly less power. This reinforces the case that the low cost, repeatable setup that is proposed would be economically and practically beneficial in providing inverter testing capabilities. As future work, the results of the proposed testbench could be compared to results from a practical application to further examine the capabilities of the setup and verify the control software to its fullest capabilities. This would be done by utilising the torque characteristic used in Fig 6.22, which the emulator can toggle between with its emulated dyno inertia easily. Dyno setups are limited in this regard given their inflexible mechanical inertia which means that many load characteristics of machine applications cannot be emulated.

The testbench design is intended for drives that are driven using an inverter topology with three phases. A point of future investigation, or expansion of the emulator design could be the implementation of the capability to emulate machines with greater than three phases. This could be machines such as six-phase topologies of PMSMs for example, or the creation of a discretised per phase machine model for the driving of SRMs. This is because SRMs often use greater than three phases, which in their own right require unique converter designs differing from the standard three phase inverter if an emulator was to be created for such an application.

Summary

In this chapter, a novel microcontroller, power electronics based emulator testbench which is capable of verifying sensorless position control is presented. The testbench is designed using established principles of emulator testbenches as a modular, efficient testbench, which aims at

minimising cost, power consumption and provide ease of use for commercial applications. The testbench concept is first verified through simulation, and then verified experimentally. In constructing the testbench, two commercial inverter modules are used with no modification to circuitry, where the drive inverter is programmed with commercial sensorless position control. The operation of the testbench is assessed with a torque characteristic from the drive inverters commercial application and is shown to provide good quality of emulation. The testbench is then compared with a commercial dynamometer testbench, and is shown to provide a strong testing alternative, being significantly cheaper, consuming less power, and not being mechanically limited in its inertia.

References

- [5-1] B. K. Bose, "Global Energy Scenario and Impact of Power Electronics in 21st Century," in *IEEE Transactions on Industrial Electronics*, vol. 60, no. 7, pp. 2638-2651, July 2013.
- [5-2] Ramesh and N. C. Lenin, "High Power Density Electrical Machines for Electric Vehicles—Comprehensive Review Based on Material Technology," in *IEEE Transactions on Magnetics*, vol. 55, no. 11, pp. 1-21, Nov. 2019.
- [5-3] Sarbajit Paul, Pil-Wan Han, Junghwan Chang, Yon-Do Chun, Jae-Gil Lee, "State-of-the-art review of railway traction motors for distributed traction considering South Korean high-speed railway", in *Energy Reports*, vol. 8, pp. 14623-14642, Nov. 2022.
- [5-4] P. Roy, J. He, T. Zhao and Y. V. Singh, "Recent Advances of Wind-Solar Hybrid Renewable Energy Systems for Power Generation: A Review," in *IEEE Open Journal of the Industrial Electronics Society*, vol. 3, pp. 81-104, 2022.
- [5-5] K. Ma, S. Xia, Y. Qi, X. Cai, Y. Song and F. Blaabjerg, "Power-Electronics-Based Mission Profile Emulation and Test for Electric Machine Drive System—Concepts, Features, and Challenges," in *IEEE Transactions on Power Electronics*, vol. 37, no. 7, pp. 8526-8542, July 2022.
- [5-6] V. Karapanos, S. de Haan and K. Zwetsloot, "Real time simulation of a power system with VSG hardware in the loop," *IECON 2011 - 37th Annual Conference of the IEEE Industrial Electronics Society*, Melbourne, VIC, Australia, 2011.

- [5-7] J. S. Lee and G. Choi, "Modeling and hardware-in-the-loop system realization of electric machine drives — A review," in *CES Transactions on Electrical Machines and Systems*, vol. 5, no. 3, pp. 194-201, Sept. 2021.
- [5-8] J. Liu, Y. Miura and T. Ise, "Comparison of Dynamic Characteristics Between Virtual Synchronous Generator and Droop Control in Inverter-Based Distributed Generators," in *IEEE Transactions on Power Electronics*, vol. 31, no. 5, pp. 3600-3611, May 2016.
- [5-9] R. O. Nemeş, M. Ruba, M. R. Raia, C. Marţiş and C. A. Oprea, "X-in-the-Loop-Based High Accuracy Test Facility for Industrial Development of Electric Vehicles," in *IEEE Transactions on Transportation Electrification*, vol. 9, no. 2, pp. 2778-2791, June 2023.
- [5-10] S. N. Afrasiabi, R. Thike, K. S. Amitkumar, C. Lai and P. Pillay, "Comparative Study on Machine Emulation Systems Based on Switching Converters and Linear Power Amplifier Configurations," *2023 IEEE 14th International Conference on Power Electronics and Drive Systems (PEDS)*, Montreal, QC, Canada, 2023.
- [5-11] K. Ma, J. Wang, X. Cai and F. Blaabjerg, "AC Grid Emulations for Advanced Testing of Grid-Connected Converters—An Overview," in *IEEE Transactions on Power Electronics*, vol. 36, no. 2, pp. 1626-1645, Feb. 2021.
- [5-12] M. Ashourianjozdani, L. A. C. Lopes and P. Pillay, "Power Electronic Converter Based PMSG Emulator: A Testbed for Renewable Energy Experiments," in *IEEE Transactions on Industry Applications*, vol. 54, no. 4, pp. 3626-3636, July-Aug. 2018.
- [5-13] K. S. Amitkumar, R. S. Kaarthik and P. Pillay, "A Versatile Power-Hardware-in-the-Loop-Based Emulator for Rapid Testing of Transportation Electric Drives," in *IEEE Transactions on Transportation Electrification*, vol. 4, no. 4, pp. 901-911, Dec. 2018.
- [5-14] N. Sharma, Y. Liu, G. Mademlis and X. Huang, "Design of a Power Hardware-in-the-Loop Test Bench for a Traction Permanent Magnet Synchronous Machine Drive," *2020 International Conference on Electrical Machines (ICEM)*, Gothenburg, Sweden, 2020.
- [5-15] K. Saito and H. Akagi, "A Power Hardware-in-the-Loop (P-HIL) Test Bench Using Two Modular Multilevel DSCC Converters for a Synchronous Motor Drive," in *IEEE Transactions on Industry Applications*, vol. 54, no. 5, pp. 4563-4573, Sept.-Oct. 2018.
- [5-16] K. S. Amitkumar, P. Pillay and J. Bélanger, "An Investigation of Power-Hardware-in-the-Loop- Based Electric Machine Emulation for Driving Inverter Open-Circuit Faults,"

in *IEEE Transactions on Transportation Electrification*, vol. 7, no. 1, pp. 170-182, March 2021.

- [5-17] R. S. Kaarthik and P. Pillay, "Emulation of a permanent magnet synchronous generator in real-time using power hardware-in-the-loop," *2016 IEEE International Conference on Power Electronics, Drives and Energy Systems (PEDES)*, Trivandrum, India, 2016.
- [5-18] Y. Song, R. Cheng and K. Ma, "Mission Profile Emulator for Permanent Magnet Synchronous Machine in Voltage-Response Mode Based on Three-phase Power Electronic Converter," *2018 IEEE International Power Electronics and Application Conference and Exposition (PEAC)*, Shenzhen, China, 2018.
- [5-19] O. Vodyakho, M. Steurer, C. S. Edrington and F. Fleming, "An Induction Machine Emulator for High-Power Applications Utilizing Advanced Simulation Tools With Graphical User Interfaces," in *IEEE Transactions on Energy Conversion*, vol. 27, no. 1, pp. 160-172, March 2012.
- [5-20] N. Sharma, G. Mademlis, Y. Liu and J. Tang, "Evaluation of Operating Range of a Machine Emulator for a Back-to-Back Power-Hardware-in-the-Loop Test Bench," in *IEEE Transactions on Industrial Electronics*, vol. 69, no. 10, pp. 9783-9792, Oct. 2022.
- [5-21] K. Saito and H. Akagi, "A Real-Time Real-Power Emulator of a Medium-Voltage High-Speed Induction Motor Loaded With a Centrifugal Compressor," in *IEEE Transactions on Industry Applications*, vol. 55, no. 5, pp. 4821-4833, Sept.-Oct. 2019.
- [5-22] G. Mademlis, N. Sharma, Y. Liu and J. Tang, "Zero-Sequence Current Reduction Technique for Electrical Machine Emulators With DC Coupling by Regulating the SVM Zero States," in *IEEE Transactions on Industrial Electronics*, vol. 69, no. 11, pp. 10947-10957, Nov. 2022.
- [5-23] Paul Krause; Oleg Wasynczuk; Scott D. Sudhoff; Steven Pekarek, "Permanent-Magnet ac MachineS," in *Analysis of Electric Machinery and Drive Systems*, IEEE, 2013.
- [5-24] L. Zhang and H. Guo, "Power Hardware-in-the-loop Emulation System for Permanent Magnet Synchronous Machines," *2019 22nd International Conference on Electrical Machines and Systems (ICEMS)*, Harbin, China, 2019.
- [5-25] A. Schmitt, J. Richter, M. Gommeringer, T. Wersal and M. Braun, "A novel 100 kW power hardware-in-the-loop emulation test bench for permanent magnet synchronous machines

- with nonlinear magnetics," *8th IET International Conference on Power Electronics, Machines and Drives (PEMD 2016), Glasgow, UK, 2016.*
- [5-26] L. Stefanski, B. Schmitz-Rode, R. Schwendemann, N. Weis, A. Liske and M. Hiller, "Power Hardware-in-the-Loop Test Bench for Permanent Magnet Synchronous Machines based on a Parallel Hybrid Converter," *2022 IEEE 23rd Workshop on Control and Modeling for Power Electronics (COMPEL), Tel Aviv, Israel, 2022.*
- [5-27] Y. Li, W. Wang and P. Wang, "A Parallel Topology Based Power-Stage PMSM Emulator With Accurate Ripple Current Reproduced," in *IEEE Access*, vol. 10, pp. 57962-57973, 2022.
- [5-28] A. Schmitt, J. Richter, M. Braun and M. Doppelbauer, "Power Hardware-in-the-Loop Emulation of Permanent Magnet Synchronous Machines with Nonlinear Magnetics - Concept & Verification," *PCIM Europe 2016; International Exhibition and Conference for Power Electronics, Intelligent Motion, Renewable Energy and Energy Management, Nuremberg, Germany, 2016.*
- [5-29] Y. Liu, L. Ralikalakala, P. Barendse and P. Pillay, "Power Electronic Converter Based Induction Motor Emulator With Stator Winding Faults," in *IEEE Transactions on Industrial Electronics*, vol. 70, no. 5, pp. 4440-4449, May 2023.
- [5-30] A. Holczer, F. D. Freijedo and R. Bojoi, "Overview of Sensorless Control Strategies for Electric Vehicle Traction IPMSM," *2023 IEEE Workshop on Electrical Machines Design, Control and Diagnosis (WEMDCD), Newcastle upon Tyne, United Kingdom, 2023*
- [5-31] L. Bigarelli, M. di Benedetto, A. Lidozzi, L. Solero and P. J. Grbovi, "FPGA-Based Permanent Magnet Synchronous Machine Emulator With SiC Power Amplifier," in *IEEE Transactions on Industry Applications*, vol. 57, no. 6, pp. 6117-6130, Nov.-Dec. 2021.
- [5-32] Y. Luo, M. A. Awal, W. Yu and I. Husain, "FPGA-Based High-Bandwidth Motor Emulator for Interior Permanent Magnet Machine Utilizing SiC Power Converter," in *IEEE Journal of Emerging and Selected Topics in Power Electronics*, vol. 9, no. 4, pp. 4340-4353, Aug. 2021.
- [5-33] D. Wang, S. Ge, Q. Li, H. Sun and P. Xu, "A Novel Control Scheme for the Electric Motor Emulator to Improve the Voltage Emulation Accuracy," in *IEEE Transactions on Power Electronics*, vol. 39, no. 1, pp. 374-383, Jan. 2024.

- [5-34] M. Fischer, P. Kemper and J. Herbold, "High Performance Power Hardware-in-the-Loop Testing of Traction Inverters at High Voltage Levels," *2022 IEEE 13th International Symposium on Power Electronics for Distributed Generation Systems (PEDG)*, Kiel, Germany, 2022.
- [5-35] Y. Inaba, S. Cense, T. O. Bachir, H. Yamashita and C. Dufour, "A dual high-speed PMSM motor drive emulator with Finite Element Analysis on FPGA chip with full fault testing capability," *Proceedings of the 2011 14th European Conference on Power Electronics and Applications*, Birmingham, UK, 2011.
- [5-36] Pollock, Charles, and Helen Pollock. "Controller for electrical machines." U.S. Patent 8,970,146 issued March 3, 2015.

Chapter 6

Conclusions and Future Work

This chapter summarizes the research carried out in this thesis, highlighting the author's contributions. Possible avenues of topics for future research are then presented.

6.1 General conclusions

Chapter 1 gives an overview of the thesis, briefly explaining the motivations for performing the research. As a promising candidate topology for improvement as it relates to efficiency and cost, the SRM and its accompanying drive are selected. Methodologies for drive system verification are also considered, where PEBE testbenches are discussed. As one of if not the most popular and currently accepted superior machine topology used in a variety of applications along with interest from industrial partners, PEBE testing methodology for PMSM drive systems is chosen.

Chapter 2 presents the operating principles behind SRM drive systems including considerations when designing them, firstly discussing SRM fundamentals of torque production, energy conversion in the machine, its non-linear inductance profile and finally, the tangential and radial force production in the rotor along with their structure as it relates to these characteristics. Modelling of the SRM is then considered, introducing a basic equivalent circuit of the machine and highlighting the need for FEA based modelling due to high non-linearity. Using this modelling, it is then explained how the SRM is controlled, TSFs are then demonstrated as a commonly used control scheme to highlight how multi-phase torque sharing is used to eliminate phase commutation torque ripple. Finally, SRM drive converters are discussed in terms of structure and how they apply voltage to the SRMs phase windings. The most common converter and best performing topologies are discussed and compared, in relation to the characteristics that are desired for SRM drive converters.

In Chapter 3, three common power semiconductor device types (SJ MOSFET, SiC MOSFET, Si IGBT) used in traction drive converters are discussed in terms of their cost, required drive circuitry,

operating characteristics inherent to their device structures, and losses (Conduction and Switching) which arise in operation. Three specific device models which have similar characteristics, are then compared experimentally using a drive converter designed for SRMs, where their losses are rudimentally measured using a non-discretised thermal superposition method. From the chosen devices and limited operating scenario, the SJ MOSFET is shown to be a lower loss, cheaper alternative to SiC MOSFETs, where across multiple current levels and switching frequencies consistently lower losses are exhibited of at least 3W. Notably though the study is limited, and for a definitive conclusion on the superior device for application into SRM drives would require more expansive experimentation using a full SRM and its drive in operation.

Chapter 4 proposed a novel current profiling method for minimal phase rms currents and ZTR across the full rated speed range of an SRM, which utilises a novel GA design in conjunction with delayed turn-on angles and multi-phase (two-phase and greater) torque sharing. Optimal rms currents are obtained by firstly introducing the theoretically minimum rms current any SRM capable of two phase torque sharing can attain, which is calculated by removing voltage constraints and calculating optimal torque sharing at each discrete angular point. This is then used as an rms current target for optimisation, but also should be applied to any control scheme aiming to minimise rms current as a benchmark.

Using this target rms current, a GA is designed which optimises randomly generated current profiles at a given speed and load torque, producing a set of optimal current profiles which range from 0.04% higher than the theoretically minimum rms current at low speed to 4.3% at the rated speed of an 8/6 SRM at 1500rpm, while eliminating commutation TR to less than 1%. The current profiles are deployed into a LUT based control scheme, which is simulated on MATLAB/SIMULINK, providing speed control, and linearising the non-linear torque production of the SRM, while maintaining ZTR and the rms currents of the profiles.

In Chapter 6, common verification methods used for drive converters, including dyno testbenches, HiL, PA-based PHiL and PEBE are all discussed in varying levels of details. From this, a PEBE testbench is proposed which is aimed at deployment in commercial drive converter verification. The testbench is an efficient, modular testbench which can be assembled from drive inverter modules and one DC supply with accompanying filtering between the AC connections. The emulator control software is programmed on a commercial inverters microcontroller unit, which

with the accompanying hardware design allows the testbench to be fabricated with no additional modification to circuitry, and avoids the use of expensive RTS and FPGA units. To verify the testbench, commercial sensorless position control software is programmed onto the IUT, which is demonstrated in a simulation and experimental context for a commercial PMSM drive inverter. The testbench is then compared with a dyno testbench, showing the ability to closely mimic the dynos inertia with full power in the inverter hardware while being significantly more efficient where it is at least 2.7 to 3.5 times more efficient at given operating points. The testbench is also programmed with the application torque characteristic of the PMSM, highlighting the advantage of the use of electrical-based inertia over the mechanical inertia of the dyno.

6.2 Author's Contribution

The thesis contributions can be summarised as follows:

1) *Drive Converter:*

- A comparison is carried out between SiC MOSFETs, SJ MOSFETs and Si IGBTs, which are common device choices used in SRM drives, consisting of a theoretical comparison as it relates to desirable characteristics for an SRM drive along with an approximation of switching losses between the devices. A limited experimental efficiency comparison is then presented which produces said device losses in a non-discretised fashion

2) *Drive Control:*

- A novel method is proposed which calculates the theoretically minimum rms phase current for a given load torque with ZTR, that is possible for any given SRM configuration capable of at least two-phase torque sharing.
- This provides a useful benchmark for any control scheme, which will gauge its torque production efficiency (effective power efficiency) to evaluate its performance. It is also useful for control scheme design for any method which aims to minimise rms current, where optimisation based methods can have a target rms which is known to be optimal.
- A GA current profiling design is proposed which minimises rms current and eliminates commutation torque ripple and can also extend the ripple free speed range of a given SRM.

- The GA uses delayed turn-on angles, and the inherent functionality of GAs to optimise rms currents as a single objective problem with the theoretically minimum rms current as a target, while also fully utilising DC supply voltage and maintaining ZTR.
- It introduces intentional greater than two-phase overlap, demonstrating three-phase torque overlap in this case, to extend the ripple free speed range of an SRM to match its full rated speed by allowing optimal current profile decay while compensating negative torque production with positive torque producing phases.

3) *Drive Verification:*

- A PEBE testbench is proposed which utilises a singular DC supply and modular commercial inverters with no alterations to circuitry, to provide a cheap, cost efficient testbench.
- The emulator control is programmed onto a microcontroller unit contained within the inverter modules and provides significant reduction in cost and ease of use compared to the use of RTS units and testbenches which require design of bespoke inverter circuitry.
- Sensorless position control is verified using the proposed testbench, while requiring no physical connection between inverter modules, demonstrating that PEBE testbenches are capable of verifying inverters programmed with both position sensor control and sensorless position control.

6.3 Future Work

1) *Drive Converter:*

- While three switching device types have been investigated, only one model of each type has been used, a more definitive analysis could be performed using more models of each device type, which may yield more insightful results on the cost/efficiency.
- GaN FET devices as a family have matured in recent years and have begun being deployed in more applications, the analysis could include these devices to examine their cooling requirements and cost/efficiency.
- For consideration of the truly optimal switching device choice for an SRM drive, a further experimental study can be carried out which utilises the converter used in the study, with an actual SRM. In this, a mission profile of the SRM in a given application could be

applied, where optimised switching devices and their drive circuitry could be compared for a measure of losses in operation and overall efficiency of the drive.

2) *Drive Control:*

- Only the minimisation of rms current has been investigated as a part of the GA design, a multi-objective GA could be design which can examine if minimising both rms current and peak currents would yield the same set of profiles, or different results.
- The GA produces current profiles which are used as an offline control scheme. It can be seen that the profiles show correlation in their shape, and therefore it could be examined whether an online control scheme could be created which could mathematically describe this shape of current profile and remove the need for the GA.
- Different meta heuristic optimisation techniques could be examined, to gauge the quality of the GAs results as it relates to how optimal can the results become as it relates to the theoretically minimum rms current.
- The ripple free speed range boundaries (and optimal rms currents) could be established, using the presented GA while incorporating DC link voltage boosting.

3) *Drive Verification:*

- The proposed testbench could be developed further to demonstrate fault states related to either mechanical faults or electrical for drive safety testing.
- While zero sequence current is low in this use case, software based suppression techniques could be analysed to ensure consistent low zero sequence current when verifying any specification of PMSM or other machine.
- To fully test the proposed testbenches emulation quality, it could be compared with the application PMSMs mission profile from its actual use case, which could offer insights on improving the emulator software.
- While the PMSM topology is has been the main focus of this work, a more generalised emulator could be designed based upon the standard three phase inverter, which can toggle between the testing of multiple topologies such as an IM, or SynRM. Along with this, the suitability of a three phase inverter for the emulation of SRMs could be investigated, and it can be established whether the design could be used, or an esoteric emulator design would be required.

Appendix A

Main SRM Specifications

This appendix gives the specifications of the SRM used in simulations

Table A.1 SRM SPECIFICATIONS

| Parameter | Value |
|--|--------------|
| No. of motor phases m | 4 |
| Stator/rotor poles N_s/N_r | 8/6 |
| Number of turns per pole N | 90 |
| Rated voltage | 415V |
| Phase resistance R | 0.8 Ω |
| Stack length | 155mm |
| Shaft radius | 15mm |
| Rotor outer radius | 45mm |
| Thickness of rotor yoke | 15mm |
| Ratio of rotor pole arc to pole pitch | 0.35 |
| Length of air gap | 1mm |
| Stator inner radius | 46mm |
| Stator outer radius | 83mm |
| Thickness of stator yoke | 12mm |
| Ratio of stator pole arc to pole pitch | 0.42 |

Appendix B

Main PMSM Specifications

This appendix gives the specifications of the PMSM used in simulations and experimentation

Table B.1 PMSM SPECIFICATIONS

| Parameter | Value |
|------------------------------|--------------------------|
| No. of motor phases m | 3 |
| Rated Torque | 8 Nm |
| Rated Speed | 1500 RPM |
| Rated Frequency | 50 Hz |
| RMS Current | 70A |
| DC Operational Voltage Range | 24-48V |
| Pole Pairs | 4 |
| Stator Phase Resistance | 0.012 Ω |
| d-axis inductance | 0.47mH |
| q-axis inductance | 0.47mH |
| Rotor Inertia | 0.000358kgm ² |
| Flux Linkage Constant | 0.0161Vs |

Appendix C

Experimental Emulator Testbench

This appendix gives a description of the experimental emulator testbench constructed to verify the testbench design proposed in chapter 6, a photograph of this testbench is given in Fig C.1

The main components of this testbench are:

- DC Supply
- Filtering inductance L_{link}
- Inverter modules IUT and EMU

Internally within the inverter modules:

- Microcontroller
- Gate driving circuitry
- Current sensor circuitry

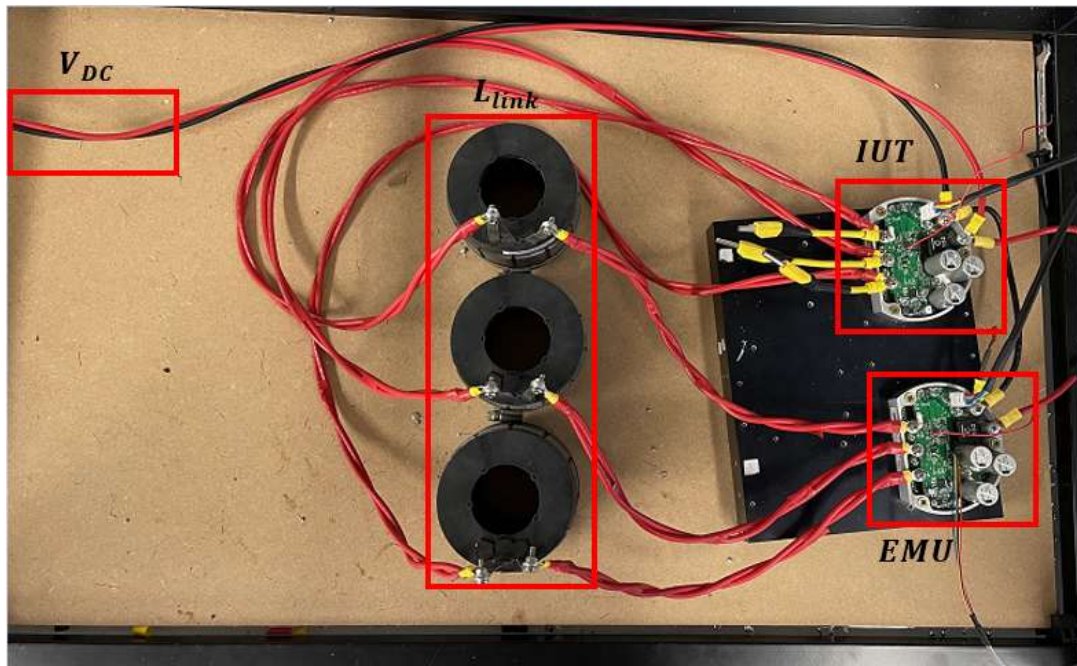


Fig. C.1 Experimental Sensorless Emulator Testbench

I. Filtering Inductance

Each phase of the testbenches three phases is connected with inductance L_{link} , which is chosen in this case as stators from the PMSM that is being emulated in this work, shown in Fig C.2 . These are chosen for their proximity to L_{dq} of the PMSM, along with their characteristics of being unlikely to saturate electrically or thermally during operation of the testbench.

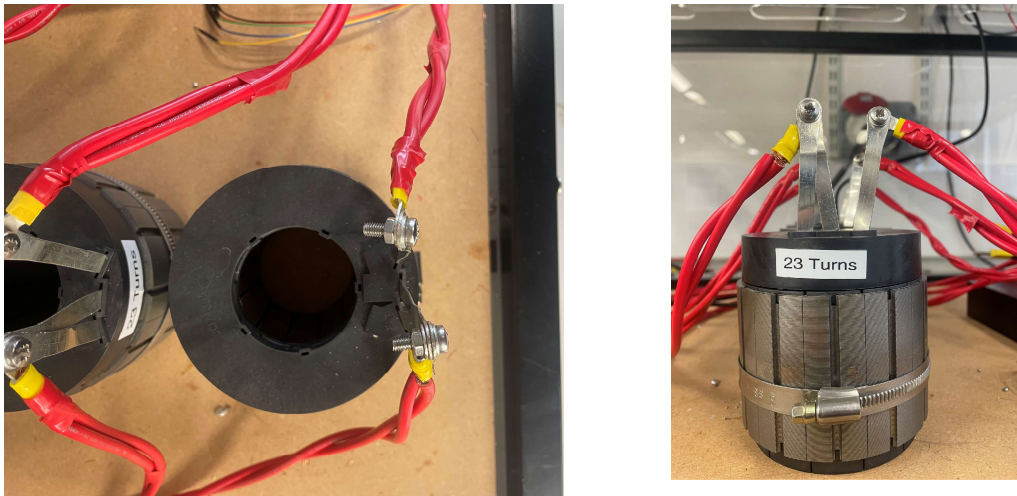


Fig. C.2 In-circuit microcontroller

II. Microcontroller

The microcontroller is utilised to provide the control functionality in the system, receiving measured data from the inverters sensors and producing gate drive PWM signals for the six switches in the inverter bridge legs. The Microcontroller used in this work is a dsPIC33CK128MP503 shown in-circuit in Fig C.3. The relevant parameters of the microcontroller are given in Table C.1, and it was chosen given it is a sufficiently power control unit for programming the emulator software, containing enough storage space along being cost efficient and economic.

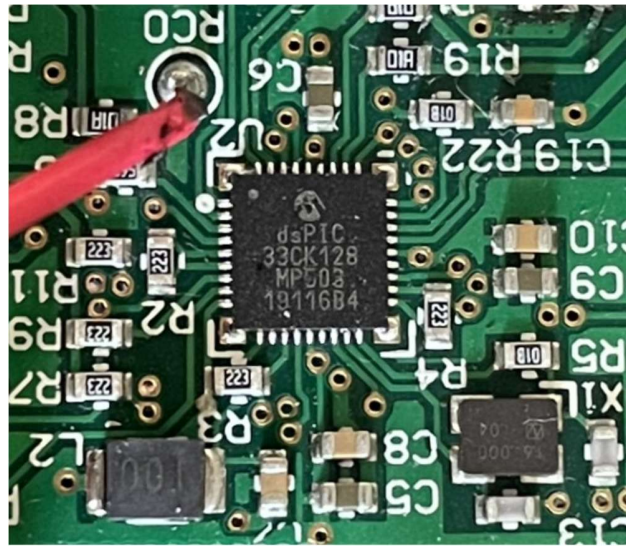


Fig. C.3 In-circuit microcontroller

TABLE C.I
DSPIC33CK128MP503 PARAMETERS AND USAGE

| Parameter | Value | Unit |
|------------------|-------|------|
| Unit Price | 3 | £ |
| Cores | 1 | |
| Processing Power | 100 | MHz |
| Program Memory | 128 | kB |
| PWM Frequency | 16 | kHz |
| Sampling Rate | 16 | kHz |
| RAM | 24 | kB |

III. Gate Driving

The gate driving circuitry used for isolating the power stage switching devices from the microcontroller and deliver gate signals to control the devices are shown in Fig C.4.

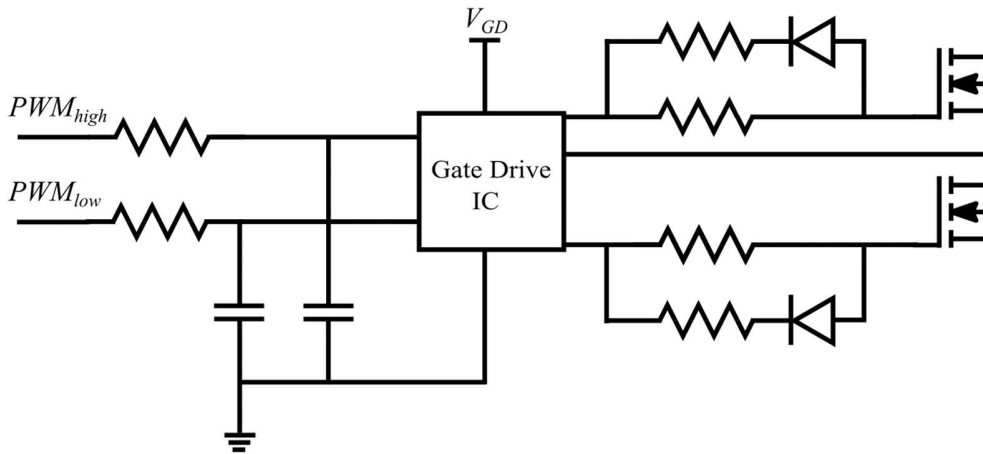


Fig. C.4 Gate drive circuitry

IV. Current Sensing

The current sensing in each inverter is carried out using low side current sense circuitry in each phase. The circuit is shown in Fig C.5, where the current op-amp is located internally within the microcontroller. Current is calculated by measuring voltage across sensing resistor using:

$$V_{out} = \left(1 + \frac{R_1}{R_2}\right) V_1$$

Current is then calculated using:

$$I = \frac{V_1}{R_{sense}}$$

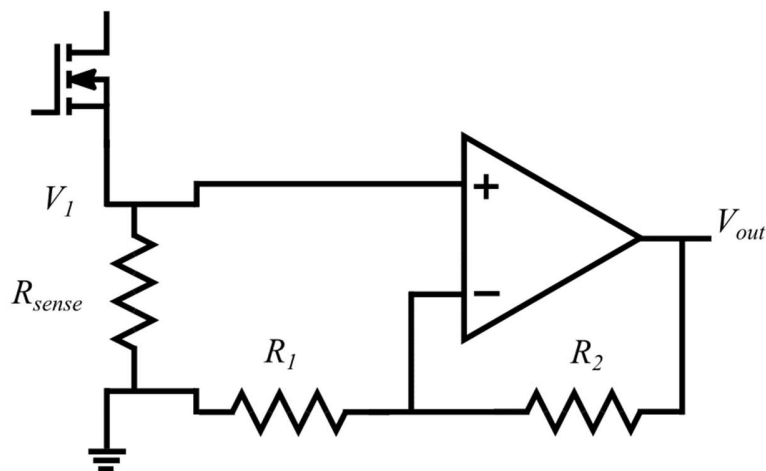


Fig. C.5 Current sense circuitry

Appendix E

List of Figs

| | |
|--|----|
| Fig 1.1 Generalised electrical drive system | 17 |
| Fig 1.2 Generalised dynamometer testbench | 19 |
| Fig 1.3 Generalised PHiL testbench | 20 |
| Fig 2.1 Axial view of a four phase, 8/6 SRM..... | 25 |
| Fig 2.2 General SRM λ - I characteristic | 26 |
| Fig 2.3 General SRM L - θ characteristic for a given phase..... | 29 |
| Fig 2.4 SRM rotor force production | 30 |
| Fig 2.5 SRM per-phase equivalent circuit | 31 |
| Fig 2.6 SIMULINK model of an SRM phase..... | 32 |
| Fig 2.7 SRM torque speed characteristic | 33 |
| Fig 2.8 Constant speed SRM operation | 34 |
| Fig 2.9 Nm/A efficiency across conduction period for an 8/6 SRM | 35 |
| Fig 2.10 Torque sharing functions torque profiles..... | 38 |
| Fig 2.11 TSF torque control scheme for an 8/6 SRM..... | 40 |
| Fig 2.12 C-Dump Converter | 42 |
| Fig 2.13 Sood Converter | 43 |
| Fig 2.14 H-Bridge Converter | 43 |
| Fig 2.15 Four phase ASHB converter..... | 44 |
| Fig 2.16 Four phase common phase ASHB converter..... | 44 |
| Fig 2.17 Bridge converter switching states..... | 45 |
| Fig 2.18 Typical phase current and voltage waveforms using CCC operation | 46 |
| | |
| Fig 3.1 Standard bridge-leg for driving one phase of a standard machine. | 51 |
| Fig 3.2 Power device output capacitance (Coss) QV characteristics. | 53 |
| Fig 3.3 Experimental power loss vs switching frequency | 55 |
| Fig 3.3 Reconfigurable test rig for SRM drive circuits. | 57 |
| Fig 3.4 Experimental circuit configurations | 58 |

| | |
|---|----|
| Fig 3. 5 Physical experimental test circuits | 58 |
| Fig 3.6 Schematic of gate drive circuits used in experimental test rig | 59 |
| Fig 3.7 Experimental power loss vs switching frequency | 60 |
| Fig 4.1 Two-phase overlap regions with maximum available θ_{ov} | 68 |
| Fig 4.2 Ansys Maxwell FEA data relating T-I- θ for a 4kW 8/6 SRM..... | 69 |
| Fig 4.3 KCu values, Phase A and Phase B currents indicating the optimal overlapping current pairing at 39.5° and 54.5°..... | 71 |
| Fig 4.4 Currents and KCu values across the full conduction period with optimal currents (with ZTR) | 72 |
| Fig 4.5 Currents across full conduction period with optimal currents..... | 73 |
| Fig 4.6 Theoretically optimal current profile..... | 73 |
| Fig 4. 7 Theoretically optimal current profile: (a) Torque waveforms (b) Flux linkage waveforms | 74 |
| Fig 4.8 Optimal profiles at different torque levels..... | 76 |
| Fig 4.9 3D surf plot of optimal current profiles with decreasing load torques..... | 77 |
| Fig 4.10 Ansys Maxwell FEA data relating λ -I- θ for a 4kW 8/6 SRM..... | 78 |
| Fig 4. 11 Inherent limits on current profiles for FLT, ZTR and voltage constraints at 1000rpm. 80 | |
| Fig 4.12 Upper and lower current limit envelopes at 1000rpm | 80 |
| Fig 4.13 Upper and lower current limit envelopes at 1080rpm, illustrating two phase overlap boundary speed | 81 |
| Fig 4.14 Upper and lower current limit envelopes at 1020rpm, illustrating boundary speed when θ_{on} is advanced | 82 |
| Fig 4.15 Upper and lower current limit envelopes at 1080rpm, illustrating boundary speed when θ_{on} is delayed..... | 82 |
| Fig 4.16 Upper and lower current limit envelopes at 1000rpm, when advancing θ_{on} | 83 |
| Fig 4.17 Upper and lower current limit envelopes at 1000rpm, when delaying θ_{on} | 83 |
| Fig 4.18 Average Nm/A efficiency with changing speeds and θ_{on} | 84 |
| Fig 4.19 Effect of delaying θ_{on} to optimal value on current boundary limit envelopes..... | 85 |
| Fig 4.20 Visual explanation of the mathematical process of the branching method | 86 |
| Fig 4.21 Optimal Profiles across 200-1000RPM using the branching method | 88 |
| Fig 4.22 Optimal profiles generated at 1000rpm using the 'Branching' method..... | 89 |

| | |
|---|-----|
| Fig 4.23 Crossover using binary string population genes..... | 93 |
| Fig 4.24 Mutation using binary string population genes | 93 |
| Fig 4.25 Overview of proposed GA process..... | 97 |
| Fig 4.26 Population generation for the GA at 200rpm | 98 |
| Fig 4.27 Crossover Stage carried out at 200rpm for two population members | 100 |
| Fig 4.28 Mutation Stage carried out at 200rpm | 102 |
| Fig 4.29 Initial GA generated profile at 200rpm | 103 |
| Fig 4.30 GA generated optimal profile at 200rpm..... | 104 |
| Fig 4.31 GA optimal profile from 0-500rpm | 105 |
| Fig 4.32 GA optimal profile from 500-1000rpm..... | 106 |
| Fig 4.33 Comparison between the GA and the Cos TSF at 1000rpm | 108 |
| Fig 4.34 GA ripple free speed range and rated $T-\omega$ curve..... | 109 |
| Fig 4.35 GA optimal profiles at highlighted torque levels | 110 |
| Fig 4.36 Three-phase conduction boundaries with reference to two-phase torque sharing..... | 111 |
| Fig 4.37 Three-phase FLT Speed limit envelopes at 1230rpm by delaying $\theta_{off3\phi}$ | 112 |
| Fig 4.38 Three-phase FLT Speed limit envelopes at 1130rpm by advancing $\theta_{on3\phi}$ | 113 |
| Fig 4.39 Three-phase FLT Speed limit envelopes at 1500rpm..... | 113 |
| Fig 4.40 Three-phase FLT Speed limit envelopes at 1600rpm..... | 114 |
| Fig 4.41 Overview of augmented GA process..... | 115 |
| Fig 4.42 Three phase GA population generation at 1200rpm..... | 116 |
| Fig 4.43 Three phase crossover stage performed at 1200rpm for two population members:..... | 118 |
| Fig 4. 44 Three phase mutation stage carried out at 1200rpm..... | 119 |
| Fig 4.45 GA Current profiles from 1100 to 1500rpm..... | 120 |
| Fig 4.46 GA produced profiles from 0 to 1500rpm | 122 |
| Fig 4.47 GA current profiling linear control scheme..... | 122 |
| Fig 4.48 Results of control scheme in two-phase overlap regions at 800 rpm: | 124 |
| Fig 4.49 Results of SRM Drive..... | 126 |
| Fig 4.50 Results of SRM Drive with applied torque steps | 127 |
| Fig 4.51 Results of Cos TSF at 1500rpm: (a) Currents and (b) Torques..... | 128 |
| Fig 4. 52 GA ZTR speed range and machine $T-\omega$ curve. | 131 |
| Fig 5.1 Dynamometer testbench | 136 |

| | |
|---|-----|
| Fig 5.2 HiL testbench..... | 137 |
| Fig 5.3 Power amplifier based PHiL testbench | 138 |
| Fig 5.4 Power electronics based PHiL testbench..... | 139 |
| Fig 5.5 PEB testbench filtering arrangements | 140 |
| Fig 5.6 Testbench power supply arrangements..... | 141 |
| Fig 5.7 Emulating inverter utilising | 144 |
| Fig 5.8 Proposed PEBE testbench | 146 |
| Fig 5.9 Implemented three phase inverter with current sense circuitry..... | 147 |
| Fig 5.11 JMAG data relating dq axis current to..... | 150 |
| Fig 5.10 Proposed PEBE control | 150 |
| Fig 5.13 Diagram of stator rotating reference frame | 152 |
| Fig 5.12 Proposed PEBE control | 152 |
| Fig 5.14 PMSM stator equivalent circuit..... | 153 |
| Fig 5.15 Modelled emulator testbench..... | 155 |
| Fig 5.17 Simulated phase A current with a command of 1500rpm | 156 |
| Fig 5.16 Simulated control response with a command of 1500rpm | 156 |
| Fig 5.18 Simulated phase A voltages with a command of 1500rpm | 157 |
| Fig 5.19 Experimental sensorless emulator testbench | 158 |
| Fig 5. 20 Proposed PEBE testbench three phase currents through oscilloscope | 159 |
| Fig 5. 22 Experimental phase A current with a command of 1500rpm and application torque profile | 160 |
| Fig 5.21 Speed response of emulator from startup with application torque profile | 160 |
| Fig 5. 23 Experimental dynamometer testbench..... | 161 |
| Fig 5. 24 Speed response of PEBE and dyno from startup with 1500rpm and 4Nm of load torque | 162 |
| Fig 5.25 Phase A currents of PEBE and dyno from startup with 1500rpm and 4Nm of load torque | 162 |
| Fig 5.26 Speed response of PEBE and dyno at steady state 1500rpm and torque step of 8Nm | 163 |
| Fig 5.27 Phase A currents of PEBE and dyno at steady state 1500rpm and torque step of 8Nm | 163 |
| Fig 5.28 Operational torque-speed characteristic with test points highlighted..... | 165 |

Fig 5. 29 Power consumption at test points between dynamometer and emulator..... 165

Appendix F

List of Tables

| | |
|---|-----|
| Table 1.1 Analytical comparison between candidate machine topologies | 18 |
| Table 2. 1 Comparison of SRM control methods for TR mitigation and control..... | 37 |
| Table 3.1 Approximated device losses | 56 |
| Table 3.2 Power semiconductor device data..... | 59 |
| Table 4.1 Current Pairings selections at 39.5°and 54.5° for TLoad of 25Nm | 70 |
| Table 4.2 Characteristics of GA produced optimal profiles from 0-1000rpm..... | 107 |
| Table 4.3 Characteristics of GA produced optimal profiles from 0-1000rpm..... | 110 |
| Table 4.4 Characteristics of GA produced optimal profiles from 0-1500rpm..... | 121 |
| Table 4.5 Performance Comparison of Recent SRM Publications..... | 130 |

Appendix G

Publications

- [1] E. Macrae, R. Pollock, N. McNeill, D. Holliday, K. Ahmed and B. W. Williams, "Experimental efficiency comparison of a superjunction MOSFET, IGBT and SiC MOSFET for switched reluctance machine drives," *11th International Conference on Power Electronics, Machines and Drives (PEMD 2022)*, Hybrid Conference, Newcastle, UK, 2022

Abstract: The IGBT and fast recovery diode are normally the preferred power semiconductor devices in machine drive power converters. High efficiency in the power converter reduces its cooling requirements and its consequent mass and volume. To attain high efficiencies, SiC devices are increasingly being considered as alternatives to the silicon IGBT and fast recovery diode. Another alternative would be the silicon SJ MOSFET, but because of its intrinsic diode and output capacitance characteristics, it is normally precluded from use in simple hard-switched machine drive applications. In switched reluctance machine drives, which differ from most machine drive power converters, the performance advantages of devices which may be considered the obvious choice are not distinct. This study compares the performance and power losses of three switching devices in a practical switched reluctance machine drive and shows that the silicon SJ MOSFET is the most suitable choice.

- [2] E. MacRae, A. Abdel-Aziz, K. Ahmed, R. Pollock and B. W. Williams, "Genetic Algorithm Based Approach of SRM Current Profiling for Torque Control and Minimal Copper Losses," *2023 IEEE International Electric Machines & Drives Conference (IEMDC)*, San Francisco, CA, USA, 2023

Abstract: This paper presents a novel approach to current profiling for switched reluctance machines that eliminates torque ripple while inherently guaranteeing minimum copper losses, along with linear torque control. Minimization of copper losses increases machine efficiency, while eliminating torque ripple is the pre requisite for SRM use in applications such as traction vehicles. This paper presents theoretical optimal current profiles, initially without consideration

of DC link voltage limitations. Utilizing a Genetic Algorithm in conjunction with current profiling limit envelopes, an optimized set of current profiles across the torque ripple free speed range of an exemplary 8/6 SRM is then created. The profiles characteristics are analysed and compared with commonly used torque sharing function control to confirm the merits of the proposed method.

- [3] E. MacRae, A. Abdel-Aziz, K. Ahmed, R. Pollock and B. W. Williams, “Genetic Algorithm Based Approach for Torque Control and Increased Efficiency Across an Optimised Speed Range in Switched Reluctance Drives” *IET Power Applications*, Vol. 18, Issue 12, Dec 2024

Abstract: This paper presents a novel Genetic Algorithm design for current profiling in switched reluctance machines that eliminates torque ripple while inherently guaranteeing minimal rms currents across the machines speed range. Minimising rms current provides an increase to machine efficiency and the elimination of torque ripple is required for potential SRM applications such as traction vehicles. This paper proposes a novel method for intentional greater than two-phase overlap in the algorithm design. This allows any SRM configuration capable of three or more phase overlap to utilise its full speed range with zero torque ripple, in the case where it is limited using two-phase torque sharing. An optimal set of current profiles is created using the algorithm across the full speed range of an exemplary 8/6 SRM and these are analysed. A current profiling-based control scheme using these results is then proposed and simulated for the 8/6 SRM. This is then compared to classical and recently published SRM control methods to highlight the merits of the overall genetic algorithm design and its resultant control scheme.

- [4] E. MacRae, C. Pollock, H. Pollock, R. Pollock, A. Abdel-Aziz, K. Ahmed and B. W. Williams, “Electronic Machine Emulation for Inverters with Position Sensorless Control” *Planned Submission at a 2025 Conference*

Abstract: Power electronics and software testing are a vital part of any product development. Motor emulation is growing rapidly in industry as an alternative to inverter testing setups such as dynamometers, given its attractive features of no mechanical elements, cost, simplicity in construction etc. Emulation allows for a second inverter to emulate motor loading, allowing

for low-cost testing to be done without the need of the full application or dynamometer setup. This paper proposes an emulator setup with two inverters using a shared DC source and connected with a coupling inductance on the AC side. The inverter-under-test is operated with position sensorless control. The emulator is deployed using a dsPIC33C microcontroller architecture, which has multiple benefits compared to real time simulators, including significant cost reduction and the ability to program onto commercially designed inverters without circuit modification. Therefore, the proposed hardware design produces an inexpensive, efficient, compact emulator testbench aimed at drive testing. Experimental verification of the proposed setup is carried out using position sensorless control on the emulator and dynamometer testbench for an e-mobility application permanent magnet synchronous machine. Dynamic behaviour of emulator and inverter under test is examined and steady state power analysis at various operating points is compared.